Aerodynamics and propulsion of synthetic jet based micro air vehicles

Whitehead, James Anthony

Award date:
2004

Awarding institution:
University of Bath

AERODYNAMICS AND PROPULSION OF SYNTHETIC JET BASED MICRO AIR VEHICLES

James Anthony Whitehead
A thesis submitted for the degree of Doctor of Philosophy
University of Bath
Department of Mechanical Engineering

2004

ProQuest LLC
789 East Eisenhower Parkway
P.O. Box 1346
Ann Arbor, MI 48106-1346

SUMMARY

Presented here is the culmination of three years of research investigating synthetic jet aerodynamics and propulsion of Micro Air Vehicles (MAVs). It is the first time that synthetic jets have been demonstrated as propulsive devices and the first time they have been suggested for use on Micro Air Vehicles.

A synthetic jet was located at the trailing edge of a low Reynolds number wing. The effects of varying jet frequency and momentum coefficient were studied using velocity profile measurements and visualisation. Effects of angle of attack and Reynolds number were also studied.

It was shown that given sufficient momentum coefficient, the drag of the aerofoil could be overcome, corresponding to a cruise condition for the MAV. Increasing the momentum coefficient further would cause a jet-like profile in the wake and the MAV would experience positive thrust.

It was found that at very low frequencies, thrust coefficients rapidly decreased due to large instabilities caused in the suction part of a jet cycle. An optimum frequency range was therefore highlighted.

Measurements of thrust force, lift force and power consumption gave indications of efficiencies on the laboratory test system used in the research.

A mechanism was constructed inside a life-size aerofoil section to demonstrate an enabling technology for synthetic jet propulsion of MAVs. It was shown that sufficient momentum could be achieved to accelerate the MAV at low Reynolds numbers to maintain flight after a catapult launch.

ACKNOWLEDGEMENTS

The Engineering and Physical Sciences Research Council (EPSRC), UK, and the Ministry of Defence (MoD), UK, sponsored all of the research presented here.

The author wishes to acknowledge the support of supervisor, Prof. I. Gursul, also that of Head of Postgraduate Studies, Dr P. S. Keogh, technicians, Mr R. Wiltshire, Mr L. Dudrudge, Mr D. Rushton, Mr S. Coombes, Mr P. Philips, Mr V. Singh, and Mr R. Grant and head of manufacturing engineering, Mr A. Green.

The author would also like to acknowledge the benefits reaped from informal conversation with many talented engineers around the world: Prof. T. J. Mueller of the University of Notre Dame, Dr J. Mabe of Boeing's Phantom Works, CA, Dr R. G. Bryant, of NASA Langley, Dr A. Vasquez of Face Corporation's Thunder division, Prof. M. Drela, author of XFOIL, and Dr M. Hyde of TSI Inc.'s UK office.

Finally to my parents and to Caroline for being supportive and understanding of my committed work regime over the last three years – thank you.

CONTENTS

NOMENCLATURE

SYMBOLS

α	:Angle of attack	[°]
A	:Current	[A]
A_E	:Aerodynamic efficiency	[no unit]
b	:Span	[m]
c	:Chord length	[m]
C_E	:Power coefficient	[no unit]
C_L	:Lift coefficient	[no unit]
C_p	:Pressure coefficient	[no unit]
C_T	:Thrust coefficient	[no unit]
C_μ	:Momentum coefficient	[no unit]
f	:Frequency	$[s^{-1}]$
h	:Slot height	[m]
p	:Pressure	$[N/m^2]$
P	:Power	[W]
p_∞	:Freestream pressure	$[N/m^2]$
P_E	:Propulsive efficiency	[no unit]
ρ	:Density	$[kg/m^3]$
q_∞	:Freestream dynamic pressure	$[N/m^2]$
R	:Resistance	[Ω]
Re	:Reynolds number	[no unit]
S	:Aspect ratio	$[m^2]$
St	:Strouhal number	[no unit]
t	:Time	[s]
u	:Velocity in x direction	[m/s]
μ	:Dynamic viscosity	[kg/ms]
U_∞	:Freestream velocity	[m/s]
V	:Velocity magnitude	[no unit]
v	:Voltage	[v]
υ	:Kinematic viscosity	$[m^2/s]$

ξ	:Vorticity = $\frac{\partial u}{\partial y} - \frac{\partial v}{\partial x}$	[s^{-1}]
x	:Freestream axis variable	[m]
y	:Vertical axis variable	[m]

ABBREVIATIONS

CCD	Charge Coupled Device
DARPA	Defence Advanced Research Projects Agency
EPSRC	Engineering and Physical Sciences Research Council
FM	Figure of Merit
GTRI	Georgia Technical Research Institute
LDV	Laser Doppler Velocimetry
LFC	Laminar Flow Control
LRNFB	Low Reynolds Number Force Balance
MAV	Micro Air Vehicle
MEMS	Micro-electro Mechanical Systems
MIT	Massachusetts Institute of Technology
PIV	Particle Image Velocimetry
RMS	Root Mean Squared
RPV	Remotely Piloted Air Vehicle
SLS	Selective Laser Sintering
Thunder	Thin Unimorph Bender
TI	Turbulence Intensity
UAV	Unmanned Air Vehicle

LIST OF FIGURES

CHAPTER 1 INTRODUCTION

1.1 BACKGROUND

Micro Air Vehicles (MAVs) are a new technology with potential that is still being realised. MAV concepts were first discussed in the mid-1990s by the MIT Laboratories (1996) and the RAND Corporation (1992). Further MAV studies were conducted at the Georgia Technical Research Institute, which were later adopted and supported by the Defence and Advanced Research Projects Agency (DARPA). DARPA released several funding packages totalling $12 million to look at both fixed and flapping wing aircraft for flight-enabling technologies which they limited in size by stipulating that no one dimension could be greater than 6 inches.

FIGURE 1.1 shows the flight regime highlighting where indoor robots and radio-controlled aircraft (or MAVs) lie in context. Requiring up to five orders of magnitude less in terms of lifting force, with flight speed up to two orders of magnitude less than a large commercial aircraft, MAVs lie towards the bottom of the flight regime.

As outlined by Parry-Jones *et al* [2001], MAVs would require considerable new and novel technology dedicated to their application; new flight concepts, super light weight materials and structures, highly compact and efficient energy storage systems, new propulsion devices and efficient aerodynamic concepts.

It was soon realised that MAVs could offer new ways of achieving objectives with aircraft incorporating new Micro Electro-Mechanical Systems (MEMS) and other technological developments still in concept phase.

Continued advancement in micro technology capability enhances the potential for the development of a truly useful micro unmanned aircraft. Technological advancement currently enables the mounting of miniature surveillance equipment on MAVs including computer chip sized hazardous substance detectors, infrared sensors and micro CCD cameras. A typical mission profile might expect flying times of 30 minutes or more with a payload of around two grams over a distance of 10km [McMichael and Francis, 1997]. With the growing array of micro-sensory and electronic equipment, the potential capability of MAVs is constantly increasing. MAVs may be summarised broadly as palm-sized flying utility vehicles.

Certainly the predicted range of military conflict within the 21st century has motivated developments in the micro technology fields. So far there seems to be a shift towards non-traditional combat environments. The need for effective, low cost technologies, particularly with local reconnaissance or chemical detection capabilities, is of increasing importance; impetus is firmly behind the development of a useful, efficient MAV.

1.2 REVIEW OF PREVIOUS WORK

In the following section, a comprehensive account of the current and historical research status of MAVs, low Reynolds number fluid dynamics, flow control and other related areas to this research is given. Whilst it is not intended to be an exhaustive review, it is intended to provide a historical context for the importance of the aforementioned areas and discuss the major contributions to date with relation to the research presented here.

1.2.1 MICRO AIR VEHICLES (MAVS)

In 1922, E. P. Warner [Warner, 1922] wrote on the challenge of creating "Miniature Airplanes". In the infant years of commercial aviation the smallest concept of an aeroplane was a single-manned, single-engined, light aircraft. Nearly 80 years later, N. Parry-Jones and J. Alldridge [2001] wrote an excellent history of UAVs and MAVs reporting of the challenge of unmanned and micro-air vehicle development, making the "miniature" aeroplanes of 1922 seem like giants of the sky. The palm-sized miniature aeroplanes discussed by Parry-Jones *et al* [2001] were born out of the late 1980s initial work at the MIT and RAND Corporation, with significant funding from the United States' Defence and Advanced Research Projects Agency following in the 1990s.

It was DARPA's funding announcement totalling $12 million that drew international recognition to the importance of MAV technology. It was a sign that a major research organisation, with significant financial backing, had acknowledged the potential of the MAV as a worthwhile investment of considerable importance. The DARPA funding was allocated over three years to enable study of enabling technologies for MAVs. Whilst MAVs may have been discussed in the previous decade leading up to the DARPA funding announcement, no serious funding had been made available to MAV research prior to that date.

In reality, prior to the late 1980s, the terms UAV and MAV were little discussed. However, the concepts of small, unmanned, aircraft on which the terms are based date back to at least the early 1900s. The importance of small-scale flying utility vehicles was actually derived several thousand years before then though. Indeed, it was the use of the carrier pigeon, first thought to be used by Noah (as Mary Blume writes in the *Herald Tribune* of 29 January 2004) where the early foundations for UAVs lie. Whilst the carrier pigeon was used routinely for carrying messages, it is less known that during World War II, German carrier pigeons were used with cameras strapped to them to take in-flight pictures. The French had a fleet of some 30,000 pigeons during this time, interference or obstruction of which carried the death penalty - a sign of the importance of the pigeon as a flying utility vehicle. It was during WWII that the use of the photographing pigeon was transferred to remotely piloted vehicles (RPVs) in Germany. Remote aerial surveillance had begun.

During the 1920s and 1930s, advances in aeronautics and electronics in England and the USA, gave impetus to RPV development. Most of the early work was intended for making drones capable of carrying explosives to targets. Most of the work prior to the late 1930s to early 1940s was unsuccessful in achieving full objectives. However, there were significant knowledge databases building and a key development came in the production of an automatic gyroscopic stabilizer used in 1917. German development could be said to have been considerably in advance of US and UK research around WWII. Their engineers worked on airborne television, guidance systems, inertial guidance systems, radar, advanced propulsion systems as well as more 'conventional' aeronautical problems of that era. The most famous UAV of this time was the V1

Doodlebug intended as a mass-production, pulsed jet powered explosive carrier. The German technology was acquired by the US and UK in the post-war era and gave impetus for new developments.

It was probably in the 1960s period of technological advancement that RPVs capabilities began to broaden. That period saw significant development in microelectronics, leading to onboard guidance and control in addition to enhanced surveillance capability. Small propulsion systems could now be developed with greater reliability and composite structures were starting to impact significantly on airframes. Fundamentally, the desire remained to operate RPVs where it would be dangerous to send piloted aircraft. The RPV was also an attempt to reduce costs of the aircraft associated with the human-computer interface. RPVs sometimes remained extremely large and due to their increasing sophistication, associated costs were higher than might have first been anticipated. Technologies associated with RPVs/UAVs were similar in nature to those used on manned aircraft.

However, the concept of a truly micro air vehicle (MAV) promoted the need for new technologies. Whilst mini-RPVs might still have a wingspan of several meters, the new conception of an MAV was something very much smaller. Originally a conception of the late 1980s, early 1990s by the RAND Corporation and MIT Lincoln Laboratories, MAVs soon drew the attention of the world's science field. Further study by Georgia Technical Research Institute (GTRI) in the mid-1990s was adopted and attracted funding from DARPA. Recognition was given to emerging enabling micro technologies that would enable the construction and instrumentation of truly small-scale systems that would perform similar functions to existing mini-RPVs and mini-UAVs. DARPA allocated funding based on MAV definitions of 15cm wingspans and 50g upper weight limits. They also expressed interest in considerably smaller aircraft.

The usefulness of an MAV was immediately apparent to the military. Mini-RPVs had successfully been demonstrated with 'fake' radar cross-sections matching those of much larger aircraft. Israel was probably the first to use this to maximum effect in sending a wave of UAVs towards missile batteries outside hostile borders. The UAVs carried fake radar signatures of larger bomber aircraft. The missile batteries turned on their radar in response to the apparent attack only to be instantly destroyed by standoff air-to-ground

missiles from real Israeli fighter aircraft many miles away. Using MAVs in such a way would be much cheaper for the military not wishing to waste much larger UAV counterparts. Also there were the obvious search and reconnaissance roles that an MAV could adopt. Development in micro camera technology could enable live broadcast pictures or still surveillance as solutions to what became known as the "over the hill" problem: if a soldier wants to know what is up ahead, an MAV with an inbuilt camera might be a cost-effective, efficient way of answering that.

Commercial applications have also spawned as MAV science evolved. Sensor technology is now so compact that numerous possibilities existed; detection of radiation leakage or reactor inspection, weather monitoring, traffic monitoring, security and surveillance (even indoors), search and rescue and outdoor cable inspection to name just a few.

A niche appeared to be developing in the aircraft industry for MAVs with the most useful hardware. Researchers instantly took up the challenge. The challenge was met with several innovative solutions. The solutions could broadly be divided into three distinct areas associated with the aerodynamics and propulsion; flapping wing, rotary wing or fixed wing MAVs.

Flapping wing flight had been demonstrated successfully by nature for millions of years. Many researchers took nature as inspiration and tried to mimic the techniques used. Insect and bird flight involves complex mechanisms of generating lift and thrust still being understood [Ellington, 1995, Freymuth, 1990, Jones *et al*, 1996, Jones and Platzer, 2000, 2003, Patil, 2003, Raney and Waszak, 2003, Raney and Slominski, 2003]. Good reviews of flapping flight in nature can found [Sane, 2003 etc.] detailing some of the mechanisms understood to date. Meanwhile, others designed and used more simplistic, albeit still ingenious, versions of flapping wing flight to good effect.

Ornithopters, not necessarily on micro scales, had been around since at least the 1870s. In 1879, Pichancourt sold rubber band powered commercial versions in Paris purely as toys. The flight mechanism was complex, consisting of steel wires that not only flapped the wings but also gave a combined twisting motion. Whilst such a complex flapping motion would not be followed for sometime, more straightforward toy flappers were

produced throughout the 1950s to 1970s as some of the best selling toys of their time. Whilst flappers were largely confined to the domains of hobbyists, work of Knoller [1909] and Betz [1912] in the early 1900s started scientific research into flapping flight. It was not until DARPA announced interest in MAVs that substantial funding enabled more dedicated research. The theory of flapping flight is really outside the confines of this research. An excellent review by Shyy *et al* [1999], details flapping flight studies from nature and technology up until then. However, several working examples or significant developments towards working examples illustrate flapping flight progress well. Jones and Platzer [2000, 2003 and others] built a flying bi-plane flapper of around mini-RPV size to MAV size. Aerovironment's Microbat (FIGURE 1.2), whilst currently limited for short duration flow only, demonstrated considerable advancement in the fields of miniaturisation and unsteady fluid modelling. Mueller *et al*, [2004] reported that whilst the Microbat did yet have a payload, it had flown at 12mph for 6mins. Porsin-siriak *et al* [2000] even reported research to enhance the performance of flapping wings on an ornithopter using MEMS technology for adaptive performance. The technology was in the developmental stage. Whilst still under development for wireless flight, Vanderbilt's Elastodynamic Ornithoptic Flying Insect used piezoelectric 'muscles' to create a flapping motion. Perhaps the most astounding of all is work that researchers at UC Berkeley are undertaking towards their Micromechanical Flapping Insect. At only 25mm in diameter, the concept was extremely demanding, nevertheless, steady and impressive progress has been made. A fuselage and mechanism has been constructed with recently demonstrated wings sufficient to provide 50μN of thrust force each. But with such development in flapping flyer technology, one might question why research into conventional aerofoils for MAV fixed wing flight continued.

Whilst it is well known that flapping flyers afford considerable manoeuvrability and even hovering capability, it has been reported that there would be a significant trade off in efficiency if designs were made to produce both forward and hovering flight. Hall *et al* [2001] performed minimum power circulation distribution calculations for flapping wings both in the three- and two- dimensional cases. They showed that flapping flight was not found to be more efficient than propeller driven flight at low Reynolds numbers. They suggested that flapping flight in mechanical systems "is probably disadvantageous for all but very narrow niche applications, such as stealth by mimicry." Jones and Platzer [1997, 2000, 2001, 2003] assess the propulsive efficiency and thrust

coefficients for combined pitch and plunge flapping mechanisms. They consistently found that conditions for maximum propulsive efficiency nearly coincided with the conditions for minimum thrust coefficient. Woods *et al* [2001] analysed the energy requirements for fixed, flapping and rotary wings in conjunction. They concluded that when there was no hover requirement, fixed wing flight was always most energy efficient for a MAV. Further comment noted that flapping wing flight could make use of the ground boundary layer whilst that was less advantageous for fixed and rotary wing MAVs, a feature noted by several other researchers. Whilst flapping wings may have been nature's general choice for propulsion through air that does not necessarily mean that the solution is the best one. As Bannasch [2001] suggests in his instructive work on propellers, "nature does not provide 'blueprints' for practical applications in engineering. The aim is to find the underlying principal and to learn how to translate that into technology." Whilst many lessons could be learnt and significant understanding could be gained, direct emulation of the natural way to fly may not be the most efficient way. A swift, after all, looks most under-worked when soaring with fixed wings rather than flapping. With conflicting reports of true flapping wing efficiency, the limited application of hovering flight and the extreme complexity of these next generation flyers, consideration is still largely focused on other aerodynamic and propulsion mechanisms – most commonly, fixed wing propeller driven aircraft.

Many flying examples exist of fixed wing, propeller driven MAVs. With few 'real life' examples, fixed wing micro-fliers were born out of concepts based on conventional aircraft and then improved with greater understanding of low speed flow (next section). Perhaps the most famous of the fixed wing fliers was one of the first successful attempts to meet the DARPA specification; Aerovironment's Black Widow (FIGURE 1.3). Several articles are available on the construction, design and performance of the Black Widow. In 2000 Grasmeyer and Keenon [2001] presented a reasonably comprehensive review showing endurance times of 30 minutes with a total mass of 80gr. Tests of several balsa three-dimensional geometries had led them to use a disc shape. The Black Widow was built with CCD camera (FIGURE 1.4) and ground control unit, which included a viewing station and automatic tracking antenna in addition to the Black Widow controls. The MAV kit also comes complete with pneumatic launcher offering a more controlled launch compared to hand-launched MAVs.

Whilst the Black Widow's propeller was driven by an electric motor, the MLB Company's Trochoid [Morris *et al*, 2000] used a commercially available 0.01cc combustion engine manufactured by Cox. The Trochoid shape took advantage of conventional lift at low incidence and vortex lift at high incidence. The team focused on maximized lift capability and a large power to weight ratio. Sophisticated avionics in larger versions of Trochoid included autonomous flight by GPS guided waypoint navigation and inertially stabilized camera systems.

The University of Florida also used the same small reciprocating engine and successfully incorporated more advanced aerodynamic surfaces into their MAV, UF (FIGURE 1.5), by the use of flexible wings [Ifju *et al*, 2002, Lian *et al*, 2003, 2004, 2004]. Their unique wing structure incorporates a flexible membrane on a carbon fibre-veined framework, not so dissimilar to a bat wing. Several studies exist, for instance by Waszak *et al* [2001], on the optimisation of the stiffening members and other features of their advanced wing. The UF MAV consistently performs well in MAV competitions with its 600m range CCD camera and transmitter able to perform well in many "over the hill" competitions.

The University of Notre Dame, having considerable experience with low Reynolds number aerodynamics, have also participated in MAV flight competitions in the USA. A good account of their contribution and experience with MAV design, development and testing is given by Torres and Mueller [2000]. Significant contributions of Mueller's group to low Reynolds number aerodynamics understanding are detailed in the next section.

Several researchers are also studying the use of delta wings to generate lift at high incidence for small-scale flight [Gursul, 2003, Gursul *et al*, 2002]. As with highly manoeuvrable larger scale aircraft, there appears to be considerable benefit in lift generation at high incidence in the use of delta-based planforms.

Most, if not all, of the existing fixed wing flyers rely on propellers as their propulsion system. Unfortunately it is well known that propeller efficiency decreases rapidly with decreasing diameter and flow separation is exacerbated by flight in the low Reynolds number regime. With MAV power sources limited in both weight and size, propulsion

efficiency is a key consideration. The only possibility of a renewable power source currently lies with advancements in solar panel technology, but Wilson *et al* [2000] from the University of Bristol showed that whilst existing state-of-the-art solar technology might just allow a 50cm mini-UAV to fly, the true scale of 15cm MAVs would almost certainly require a different power source. Power supplies for propeller driving mechanisms therefore remain as battery or fuel-powered internal combustion engine with finite supplies able to be carried in flight. Power source was a key consideration and found to be a limitation for Peterson *et al* [2003] who derived an MAV without payload with the maximum endurance-minimum size methodology. There is also little information regarding the effects of the propeller wash over the aerodynamic surfaces of the aerofoil. Some researchers claim not to have experienced any drop in performance from propeller wash whilst others claim reduced performance levels. Few studies exist on the flow of low Reynolds number propellers although they are increasing. An example is work conducted by Arai *et al* [2003]. They found relations between propeller efficiency, thrust coefficient, and torque coefficient, for several low Reynolds number propellers. Miley *et al* [1985] observed periodic fluctuations in a low Reynolds number propeller wash which they observed to create both turbulence and relaminarisation dependent on the point in the cycle.

More experimental and future generation propulsion systems include the investigation of micro-gas turbines. The Phoenix technology firm, M-DOT is developing an egg-sized micro-gas turbine that will be capable of producing 1.4 pounds of thrust. Government funding going to Aerodyne Corp. is to be used in employing the M-DOT turbines to power a radical fin-stabilised oblate spheroid hovering vehicle; initial concepts appear to be outside the domain of MAVs. Cheung and Tilston [2001] gave an initial report in their findings after attempts were made to model and construct a bi-propellant hybrid rocket-turbine engine for MAVs. Whilst they encountered problems of heat loss from the nozzle and fuel ignition, they were encouraged by the results, suggesting overall plausibility. Micro-electromechanical systems (MEMs) also look set to impact on the MAV world. Researchers at MIT led by A. Epstein [2003] aim to produce a MEMs micro-turbine the size of a shirt button that weighs around 1 gram. Such technology may well be a third-generation MAV basis. The fact remains that the quest for efficient propulsion solutions for MAVs continues. In conjunction with the difficult aerodynamic regime in which they must fly, the combined propulsion and

aerodynamics issues for MAVs is a demanding scientific problem requiring considerable further research.

Problems in design and construction of efficient MAVs are apparent. Clearly guidance, control, power and propulsion systems need to be very lightweight and compact, as does the airframe. Benefits are rich if very efficient components are sought when space and weight is at such a premium. As power or and fuel supplies are limited there is also need to maximize the efficiency of the aerodynamic surfaces, lowering drag yet providing sufficient lift at very low flight speeds to support the weight of the total aircraft.

It should be noted that completely separated flows are dominant in this low Reynolds number range. Even those airfoils designed specifically for low Reynolds number flight still exhibit considerable sensitivity to Reynolds number as it drops below $Re=10^5$. Viscous forces are increasingly significant as airspeed lowers into the regime of MAVs. Drag is larger in proportion to high-speed flow of an equivalently scaled larger vehicle [Ashley, 1998]. Boundary layers also change in their characteristics, tending to be laminar rather than turbulent and easily separated. The challenge is creating an aerodynamic solution with low drag and sufficient lift for the low flight speeds of MAVs.

The aerodynamic problem was compounded by operating at low flight speeds due to the nature of the airflow changing from turbulent to laminar in the low Reynolds number regime (discussed in the next section). Flight at low Reynolds numbers is rather more like trying to move through honey; the viscous nature of the fluid can no longer be ignored. Propeller Reynolds numbers are so low, their aerodynamics are governed by completely laminar regimes. The laminar regime of propellers gives special design requirements of pitch, camber and thickness for efficient propeller design [Grasmeyer and Keenon, 2001]. For aerofoils in the low Reynolds number regime (MAVs would be expected to fly anywhere around Reynolds numbers of 10,000 to 300,000), separation bubbles can form over an aerofoil surface due to the complex fluid interactions associated with the transition from laminar to turbulent boundary layer flows. Separation bubbles covering large portions of the aerofoil can lead to decreases in lift and increases in drag. Design of efficient lifting surfaces for fixed wing MAVs would

involve considerable insight into low Reynolds number aerodynamics, possibly in conjunction with flow control techniques.

1.2.2 LOW REYNOLDS NUMBER FLUID DYNAMICS

The notion of an MAV is a relatively recent one and the low Reynolds number fluid dynamics associated with small scale, low speed flight had been little studied until the concept of mini-RPVs, mini-UAVs and MAVs was really beginning to be developed. The desire to extract the maximum aerodynamic performance possible for the small-scale aircraft so limited in their load carrying, motivated the increased interest in efficient lifting surfaces and propulsion systems at such low speeds.

Attention to low speed aerodynamics was given in the early years of flight when higher speed flight was still in the early stages of conception. For example, Jacobs and Sherman [1936] performed tests at Langley Memorial Aeronautical Laboratory in the early 1930s, where chord Reynolds numbers as low as 42,000 were studied. Pressure measurements were taken as low as Reynolds number 100,000 at the same facility by Pinkerton [1937] around the same time, although he noted, "At the lowest Reynolds Number the capacity to repeat measured pressures is markedly less than for higher Reynolds Numbers". In fact Jacobs and Sherman [1936] suggested that measurement system limitations prevented accurate measurements of Reynolds numbers less than 80,000. However they did show that there was a strong dependence on aerofoil surface pressure with Reynolds number variation. They also performed smoke flow visualisation of the separation characteristics for several Reynolds numbers. Around the same time, Pinkerton also worked on calculating the pressure distributions relating to experiments from potential flow. Analytical theories were increasing in capability at similar rates to experimental techniques although there was little reliable experimental data at very low speed to compare. Certainly there were already acknowledged differences between inviscid theory and fluid dynamics at low Reynolds numbers.

Attention of engineers was then largely drawn to making aircraft fly faster and farther, especially during the first and second World Wars. During that time, research on low Reynolds number airfoil performance was largely confined to hobbyists and scientific study looking at gliders and model aircraft. A German publication called "Flugsport" published heavily on the topic of gliders from its first publications in around 1910.

Schrenk wrote in "Flugsport" [1922] on the aerodynamic computation of gliders in Germany and spoke of remarkable soaring flight performances and the desire to improve; such was the motivation for low Reynolds number flight improvements at this time. In the same year, Espenlaub [1922] identified the importance of thin wings with camber for good gliding performance. He noted also that thick wings could only be used on large models with heavy loads. In his experiments on model aircraft, F.W. Schmitz [1942] was one of the first to realize that boundary layer tripping could reduce drag at low Reynolds numbers, maintaining attached flow over a larger portion of an aerofoil. Gault [1955] conducted several experiments characterising the boundary layer types whilst investigating separated laminar flow.

As a knowledge base was developed on basic low Reynolds Number aerodynamics, a clear shift can be seen during the 1950s, 60s and 70s as researchers looked at the more detailed fluid structures and their effects at low speed. Whilst it was probably Jones [1933] that first looked at the separation bubble, research to understand the separation bubble and transition was becoming more frequent.

The separation bubble, a common feature of low Reynolds number flows, is one of the main causes of poor aerodynamic performance of aerofoils in the low Reynolds number range. The features of the bubble are formed when a laminar boundary layer separates from the aerofoil surface as a result of the sudden adverse pressure gradient past the point of minimum pressure [Batill and Mueller, 1981]. As laminar shear layers are susceptible to disturbances in the freestream, transition usually occurs shortly downstream of the separation point. With the increasing energy mixed from the freestream, the transition region can reattach to the aerofoil surface. The region bounded by the laminar separation, transition and aerofoil surface is known as the separation bubble. The key features of the separation bubble are shown in FIGURE 1.6. Mueller [1999] summarised the effect of the separation bubble at low Reynolds numbers neatly in FIGURE 1.7. As the bubble forms at low Reynolds numbers, its size increases with decreasing Reynolds number. Mueller showed how larger bubbles lead to decreased lift coefficient and increasing drag coefficients at low Reynolds number. Besides the studies at Notre-Dame, there is a reasonably substantial body of research concerning the separation bubble [Gleyzes *et al*, 1985, Hsiao *et al*, 1987, Patrick and Edwards, 1985 etc.]

Improving experimental techniques aided more detailed studies of the small-scale fluid dynamics of small aerofoils at low speed. For example, Arena and Mueller [1979], Brendel and Mueller [1985, 1988] used a low turbulence subsonic wind tunnel at the University of Notre Dame, Indiana to make detailed observations on "The laminar separation, transition, and turbulent reattachment of low Reynolds Number flows near the leading edge of airfoils." Research published in the 1950s to 1980s is notoriously difficult to acquire; publications before this period were considered of historical significance and those after of increasing relevance to the studies of today. Despite resourcing problems, several relevant publications are evident. Nakamura *et al* [1969] studied stalling characteristics for a NACA 0012 at Reynolds numbers as low as 30,000. Observations included the increasing length of the separation bubble with decreasing Reynolds number. Several other researchers led work on the understanding of stall, separation bubbles and transition around then. For example, Tani [1964] looked specifically at the laminar separation bubbles and bubble bursting in low speed flows. In 1981, Nagamatsu *et al* [1981], took surface pressure measurements on a low-drag NACA63-208 aerofoil at Reynolds numbers as low as 35,400; a considerable improvement in capability over the early 1936/7 attempts by Pinkerton *et al* [1936] at Langley. Nagamatsu *et al* [1981] showed detailed features in the surface pressure distributions corresponding to separation bubbles for low Reynolds number conditions. They observed the pressure distribution was independent of low Reynolds numbers for $\alpha<2^{o}$ and for all $\alpha>14^{o}$ in the post stall region. For all other angles of attack, the pressure distribution was found to be strongly dependent on Reynolds number for the aerofoil they tested. Their facility was an 18 in x 27 in, transparent side-walled closed-circuit wind tunnel having lowest speed around 16 ft/s with TI~0.2%.

During the development of such increasingly capable wind tunnel facilities, there was also considerable growth in theoretical and analytical study of fluid flows. Roberts [1979] published work on "A modified semi-empirical theory for the development and bursting of laminar separation bubbles" giving agreement between experimental data and prediction described as "reasonably good." He also clearly identified the differences between inviscid theory and experimental data at low speed as others had done before him. Viscous effects were clearly evident at low speeds.

At the same time, the University of Notre Dame, under the guidance of T. J. Mueller, was embarking on the early years of some of the most comprehensive experimental studies on low Reynolds number aerodynamics. Initial work published improved on the early bubble studies of the 1940s and 1950s and looked at the separation bubble features combining visual techniques with force balance measurements in a little studied area. Using high contrast, fine streakline smoke techniques [Arena and Mueller, 1979, Mueller and Batill, 1982, Bastedo Jr. and Mueller, 1985, 1986, Schmidt *et al*, 1985, 1987, O'Meara and Mueller, 1987 etc.], the laminar separation, transition and subsequent reattachment could all be visualized for a greater understanding of the fluid dynamics. In conjunction with both force balance and surface pressure measurement data, the smoke flow visualization revealed the nature of aerodynamic performance for a number of low Reynolds number aerofoils. Due to the precise visual indication of laminar transition coupled with surface pressure signatures, Notre Dame were able to locate trips of surface roughness into the laminar regions [Bloch and Mueller, 1986, Huber II and Mueller, 1985], promoting early transition to avoid large separation bubbles. They observed considerable benefits in lift as reported by others [Corke and Morkovin, 1985, Nelson, 1985, Lyon *et al*, 1997, etc.]. The group also used external acoustic excitation as a 'tripping' mechanism to similar effect and promoted further work to explore the effects of disturbances on low Reynolds number aerofoils.

Motivation for study in the low Reynolds number regime during the 70s and 80s came from several sources which required improvements to aerodynamics; high altitude performance of Remotely Piloted Vehicles (RPVs), low altitude, low speed performance of RPVS and axial flow jet engine compressor blades amongst others. In an excellent review of aerodynamics of small aircraft, Mueller [1985] discussed progress on the aerodynamic problems associated with design and testing of low Reynolds number vehicles. Mueller reviews the applications of low Reynolds number studies, design aims, flow problems, boundary layer behaviour, the Eppler design and analysis theory, some typical results and experimental difficulties and practices. To that date, his discussion of low Reynolds number boundary layer behaviour was one of the most comprehensive. Mueller discusses the effect of the separation bubble on aerofoil performance highlighting that a long separation bubble could noticeably affect the surface pressures and lead to deteriorated aerofoil performance. A very short laminar bubble on the other hand could be used as a trip to minimize the possibility of massive

separation further downstream. Mueller writes quite comprehensively of low Reynolds number experimental test technique, which will be reviewed in a later section.

During the mid- to late-1980s, there were several international conferences convened specifically for low Reynolds number fluid dynamics. In 1985, at the first such conference held at Notre Dame, Indiana, applications for low speed studies, such as mini-RPVs, ultra-light/man-powered aircraft, sailplanes and wind turbines/propellers, were brought firmly into the international arena. Eppler *et al* [1985] continued work on the prediction of low Reynolds number aerofoil performance with a view to designing more suitable aerofoils (the Eppler Aerofoils). However, whilst they had some success for Reynolds number ranging from 50,000-500,000, those below 50,000 came with the added difficulty of considering entirely laminar boundary layers leading Eppler to write, "It could even be said that Reynolds numbers below 50,000 should be prohibited by law."

By incorporating finite trailing edge pressure gradients, wake thickness and wake curvature, Maughmer and Selig [1985] (the author of the low Reynolds number publication, *Soartech,* aimed at glider constructors in the 1980s) were able to improve on the accuracy and performance of the Eppler code in conditions were bubble separation calculation was more critical (minimising the strong viscous interactions around the trailing edge). They also predicted that the empirical design methods they were evolving would be unlikely to be replaced by rigorous analytical solutions due to the computer processing expense involved. Donovan and Selig [1985], in a review of the low Reynolds number work conducted at Princeton University, show good agreement between the Eppler based code and experimentation at the same facility. Hassan [1985], amongst others, detailed research into viscous-inviscid coupled methods, provided that the boundary layer was fully attached over the aerofoil surface. The coupling method, not unique to Hassan, was a method to utilize existing iterative formulae already developed and combine them in such a way as to 'circumvent' the problems of accurate transition prediction by a single method. In fact the most discussed topic was on the laminar separation bubble, a key feature of low Reynolds number flow and arguably one of the most complex.

Shortly after, Drela [1988, 1989] published work on another viscous-inviscid interaction prediction method for use on a prototype long-range human-powered aircraft, Light Eagle. After successful analysis and design of three prototype aerofoils, flight tests showed that the method predicted the transition region extremely well and C_{Lmax} corresponded very closely to design predictions. Drela later went on to make some of his work publicly available as a stand-alone package called XFOIL. A good account of the methodology he used was given in the 1989 low Reynolds number aerodynamics conference [Drela, 1989]. Whilst XFOIL was a step forward in terms of accuracy and processing time, and it did represent all of the key features for low Reynolds number aerofoil prediction (bubble losses, instability, separation etc.), accurate prediction of transition for larger separation bubbles remained extremely difficult. Navier-Stokes solutions for low Reynolds number fields had been derived in other cases [Kothari *et al*, 1985 etc.], but as Coiro *et al* [1989] reported, NS solutions gave huge computational requirements and were unfeasible for industrial needs. Ghia *et al* [1989] published research into direct numerical simulation of unsteady Navier-Stokes analysis although it was the early phases of development. Again, the essence of the 1989 conference drew attention to the problems associated with transition and bubble prediction and the sensitivities of those features to experimental testing conditions. As O'Meara and Mueller [1987] clearly point out, there were continuing difficulties of obtaining consistent results with other researchers working on low Reynolds number studies. Discrepancies were noted in transition locations, separation angle and turbulent spreading angles. Inconsistencies were attributed to differences in flow disturbance – turbulence intensity of the testing environment.

Whilst considerable efforts strive to improve and perfect computational predictions of low Reynolds number fluid dynamics, experimentation continued. In a series of studies through the 1980s, Winkelmann *et al* [1990] visualized the flow-field on finite wings at low Reynolds numbers down to 11,000. At the same time, they studied the shedding frequencies of the aerofoils at various angles of attack. It was noticed that for fixed incidence and Reynolds numbers greater than 25,500, the non-dimensionalised shedding frequencies were nearly constant values. Further, that for $\alpha < 8^{o}$, when plotting non-dimensional shedding frequency against α, the data from all of the Reynolds numbers tested (11,750-50,350) collapsed around the same line.

Increasing precise and non-invasive measurement capability aided experimental studies still further. Mangalam *et al* [1985] published some of the earliest work proposing laser velocimetry as a quantitative technique to study laminar separation bubbles. For the single case they studied, they presented a clear picture of the extent of the laminar, transition and reverse flow regions as the turbulent reattachment zone. Crompton and Barrett [2000] from the University of Bristol exploited the technique more fully researching the separation bubble formed behind the sharp leading edge of an inclined flat plate. For the first time, detailed resolution in measurement methods enabled them to report a small secondary separation bubble adjacent to the leading edge, thought to have an important influence in the main bubble structure. Yarusevych *et al* [2003, 2003] looked in detail and the spectral content of the laminar separations before transition and reattachment. They suggested that just prior to transition, a band of frequency components was amplified in the separated shear layer, followed by rapid transition to turbulence. Looking at the most amplified disturbance in the shear layer might, it was surmised, gave some insight as to how and why the shear layer can be affected by certain frequencies and instabilities more than others.

As testing facilities became increasingly capable, the lower Reynolds number range could be studied with increasing confidence. Selig *et al* [1996] studied a range of aerofoils at Reynolds numbers as low as 40,000 with impressively repeatable results. From such accurate work, Selig *et al* were able to report on detailed features of the low Reynolds number survey they conducted. Firstly they reported the plateau of the lift curve around the 0^{o} condition for symmetrical aerofoils. Such non-linearity was largely improved by the use of trips in the boundary layer in order to reduce the size of the laminar separation bubbles. Also, sizeable hysteresis loops in the lift curves were found to occur both in the clockwise and anticlockwise orientations for high lift aerofoils for a given Reynolds number. Such features were again attributed to the size and nature of the laminar separation bubble occurring under such conditions.

In the mid-1990s, Laitone [1996, 1997] conducted an important study in relation to the piece of research presented here. Laitone constructed a force balance sensitive to drag forces as low as +/-0.01g, enabling accurate L/D ratios to be measured as low as Reynolds number 20,000. His balance was considerably more accurate than those of Schmitz, who attempted similar work in 1940 for model gliders, and Mueller's first

balance, although used largely in water. In doing so, Laitone presented some key findings (FIGURE 1.8). He showed that at Reynolds numbers below 70,000, L/D_{max} was higher for a reversed NACA 0012 compared to a standard orientation for a NACA 0012. A sharp leading edge produces more lift than a blunt leading edge indicating that ideal potential flow was no longer applicable. Furthermore, he suggested, if ideal potential flow were not applicable then perhaps the Kutta condition was not applicable at the trailing edge. A blunt trailing edge appeared to offer no deterioration in aerofoil performance compared to a sharp trailing edge. Laitone continued to show that thin wings with small amounts of camber (around 5-6%) outperformed thicker counterparts at low Reynolds numbers. He showed that the initial lift-curve slopes of the 5% camber were nearly 20% greater than that predicted by potential theory, indicating that at Reynolds numbers below 150,000, the theory was less applicable.

Meanwhile, Mueller's low Reynolds number work that began in the 1970s at the University of Notre Dame, continued to report increasing accuracy in experimental data. Pelletier and Mueller [2000] and Mueller [1999] showed that increasingly accurate force measurements could be taken at Reynolds numbers as low as 30,000-40,000. Mueller and his colleagues looked at several aerofoil parameters; thickness, camber, leading edge, trailing edge to name just a few. Agreement was found with Laitone [1997], that a sharp or blunt trailing edge appeared to make no difference to aerofoil performance at low Reynolds number. He noticed that a thin tapered wing performed similarly in whichever orientation it was in; sharp leading edge, or sharp trailing edge. Pelletier and Mueller [2000] also showed that cambered thin wings outperformed flat or tapered thin wings for given Reynolds numbers in the range tested. Furthermore, reducing the Reynolds number showed that aerodynamic performance deteriorated with a large reduction in L/D ratios. Mueller [1999] experimented with the effects of turbulence intensity of the test conditions and found very little difference between aerofoil forces measured with 1.3% TI and 0.25% TI tested between Reynolds numbers of 39,000 and 120,000 in the wind and water tunnels. However, he did find that end plates effected the aerodynamic force measurements due to the interaction of the end plate boundary layer and the flow around the wing. Whilst the findings were still under investigation, Mueller noted a reduction in lift and increase in drag when using endplates compared to a 'true' two-dimensional model. His true two-dimensional model was a long section of aerofoil with a floating mid-section attached to the force balance.

In that way, the interaction region between the end plate boundary layer and the aerofoil flow did not extend over the section under measurement.

In 2000, a significant collection of low Reynolds number aerodynamics papers was collated by the AIAA under the editorship of Mueller following the 2000 low Reynolds number aerodynamics conference held at Notre Dame. Research published in the collection included contributions from Torres and Mueller [2001] at Notre Dame who continued to use their state-of-the-art force balance in low Reynolds number surveys researching the effect of aspect ratio. They showed that for aspect ratios less than or equal to 1, the rectangular or inverse Zimmerman planforms were generally most efficient. Laitone [2001] also published work on effects of aspect ratio for low Reynolds number aerofoils and rings. He showed capability of measuring aerodynamic forces in Reynolds numbers as low as 10,000 and reaffirmed the advantages of an aerofoil with 5% camber in increasing the L/D ratio significantly compared to the 0% cambered counterpart. Significant contributions continued to be made towards computational solutions and design concepts for low speed aerofoils. Drela [2001] made continued progress on improving the accuracy of XFOIL by increasing the inclusion of higher order terms into the boundary layer approximation used in earlier versions. Earlier versions included only first order approximations looking at the transport and normal diffusion parts of the streamwise Navier-Stokes equations. The second order improvement also included curvature-induced transport under the rationale that important regions such as the trailing edge and separation bubble required greater orders of accuracy due to their sensitivity. Drela reported that whilst computational time was still kept to a minimum relative to full Navier-Stokes solutions, the accuracy was a significant improvement compared to the first order boundary layer approximations. Selig *et al* [2001] showed considerable progress in inverse aerofoil design at low Reynolds numbers basing work on the Eppler code and XFOIL, improving on their PROFOIL package still further to an extremely useful design aid for low Reynolds number aerofoils to less than Reynolds numbers of 300,000.

Sunada *et al* [2002, 2004], working at Reynolds numbers as low as 4000, analysed the effect of maximum camber location and percent of camber. The parameters were comprehensively analysed in a water tunnel using a force balance. In addition to the findings of Mueller [1999] and Laitone [1997] at higher Reynolds numbers, they also

found that at ultra-low Reynolds numbers, the maximum camber ratio was around 5% to achieve maximum L/D ratio. The location of maximum camber for the 5% camber ratio aerofoils was around 25% of chord. The 25% chord location for the maximum camber exhibited a performance gain of around 25% over location at the 75% chord location and around 15-20% compared to the mid-chord location. Sunada *et al* also showed that the as the deflection of the leading edge angle was decreased from 90 to 15 degrees, the L/D ratio generally improved linearly, increasing by around a factor of two in the range tested. Null *et al* [2002] also published work highlighting the benefits they found of using a 3%-9% cambered aerofoil. Their research on three-dimensional wings showed that 3% was most efficient for high-speed flight and 9% most efficient for loitering; a value in between would therefore yield the best compromise. In addition, in the Reynolds number range 10^4 to 10^5, aerofoils show considerable sensitivity to changes in thickness [Carmichael, 1981].

Strides have been made towards more accurate prediction of transition and the key separation bubble features by computational studies. Whilst the faster iterative approximations of XFOIL and similar have greatest disparity with experimental results when accurate bubble and transition prediction are dominant features of the flow, work on accurate solutions to the Navier-Stokes equations continues to yield impressively accurate results in the very low Reynolds number field. Mateescu and Abdo [2004] published a Navier-Stokes solution that compared extremely well with experimental research performed by Kunz and Kroo [2000] at Reynolds numbers between 1000 and 6000. Whilst, to date, studies between 10,000 and 200,000 are more limited, it is surely only a matter of time before computational techniques enable accurate representation of that regime in addition. Reviewing on boundary layer receptivity to freestream disturbances Saric *et al* [2002] identify the main challenge of boundary layer prediction remaining with respect to freestream turbulence. Whilst understanding has been gained of the effects of instabilities, accurate theories and understanding of the mechanisms involved still remain incomplete.

More recent trends in low Reynolds number studies include research in three-dimensional planforms and work to understand behaviour in unsteady conditions. Research at the University of Bath by Wooding and Gursul [2003] studied not only low aspect ratio wings at low Reynolds numbers, but also the effects of unsteady gusting as

might be experienced by low Reynolds number aerofoils in true conditions. Further, Wooding and Gursul showed that some flexibility or compliance in aerofoil structure allowed better aerodynamic performance or resilience to unsteady aerodynamic flight conditions. Lian *et al* [2003, 2003, 2004] and Shyy *et al* [1999] also consider a low Reynolds number aerofoil with flexibility formed from a membrane glued to a carbon fibre latice framework. From Notre Dame, Torres and Mueller [2004], published arguably one of the most complete studies of planform and aspect ratio effects at low Reynolds number. They concluded that aspect ratio was by far the most important parameter to consider, then planform, then Reynolds number. No hysteresis was observed on any of the 28 geometries they studied, attributed by them to the low thickness to chord ratio of around 2%. Torres and Mueller compared results to general lifting line theories but found little good comparison over the range under test. Rectangular and inverse Zimmerman geometries showed significantly better performance than others around aspect ratios of 1.0.

The past century has seen significant development in the capabilities of both experimentalists and computational analysts in the field of low Reynolds number fluid dynamics study. Whilst there still appears to be significant gaps in the research and understanding of the Reynolds number range 10,000-100,000, understanding of the fluid dynamics around that range has grown considerably; details of the boundary layer types and main features have been categorised and in the last twenty years or so, significant effort has to been made to understand the main features. Flow visualization techniques have developed to show accurate visual representation of the main features and experimental facilities and measurement equipment now has accuracy several orders of magnitude greater than early predecessors. In particular, it has been shown that low Reynolds number aerofoils experience a loss in performance in decreasing lift and increased drag if the laminar separation bubble covers a large portion of the aerofoil surface. Small bubbles appear to have less effect. Computational research has led to an acceptable degree of accuracy for higher Reynolds number simulations and have aided in low Reynolds number aerofoil design [Gopalarathnam and Selig, 2001, Pfenninger and Vemuru, 1990 etc.], but below around 300,000, where separation bubbles and transition become dominant features, even the best current large eddy simulation (LES) and direct Navier-Stokes (DNS) are still in the development stages of how well they predict at small Reynolds numbers. With the effects of freestream disturbance, the

challenge of mastering the aerodynamics of the low Reynolds number regime is probably only going to be solved with a combination of computational and experimental methods to address the important problems.

A summary of some of the key desirable features of a low Reynolds number aerofoil:

- Less than 6% thick
- Blunt leading edged aerofoils perform less well
- Slight camber (3%-9%) increases performance
- A thin or tapered trailing edge is not necessary

As a thick trailing edge appears not to have an adverse effect on the lift generation of MAVs, it would make sense to locate flow control techniques and propulsion systems here. The positioning of the control device or propulsion system in the trailing edge of a fixed wing MAV utilises the property that a sharp trailing edge is not required for developing lift at low Reynolds numbers. By contrast, the locating of a propulsion device that would cause disturbance to the leading edge of lifting surfaces would be less desirable.

So far attention has only been paid to 'conventional' aerofoil technology. But there are further possible improvements that could be made to the aerofoil to control the flow in more favourable ways; delaying stall, delaying separation, delaying the onset of large separation bubbles to name just a few.

1.2.3 FLOW CONTROL

Even in the early part of the 20th century, researchers experimented with novel ways to improve performance of aerofoils. Prandtl [1904] was one of the first to propose research aiming to control boundary layer flow. Schrenk [1926] experimented with a sphere's boundary layer that he found could be removed by suction. Reid and Bamber [1928] employed surface suction and injection to control boundary layers and improve lift of NACA aerofoils. They found that surface suction was more economical to operate than accelerating the boundary layer by direct injection. By the 1940s, studies like those, of Quinn Jr. [1944], became more comprehensive in approach, looking at the effect of surface suction on the boundary layer character and looking for an optimum

blowing location. It is little known that both the MiG-21 (some of which remain in service) and the F-104 of 1955-1983, both employed boundary layer suction to enhance performance. More recently suction was shown to suppress disturbances in laminar flows caused by insect and other surface debris [Eustace and Barrett, 1999].

Poisson-Quentin and Lepage [1961] reviewed work on constant blowing flow control by ONERA, France in 1946 that showed that the key to separation control was the momentum addition and not the addition or subtraction of fluid mass. Poisson-Quintin [1948] introduced the use of a parameter called the momentum coefficient, which was needed as an indication of the momentum transfer of their blowing flow control jets. This made possible the comparison between the expended jet power and the effect on the aerodynamic system. Due to the relative decrease in near-wall momentum (jet velocity less than local velocity), very low momentum coefficients were seen to decrease performance in steady blowing control [Attinello, 1961] and even in unsteady blowing (discussed later, in Melton *et al* [2003] for example). Both trailing and leading edge blowing were used to enhance circulation of aerofoils [e.g. McLachlan, 1989].

The pursuit of mechanisms to improve aerodynamic performance continued with renewed impetus into the twenty-first century. Added incentives for flow control studies included reduction of skin friction drag with growing concern of greenhouse emissions and fuel efficiency, improvement to allow super-manoeuvrability and desire for faster and quieter air and underwater vehicles.

Today flow control is fluid mechanic's most topical area of research. Many comprehensive reviews exist for flow control: Kumar *et al* [2000], Thomas *et al* [2002], Gad el Hak [2001], Hess and Fu [2003] present an excellent assessment of the impacts of flow control on naval platforms, Gad-el Hak [1989, 2001] gives a review of low Reynolds number flow control. There are many others. To look at all flow control technologies is outside of the requirements of this research, but broadly speaking, flow control mechanisms fall into two categories: Active Flow Control (AFC) and Passive Flow Control (PFC). As the terms suggest, the categories are distinguishable by whether or not any energy is supplied to create the control effect. Some researchers consider active flow control to incorporate devices which are both powered and reactive, whilst others consider that just a powered flow control technique is active. A mechanism

requiring energy to perform its role is defined as active in this study. The surface roughness tripping mechanism as used by Huber II and Mueller [1985] in low Reynolds number work, is therefore defined as a passive mechanism.

Many passive and active mechanisms exist with a variety of effects. Both AFC and PFC can have predetermined states and mechanisms. However, the advantage of active flow control is that a reactive state or variable state can be used. In other words, as flow conditions change, so can the behaviour of the active flow control device. Shepshelovich and Koss [1990], looked at several active, electronic versions of low Reynolds number trips (piezoelectric ribbons for example) and found changing the frequency of their trips caused different effects under different conditions. For several years, complex active flow control mechanisms have been studied that incorporate a feedback loop for optimum control. Work will continue into flow control, as the rewards of improving flight performance are high.

Flow control mechanisms work to maintain a condition or create a change in a condition. Many of the systems currently being studied energise the flow in some way. Trips, discussed briefly in the previous section, are positioned in laminar regions of flow before transition or separation bubbles would naturally occur. At low Reynolds numbers, the trips act to energise the laminar boundary layer, promoting a controlled transition to turbulence to avoid problems associated with either an unstable laminar boundary layer of a large separation bubble. At higher Reynolds number regimes, there is an advantage of trying to promote laminar boundary layers over the surface of wings for decreased cruise drag. Normally, transition might occur early over the surface of the aerofoil towards the leading edge. By inducing curvature and enhancing linear stability characteristics, laminar flow control can delay the transition to turbulence, sometimes over the complete aerofoil.

A turbulent boundary layer has greater resistance to separation compared to a laminar boundary layer. However, the skin friction drag of a laminar boundary layer can be at least an order of magnitude less than that of a turbulent boundary layer. Therefore, delaying transition, promoting a laminar boundary layer, at typical cruising attitudes reduces skin friction drag and surface noise. However, a laminar boundary layer is sensitive to flow disturbance and liable to breakdown resulting in separation. At very

low Reynolds numbers, the laminar layer separates readily. Given sufficient mixing with the freestream, the separated free shear layer then becomes turbulent and reattaches due to increased entrainment with the higher speed fluid (turbulent mixing). Saric *et al* [2002] investigated leading edge roughness in a slightly different way. They used distributed three-dimensional roughness to delay cross flow transition in quite spectacular fashion. In essence, the roughness was designed to energise those weakest instabilities in the cross flow vortices of swept wings, in doing so extracting energy from the strongest instabilities. If the goal is to decrease the drag of an aerofoil, it would be favourable to promote a laminar boundary layer and reduce separation as much as possible. A 10% reduction in drag would save billions of dollars in fuel bills from the US alone based on today's oil prices.

Besides surface roughness there are other mechanisms that can be used to energise the laminar boundary layer or even enhance turbulent boundary layers. Vortex generators are also passive devices that energise the flow at sited locations. L/D improvements have been reported of up to 100% and the devices are small enough to be fitted onto flaps and yet still allow complete retraction into the flap faring to avoid cruise drag penalties. The devices have been used successfully on the Gulfstream V and other aircraft for shock separation control. Riblets, passive devices used for turbulent boundary layer control, have been trailed for use on commercial aircraft both in the US and across Europe but the benefits were unclear. Originally researched by NASA, Mylar film was produced with inbuilt riblets spaced by pre-determined values. The Mylar film could therefore adhere to any existing airframe with relative ease.

1.2.4 SYNTHETIC JETS

Perhaps what is currently the most studied area of active flow control is the synthetic jet, a type of oscillatory flow control device. The formation of a time-averaged jet resulting from periodic excitation of a cavity and diaphragm arrangement has been known about since at least 1950 [Ingard and Labate, 1950, Ingard, 1953], although the first to unleash the potential of oscillatory devices for use in flow control were Schubauer and Skramstad [1948]. They realised that introducing certain frequency oscillations into a laminar separating shear layer could alter the nature of the flow around a flat plate. Figure 1.9 shows a schematic of a synthetic jet device. In the last ten years or so, zero nett mass flux jets have been increasingly employed in flow control

applications, albeit under different names: oscillatory excitation [Seifert and Pack, 1999], oscillatory control [Seifert and Pack, 1998], internal acoustic excitation [Hsiao *et al*, 1990], unsteady bleed technique [Williams *et al*, 1991; Williams and Papazian, 1991], and synthetic jets [Smith and Glezer, 1997; Amitay *et al*, 2001; Roos, 1997; Smith *et al*, 1998; Crook *et al*, 1999; McCormick, 2000, Lee and Goldstein, 2002] as they are referred to here.

A synthetic jet usually consists of an enclosed cavity with a single orifice opening (FIGURE 1.9). The cavity volume is then reduced in some way (usually via a membrane or deformable surface built into the cavity wall), displacing a volume of fluid out of the orifice. The cavity volume is then restored, sucking or replacing the fluid back in again. The orifice is usually small in comparison to the surface area of the actuated cavity wall, which causes relatively high exit velocities on the ejection half of the synthetic jet cycle. In the classical sense, a synthetic jet orifice is usually a circular orifice or thin slot. With a slot, on each cycle, a vortex pair is produced when fluid or a 'slug' is passed quickly through the slot causing separation then roll-up from the orifice lips. The vortex pairs propagate away from the orifice under their own entrainment. On the suction half of the cycle, external fluid is entrained into the cavity. In the time-averaged sense, the train of vortices appears similar to a jet. Given sufficient strength of the ejection part of the cycle, the vortex pairs propagate away from the slot, unaffected by the local entrainment on the suction cycle. The advantage of a synthetic jet is that the mean jet flow is formed from the flow in which they are propagated. In other words, a synthetic jet requires only one opening. Whilst there is zero nett mass flux through the orifice, there is non-zero momentum transfer into the flow system in which they are being used.

Because synthetic jets do not require an additional fluid injection and their power requirements are minimal, they are especially attractive for flow control devices. Additionally, they can be easily controlled by driving electronics and could therefore incorporate feedback systems providing adaptive responses. Existing uses include flow reattachment or delayed transition over an aerofoil [Choi *et al*, 2002, Amitay *et al*, 2001, Amitay and Glezer, 2002, Hsaio *et al*, 1990, Smith, 1998 and others], research into thrust vectoring aircraft and space craft, control of vortices over slender bodies and similar [Williams and Papazian, 1991, Margalit *et al*, 2002, Roos, 1997 and others] and

even as circulatory fluid cooling devices. The use of synthetic jets as flow control or flow re-attachment devices is increasingly studied for medium to high Reynolds number flows. As the potential for the synthetic jet is realized, computational data is also becoming an increasingly powerful tool in synthetic jet studies [Conrad and Goldstein, 2002, Mallinson *et al*, 2001, Rizzetta *et al*, 1999, and so on]. The two-fold experimentation and computational techniques complement each other and may provide extremely comprehensive studies of complex flows. Although both experimental and computational studies are still required for many areas of synthetic jet applications, a growing body of research exists revealing some interesting features.

There are several reviews of synthetic jet research, for example Glezer and Amitay [2002] or Smith and Glezer [1998]. It would be an impossible task to detail all synthetic jet research. Instead, key points relating to this research are focused on.

To form a synthetic jet an acoustic field can be used however there are two key criteria. Firstly for a fixed frequency, sufficient amplitude has to be used in order to cause roll up and advection of the discrete vortices. Also, the vortices have to be strong enough to overcome the orifice image and not be re-ingested into the cavity on the following suction part of the cycle. Smith and Swift [2001] and Utturkar *et al* [2003] gave parameters for minimum exit velocity and stroke length required to produce a vortex train.

Several researchers, for example Smith and Swift [2001], Smith and Glezer [1998], have shown that whilst in the time-averaged sense there are similarities with a continuous jet, there are also notable differences. Owing to the reversal in flow direction near the orifice during the suction part of the cycle, the mean jet centreline velocity near the orifice has a zero value several slot widths away from the orifice. Beyond the centreline stagnation point, there is mean positive velocity. The inflow relating to the suction part of the cycle is therefore drawn from very near the orifice exit and for that reason parallels are often drawn with sink flow.

Smith and Glezer [1998] noted that whilst the first vortex pair of the blowing part of the cycle was essentially laminar, as was the exit slug, very soon after the suction cycle began ($t/T = 0.5$), the vortices would transition to turbulence around $0.5 < t/T < 0.8$.

They found the vortex pair has a celerity minimum around t/T ~ 0.8 but then increased like $(t/T)^2$ until the vortex core became indistinguishable from the mean jet flow. Smith and Glezer showed that the transition from laminar to turbulent flow in the jet was dependent on, as one would expect, velocity of the flow through the orifice. The laminar flow experienced larger pressure loss coefficients and had fewer tendencies to expand and recover pressure. They continued to explore the effectiveness of the sudden expansion for generating time-averaged pressure differences with minimal acoustic power dissipation. They found the effectiveness to be increasing with decreasing r/h (where r is slot exit radius) and exit velocity, and increases with increasing stroke length for laminar flow. In comparison to continuous jets, Smith and Swift [2001] showed that synthetic jets were wider, slower and had more momentum.

As the jet is propagated to the far field, Mallinson *et al* [2001], and Smith and Glezer, [1998], showed both by experimentation and computation that the streamwise velocity decay is approximately like 1/x. Smith and Glezer [1998] also showed that whilst the near-field spectral content of the jet was dominated by the driving frequency and its many harmonics, there was rapid stream-wise attenuation of the spectra indicating a reduction in the total turbulent kinetic energy. Beyond around x/h = 19.7, only the driving frequency was evident and was reduced in around seven orders of magnitude.

Considerable effort has been made to optimise the performance of synthetic jets. Most of these studies are performed in quiescent conditions. Ingard [1953] was one of the first to notice differences in acoustic resonator performance dependant on aperture geometries. The generation of momentum of the actuator for a given input can be optimised in several ways. The cavity and orifice impart acoustic effects on the system and have a peak resonance condition, called the Helmholz Frequency, dependant on their geometries. Additionally the driver (usually a piezoelectric membrane) usually has a non-linear performance and peaks at certain resonance frequency. Several studies have reported the considerable advantages to jet exit velocities when the two resonant frequencies, the Helmholz resonant frequency and the membrane resonant frequency, are matched. Gallas *et al*, [2003, 2003], used a Lumped Element Modeling approach to optimise both cavity geometry and a piezoelectric element. On comparison with experimental data, one of their studies yielded over 50% improvement. A NASA Technical Brief [NASA LAR-16234] details the experimental optimisation of a

synthetic jet unit for commercial flight proposal (FIGURE 1.10). The study attended not only to cavity geometry optimisation (matching its resonant frequency with actuator frequency (FIGURE 1.11)), but also to the mounting of a piezoelectric disc. The brief also details the improvements found by clamping using the minimum of contact surface area – using metal o-rings rather than square section ring clamps which would restrict membrane vibration.

Whilst many studies identify the importance of matching acoustic cavity resonance with piezoelectric vibration resonance, few studies exist analysing geometry effects on the synthetic jet. Ahmed and Bangash [2001], noted that whilst they used small enough amplitudes in certain conditions so as not to produce a jet (the produced vortices being re-ingested on the suction part of the cycle), movement of their mean piston location closer to the orifice in certain cases did allow a time-averaged jet to form. The explanation for the jet formation variation lies in the change in cavity resonance due to the varying cavity volume. Uttakar *et al* [2002], performed calculations on square and rectangular geometry cavities with a variety of piston locations. They predicted that wide-ranging modifications of cavity geometry had relatively little effect on jet performance with momentum coefficients varying by at most 7% for the cases studied. Asymmetric location of the actuator did have a small effect on the external vortex strength producing slightly uneven vortex pairs and jet asymmetry. Smith and Swift [2001] noted that increasing the exit radius of the orifice reduced the adverse pressure gradient experienced by the exiting flow and allowed the flow to expand more resulting in smaller acoustic power losses. The effect was enhanced if the jet exit velocity was increased. Bridges and Smith [2003] showed variation in boundary layer interaction caused by changing the synthetic jet orifice orientation As Schaeffler *et al* [2002] identify in their review of NASA Langley flow control activities, it is important in design to know how the actuator can be located and what cavity geometries can be used to enable the designer to use more conformal shaping.

One of the most complex areas of synthetic jet study is the flow fields associated with a synthetic jet in non-quiescent conditions such as a cross-flow. A growing body of research exists on cross-flow studies [Camussi *et al*, 2002, Cook *et al*, 2000, Cui and Carry, 2003, Kim and Sung, 2003, Orkwis and Filz, 2003, Schaeffler, 2003, Smith, 2002 and others]. The goal is to understand the fluid dynamic interactions and the effect

on the surroundings. Understanding of the interaction between multiple synthetic jets is perhaps even more demanding to research [Holman *et al*, 2003, Watson, 2002 etc.]. With such complex flow fields, both experimental and computational research is needed to understand the mechanisms involved.

The synthetic jet is one of several oscillatory flow control devices being explored. There is a growing resource of information on oscillatory control devices with some important results to note for their use and application. Many researchers have demonstrated the ability to control flow favourably around aerofoils with separation points caused by flap joints or humps producing adverse pressure gradients [Melton *et al*, 2003, Wu *et al*, 1998, Amitay *et al*, 2001, Seifert and Pack, 1999, Seifert *et al*, 1998, Seifert and Pack, 1998, Chen and Beeler, 2002, Hassan, 2003]. There is even research to investigate the use of synthetic jet blowing as a virtual flap or enhanced aerofoil circulation device, for example by Rogers [2000].

Collins and Zelenevitz [1975] discovered perhaps the most surprising oscillatory flow control technique in 1975. They avoided the use of a direct momentum injection method and used external acoustic excitation to similar effect. They showed that momentum near an aerofoil surface could be increased by sound radiating from some distance away, passing momentum directly from the freestream. Several studies followed using many variations of Collins' and Zelenevitz's work. Different studies reported different optimum actuation frequencies vary in several orders of magnitude. Some indicated a pronounced shift to lower frequencies when the levels of excitation were high. Zaman [1987] found non-dimensional frequencies less than 5 worked most effectively in terms of lift enhancement. Zaman [1992], went further and showed that for Reynolds number 75,000, St=4 was the most effective frequency with $2<St<5$ being the most useful range giving the largest lift increments. He noted that the instability was an order of magnitude lower than the instabilities in the separated shear layer (around St=30). Several other researchers also indicated the effectiveness of Strouhal frequencies of the same order, for example Amitay and Glezer, [2002]. Greenblatt *et al* [1999], showed that even leading edge excitation showed optimum performance around $2<St<4$, with higher momentum coefficient cases corresponding to increasing optimum Strouhal frequency for the range they tested.

Several researchers have studied large surface fluctuations as flow control mechanisms. Munday and Jacob [2001, 2001] and Munday *et al* [2002] for instance placed piezoelectric actuators under the latex skin surface of a NACA 4415 aerofoil. The actuators were then oscillated and it was found that significant improvements on flow separation occurred for St in the range $0<St<11$. Pinkerton and Moses [1997] explored the feasibility of using large-scale piezoelectric actuators to control the shape and camber of a low Reynolds number wing. Whilst control was achieved, further study was required to assess the performance benefits. Pinkerton *et al* [1996] represent many researchers looking at the benefits of using piezoelectric stiffeners in-built into aerofoils and fins to control fin-buffeting and undesirable oscillations.

1.2.5 FLOW CONTROL AT LOW REYNOLDS NUMBERS

Whilst many studies exist showing the use of synthetic jets in high to medium Reynolds number flows [Pack and Seifert, 2000, Seifert and Pack, 2002, 2003 for example], and even several for more complex tasks like delta wing and jet control [Margalit *et al*, 2002, Duraisamy and Baeder, 2003, Dahai *et al* 2003 [2003], Bera *et al*, 2003, Avihar *et al*, 2003, Guo *et al*, 2003, Jacobson and Reynolds, 1998, Pack and Seifert, 1999], there are comparatively few studies performed at low Reynolds numbers.

Several studies exist based around flexible wings of MAVs and their use for improved aerodynamic performance; Wooding and Gursul [2003] looked at improved gust response performance using flexible wings, the university of Florida MAV incorporates flexible wings that have been the subject of several studies [Lian *et al*, 2003, Reaves *et al*, 2004 etc.] Null *et al* [2002] studied flexible cambered foils for MAV flight and there are several others. Zheng and Ramaprian [2000] commenced study of active piezoelectrically controlled wings for MAVs and Goodman [2002] showed the feasibility of propelling MAVs using trailing edge piezoelectric foil oscillation.

In fact the small scale and weight of an MAV enables synthetic jets to be tried not only as a flow re-attachment device, but also, maybe more importantly, as a propulsion device. Utturkar *et al* [2002] showed that wide ranging changes to synthetic jet cavity design had relatively limited effect on jet exit velocities; very useful when considering the limitations of a MAV synthetic jet cavity. Minimal power requirements and lack of complex mechanics readily lend such devices to MAV technology. The research

presented here utilizes large synthetic jet cavity dimensions, which are only limited by the wing volume. A fixed wing MAV and efficient synthetic mechanism of propulsion would appear a good combination for MAVs operating in the low Reynolds number flows.

1.2.6 ACTUATION MECHANISMS

Active oscillatory flow control requires actuation systems. Several mechanisms currently exist for internal techniques; speakers and acoustic drivers, piezoelectric diaphragms, piston and valve systems [Traub *et al*, 2004] and more recently sparkjet actuators (Cybyk *et al* [2003]) and silicon based MEMs devices. Surface disturbances are normally created using fliperons, ribbons, piezoelectric benders, and more recently ionised plasma.

1.2.7 PIEZOELECTRICS

Whilst early parts of the research described here used a laboratory speaker to drive the synthetic jet, later studies used piezoelectric drivers. Therefore a brief resumé of piezoelectric materials is given.

Piezoelectrics belong to a group of materials called smart materials – materials that transform through some physical interaction. Piezoelectric materials, shape-memory alloys, electrostrictive materials, magnetorestrictive materials are examples of smart materials presently being studied.

The term 'piezoelectric' stems from the Greek word meaning pressure. When subjected to pressure or stress, a piezoelectric material experiences a voltage potential across its boundaries. The effect is known as the piezoelectric effect. Conversely when a piezoelectric material experiences a voltage potential across its boundaries, the material is strained, known as the reverse piezoelectric effect. Naturally occurring materials that exhibit such properties include quartz, Rochelle (rock) salt and tourmaline. However, the voltage yield of such materials is very low.

Whilst piezoelectrics were used extensively in underwater applications, microphones and transducers up to the 1940s, it was not until then that a major discovery came with research into the properties of lead zirconate titanate (PZT). These materials were found

to exhibit extremely high piezoelectric responses in comparison to anything used previously. Furthermore, a high degree of freedom in their design characteristics could be achieved using dopants or material additives. That paved the way for the many hundreds of applications piezoelectrics are used for today.

Broadly, piezoelectrics are manufactured in a two-stage process. First the material (formed by careful powder mixing and sintering) is fired at high temperatures of around 1200-1300°C to achieve a crystalline structure, which is then cut and machined to the desired shape.

The second stage of the process is called doping. After firing, the electrical dipoles within the crystals are orientated at random. To make the material piezoelectric they must be polarized. Polarisation is achieved by passing a high (several kV/mm) DC voltage across the boundaries of the material. Whilst the process does not fully orientate all dipoles into the same direction, overall, the axes are then permanently biased in one direction.

When an AC voltage is applied to a piezoelectric an oscillatory material stress is created within the material. Depending on the frequency of the alternating current, the piezoelectric might vibrate more or less, dependent on the material-specific elastic frequency. If the driving frequency matches the specific elastic frequency then the piece is said to be operating at resonance and the stresses on the material are greatly amplified. As the device is at its highest electromechanical deforming efficiency at its elastic resonance, many applications make use of such property and tailor pieces with resonant frequencies in their application range.

Piezoelectric actuators can now be fabricated in a variety of geometries and formats. Conventional devices are normally circular discs mounted on thin metallic shim as used in small speakers and buzzers. Recently, piezoelectric benders and flappers have become more commonplace.

The piezoelectric is the most common synthetic jet actuator and several studies have een performed to improve their operation, understanding and application [Cattafesta III *et al*, 2001, Diez and Dahm, 2003, Lee *et al*, 2003 etc.]. The field of piezoelectrics is

evolving rapidly and yielding consistently more capable components for increasingly demanding applications.

As part of their ongoing advanced materials research considerable effort has been made at NASA to advance displacement and strain performance of actuators. Early parts of their research led NASA to make considerable improvements into high strain applications using high displacement RAINBOW (Reduced and Internally Biased Oxide Wafer) actuators [e.g. Dausch and Wise, 1998, Hyer and Jilani, 2002]. They showed capability of unimorph, single element displacements, under general loads of around 1mm. More significantly, two new actuator types were borne out of the experience with the RAINBOW devices.

Most recently Bryant *et al* [2002, 2002] constructed a large thin circular piezoelectric ceramic disc where the positive and negative terminals covered the surface of the disc in a system of inter-locking spirals. Upon excitation, the piezoelectric diaphragm (or Radial Field Diaphragm, RFD) would dome up or down depending on the charge direction. Displacements of up to around 0.6mm were achieved. More significantly RFDs demonstrated the potential for out-of-plane deformation using a fixed boundary. The three dimensional out of plane movement could also be tailored in geometry depending on the inter-locking electrode pattern – in other words, the shape was not limited to inter-locking spirals, but could be squares or more arbitrary geometries. Bryant, 2003 (pers. comm.) revealed that the forcing levels of the piezoelectric ceramic used were perhaps not yet suitable for truly high torque applications.

By far the biggest leap in piezoelectric performance (FIGURE 1.12) came with the development of NASA's Thin-layer Composite Unimorph ferroelectric driver and sensor (Thunder) [Bryant *et al*, 1997]. The actuators were constructed in layers; a thin steel shim base layer, a special polymer adhesive patented by NASA Langley called LaRC-SI, PZT, more LaRC-SI then an aluminium skin on top (FIGURE 1.13). After the layers are assembled, the piece is placed in an autoclave and cooked at high temperature (250-300°C) under compression. The piece is then cooled under controlled conditions to room temperature. As the various layers have different thermal coefficients, they contract in different ways. However the adhesive holds the layers firmly together. The result is a curved or domed piezoelectric composite with significant pre-stress in-built.

It is this pre-stress that allows Thunder actuators to perform extremely high displacement actuation without damage under high load.

There are several publications available on the construction, performance prediction and enhancement of Thunder technology [e.g Wieman *et al*, 2001, Ounaies *et al*, [2001], Taleghani and Campbell, 1999, Taleghani, 2000, Yoon *et al* 2002, 2004, Horner and Taleghani, 1999] Face International Corp., Norfolk, Virginia, USA, now manufactures Thunder actuators for commercial requirements under license from NASA. Specification of off-the-shelf pieces is available from their web-site in addition to further information on the Thunder technology which remains some of the highest performance levels of piezoelectric components seen to date. Face International Corporation's TH-7R unimorph Thunder bender, for example, measures a mighty 96.52mm x 71.12mm and can demonstrate peak-to-peak amplitudes of over 30mm when clamped in simply supported mode operating at resonance. Typical performance values would limit the peak-to-peak displacement to a few millimeters though for sustained, reliable operation. Bigger actuators can be made to order.

Pinkerton and Moses [1997] and Pinkerton *et al* [1996] conducted a feasibility study of controlling aerofoil camber using Thunder actuators. However, changing the camber for long durations required the actuator to be powered for long durations and the system was therefore too inefficient to explore further.

Several other actuator variations exist: Hooley [2000] of Ilimited, Cambridge, England, designed and now manufactures helimorph actuators for use in advanced loud speaker technology (based on a helical strip, the actuator can deform omni-directionally), Boeing [Calkins and Mabe, 2001, Calkins *et al*, 2002] have used stacked piezoelectric benders to obtain sufficient force necessary to power synthetic jet flow control mechanisms on the V-22, Caterpillar [Waterfield, 2003] designed pre-stressed benders similar to Thunder with high forcing levels for valve control, the list is endless.

Piezoelectrics lend their technology well to flow control devices because they are simplistic in operation, efficient and fully controllable by electronics and are relatively light weight compared to mechanical actuators. Presently, most of the high-end piezoelectric technology requires high voltage driving electronics at low current. Whilst

improvements are being made with that regard, there are developing microelectronics capabilities contained in small packages weighing only a few grams that would provide such voltages from a modest power source. Chol *et al* [2004] are developing microwave power for smart material actuation. Improving the efficiency of the energy conversion is ongoing research [e.g. Richards *et al*, 2004]. Research is also ongoing on the possibility of using self-powered piezoelectric in flow control devices. For instance, Horowitz *et al* [2002], worked on creating an energy harvester based on the acoustic energy available in an incident acoustic field that was used to self-power an electret microphone.

1.3 SUMMARY

Several working examples of MAVs exist although many may not be efficient or optimal solutions. MAVs have been identified for important utility applications in the commercial, industrial and military sectors. DARPA, for one, remains a significant financial supporter of MAV research giving an indication of the level of importance.

There is an identified need to improve aerodynamic and propulsion solutions for MAVs flying in the low Reynolds number regime. A number of key aerofoil design criteria have been identified for low Reynolds number aerofoils although further work is required in this very difficult regime. The separation bubble can lead to detrimental effects on lift and drag coefficients. Greater design considerations are required to design low Reynolds number aerofoils with sufficient lift coefficients without the penalty of high drag coefficients. There may be considerable benefits of utilising flow control devices to enhance aerodynamics in the low Reynolds number regime.

The synthetic jet, amongst other devices, has been used successfully for flow control applications at higher Reynolds numbers although there is insufficient relative momentum generated to produce thrust forces at these scales. Given the growing effectiveness and capability of piezoelectric technology, it would seem sensible to explore the possibilities of using synthetic jets as a means of low Reynolds number propulsion and flow control for some of flight's most difficult aerodynamic conditions.

1.4 RESEARCH AIMS

The research aimed to investigate a novel integrated aerodynamics and propulsion solution for MAVs. A key criterion of the investigation was to explore and determine parameters for an innovative use of synthetic jets as a solution to MAV propulsion and aerodynamics challenges.

Initial experiments analysed the interaction of a synthetic jet located at the trailing edge of a wing with flow visualization and velocity measurements at low Reynolds number. The effects of excitation frequency, momentum coefficient, angle of attack, and Reynolds number were investigated to assess their fluid dynamic effects and therefore their effects on the performance of the system. Understanding of such key parameters will help determine operation parameters for the system and provide a catalogue of supporting research to enable the design of an optimised system variation in future research.

Gauging the levels of efficiency of the propulsion and lift mechanisms would be an invaluable statistic in an assessment of the concept. Whilst the initial synthetic jet driving system was not designed with efficiency in mind (more the capability of providing a broad range of operating parameters for the fullest possible study), both aerodynamic efficiencies based on lift-to-drag ratios and power efficiencies were assessed to help with future design considerations.

Once the synthetic jet propulsion parameters were understood, work was undertaken evaluating a potential MAV synthetic jet mechanism. Its construction, operation parameters and efficiency were considered. Areas of development and future work were also identified.

The overall research therefore aimed to combine a mass-less jet mechanism with a suitable aerodynamic wing plan-form and presented a combined aerodynamics and propulsion solution for MAVs. Other potential applications and benefits of the research were also discussed.

1.5 OUTLINE OF THESIS

Chapter2 described the experimental apparatus and techniques used during the research presented here. The key wind tunnel and water tunnel facilities were outlined, in which most ofthe research discussed here was conducted. A variety of conventional and state-of-the-art measuring systems were used. Key hardware and software features of the measurement systems were reported.

Chapter 3 reported the techniques used to conduct experiments using the equipment outlined in Chapter 2. Consideration to low Reynolds number testing was given, as well as how accuracy and consistency of experimentation was achieved. A significant assessment of experimental errors, measurement bias and a related discussion was given.

Chapter 4 presented experimental results highlighting the fundamental features of the synthetic jet and aerofoil system. This included the choice of an aerofoil and introduction of the frequency, momentum coefficient, Reynolds number, incidence parameters of operation of the system and their effects.

Chapter 5 revealed the detailed effect of the frequency parameter on the jet performance. The effect was then explored to provide an understanding of the fluid dynamic variations involved at different frequencies. Consideration was given to the jet in quiescent flow as well as in freestream conditions. The dissipations of jets of various frequencies into the wake were shown and phase locked PIV experiments presented.

Chapter 6 gave an account of surface pressure measurements conducted, specifically to estimate lift coefficients, but also to study the effects on the surface pressures and to derive estimates of thrust coefficient. With estimates of lift and drag under a range of operating conditions, aerodynamic efficiency was assessed. Measurement of the electrical power consumption was also used to assess propulsive efficiency and an overall consideration of the system.

In chapter 7, successful construction of a novel internal jet mechanism was presented. The key design criteria and main considerations were discussed. Analysis of the entire

system was conducted using a two-component force balance and a power measurement system.

Conclusions, areas for further development and references followed in the final chapters.

1.5 FIGURES

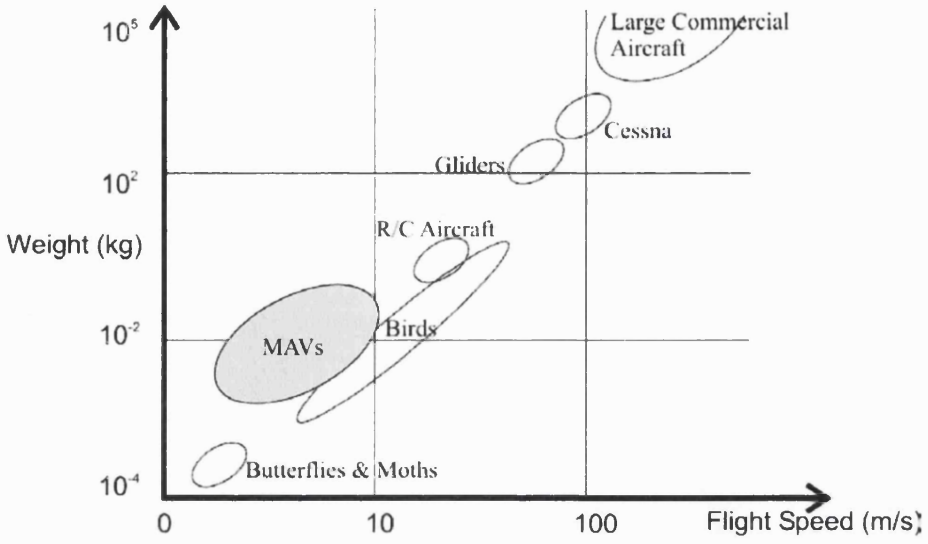

FIGURE 1.1 Flight regime of the MAV compared to other avians [Adapted from http://www.darpa.mil/tto/mav/mav_auvsi.html, 1997, and Mueller and DeLaurier, 2003]

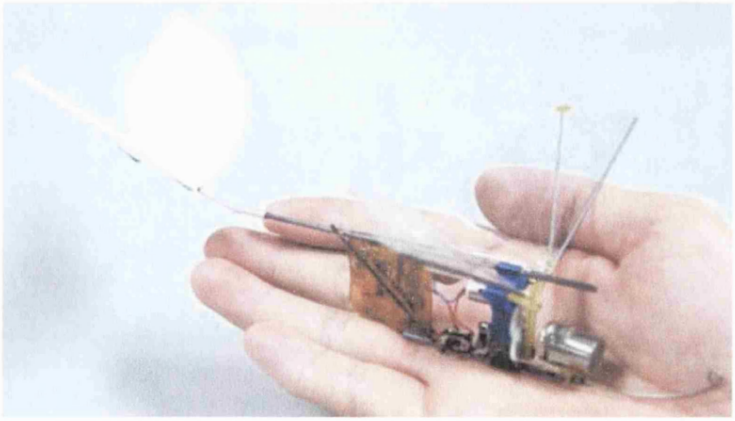

FIGURE 1.2 Aerovironment's Microbat flapping wing development MAV [Photo courtesy of Aerovironment].

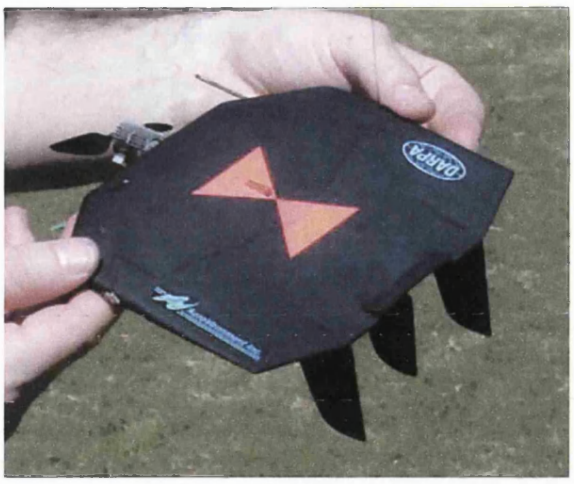

FIGURE 1.3 Aerovironment's Black Widow MAV, [Grasmeyer and Keennon, 2001]

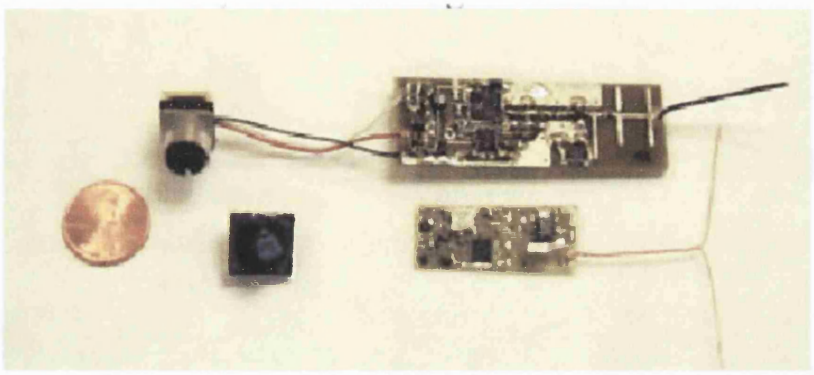

FIGURE 1.4 Micro camera, transmitter and receiver system for the Black Widow. [Grasmeyer and Keenon, 2001]

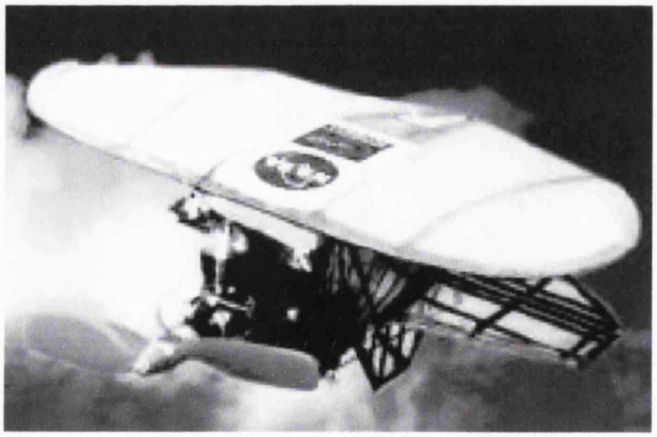

FIGURE 1.5 Flexible membrane wing based Micro Air Vehicle of the University of Florida, [Waszak *et al*, 2001].

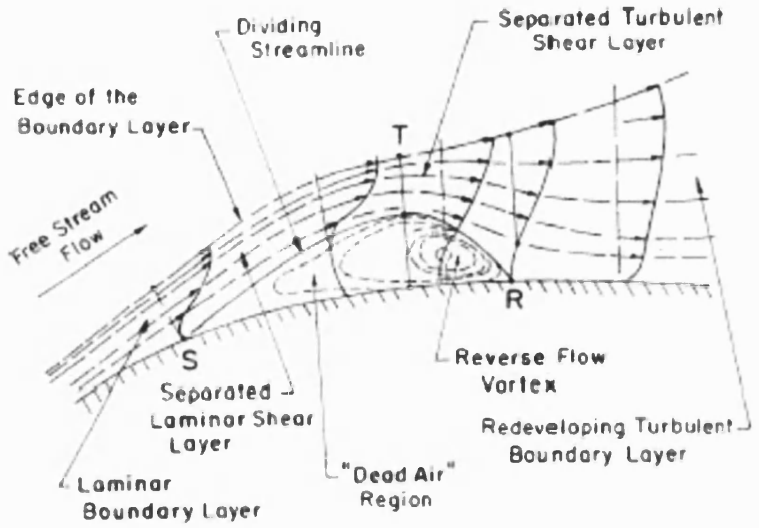

FIGURE 1.6 Features of the laminar separation bubble. [Horton, 1968].

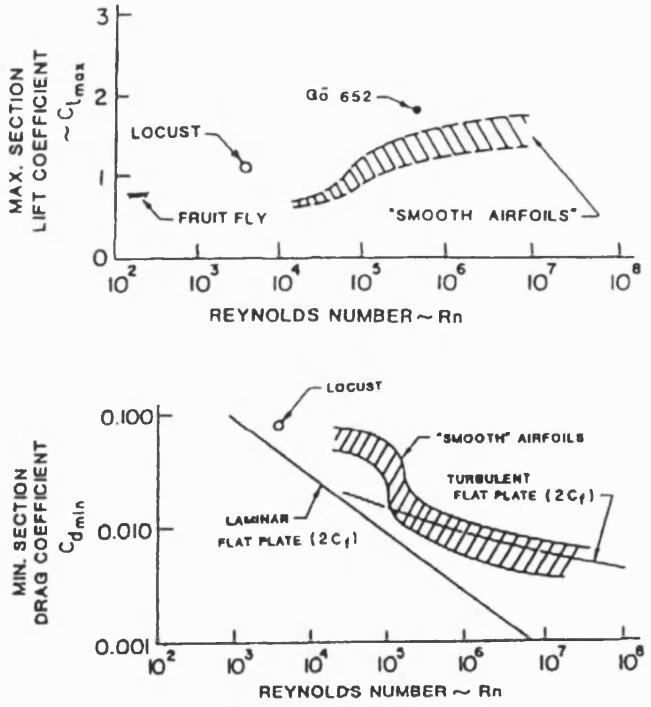

FIGURE 1.7 Variation of drag (top) and lift (bottom) coefficient with Reynolds number. [Mueller, 1999].

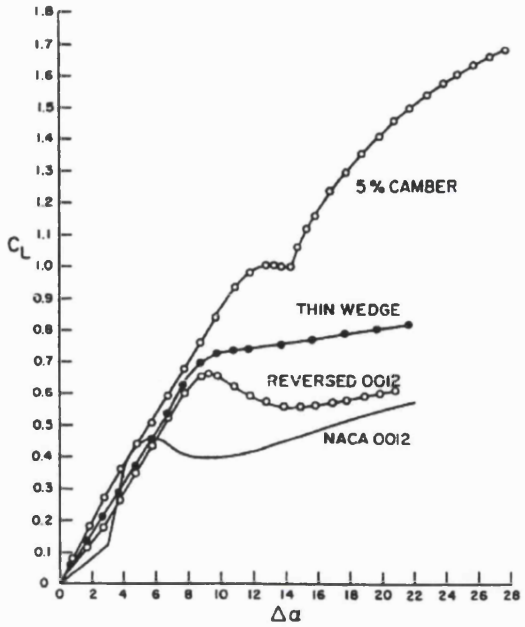

FIGURE 1.8 Variation in lift coefficient for a variety of aerofoil geometries at Re=70,000. [Laitone, 1997].

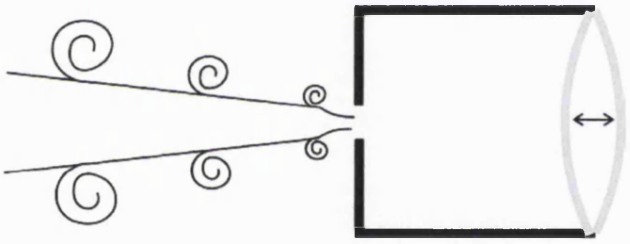

FIGURE 1.9 Schematic of the synthetic jet showing oscillating diaphragm and vortex pairs.

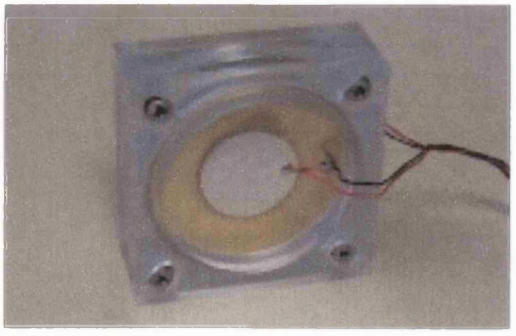

FIGURE 1.10 A potential commercial unit: the NASA optimised synthetic jet. [NASA TM LAR-16234].

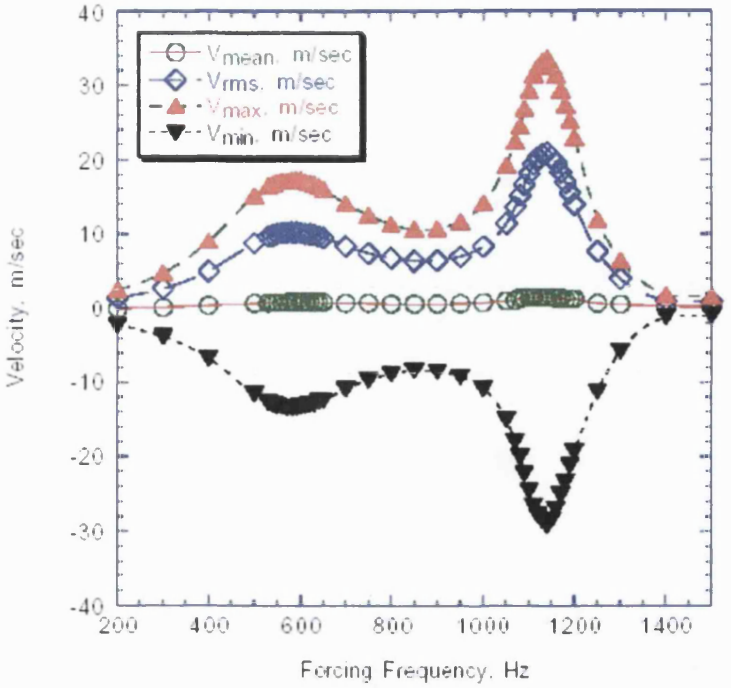

FIGURE 1.11 Variation of exit centreline velocity with forcing frequency. The first peak is attributed to the cavity resonance, whilst the second is due to the actuator resonance. [NASA Technical Brief LAR-16234]

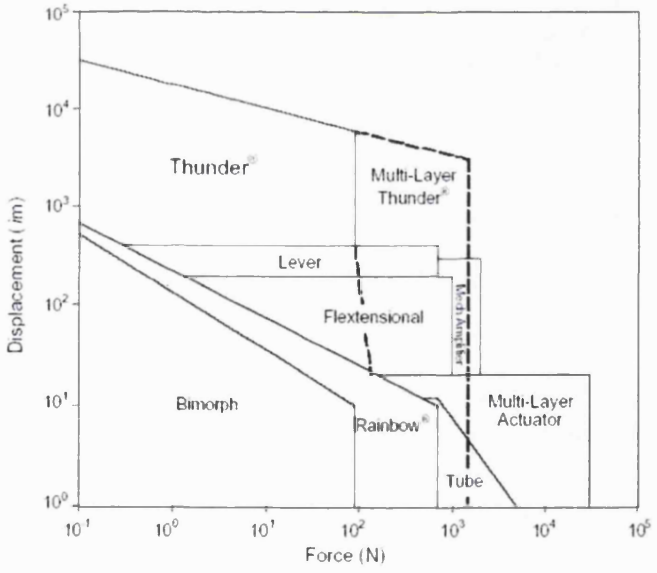

FIGURE 1.12 Displacement and force properties of the key piezoelectric devices (units *i*m is μm). [Face Corporation White Paper, 2001]

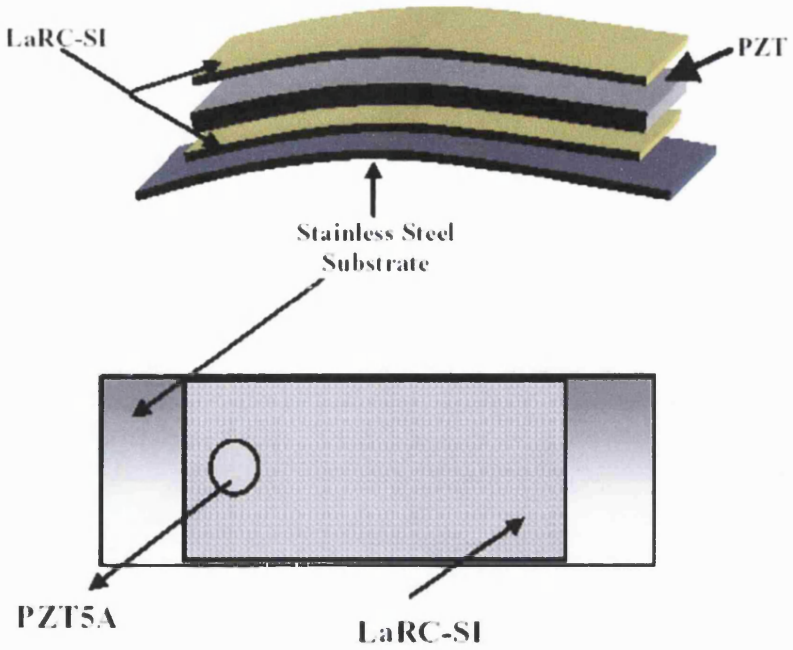

FIGURE 1.13 Construction layers of Thunder actuators. [Ounaies *et al*, 1999].

CHAPTER 2 EXPERIMENTAL APPARATUS

2.1 WATER TUNNEL

Water tunnel experiments were all conducted in a recirculating Eidetics Water Tunnel model 1520, with test section dimensions 0.38m x 0.54m x 1.53m located at the University of Bath (FIGURE 2.1). The tunnel can produce water freestream velocities between 0m/s and 0.45m/s with turbulence intensity quoted by the manufacturers of less than 1%.

The water tunnel comprised an all round view test section with tempered glass in the sidewalls, base and streamwise end wall. A large contraction section contains several filters and honeycomb straighteners. The collection section has two filtered outlets to a large bore recirculation pipe. When filled, the tunnel contains approximately 1000 gallons of water. The driving motor for the pump is a 2.0HP, 900 gpm 3-phase axial flow unit. A disadvantage of this unit is the generation of considerable electrical noise even when much below its 20-amp maximum current drain. The speed of the tunnel was set using a three-phase motor controller. Once a steady stream was established after a change in velocity, the freestream velocity remained extremely stable at all speeds used here.

Coloured food dye could be introduced into the flow using a system of six pressurised containers and capillary delivery tubes. Capillaries were kept as small as possible – in the region of 1.0mm OD to avoid disturbance to potentially sensitive aerofoils being

studied. Batill and Mueller [1981] suggested that round wires introduced into air flow for smoke visualisation purposes should have Reynolds number based on diameter of around 20 to avoid wake interference effects. Mindful of the capillary wake interference the capillary, chosen with small a diameter as possible, was put into the flow at least two chord lengths upstream of the aerofoils and bent to run parallel to the streamlines for the approach to the airfoil, avoiding intrusion into the flow as much as possible. Ink injection matched to the freestream velocity avoided any velocity deficit in the wake at the tip of the dye tube.

Dye delivery velocity was visually matched to freestream velocity to avoid interference or flow disturbance. A smooth dye injection filament was the goal. If the exit velocity is slow compared to freestream then wake structures can be seen at the dye injection. If the exit velocity is too fast then jet structures are evident. Dye tubes were also spliced carefully and neatly to ensure burr and turbulence-inducing roughness was removed. Even slight roughness in spliced dye tubes was observed by the author to invoke vorticity and turbulence. Correctly prepared dye tubes often made the difference between poor quality pictures and a visualisation of clarity. The best flow visualisation pictures were obtained using the cleanest dye tubes deploying the smoothest ink flow at the correct rate.

In the conditions tested here, blue and red food colouring was found to be an effective colourant with several others colours trailed not offering sufficient contrast for high quality images. Continuous use of dye eventually discolours the water and does not make for high quality, contrasting flow visualisation pictures. Excess dye could be removed within 30mins using around 1 cup of concentrated swimming pool chlorine in conjunction with a filter system using fine grade diatomaceous earth filter material, restoring the clarity of the water completely. Diluted chlorine was observed to deteriorate metallic surfaces quickly. Considerable effort was made to remove the test apparatus as soon as possible for drying and, if necessary, surface reparations.

Lowering models to be tested into the water tunnel from the open topped test section often caused air bubbles to be trapped in and around the model and its supporting structures. Care was taken to remove as much air as possible, especially from intricate

cavities that would affect water flow and model performance. Models lowered into the water were always wiped free of micro bubbles to ensure undisturbed fluid flow.

Wings were placed between end plates for a two-dimensional simulation in these experiments. Hollow wings were connected with piping to a piston-cylinder arrangement located outside the test section. The synthetic jet was constructed from a stretchable rubber diaphragm oscillated using mechanical armature and an electric motor. The diaphragm was sealed using flexible waterproof epoxy at the top of an orifice with an opening at the opposite end to pipe the flow into the hollow wing. The diaphragm could then be oscillated by an attached piston arrangement to displace fluid from the cavity volume and then suck back in fluid sinusoidally. A variable speed controller for the motor allowed the jet excitation frequency to be varied, and a change in the piston armature could vary the jet amplitude. A small pipe inlet near the leading edge of the wing would then supply the oscillating fluid from the cavity into the hollow wing. The wing was then mounted between end plates held using a metal framework. The top framework was also a convenient mounting point for the motor, piston and other apparatus. The water tunnel apparatus used for flow visualization is shown suspended in the water tunnel in FIGURE 2.2.

2.2 OPEN JET WIND TUNNEL

One limitation of the water tunnel setup was that the excitation frequency and momentum coefficient could not be varied independently as the piston velocity is proportional to the frequency. In order to gain easier and independent control of frequency and amplitude, further experiments were conducted in air, using a speaker to drive the synthetic jet. The setup was placed in the open section wind tunnel at the University of Bath as shown in FIGURE 2.3. The speaker could then be controlled precisely using a signal generator and amplifier monitored on a high-end digital fine measurement oscilloscope, giving both frequency and amplitude adjustments and measurement. The electronic apparatus used is represented in FIGURE 2.4.

As the speaker required amplification from the laboratory signal generator, a commercial audio amplifier was used in a bridged set up to use both left and right channels in operation of the speaker. The bridged amplifier offered about 50 times

voltage amplification from a standard laboratory signal generator over the range tested. For ease of operation, the output signal from the signal generator was monitored rather than the high voltage amplified outputs. Waveforms could be saved and exported in CSV format from the oscilloscope using 3.5" floppy discs.

All wind tunnel experiments in this research were conducted in the open section wind tunnel. The open section has a 1m long test section from a 0.76m outlet. The operational range of the tunnel was initially 0.6-30m/s for the first part of the research. Unfortunately a motor and controller replacement was necessary during the research, which gave a new range of 1-32m/s but with increased stability in the low speed range.

Tunnel turbulence intensity was monitored regularly using LDV but was always within the range 0-0.4% in the open jet wind tunnel. Whilst several better facilities exist, turbulence intensity below 0.5% at low Reynolds number is considered reasonably clean flow. Of utmost importance during the research is consistency over the entire period, something that was achieved here. Low turbulence intensity levels are suitable for studying Reynolds number sensitive airfoils and devices [Howard and Kindelspire, 1990 etc.]. The working area is 1m long until the collection section (radius 0.78m) gathers airflow into the return section (radius 0.49m) for recirculation. Turning vanes are fitted to each corner of the wind tunnel loop and filter screens are place significantly upstream of the contraction to outlet to avoid flow disturbance.

Whilst the first wind tunnel motor and controller was difficult to maintain at low speeds, the replacement motor was controlled using an EMI three-phase analogue controller to greater effect. Whilst the tunnel controller did not have direct feedback for speed regulation, once the tunnel speed is set, freestream velocities rarely fluctuated above +/- 0.01m/s during experiments. Freestream velocity was monitored during experiments using a two-component LDV probe for the best precision. Fluctuations in freestream were problematic with the original motor and controller. However, with the new system, fluctuations were rarely a problem although more common when running in the lower ranges around 1.4m/s.

2.3 AEROFOIL GEOMETRIES AND CONSTRUCTION

2.3.1 EXTERNALLY ACTUATED AEROFOILS

Several aerofoils were constructed for initial testing. The section layouts are shown in FIGURE 2.5. The first model tested had, in essence, a thin wedge shape with a rounded trailing edge. The leading edge and trailing edge had a thickness of 2 mm and 8 mm (corresponding to 1% and 4% thickness), respectively. For ease of modeling, both the leading edge and trailing edge were semi-circular in cross section with a diameter equal to the local thickness. The span and chord were 200 mm, and a 0.5mm slot at the trailing edge ran the entire span, centered in the center of the trailing edge. Two other models with the same chord length and trailing edge geometry were manufactured. One of these was flat with 4% constant thickness and an elliptical leading-edge (4:1 ratio), and the other was identical but with a 5% camber. It is well known that cambered wings show good aerodynamic performance at low Reynolds numbers. Laitone [1997] showed that a wing of 5% camber appeared to outperform a thin wedge in the low Reynolds number regime. Even more recently, Mueller [1999] presented similar results with a 4% cambered planform. Very recent research [Sunada *et al*, 2001] has shown evidence suggesting that 10% and 0% camber were not as good as 5% camber, inferring the possibility that somewhere in the range 0%-10%, there lay an optimum. Consequently, in the investigation presented here, 5% camber was chosen.

All of the aerofoils used in the water tunnel and wind tunnel investigations were constructed from aluminium. The basic framework and leading edge geometries were machined using a digital three-axis milling machine. The upper and lower 1mm aluminium skins of the hollow wings were fitted and finished by hand. Every effort was made to ensure a uniform jet slot width across the span of the wing. The slot width was honed until it satisfied a height of 0.5mm+/-0.05mm. The tolerance of the other wing geometries was within 0.5mm of the required geometry. A former was constructed for the 5% cambered aerofoil, which gave an accurate curve of 5%.

A pipe was fitted near the leading edge of all of the aerofoils from which to connect to the synthetic jet driver mechanism. The pipe cross-section area was chosen to be significantly larger than the jet exit area to prevent a restriction on the driving jet system.

Attempts were made to try and maintain a consistently smooth surface to aerofoils used throughout the research in an attempt to remove any variation in transition caused by surface roughness [Lin and Walsh, 1984]. For that reason, all of the aerofoils used in the research were finished by hand using increasingly fine emery paper stopping at P100 grade wet and dry on a matt black spray paint finish for an extremely smooth surface.

After each experimental period, the aerofoil was cleaned to remove ink or seeding oil, repainted and re-finished to maintain a constant surface throughout. It was noticed that both the chlorinated water and the seeding oil attacked the paint after time. Particular attention was paid to ensure aerofoils did not deteriorate during testing.

Any condensed seeding build-up on the surface of the aerofoils was also cleaned off right away. Marchman III *et al* [1987] and Hansman Jr and Craig [1987] showed that surface moisture could alter aerodynamic performance at low Reynolds numbers.

2.3.2 INTERNALLY ACTUATED AEROFOIL

To demonstrate a potential enabling technology for a real mechanism and to allow direct force measurements to be taken, a dedicated aerofoil was constructed with an in-built mechanism capable of producing a suitable performance for the Re=20,000 condition.

Whilst a full-scale aerofoil was used, in the realms of MAVs, the internal space available to accommodate a mechanism was extremely limited and consequently very challenging. The internally actuated wing was based on the cambered wing geometry with a small enlargement of the trailing edge underside to create additional internal space (FIGURE 2.7).

Prior to construction, several mechanisms were trialed in a simple test box. The box was constructed to have the same internal geometry as the cambered wing. Unlike an aerofoil, the box test bed was accessed through a removable lid. The main design criterion for the internal synthetic jet actuation system were the ability to resonate around the optimum frequency or between St=2 and St=5 identified in the research, the

amplitude of oscillation should be sufficient to create a positive nett thrust and the mechanism should be sufficiently light to be suspended from the Low Reynolds Number Force Balance (LRNFB) (section 2.4.7).

Most research involving synthetic jets use piezoelectric elements as the actuation system. Piezoelectric actuators have advantages of being lightweight, electronically controllable and reasonably efficient.

As a first trial, 24 commercial piezoelectric speaker discs were arranged in a single sheet and inserted into the test bed for experimentation. The momentum coefficients required for successful synthetic jet propulsion were considerably higher than those usually generated with a synthetic jet driver.

Early in the development it was realized that whilst the slot provides resistance to the movement of the actuation mechanism, the restriction of the actuator on the other side would also have to be a consideration. The speaker and piston apparatus were unrestricted on the opposite side of the synthetic jet system. Enclosing the synthetic jet within an aerofoil would alter the layout and would create a restriction in movement if the opposite side of the actuator were not free to resonate. In order to decrease the restriction of movement on the actuator it was decided to form one of the aerofoil surfaces as the vibrating actuation surface (FIGURE 2.7). Upper surface vibration has been used for positive effect and it was hoped that the upper surface could be used.

The test bed was modified, replacing the upper aluminium surface with the 24 piezoelectric actuators driven in forward bias mode forming the new 'active' upper surface. Upon testing, it was found that the new configuration of (unrestricted) 24 piezoelectric actuators had greatly increased amplitude but still lacked insufficient amplitude to create momentum coefficients larger than around 0.028 at Re=20,000. Despite attempts to gain performance by maximizing the cavity size in order to create a cavity resonance closer to the actuation resonance, no increase in performance was seen. The Helmholtz resonance was estimated to be several orders of magnitude higher than the first resonance mode of the actuators. In addition, the actuators were extremely sensitive to over powering and quickly deteriorated in performance.

Extensive research into high power piezoelectrics led to the NASA development in Thunder actuators, now produced under NASA license by the Face Corporation. The actuators offered high displacement and forcing levels at a first resonant frequency close to that required for the synthetic jet operation of the internal actuator. One of the largest commercially available Thunder actuators is the TH-R7 shown in FIGURE 2.6. It was realized that based on the predicted performance of the actuators, two TH-R7s could be used in conjunction to drive the synthetic jet. The geometry of the TH-R7 was close to that allowed by the limitations of the cambered wing cavity. However, due to their camber and natural downward displacement, the lower surface had to be to constructed as the flexible actuation surface. The actuation surface was chosen carefully. Not only did it have to be strong enough so as not to 'balloon' under the pressure of the jet excitation, it also had to be sufficiently flexible so as not to resist the limited forcing levels of the actuators. After trials on the test bed yielded results with the Thunder actuators close to those required at Re=20,000, a light weight aerofoil structure was designed.

The aerofoil, based on the externally powered, cambered aerofoil in geometry, was designed with a small thickening on the lower surface towards the trailing edge to accommodate a greater range of movement from the actuators. The schematic layout of the principal is shown in FIGURE 2.7. The Thunder actuators can be seen inside the cambered aerofoil geometry, used in cantilever mode to resonate the lower surface close to the optimum frequency. The aerofoil structure was constructed using high precision SLS prototyping at the University of Bath. The aerofoil was constructed in three sections; the main aerofoil structure acting as a supporting framework for the actuators, a detachable trailing edge replicating the existing trailing edges very closely, and an upper surface lid to allow installation and maintenance of the actuators (FIGURE 2.8). On the left and right sides of the aerofoil, stubs were fitted to enable easy attachment to the force balance.

Once prototyped, the aerofoil had the Thunder actuators clamped and fixed into position using industrial strength epoxy. By far the most tedious part of the construction was fixing the lower surface membrane with the correct amount of tension. An unlockable glue was used to temporarily hold the membrane in place. The actuator would then be run and its performance assessed. If the membrane was too tight, performance from the

optimum setting was seen to decrease by more than 70%. If the membrane was too loose, the displacement in volume caused by the actuator would be taken up by the slack in the membrane and not ejected or sucked through the narrow jet exit. Eventually a compromise was found. Experiments were also conducted to ensure that no stationary nodes existed in the resonating membrane. Optimum performance would be achieved by resonating in the first mode only. Small particles were placed on the membrane of the final configuration to confirm that the membrane was resonating with the most efficient first mode.

The aerofoil system, whilst only crudely optimised was therefore a considerable step forward from the large speaker used external to the original aerofoil. Further discussion of the internally actuated system is given in Chapter 7.

The driving electronics used for the internal system was a conventional signal generator connected to a small torroidal transformer. The transformer, more suitable for use at lower frequencies than conventional transformers, amplified the signal from the signal generator to a maximum of 384Vpp. As the current drain of the actuators is extremely small, there was only a nominal power requirement nevertheless every precaution was taken in handling the high voltage electronics. The signal generator was used to fine-tune the operation frequency to the resonant frequency of the actuators, found to be around St=4.86. The two actuators were deliberately purchased from the same batch build in order to ensure uniformity of operation.

Control of the amplitude (momentum coefficient) of the actuators was performed via the signal generator and monitored near the actuators using a bridged output to a high-end digital oscilloscope.

2.4 MEASUREMENT APPARATUS

2.4.1 CONSTANT TEMPERATURE ANEMOMETRY

Initially, in both water and wind tunnel experiments, momentum of the synthetic jet was obtained by measuring the jet velocities with Dantec constant temperature anemometry equipment. In the water tunnel, hotfilm probes were used in conjunction with the anemometry box to produce time-averaged and instantaneous velocity measurements

around the trailing edge of the wing and further downstream. The probe was a single component type therefore interpretation was necessary to identify reverse velocities when analyzing the jet profiles. Single probe types have been used to good effect by several other researchers [Mallinson *et al*, 2004, for example].

A series of velocity measurements could be obtained using an automated traversing system controlled by a computer program written by the author. For ease of manipulation, the traverse was mounted in the overhead position across the water tunnel (FIGURE 2.9). Processing and analysis of the data were undertaken using Microsoft Excel in conjunction with Visual Basic scripts written by the author.

A similar arrangement for data acquisition was used in the wind tunnel; coupling hotwire probes to the constant temperature anemometry box. The automated traverse could also be used to capture a sequence of data from pre-programmed data capture points. As the overhead mounting position was not a convenient place to mount the traverse in the open jet wind tunnel, a small modification was necessary to enable the traverse to be used from the side of the tunnel (see FIGURE 2.10).

2.4.2 LASER DOPPLER VELOCIMETRY

Shortly after starting the wind tunnel experiments, a laser Doppler velocimetry system was purchased by the University of Bath. All hotwire measurements conducted in the wind tunnel were repeated with LDV and replaced. In addition to a potentially much more accurate velocity measurement system, the LDV could also measure reverse flow unlike the constant temperature anemometry systems used here. Bragg cells are incorporated into both axes to give this directional measurement capability. After increasing reliability issues with the aging Dantec anemometry box, the LDV became the main velocity measurement system used in the research.

The Laser Doppler Velocimetry system used for single point velocity measurements here was supplied by TSI Inc., USA. The two component system used a 300mW Air-Cooled Argon-Ion laser, a beam splitter to produce both green and blue beams from one laser source and a Bragg cell to frequency shift one of each pair of beams. Several meters of armoured fibre-optic cable supply the four beams to the probe and receive

signal from the photomultiplier tube, giving considerable flexibility to aid in probe location.

The two-component LDV probe collects refracted light in backscatter mode. Whilst backscattered mode is not the most efficient in terms of magnitude of reflected light signal, the convenience of being able to couple a light source probe and a light collected probe in to one unit outweighed the advantages of other arrangements.

Assuming the reflective particles are small enough to follow the flow, the backscattered light can be used to find the velocity of the particles; the velocity of the flow. The intersection of the two (for each component) laser beams results in a fringe pattern of light and dark fringes. As a reflective particle passes through the fringe pattern, light is scattered and reflected when passing through a light fringe, and not when passing through a dark fringe. Velocity direction is found by introducing a movement in the fringes in one direction. Fringe movement is obtained by shifting one of the beams using a 40MHz Bragg cell.

The two-component LDV probe used here emitted Argon Ion laser wavelengths of 514.5nm (green), 488.0nm (blue) and optionally 476.5nm (violet) with additional hardware. Care has to be taken to orientate the beams in the correct direction. The fringe motion will be from the shifted to the unshifted beam. The positive velocity direction for a given velocity component will be when the particles are moving against the direction of the fringe movement. Hence it is usual to orientate the beams unshifted to shifted in the streamwise direction for fluid velocity measurements (from the vantage point of the transmitter).

The collected readings from the photodiode are passed through a data processing unit to a dual processor computer with controlling software. The Bragg cell frequencies, band-pass filters, photocollector voltages and burst threshold parameters are set manually in the controller software settings. The software also displayed both data rate and burst efficiency to confirm the optimisation of the set-up.

A variety of focal length lenses could be fitted to the LDV probe, including a beam expander, and operated with only small changes in the software set-up. The standard

screw-on focal length lenses (without the beam expander) change the measurement volume dimensions significantly. Use of the small measurement volume was especially important for small-scale measurements. The length of the measurement volume l_m and the width of the measurement volume d_m can be calculated from simple geometry using:

$$l_m = \frac{4f\lambda}{\pi D \sin\kappa} \qquad d_m = \frac{4f\lambda}{\pi D \cos\kappa}$$

where κ is half of the beam convergence angle and D is the beam diameter.

As the beam spacing was 50mm, and the two optics used had focal distances of 250 and 349.8mm, the measurement volume attributes could be calculated:

Focal Distance (mm):	250.0	349.8
Kappa:	5.49	3.95
Fringe spacing (μm):	2.69	3.73
Meas Vol Dia (μm):	65	90
Meas Vol Length (mm):	0.68	1.3
Number Fringes:	24	24

FIGURE 2.11 shows the relative size of the measurement volume of the 250mm focal length optic compared to the 0.5mm slot. The 0.065mm diameter measurement volume was the smallest measurement volume available. Traversing for 51 points over 1mm near the slot exit would therefore entail spacing between points of 0.02mm. The measurement volume therefore overlapped three traverse stations. However, the small step size and the overlap were necessary near the jet centreline to obtain sufficient resolution.

The probe could be held perpendicular to the freestream to measure both vertical and horizontal or streamwise components of velocity. The probe could be fixed to a three-axis computer controlled traverse for automated measurement of a matrix of coordinates.

Experiments conducted in the wind tunnel required the use of end plates constructed of 6mm polycarbonate sheet in order to generate 2D conditions. Whilst every effort was made to keep the end plates extremely clean, there was a noticeable loss of efficiency when using the LDV through the polycarbonate sheet. This was deemed unavoidable therefore extra effort was afforded to increase efficiency of seeding and received data to compensate.

In certain circumstances, for instance when measuring velocities close to a surface with the probe orientated to look along the surface, a small coincidence angle had to be introduced to prevent the path of the converging beams being blocked by the object. Any angle of offset between the probe and the flow was accounted for in velocity measurements although angles of offset were typically below 15 degrees and therefore of insignificant contribution.

Measurements made through the polycarbonate with an offset angle and then angle compensation, were compared to data taken perpendicular to the polycarbonate sheet. The data compared extremely well and with the small offsets considered here, no discernable difference was noted at these small angles.

Noise in LDV measurements distorts the received signals and can give incorrect velocity signal peaks after a Fast Fourier Transform. To avoid noise, it is important to keep optics clean, dust-free and scratch-free. As the beams passed through polycarbonate splitter plates, these plates were also kept extremely clean, especially from oil build up and dirt residue. Despite using non-scratch cleaning materials, this build-up merited regular replacement of the splitter plates with identical new ones.

Eliminating direct reflections can substantially reduce noise; models being tested here were thinly painted with mat black paint. The models were cleaned frequently to prevent reflections from seeding oil build up which was noted to produce spurious measurements due to reflections. The mildly corrosive oil used here eventually reacted with the paint necessitating stripping and repainting of the models under test.

In general, measurement gain can be increased linearly with increasing photomultiplier tube voltage. Typically in all of the experiments here, PMT voltage was around 600V-

650V. Increasing the PMT voltage increases signal strength from smaller particles enough to be detected by the processor. The effect is to increase the data rate. However, a cut off point is reached where the amplitude of the particle signals have reached a maximum but the noise levels continue to be amplified. The effect is an increase in SNR after which the PMT becomes saturated.

Typical burst threshold values (above which a measurement in taken) are 30mV-300mV. In nearly all of the experiments conducted in the research detailed here, 30mV was used as a burst threshold. A small burst threshold value was used because the particle size was small (less than 10μm) giving smaller signal amplitudes than large particles.

As the TSI Flowsizer software was not supplied with drivers for the three-axis traverse, compatible drivers were written in C++ by the author. Whilst the traverse did not have a position sensor, the software was written to memorise the last position of the traverse on the next instance of it being used.

The traverse could move with a tolerance greater than 0.005mm whilst the software could automate an almost limitless number of points at which to measure velocities. Each position on a traverse matrix could be initialised with a different group of software settings. This enabled optimisation of the software for use in say the wake region of an airfoil or in the freestream of the wind tunnel. The traversed LDV rig in the wind tunnel is shown in FIGURE 2.12.

TSI's Flowsizer software controlling the LDV hardware also provides useful data manipulation. Once manipulated, all types of data (velocity, time, power spectra, frequencies etc) can be exported to ASCII type CSV files for post processing and further data analysis.

Two sampling methods exist in the Flowsizer software: 'Eventime' Sampling or 'Realtime' Sampling. Eventime sampling should only be used if the data rate is sufficiently high enough so that at each sampling point in time, there is likely to be a measurement. The main advantage of eventime sampling is to remove velocity bias associated with uneven collection of data. As velocity increases, it is clear that the data

rate will increase. Averaging the individual measurements therefore introduces a bias towards higher velocities.

Real time measurements were preferred here with the consideration that the data rate was sufficient to reproduce the velocity profile accurately. For this reason, velocity profiles being recorded were always constantly monitored to ensure that the data rate was sufficient over the entire velocity range to accurately reproduce both high and low velocities. As it was more difficult to ensure low velocities were seeded sufficiently, particular attention was paid to this, which always guaranteed, under conditions here, that higher velocities were sufficiently seeded.

Power Spectrum analysis could be performed within the software using a Slotting Analysis method. A variety of methods exist for non-eventime Power Spectrum analysis. The slotting method interpolates an eventime dT interval over the data time duration and then performs a standard FFT analysis to find the spectral content. The slotting analysis method used in the Flowsizer software first estimates the slotting time increments and then uses this to estimate an autocorrelation function. The estimated autocorrelation function is then used to assess whether the estimate of dT introduces bias in the results; either in velocity or variation. In fact, as Bell [2001] concludes, it is possible to detect and avoid bias using the estimation without resampling the data set by decreasing dT.

2.4.3 PARTICLE IMAGE VELOCIMETRY

The Particle Image Velocimetry (PIV) system used here was a TSI two-dimensional digital PIV system. A dual mini Nd:Yag 120mJ pulsed laser with a variety of sheet optics provided the laser light source at up to 15Hz. Conveniently the dual Nd:Yag laser is coupled with a closed loop water cooling system allowing greater portability, although possibly to the detriment of gradually contaminated water as was discovered on several occaisions. TSI claim that the power is sufficient to image areas up to 50cm by 50cm in optimal conditions.

Through a synchroniser unit, a 4.2Mpixel camera, shown in FIGURE 2.13, capable of capturing single images at 7.5Hz or dual images at 3.75Hz was used to capture the PIV images for processing. As the camera is fitted with a standard Nikon F mount ring, a

variety of lenses were available to fit. Lenses commonly used here were a Nikon 28mm, F2.8 wide-angle, a Nikon 60mm F2.8 macro, a Nikon 105mm F2.8 macro and a Nikon 200mm F4 macro. In order to maintain optimum performance of the CCD array in the camera, considerable care was used to avoid shining direct laser light into the field of view of the camera or anything more than minor, diffuse reflections. The scientific grade CCD array has pixel sizes 7.4μm x 7.4μm with a total active surface area size of 15.2 x 15.2mm.

The camera focusing mechanism could be controlled remotely via a TSI remote focus controller with coarse and fine adjustment for precise focus control. Whilst this mechanism has the disadvantage of distancing the user from the 'feel' of focusing a camera, the benefits of being able to leave a set-up undisturbed, avoiding interference, far outweighed this.

A variety of optics supplied with the laser gave control over the focal length and width of the light sheet; 200mm, 500mm, and 1000mm spherical focal length lenses and –15, -25 and –50mm focal length cylindrical lenses were supplied which could be used in any combination.

Not wishing to introduce the laser unit directly into the freestream for fear of damage or massively increased freestream blockage, a small laser light mirror was used to direct the light into the stream in the correct orientation keeping the laser safe and clear of the freestream. The width of the light sheet in the area of interest was around 1mm. The layout of the PIV system in the wind tunnel is shown in FIGURE 2.14.

Images were collected, saved and processed on a dual processor computer running TSI's Insight PIV software. The software allowed full control of the laser and synchroniser settings. The maximum capture rate at the highest quality was always used. The delay between frame captures for each correlating image pair was adjusted according to freestream velocities. For time-averaged data, a sequence of 100 images was found sufficient achieve smooth averaging of data. Whilst more image captures undoubtedly aid in accuracy of time-averaged data, the computing resources available was also a consideration and the image pairs for many experiments required

considerable hardware storage capability. Care was also taken not to operate the frequency of frame acquisition near to the excitation frequency of the synthetic jet.

The software offered a facility to mask off areas in the field of view that were of no interest. Whilst airfoils were always painted in non-reflective matt black paint, some spurious vectors are always generated close to a surface through lack of correlation or reflections. These areas were always masked off and validated in post-processing of the generated vectors.

Post correlation vectors found to be disproportionate to surrounding or expected vectors could be filtered out with the software using manually set filtering, applying a band pass filter of the desired width. Experimentation with band pass filters determined the velocity ranges for each experiment. Band pass filters were sufficient not only to allow correct time-averaged PIV, but also real time maximum and minimum velocities in each case.

When a wide-angle lens was used, the centre portion of the field of view was used in preference to the outer region, avoiding parallax errors where possible. The captured pictures were 'calibrated' by capturing an image of a scale. The scale image could then be used to set the software scale with the correct number of pixels per mm for the particular set-up and field of view. A polygonal grid-masking tool enabled objects within the field of view to be excluded from vector processing.

Timing

A good theoretical understanding of PIV technique was established to fully utilise the system. The TSI system uses a synchroniser unit with a nanosecond clock to control events in the PIV sequence. The order of events is highlighted here:

1. If using external triggering, a delay of around 20μs is incurred between the system receiving the trigger and any further process being activated. This delay fluctuates by only a few nano-seconds on each repeat so can be accurately accounted for. A further delay can then be set by the user to extend the duration between the external trigger and the system being activated. This delay can be set to the nearest milli-second.

2. Once the system is activated (either triggered externally or by a manual button press) the laser is activated and the camera readied for image capturing. The dual Nd:YAG lasers have a delay of around 150-200μs (depending on the exact laser and the power level setting) between firing the flash-lamp and opening of the Q-switch.
3. Both lasers are sent the activation trigger, the second delayed by the setting of dt (the time spacing between the individual captures of the image pairs) in milli-seconds. A dt can be estimated from the average expected field velocity and the premise that a captured particle should ideally be displaced around one quarter of a correlation region between image pairs.
4. The camera opens its shutter and is receptive in time to capture the illuminated image associated with pulse 1 from the laser. The camera then closes its first frame, frame A, as soon as possible. Around 5μs later it can be ready to receive the frame B image.
5. Data from the camera captures is downloaded to the camera as fast as possible after each frame capture. The capture can then either be repeated at up to 7.5 image pairs per second, or the single pair can then be processed.

The TSI system has capability to capture multiple frames from a single trigger and also to capture many continuous phase locked images from continuous triggers only limited by the RAM. Typically the RAM limited the number of captured pairs to around 100. If the triggering signal frequency exceeded the maximum capture frequency of the system, then the system ignores all triggers until the system is again free, and awaits the next trigger in the time sequence.

Once images were captured, displacement vectors could be calculated. TSI's Insight supports multi-threaded processes so vector fields could be generated on a dual processor computer to speed time-consuming processing time. TSI estimates of processing time list a full 32 x 32 interrogation size to compute at 7100 vectors per second although this was found to be very much faster than the real case.

Two correlation algorithms were available for generating displacement vectors from the captured images; a standard FFT method and a TSI patented Hart Correlation. Both of the correlation engines allowed full control of interrogation spot size, overlap, the field

of view in the images to be processed and aspect ratio. Displacement peak location could be found by using one of several algorithms.

The FFT algorithm was found to be the most successful in general for the experiments in this research. However, it was found that FFT required a slightly denser seeded flow than that of the Hart Correlation. Also FFT required more careful optimisation of dt, ensuring very few particles had moved out of their interrogation regions as well as having sufficient delay to ensure accurate displacement could be calculated. With these two conditions in mind the FFT seemed to outperform the Hart Correlation in terms of spurious vectors.

Vector validation was carefully set-up and run using a batch algorithm post-processing. A displacement vector range was set very wide, to remove spurious vectors; holes were filled using the mean value of the neighbouring 3x3 square of values.

Vector files could then be displayed and non-dimensionalised using an ASCII file importer in the Tecplot data-plotting package.

2.4.4 LASER SAFETY

Whilst general safe laboratory practice was adhered to, there were several key additional safety requirements concerning laser safety.

The LDV laser is a Class IV laser product hazardous even for scattered, diffuse reflections as well as for direct exposure. Whilst the laser beam intensity is greatly reduced in passing through the beam splitters, fibre optics and transmitter head, considerable care still has to be used. The University of Bath laser safety officer provided safety training and good practice of laser use was adhered to.

Considerable measures were employed to cope with hazards of both LDV and PIV laser use. Before use, laser safety manuals and training guides were reviewed. Laser safety glasses of the correct filtering frequency were used regularly, the experimental area was enclosed with blackout material and access to the testing facility was very strictly controlled, coupled with the use of laser interlocks and warning lights. Close attention was always given to avoid the chance of direct or diffuse reflections; blackout curtains

were used around the test area for the prevention of reflections and to enhance operational safety.

2.4.5 SEEDING

All laser measurement related experiments described here were conducted in air. A TSI Inc., USA, six-jet oil particle atomiser (shown in FIGURE 2.15) filled with Ondina-EL oil was used to generate seeding particles for both LDV and PIV.

The ability of the atomised particles to track the flow accurately is related to the size of the oil particle. Melling [1997] showed particle diameters up to 2-3μm were suitable for frequency responses up to 1kHz. However for better frequency response of up to 10kHz, the diameter should not exceed 1μm. Particles of the 1μm -3μm diameters would therefore yield a tracking fidelity sufficient to follow the streamlines of flows in all of the measurements of this research.

The particle diameter from the TSI atomizer used was quoted to be around 1μm. The sedimentation velocity for this particle size in air was estimated at 3.0×10^{-5}m/s by TSI. The TSI six-jet atomiser could output up to around 12L/min at high air pressure or around 6.5 L/min at normal pressure. The concentration of particles is typically 6×10^{6} particles/cm^3, providing sufficient seeding density in each interrogation region of the PIV system.

The six-jet atomiser had controls for activating any number of jets to adjust volume of smoke and also offered a variation in the density of smoke by air intake regulation. To a lesser degree this also gives a small control over particle sizes emitted but typically this was of the order of 1um from Ondina-EL oil.

Seeding was introduced upstream of the fan, downstream of the test section in the recirculating wind tunnel to allow for mixing and removing any possibility of disrupting the freestream velocity.

Three levels of seeding were required for three different experimental conditions. PIV required a denser seeding level for highest quality accurate vector rendition. Typically, use of four jets of the atomizer provided a good density of particles to use for PIV and

enabled the most effective particle correlation functions for PIV image processing. LDV experiments with freestream required fewer particles to achieve a good data rate. Sufficiently fast data could be acquired using one or sometimes two of the atomizer jets.

LDV experiments without freestream (synthetic jet activated with zero freestream velocity) had additional considerations. Experiments performed without freestream were enclosed as much as possible. A complete enclosure was not possible due to the lack of restrictions necessary in free air experiments. Whilst a reasonable density of seeding was required for a good data rate, too much did not allow for sufficient laser light penetration and backscattered light collection. A constant replenishing supply of seeding was required. Use of more than two jets gave a significant disturbance to the surrounding air in the quiescent flow experiments. There was no significant interference from the use of one jet to seed the static experiments.

2.4.6 THE PRESSURE MEASUREMENT SYSTEM

A special aerofoil with 47 surface pressure tappings was constructed for surface pressure measurements. The distribution and location of the tappings is shown in FIGURE 2.16. The distribution was chosen to focus resolution near the steep pressure gradients at the leading and trailing edges. Whilst no pressure tappings could be placed at the slot exit, estimates of velocity and momentum coefficient at the trailing edge could be used to estimate trailing edge features.

An attempt was made to construct the surface tapped aerofoil using a state-of-the-art Selective Laser Sintered (SLS) rapid prototyping machine. However, it was found that the machine did not have the tolerance sufficient to produce the surface tapping holes and connecting tubes. Instead the surface tapped model was successfully and painstakingly constructed by hand.

To match the aerofoil geometry as closely as possible to the original 'un-tapped' wing, thin wall, pre-drilled, 1mm OD tubes were used to skin the surface of the aerofoil rather than the 1mm aluminium sheet. Where the surface tappings were more than 3-4mm apart, the gap was filled with 1mm aluminium sheet.

Small gaps were filled with fine filler and the replicate trailing edge was screwed into place. With pins sealing the surface pressure holes, the wing was painted and abraded many times to achieve a very smooth finish consistent with that of the original aerofoils. Pressure tapping holes were viewed under magnification to remove burring and roughness that might otherwise promote early transition. Tapping holes were made 0.5mm in accordance with Somers *et al* [1982] who showed that keeping the tapping size to a minimum reduces the likelihood of transition interference to a minimum. Whilst staggering of the pressure tapping holes would have been even more ideal, this was not possible due to machining complications of the 0.5mm holes in the 1mm brass tubes.

Due to the 47 pressure tube exits on one side of the aerofoil, the wing angle of attack could not easily be changed if using fixed end plates. Instead, the aerofoil was mounted to plastic discs of one chord length in diameter. The discs (and wing) were then mounted in the end plates with holes of one chord length in diameter. Therefore, the wing was free to rotate by turning the end plate discs. Every effort was made to mount the inner discs as flush as possible to the end plates. No edge or surface roughness was discernable by touch. A locking screw prevented the discs from rotating during a test.

The 47 pressure tubes were connected to a Scannivalve computer controlled rotary valve system. The system allowed the use of just one pressure transducer to measure from the 47 pressure tappings. Two pressure transducers were tried for pressure measurements here. Both were selected from Druck's ultra-sensitive, large surface area transducers, one measuring in the range +/-0.01mBar and the other +/-.1mBar. It was hoped that the 0.01mBar would be sufficient to measure at Reynolds numbers around 20,000-40,000, whilst the larger would measure 60,000-100,000.

An adapter was constructed to connect the Druck transducers to the Scannivalve system. Unfortunately whilst the Scannivalve was located as near as possible to the wing to keep tubes short, it was found that too much hysterisis was evident on the low range transducer to be useable; instead of the transducer measuring the static pressure, it measured pressure variations within the tubing and actuator housing. The length of the tube was around 0.65m. Tests showed that only in using tubes less than 0.3m long would the problem be eliminated which was impractical Fortunately, the higher range

transducer was found to be sufficiently accurate and unaffected by tube length at the lowest Reynolds number to give representative pressure measurements.

The outputs to the factory-calibrated transducer were connected to a PC with a data-card and acquisition software in HP-Vee. The voltages were collected and post-processed using a commercial spreadsheet package and object orientated macros system. A layout of the pressure measurement system in the wind tunnel is shown in FIGURE 2.17.

2.4.7 THE FORCE BALANCE

A force balance was constructed in conjunction with Russell Jones, a final year undergraduate project student. The balance comprised a two-component binocular strain gauge measurement device mounted on a rigid framework. The aerofoil could be hung sideways from the measurement beam, suspended between two closely positioned 6mm polycarbonate splitter plates. Arranged in a wheatstone bridge and connected to an amplifier and PC data acquisition system, each component then records a voltage change under load.

There are several known issues with low Reynolds number force balance work, especially with experiments conducted in air. The balance has to be sensitive enough to measure extremely small forces. Lift force is in general an order of magnitude larger than drag forces so therefore easier to measure. A good quality amplifier and conditioning box has to be used in conjunction to avoid small signal drifts that, whilst inconsequential in high Reynolds number testing, would lead to large errors in low Reynolds number testing.

The design of a binocular strain gauge is governed by two key criteria:

1. The material should flex sufficiently at the measurement point to allow a reading to be taken accurately.
2. The material should not flex as much as to induce material distortion (deformation) or strain gauge damage.

In the research here, the actuation system caused large vibrations in the plane of motion, which was in the lift direction. The vibrations caused readings several orders of

magnitude greater than the expected lift forces. Despite considerable effort to find a compromise between a vibration tolerant, rigid material and one which allowed sufficient flex to measure, no accurate lift measurements could be taken with the jet turned on. However, lift measurements could be taken without jet excitation. Measurements in the drag direction were achieved for both jet-on and jet-off cases as the jet vibration had less affect on the drag force gauge. The wind tunnel layout of the force balance is shown in FIGURE 2.18.

As the force balance was an untested design, experiments were performed to assess and confirm the measurement accuracy and reliability of the system. Details of the calibration and assessment of the force balance are given in the next section.

The outputs of the bridged strain gauges were amplified and conditioned before acquisition by a PC data-card. HP-Vee was programmed as controlling software. The programme allowed frequency of measurement and number of data points set for each experiment. The data could then be acquired and downloaded in CSV format for analysis.

2.5 FIGURES

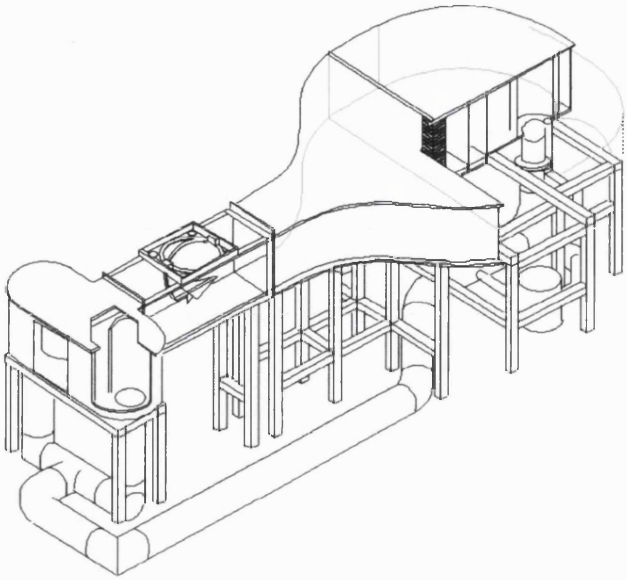

FIGURE 2.1 Eidetics' recirculating water tunnel. Drawing courtesy of Eidetics.

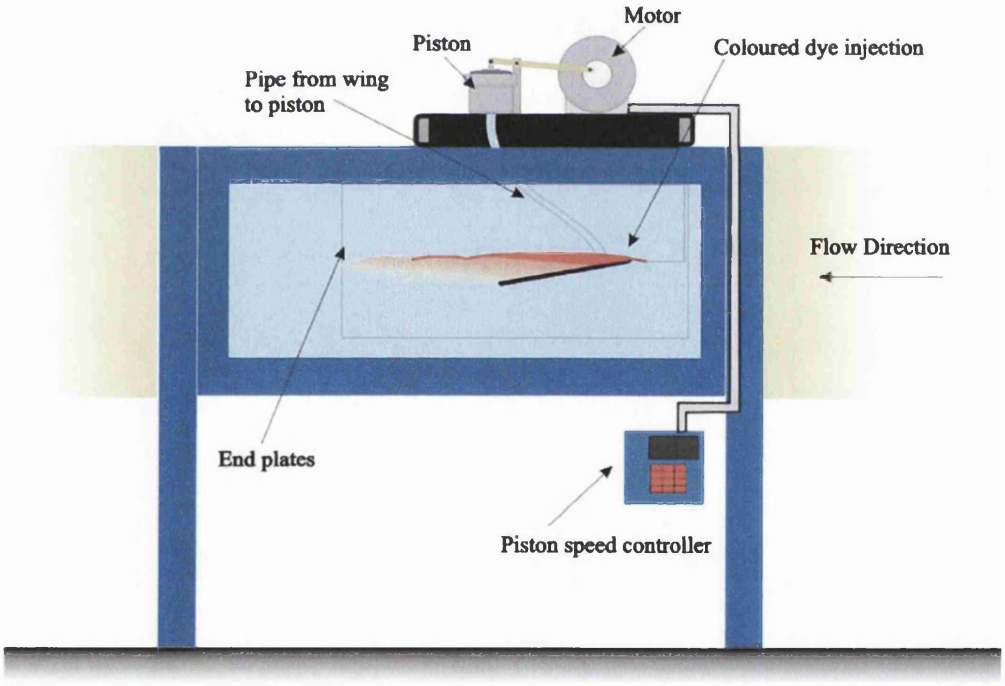

FIGURE 2.2 Side view of the water tunnel apparatus mounted in the University of Bath water tunnel.

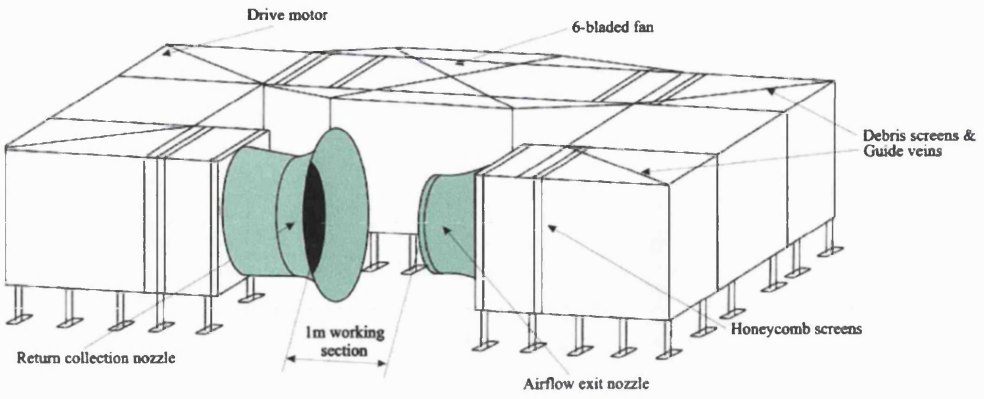

FIGURE 2.3 The University of Bath open-section recirculating wind tunnel.

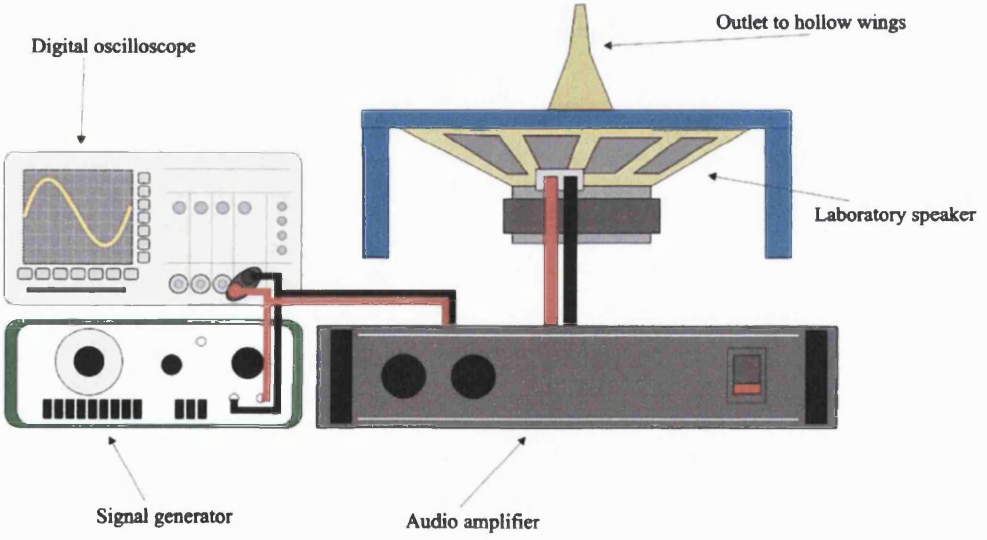

FIGURE 2.4 Electronics set up for speaker powered testing of wind tunnel models

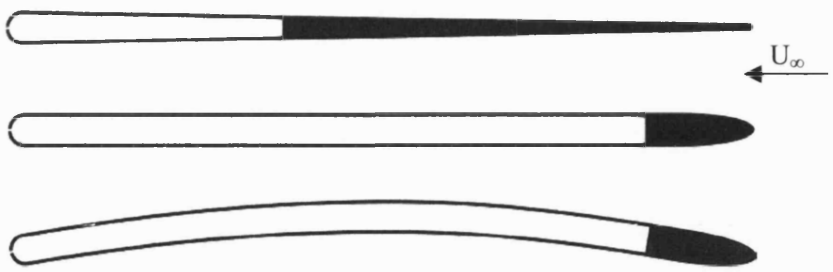

FIGURE 2.5 Section layouts of the three hollow aerofoils: tapered aerofoil (top), constant thickness flat aerofoil (middle), and cambered aerofoil (bottom). All with 0.5mm slots in the trailing edge.

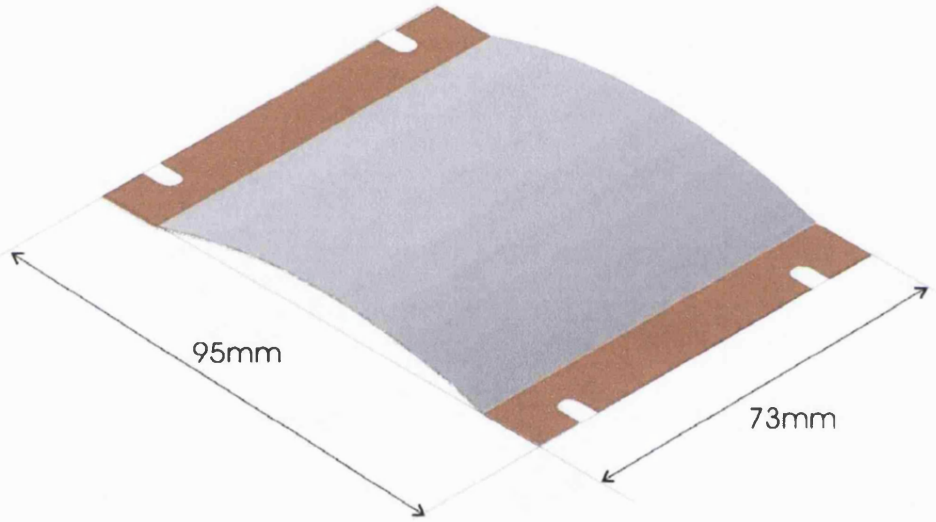

FIGURE 2.6 NASA's giant TH-R7 Thunder actuator produced by Face Corporation.

FIGURE 2.7 Schematic of the internally actuated wing system

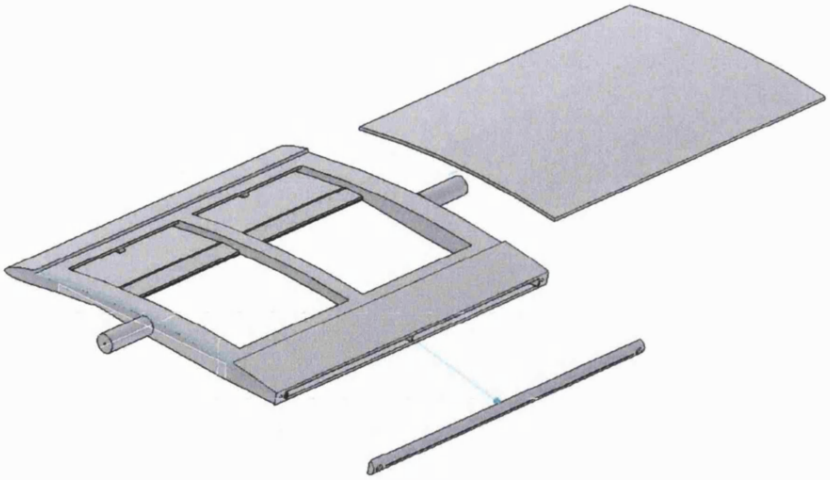

FIGURE 2.8 Exploded view of the internally actuated aerofoil structure showing the main aerofoil, upper surface lid, detachable trailing edge and internal space for Thunder actuators.

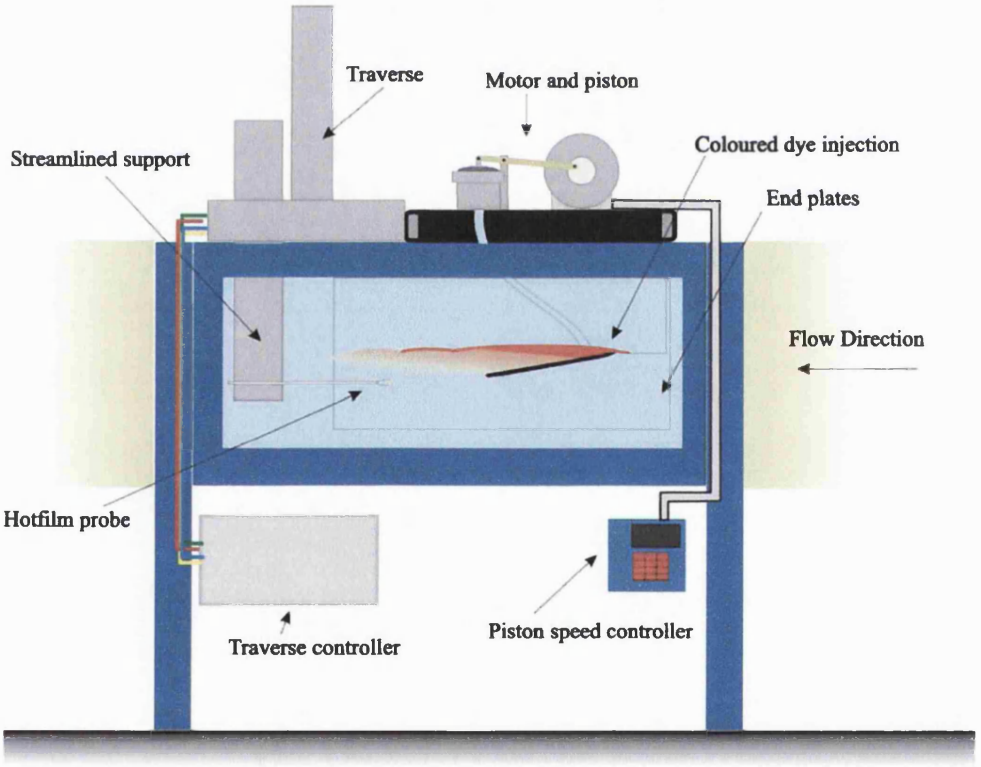

FIGURE 2.9 Side view of the water tunnel hotfilm and flow dye set up.

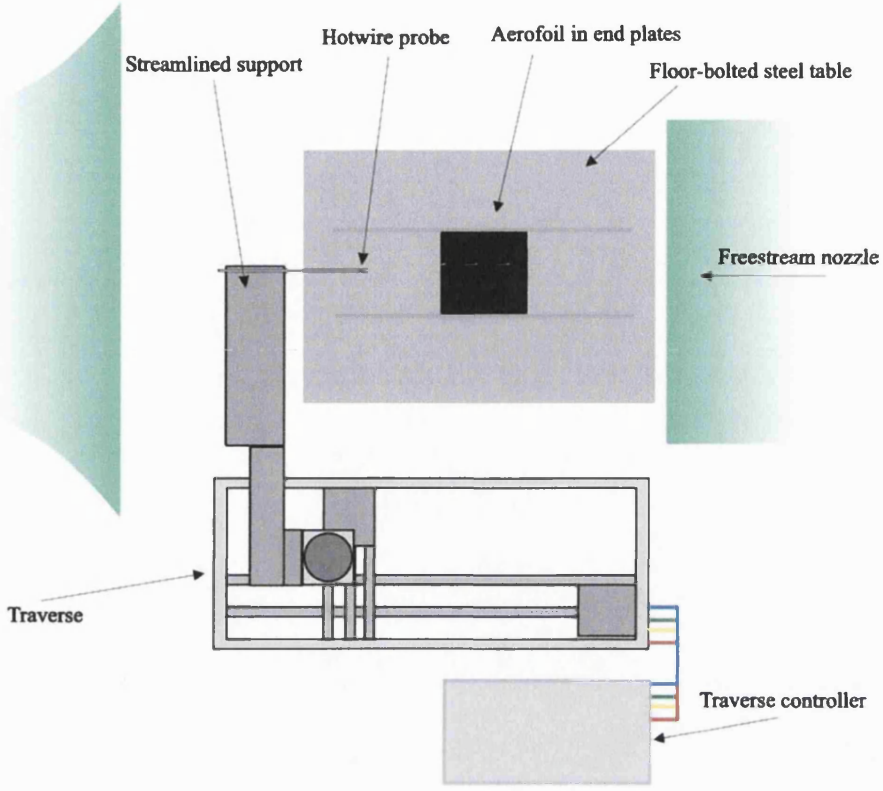

FIGURE 2.10 Plan view of hotwire set up in the wind tunnel.

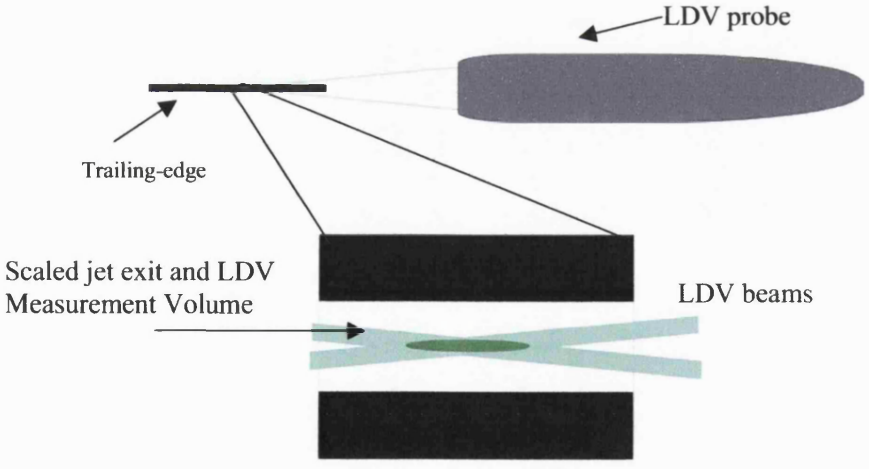

FIGURE 2.11 Scaled comparison of 0.5mm slot geometry to measurement volume geometry.

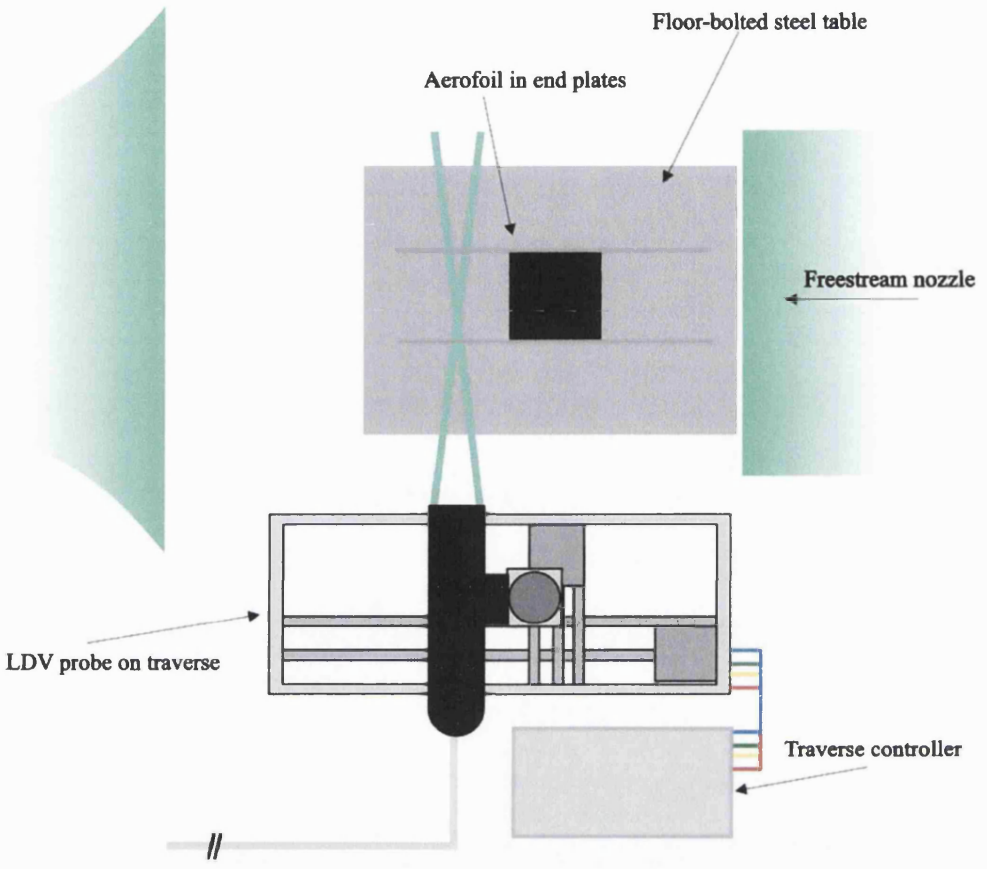

FIGURE 2.12 Plan view of the traversed LDV wind tunnel apparatus.

FIGURE 2.13 TSI's 4Mpixel camera. Photo courtesy of TSI.

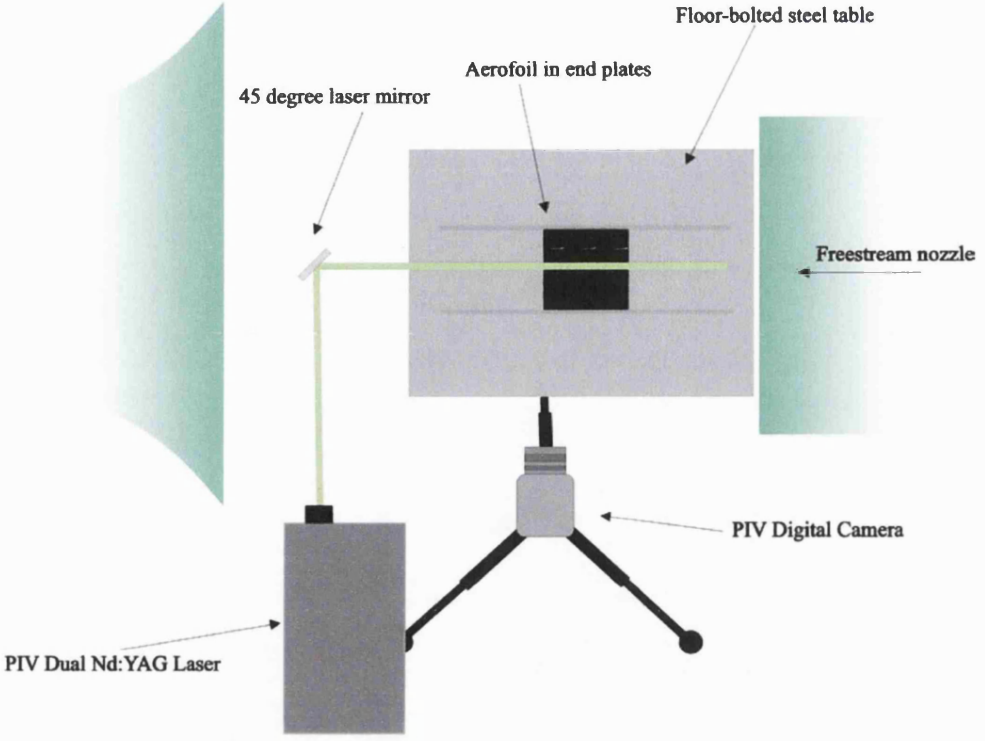

FIGURE 2.14 Plan view layout of the PIV set up in the wind tunnel.

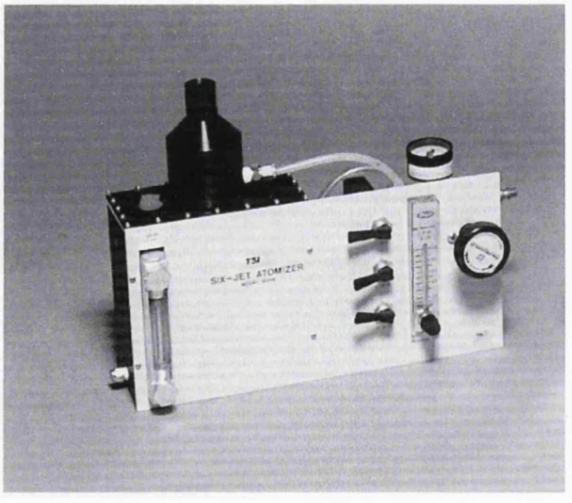

FIGURE 2.15 TSI's six-jet particle atomiser. Photo courtesy of TSI.

Upper Surface	Tapping Number	x/c	Lower Surface	Tapping Number	x/c
Leading	1	-1.000			
Edge	2	-0.983	Trailing	26	-0.040
	3	-0.972	Edge	27	-0.057
	4	-0.959		28	-0.080
	5	-0.942		29	-0.104
	6	-0.926		30	-0.136
	7	-0.903		31	-0.196
	8	-0.872		32	-0.254
	9	-0.813		33	-0.311
	10	-0.756		34	-0.369
	11	-0.697		35	-0.426
	12	-0.639		36	-0.484
	13	-0.581		37	-0.541
	14	-0.523		38	-0.599
	15	-0.465		39	-0.656
	16	-0.407		40	-0.714
	17	-0.349		41	-0.771
	18	-0.291		42	-0.829
	19	-0.233		43	-0.886
	20	-0.175		44	-0.919
	21	-0.117		45	-0.940
	22	-0.093		46	-0.957
	23	-0.071	Leading	47	-0.970
Trailing	24	-0.054	Edge	48	-0.983
Edge	25	-0.040			

FIGURE 2.16 Location of pressure tappings on the cambered aerofoil dedicated pressure measurement system using the coordinate system as defined in section 3.2.

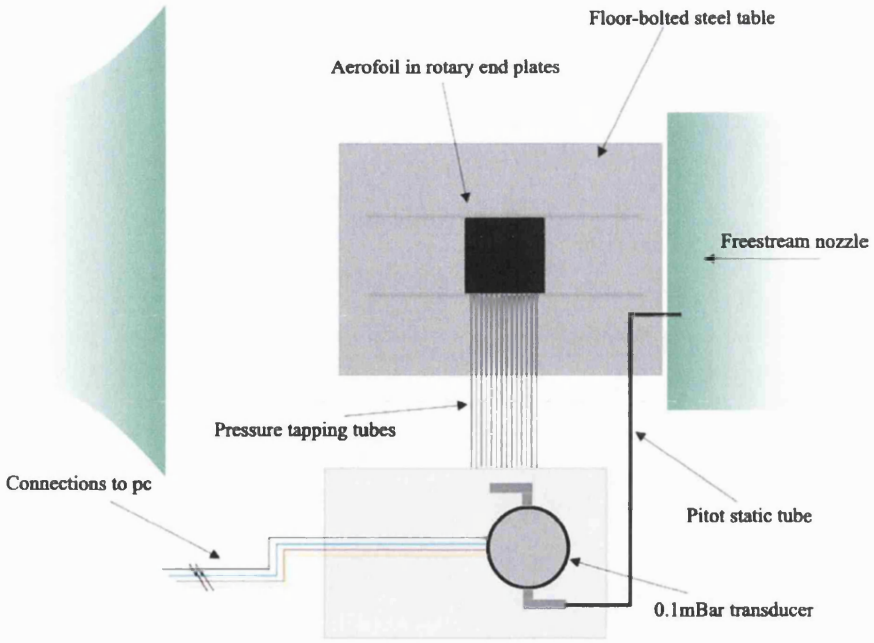

FIGURE 2.17 Plan view layout of pressure measurement system.

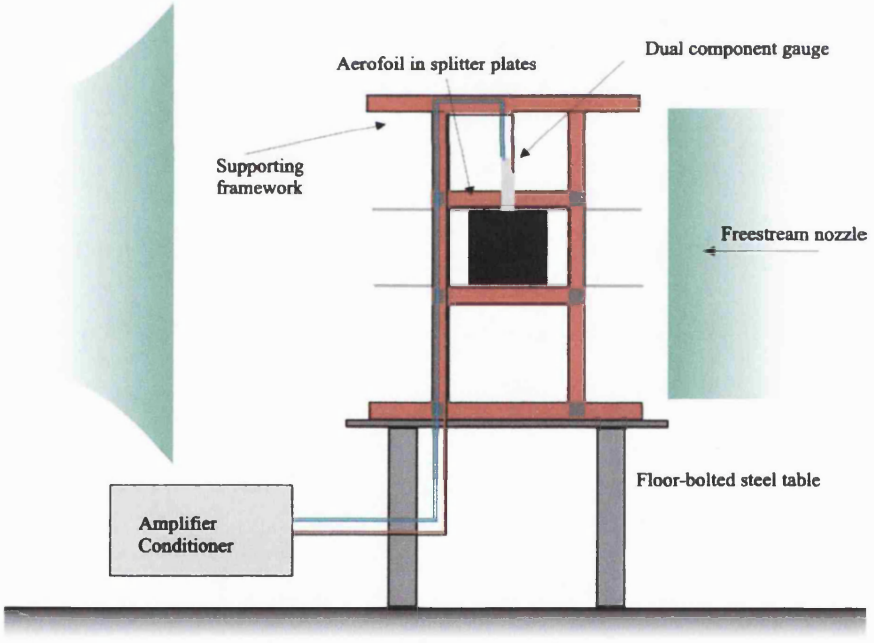

FIGURE 2.18 Side view of force balance arrangement in the open section wind tunnel.

CHAPTER 3 EXPERIMENTAL TECHNIQUES

3.1 CONSIDERATIONS OF LOW REYNOLDS NUMBER RESEARCH

Conducting experiments in the low Reynolds number regime is inherently difficult but becoming easier with advancing precision measurement and testing technologies. Considerable effort was spent in reviewing the variety of low Reynolds number testing considerations of other researchers [e.g. Mueller, 1999, Marchman III, 1987, Lissaman, 1983, McGhee and Walker, 1989]. Velocity measuring techniques need to be several orders of magnitude more capable than for higher speed research. Even the most carefully designed, dedicated low-speed Pitot-static tubes can read pressures incorrectly at low Reynolds number due to separation and circulation around the probe. Tunnel turbulence intensity and acoustic disturbances are known to affect the aerodynamic performance of low Reynolds number aerofoils. Considerable attention was paid to the available literature on low speed wind tunnel testing and features particular to low Reynolds number flow.

It was during the 1980s that important details in low Reynolds number experimental techniques were studied and understood. The importance of airfoil roughness/texture was noted; the effects and implications of end plates on two-dimensional airfoil studies was beginning to be realised; the effect of turbulence intensity on low Reynolds number experiments; the problems of flow separation on pressure measurement orifices. All of these features went some way to explaining the variation in results found in different

fluid dynamics studies around the world. They also had implications on improving accuracy of measurement on very small scales, something that will be highlighted later.

Mueller [1985] showed lift force can be measured with acceptable accuracy using a strain gauge balance. Reasonably accurate lift forces can also be obtained integrating surface pressures provided the pressure measurements system is sufficiently sensitive.

Drag forces, being an order of magnitude less than the corresponding lift forces, are more difficult to measure. Mueller [1999] used a very sensitive strain gauge balance with high signal to noise ratio and low drift electronics considered state-of-the-art at that time. He does identify some shortcomings of such a system though. Primarily, that to conduct a two-dimensional study, end plates are required to bound the wing in the span-wise directions. At Reynolds numbers below 100,000, Mueller [1999], Murthy, [1988], Pelletier and Mueller, [2001] report that the end-plate/wing interaction was in the form of a corner vortex, increasing the measured drag over the actual drag force experienced by the true two-dimensional aerofoil. The corner vortex was seen to effect up to 10% (5% each side) of the aerofoil surface.

Furthermore, Mueller [1985] highlights that as overall aerofoil performance of low Reynolds numbers is very sensitive to the location of transition, disturbances in the test environment, in particular the turbulence intensity, must be understood.

3.2 ORIENTATION

An orthogonal x- and y-axis system is used with (0,0) centered at the center of the jet aperture. The horizontal x/c axis increases in the streamwise direction (right to left) and the vertical y/c axis increases in the vertical direction. This orientation is shown in FIGURE 3.1. Whilst some experiments, for convenience of camera filming, were arranged with the wing in upside down or sideways orientation, all results are presented in the upright orientation with the correct axis adjustments.

3.3 FLOW VISUALISATION

Initial flow visualisation experiments were conducted using the water tunnel setup with speeds of 5-15 cm/s equivalent to chord Reynolds numbers of 10,000-30,000. Flow visualisation was conducted by injecting coloured dye at different locations of the wing. Flow visualisations for the tapered wing were performed by Zeshan Khan, a final year undergraduate student, and are limited in quantity. Injecting a high contrasting red or blue dye near the leading edge gave the best visualisations. Dye could also be added to the jet by direct injection to the piston cylinder.

3.4 MEASUREMENT OF MOMENTUM COEFFICIENT

Jet momentum coefficient was estimated in the water tunnel based on the jet exit velocity profiles at x/c=0.005, x/h=2 in quiescent flow. A vertical line of 51 evenly spaced points were used in the jet wake extending from y/c=-0.0025 to y/c=0.0025, where the velocity fluctuations were negligible. Following previous work [Amitay *et al*, 2001; Seifert *et al*, 2002, and so on], momentum coefficient C_μ was calculated as:

$$C_\mu = \frac{\rho \int_{-\infty}^{\infty} \overline{u^2} dy}{\frac{1}{2}\rho U_\infty^2 c},$$

where U_∞ is the freestream velocity on which the momentum coefficient will be based.

Whilst the constant temperature anemometry systems had no capability to resolve flow direction, the negative velocities in the jet were an order of magnitude less than the positive velocities and therefore contributed little to integrals involving u^2. All wind tunnel momentum coefficients (studied in greater depth) were estimated using the LDV under the same conditions, using the same 51-point traverse matrix. Whilst directional ambiguity is resolved in using LDV, the complication of uniform seeding and velocity bias potential meant that considerable effort went into monitoring the real-time LDV signal for all measurements. During momentum coefficient measurements, care was taken to distribute the seeding locally enough to be entrained into the near jet, and globally enough so as not to interfere with the jet flow.

Excitation frequency was made dimensionless by defining the Strouhal number as:

$$St = \frac{fc}{U_\infty}$$

Strouhal numbers in the range 0.7 to 34.3 were studied in this research. Low Strouhal numbers were extremely easy to seed with the TSI atomizer. However, due to the shorter time scales involved in the higher Strouhal numbers, a greater seeding density was required for these experiments. Typically, the most accurate real time velocities were recorded when LDV data rates were over 10 times the dimensional frequency of the jet. Erroneous signals captured using a lower data rate to jet frequency ratio would often have clipped low velocities.

Depending on the severity of the clipping, poor signals were found to overestimate the momentum coefficient by up to 15%. All clipped and poorly seeded signals with such velocity biases were rejected and repeated with improved seeding data rates. Momentum coefficients calculated using these methods, with all of the details attended to, showed remarkable repeatability with all variation inside +/-3%; some of this can also be attributed to the accuracy required in setting the signal generator peak-to-peak voltage settings using the oscilloscope.

3.5 WAKE SURVEY TECHNIQUES

Two techniques were used to analyse the wake region of the aerofoils. PIV was used to give a two-dimensional whole field quantitative visualization of the wake under different conditions. LDV was used to give high-resolution velocity measurements downstream of the aerofoil to give obtain a velocity profile in the wake, which was also used to estimate thrust and drag coefficients.

3.5.1 PIV

Time-averaged PIV captures were taken from 100 images usually captured at 7.5Hz, the maximum capture rate of the PIV. The capture rate was altered when the jet frequency

and capture frequency would otherwise be synchronizing, for example with the jet oscillating at 30Hz, to ensure a true time-averaged result.

Slight instability in the alignment of the twin laser sheets meant that regular adjustment was required. As the region focused on was small, and the typical light readings required an f-stop of around f4.5, the depth of field of the camera was extremely small – estimated to be in the region of 0.5mm. The laser light sheets were sometimes seen to drift outside of the focal length by greater than 5mm. Monitoring of the real-time velocity vectors showed instantly when the lasers lost perfect alignment and allowed immediate adjustment.

Phase-averaged PIV images were also taken from an average of 50 image pairs. Where significant variation between the 50 results was observed, mention is made in the results section. Most phase-averaged captures were the average of similar images.

3.5.2 LDV

At each station in the wake, the LDV was set to capture 10,000 data points ensuring sufficient data rate to avoid velocity bias. A typical traverse matrix in the wake comprised 50 points. One traversed wake survey typically took around one hour to complete and some required up to four repeat measurements if the freestream fluctuated mid-experiment.

The velocity profiles captured in the wake were used to provide an estimate of thrust and drag coefficient using the well-known control volume method. The basics of the method can be applied to PIV fields to estimate forces in two directions [Noca *et al*, 1997, Unal *et al*, 1997]. However due to the small-scale fluid features associated with MAV research, the higher resolution and real-time measurement capability of LDV was preferred for accurate force prediction.

There are many good explanations of the method available; a good account is given in Douglas *et al* [1985], Pankhurst and Holder [1969] and many others. The technique has been used from the early 1900s. Cambridge University Aeronautics Library [1936] released one of the earliest comprehensive reviews of the technique. Under different guises the technique is still frequently used by current research [Brune, 1994, Gullman-

Strand and Angele, 2000, Lu and Bragg, 2002, Wang *et al*, 2004]. Takahashi [1997] showed how limited derivation of the drag components could be derived from the wake flow measurements. A brief summary of the basic theory is given here.

From the diagram shown in FIGURE 3.1, it is evident that fluid passing over the aerofoil has experienced a loss of momentum, which equates to the profile drag per unit span associated with the aerofoil. Therefore, the drag per unit span can be found by multiplying the mass flow rate with the velocity change:

$$D' = \int_{-\infty}^{\infty} \rho u(u - U_{\infty})dy$$

In actual practice, the integral can be taken over a finite range of y as the influence of the wake on the upper and lower bounding fluid becomes increasingly negligible.

Careful consideration has to be given to the location of the wake velocity measurements downstream of the aerofoil. It is often impractical to perform a wake survey far downstream from an aerofoil due to hardware limitations and a loss of measurement accuracy. Certainly in low Reynolds number measurements, there are greater issues of measurement accuracy the further the downstream test location is sighted. Furthermore, the two-dimensional experiments required end plates, which could not be extended further than one chord length downstream due to practical limitations of the model and end plate size in the wind tunnel area. The wake height also increases in size with downstream distance therefore requiring a greater traversing distance and longer test durations. As there were difficulties in maintaining the freestream velocity accurately over short durations, this was also a consideration.

However, whilst there are advantages of traversing as close as possible to the aerofoil, a disadvantage is that the static pressure in the near wake will not have recovered to the freestream static pressure, resulting in under-prediction of drag coefficients. In the experiments performed here, the x/c=0.5 location was used for LDV wake survey stations. Barlow *et al* [1999] suggest high levels of accuracy can be achieved without static pressure corrections down to x/c=0.7, but they do not use thin aerofoils which would produce even smaller wake widths as used in this research. Furthermore, in early calculations and attempts at static pressure corrections in the near wake, Jones [1936],

showed little variation in measured corrected and uncorrected drag coefficient values outside x/c=0.4. Jones [1936] also showed that by using his own corrections or those of Betz for near wake static pressure variation, agreements of around 8% at the x/c=0.16 location could be found.

Even with blunt bodies, Antonia *et al* [1990], showed that the drag of a cylinder measured five near-wake widths downstream was only 5.5% under-predicted when compared to the true value measured far downstream. It was felt that measuring a streamlined body at a similar downstream location (in terms of wake width) would therefore offer sufficient accuracy in this research, especially at low incidence where most of the study takes place. Where possible, comparison will be made with similar research performed by other aerodynamicists in order to gain confidence.

There is some discussion in the literature regarding the use of wake surveys at low Reynolds number. Barlow *et al* [1999] give a good discussion of the key problems. However, most of the issues revolve around the use of pressure rakes in the wake rather than velocity measurements. Pressure measurements become more difficult in fluctuating, turbulent conditions or conditions with a cross-stream component, which can induce errors. The advantage of using LDV is that the streamwise component can be exclusively studied with high accuracy. Bastedo and Mueller [1986], Broeren and Bragg [2001], Finaish *et al* [1985] and Guglielma and Selig [1996] have shown some degree of cross-stream variation in two-dimensional low Reynolds number surveys. Despite repeated checks for this phenomenon during this research, no significant cross-stream variation was detected inside the central half-span of the aerofoils under test. LDV wake surveys were always performed along the centreline away from the influence of the end plates.

Undoubtedly, the LDV wake surveys were the most time-consuming tests detailed in the research. Several hours was often dedicated to obtaining one drag or thrust coefficient estimate under acceptable conditions. There are nearly 100 thrust and drag coefficients presented here from the wake survey technique although many more were taken. Despite that, repeats were made to check for repeatability and accuracy was always achieved. Traversing LDV measurements had to be relied upon due to the lack of real-time resolution with the 7.5Hz rate PIV system. A real time PIV system may go

some way to resolving this problem, although only in conjunction with a camera affording sufficient spatial resolution.

3.6 SURFACE PRESSURE MEASUREMENTS

Several preliminary experiments were conducted with the surface pressure rig to determine optimum operating conditions. Initially experiments determined the duration and data sampling frequency at each static tapping. It was determined that six seconds of captured data at 1kHz was sufficient to produce an average lift and drag coefficient estimate that could not be improved in accuracy with increasing time duration. Data captures of three to four seconds duration could give an average value differing by some 12% when compared to a longer duration; also evident in the variation of pressure readings. Durations of seven to ten seconds showed no variation in average values compared to the six seconds duration for the higher Reynolds numbers tested.

Pressure measurements at the lowest Reynolds number of 20,000 were more complicated. The lowest range pressure transducer could not be used due to stability problems. The higher range pressure transducer still possessed sufficient accuracy to take measurements at the lowest Reynolds number. However, it was noticed that if the pressure differences across the transducer were extremely small, the signal would experience significant drifting after around seven seconds of stable read-out. It was determined by experimentation that for the lowest Reynolds numbers, around six seconds was the largest duration of capture not susceptible to signal drift for the lowest pressure differences measured.

The six seconds duration was chosen as the shortest time requirement to obtain sufficient sample to produce a representative average value. Longer durations were therefore unnecessary and would allow greater opportunity to introduce freestream fluctuations and signal drift at the lowest pressure differences. Small variations and unevenness in the surface pressures at the lowest Reynolds numbers can be seen. In practice these contribute little to the measurement accuracy of lift and drag from the entire profile.

A data rate of 1kHz was determined sufficient to capture surface pressure fluctuations to an acceptable degree of accuracy (jet operation for instance ran up to 120Hz), although no real-time pressure variations were monitored here. As the PC connected to the pressure system was very basic, more data points were increasingly difficult to process. Acceptable repeatability was also confirmed in the pressure measurements detailed in the research.

The LDV was used to monitor and help maintain the exact freestream velocity during the tests. With durations of six seconds per pressure tapping, and short delays in between tappings as the Scannivalve rotated, one complete surface pressure measurement would take around five to six minutes to complete.

It is well known that lift and drag estimates can be derived from surface pressures from aerofoils. Given sufficient resolution of pressure measurements on the surface of the aerofoil, the estimates can be in extremely good agreement with direct force balance measurements. Direct force balance measurements were not possible with the wing fixed to the speaker. The lift drag coefficients were estimated using:

$$C_L = -\oint C_p \cos(\theta) ds$$

$$C_D = \oint C_p \sin(\theta) ds$$

where θ is the clockwise tapping angle to the normal in degrees and ds is a discrete surface element length.

Discrete surface pressure measurements were taken and processed using a commercial spreadsheet package with macros. As no pressure measurement could be taken at the trailing edge, the resulting forces C_L and C_D were then corrected with the estimated component of C_μ acting in the direction of the corresponding forces. In practice, the equations used were therefore:

$$C_L = -\oint C_p \cos(\theta) ds + C_\mu \sin(\alpha + 11.42)$$

$$C_D = \oint C_p \sin(\theta) ds + C_\mu \cos(\alpha + 11.42)$$

where (α + 11.42) is the downwards deflection angle of the jet from the horizontal.

The contributions of the momentum coefficient corrections to the estimated lift coefficients were small. The contribution of the momentum coefficient for the drag coefficient estimates was larger for larger momentum coefficients. Several estimates of drag coefficient using the surface pressures with non-zero jet excitation were compared to estimates derived using an LDV wake survey. The two estimates compared favorably for low incidence.

Care was used to induce the minimum amount of LDV seeding necessary to monitor the flow in an attempt to avoid any condensing of the seeding oil in the pressure tappings causing blockage.

3.7 FORCE MEASUREMENTS

Direct lift and drag/thrust force measurements were performed on the internally actuated wing. A full complement of drag and thrust force data was obtained whilst lift could only be measured without the jet excitation due to jet vibration interference in the lift measurement direction.

A calibration was performed on the strain gauge with 15 weights covering the range of forces to be experienced by the wing. The weights were calibrated by a digital scientific balance with tolerance greater than 0.00001g, considerably higher than the tolerance required. A low friction pulley and non-stretch strong thread were used to hang weights normal to the measurement support. The calibration set-up is shown in FIGURE 3.2. For each axis was calibrated to a first order equation in both directions whilst loading and unloaded the other axes. Calibrations were repeated several times but little hysteresis was found. A calibration was performed before each experiment to avoid introducing uncertainty. However the calibrations did prove very consistent throughout the experiments and the calibration gradient showed little deviation in all cases.

A small signal drift was observed when the loads on the strain gauges were low, for example in the measurement of drag at low incidence at Reynolds number 20,000.

Studying the real-time signature, it was found that there was no sudden jump in the signal, rather a gradual change over the duration of the test. It was therefore possible to make a sensible correction for the drift by accounting for the unloaded reading before and after the tests. Averaging these values gave a mean correct 'zero' reading over the experiment duration. As only mean force measurements were used, this was a valid procedure but would not be valid for real-time measurements. There was negligible drift under experiments involving larger forces.

As with the scanning pressure measurements, a study was performed to determine suitable signal capture durations and data capture rates. Again, the maximum data rate to achieve good real-time signal was determined to be 1000Hz, around 30 data points per cycle at the jet operating frequency. ten seconds of data (350 jet cycles with the jet in operation) was found to offer a repeatable mean force measurement for both jet-on and jet-off experiments. Longer durations could be used but were not necessary to find repeatable averages and would allow greater change of freestream velocity fluctuation. Computing resources were also limited for the purpose of obtaining force balance measurements.

3.8 POWER MEASUREMENTS

Power consumption measurements were conducted on both the speaker powered wing and the internally actuated wing. A method similar to that used by Jordan *et al* [2000, 2001], Brennan and McGowan [1997], and Chandrasekaran and Linder [2000] was used. A nominal resistance load, R, was introduced in each circuit to allow current drawn by both mechanisms to be measured. A real-time digital voltage signal was captured before and after the resistor by a high-end digital storage oscilloscope. As the voltage drop off across R could then be calculated as the real-time voltage difference, the real-time current flow through R to the actuators could be found.

Careful consideration has to be given as to the value of R used. If R is too large, it becomes too invasive into the circuit in question and influences the current drain significantly. If R is too small then the voltage difference across R is difficult to measure accurately. The recognition of an optimum value of R used here was to start with small values of R and increase them until sufficient accuracy could be achieved in

voltage difference measurements. That method allows the circuit invasion to be as small as possible.

Real-time current and voltage drain were exported to a PC for analysis in CSV format. The time-averaged power per unit span for one cycle was then calculated and non-dimensionalised, consistent with Seifert *et al* [1998], as:

$$C_E = \frac{P}{\frac{1}{2}\rho U_\infty^3 S}$$

where P is the mean power for one cycle measured in watts.

3.9 MEASUREMENT ACCURACY, BIAS AND REPEATABILITY

3.9.1 WATER TUNNEL CONSIDERATIONS

Initially attention was paid to the quality of the flow of the water tunnel and wind tunnel used for the research presented here. The manufacturer of the water tunnel has quoted turbulence intensities of less than 1% over the workable freestream range. A turbulence intensity of over 0.5% has been shown to promote earlier transition on low Reynolds number aerofoils due to the increased freestream instabilities affecting the laminar regions of the boundary layer. Consequently, measurements taken in the water tunnel were not used due to the unfavorable conditions. Flow visualisation in the water tunnel will be shown in the results sections. When the fluid dynamics suggest both laminar and turbulent boundary layers over the aerofoil, the proportions may not scale exactly with the matching conditions of the wind tunnel having turbulence intensity around 0.3%-0.4% and this was considered. The laminar regions are likely to persist slightly farther downstream than in the water tunnel. With that in mind, the flow visualisation should give a broad indication of the flow fields and fluid dynamic interactions.

3.9.2 WIND TUNNEL CONSIDERATIONS

Turbulence intensity

With a considerably lower turbulence intensity compared to the water tunnel conditions, the experiments conducted in the wind tunnel should compare with other work in similar conditions. Whilst to the best of the author's knowledge, no other researcher has

published findings on trailing edge synthetic jet propulsion of MAVs, other researchers have considered similar aerofoil geometries in the low Reynolds number range. Comparisons will be drawn later in this section.

Freestream measurement and consistency

The first wind tunnel motor and controller used an electro-magnetic clutch system. Whilst the system was many years old, it was capable of holding the wind tunnel freestream extremely stable at freestream velocities of greater than 2m/s. Measurements at Reynolds number of 10,000 using this system corresponded to freestream velocities of 0.7m/s. Measurements at 0.7m/s were therefore painstaking and sometimes took many hours to obtain. The first motor and controller was generally susceptible to drifting to higher or lower freestream velocities when run at such low speeds. There was little that could be done to prevent drift. Instead, real-time monitoring of the freestream velocity was performed throughout all of the experiments to ensure that there was less than 10% drift in the freestream velocity during any measurements. Whilst that methodology did cause many tests in the very low Reynolds number range to last many hours, it was considered the only viable solution to obtaining accurate results at the correct freestream velocity. The freestream velocity at the Reynolds number 10,000 condition was maintained to within +/-10% of the desired velocity.

With the installation of the new EMI controller and electronically controlled motor, the freestream stability was significantly increased. Whilst the velocities of 1.4m/s with the old system would sometimes drift to 1.7m/s or 1.1m/s, the natural drift of the low range of the new system was around 1.4m/s +/-0.1m/s. Therefore, although the new system had minimum velocity of 0.9m/s, it offered a considerable improvement in stability. With the installation of the new system, the lowest Reynolds number tested was 20,000, corresponding to 1.4m/s. Once again, freestream velocity was rigorously monitored to reject all experiments where freestream velocity was outside of the range 1.4m/s +/-5% Whilst monitoring was still performed at the higher velocities, it was found that the freestream velocity was much easier to hold within the 5% of requirement range. Experiments with higher Reynolds numbers were therefore less challenging.

Throughout all experiments, the freestream velocity was therefore accurate to +/-10% of required freestream velocity at Re=10,000 and +/-5% at Re=20,000 and higher. In terms of effects on the velocity profiles, the error is virtually imperceptible. The difference in Reynolds number for instance at the Re=20,000 condition would mean that conditions varied between Re=21,000 and Re=19,000. Over such a small change, there is no visual effect in the profile of the normalised wake velocities and they would appear identical and were therefore deemed suitable for use in this research. That allows for valid interpretation of the wake velocities and flow features in the wake using such freestream tolerance.

However, when considering the estimates of thrust, drag and momentum, based on the wake velocity profiles, recall that the non-dimensional coefficients rely on a freestream velocity-squared term in the denominator. The error is therefore squared and becomes more significant. The 10% fluctuation at the lowest Reynolds number would correspond to a 21% fluctuation in the squared freestream term used in estimation of coefficients. To counter such large error, measurements taken specifically for the purpose of coefficient estimates were repeated at least four times. The freestream velocity error could therefore be reduced significantly with careful monitoring of the fluctuations. Whilst a reduction in error by a factor of four was not achieved in all cases, in general the error was reduced by a factor of three reducing the coefficient error to +/-7% at the very low Reynolds number of Re=10,000 and +/-3.42% at higher Reynolds numbers.
As the duration of the experiments for measuring surface pressures and direct force coefficients was short, the freestream velocity could be maintained with greater accuracy. Variations in freestream velocity of +/-1% were the maximum allowed fluctuations for these experiments. Compared to other researchers working in low Reynolds number experimentation, this was a very encouraging level of accuracy.

3.9.3 TWO-DIMENSIONALITY

To afford two-dimensionality to the aerofoils under test end plates were always fitted. The force balance measurements were conducted between floating end plates with gaps from aerofoil to end plate less than 1mm. Observation of flow visualisation in the water tunnel showed than the outer 10% of each aerofoil could be considered non-two-dimensional due to interactions with the end plate boundary layers. However, two-dimensionality was confirmed visually over the remainder of the aerofoil. Activation of

the jet decreased the region of interaction around the end plates. However at high momentum coefficients the end plate boundary layer was seen to interact with the strong jet in the wake. Several experiments were conducted in the wind tunnel inside the central 50% of the aerofoils' span. It was found that within this region, there was span wise uniformity yielding drag coefficients within 10% of the estimate from the central span location. It is expected that both a small degree of span-wise non-uniformity and wake survey measurement errors due to freestream fluctuations combined to yield the overall variation. As measurements were always taken at the central span location it was felt representative values of the aerofoil lift and drag coefficients could reasonably be determined from that station.

3.9.4 PIV

There are several sources of measurement error with PIV experiments. A thorough review of PIV error and limitation was performed. Adrian [1991, 1997], Bolinder [1999], Hart [1988], Hocker and Kompenhaus [1989], Huang *et al* [1997], Keane and Adrian [1990, 1991], Nogueira *et al* [1997], Westerweel [1997] and Willert and Charib [1991] were reviewed for their significant consideration of PIV limitations and error analysis. The critical considerations are reviewed here. By far the biggest of these is concerned with user error. Unfortunately it would be very easy to capture images and then generate a vector field from them based on an entirely different value of the time delay (between the two images of an image pair) to that actually used in the experiment. To avoid mistakes such as these, the PIV field was always generated and the surrounding freestream velocity in the field always compared to the actual value used for the experiment.

In section 2.4.5, it was noted that the seeding particle properties were sufficient to track the fluid features accurately. Sufficient seeding, optimally at least three seeding pairs per interrogation window, was also introduced to allow accurate correlation. Fortunately, generating seeding in sufficient quantities for low speed measurements is not as difficult as for high-speed measurements. As experiments were monitored real-time, poor quality PIV results with significant low correlation features were interrupted and improved. As it was possible to get a high percentage of valid vectors at low speed, any experiments with a low percentage were discarded and repeated. The most common

reasons for poor quality PIV images was either dirty optics preventing the capture of sharp images, or poor seeding density in the flow.

As PIV was not used in a quantitative assessment of the aerofoil performance and only used as an accurate visual representation of the flow fields, the most accurate, finest resolution PIV was not required. Despite that, every effort was made to maintain the freestream velocity as accurately as possible and to calibrate the area of interest accurately. LDV wake survey profiles were also used to check the general reliability of the PIV results which, whilst lacking the sufficient spatial and time resolution, always gave good general agreement.

3.9.5 LDV AND THE WAKE SURVEY TECHNIQUE

To understand the limitations of the LDV measurement system, a full review of LDV literature was performed with that regard [Adrian, 1978, Argarwal and Keady, 1980, Broersen, 2000, Kaufman, 1986, Menon, 1982, Menon and Lai, 1991, Menon *et al*, 1993, Ramaprian and Chandrasekhara, 1985, amongst others] in addition to the seeding considerations, mentioned previously, consistent with Melling [1997] Menon and Lai [1991].

In section 2.4.5, it was noted that the seeding properties enabled accurate tracking of the fluid dynamic features of the flow. Further consideration of LDV seeding for accurate momentum coefficient estimates was given in section 3.4. By itself, LDV is a potentially extremely accurate measurement system. However limitations of seeding and background noise work against the accuracy of the technique. Momentum coefficient measurements were repeatable within +/-4% with the best seeding conditions strived for throughout this research. The minor variation was due to inconsistencies in the seeding quality and the accuracy of setting the operating voltage of the jet mechanism using the oscilloscope. From the obtainable accuracy levels, the momentum coefficient was therefore considered easier to obtain accurately than wake survey estimates of drag coefficient. Poor quality seeding was instantly recognisable upon examination of the real-time LDV signal, which would appear clipped and discontinuous. Poor quality seeding could cause momentum coefficients to vary by more than +/-50%, but such conditions were soon understood and heavily guarded against by improving the seeding conditions.

Discussion of the limitations of the LDV wake survey technique for estimated thrust and drag coefficients was given in section 3.5.2 Here, we briefly discuss the levels of accuracy achieved using this technique and compare findings with measurements using other techniques and from other researchers.

As the incidence of the aerofoil increases, the wake also increases in height accordingly. A bluff body could approximate the streamlined aerofoil at very high incidence. Therefore it is expected that accurate estimates of thrust and drag from the wake survey technique at the x/c = 0.5 station would only be accurate for low incidence. At $\alpha=10^{\circ}$ or $\alpha=15^{\circ}$ significant disparity is expected between estimated drag coefficients from the wake and direct force measurements. The disparity is attributed to the existence of a static pressure variation from the freestream pressure in the near wake region and is well known. At low incidence, the streamlined body of the aerofoil was not expected to cause such a large pressure variation.

Despite extensive searching, the only closely related research to cross reference results with was found in a publication by Mueller [1999]. Whilst Mueller uses a tapered trailing edge, one of the aerofoils in his study has a similar leading edge, camber and thickness to the cambered aerofoil studied here. In order to find additional comparative data, Selig's XFOIL CFD program was used to generate solutions under matching conditions. The basic outline of XFOIL theory is given in section 1.2.2. The accuracy of XFOIL is limited in prediction of transition and the most difficult low Reynolds number features. Whilst the area of study presented here is the most demanding condition for XFOIL, it is nevertheless an additional comparison, albeit with the consideration of accuracy. The exact conditions of testing, including the turbulence intensity and 200 point based aerofoil geometry were used in generating XFOIL solutions.

FIGURE 3.3 shows a comparison of the drag coefficients measured by Mueller, and estimations from LDV wake survey and XFOIL CFD solutions. Sufficiently good agreement is found between all of the methods compared at low incidence. However, at $\alpha = 10^{\circ}$ or $\alpha = 15^{\circ}$, significant disparity is observed between the estimates of drag coefficient for the LDV wake survey technique and those values suggested by the other

methods and Mueller. The LDV wake survey would therefore only be used for low incidence estimates of drag and thrust of the aerofoil system.

The real-time velocity measurements in the wake measured by LDV were also used to perform frequency analysis in the wake. TSI's inbuilt slotting analysis method was used to generate the Power Spectrum Density (PSD) distributions. The technique is well known. Other methods of analysis were considered but research suggested they may not lead to improved accuracy or to a faster processing time [Bell, 2001, Britz and Antonia, 1996, Jancek, 1998, Matovic and Tropea, 1991]. When used to analyse the jet, the iterative slotting technique calculated peaks at frequencies corresponding extremely closely to the excitation frequency of the jet. Sufficient confidence was therefore gained to allow the TSI method to be used for all PSD measurements throughout the research presented here.

3.9.6 PRESSURE MEASUREMENTS

The pressure measurement system was constructed after the effects of the system had been understood in using the aerofoil without pressure measurement capability. The performance of the tapped wing was slightly more restricted due to the internal tubes and fixing materials. It was primarily designed to operate only at the optimum conditions identified from studies on the baseline aerofoil. Therefore, for the majority of the wake survey estimates, the pressure measurement system would have been unsuitable.

The pressure transducer used was a Druck LPM 9000 series +/-1mBar comparative type. Built to order, the LPM 9000 series offered extremely high accuracy of 0.1% full scale. Measurements at the lowest incidence at Re=20,000 were bordering on the capabilities of the accuracy of the transducer. However, after discussion with the manufacturer, it was noted that the tolerance was likely to be accurate to well inside the minimum specified tolerance. Small fluctuations were observed at the lowest pressure differentials but the measurements were in-line with expectations.

The main purpose of using the pressure measurement system was to obtain lift coefficient estimates and to obtain estimates for drag coefficients at higher incidence. Good comparison was found between the data of Mueller [1999] and the lift estimates

as shown in FIGURE 3.4. The solutions predicted by XFOIL do not compare as well, neither do they compare with the high accuracy measurements of Mueller. The disparity could be attributed to XFOIL's limitations in predicting accurate transition, which features more commonly at the higher incidence. Nevertheless XFOIL remained a useful tool to compare results with. FIGURE 3.3 shows how well the pressure measurement system compared with the data of Mueller and solutions from XFOIL, also with the low incidence wake survey estimates from LDV. The pressure measurement system was therefore believed to give good estimates of lift and drag for the limited range of conditions it was suitable for.

Furthermore, because the pressure scanning valve cycles were reasonably quick in comparison to a wake survey, measurements of surface pressures benefited by a greater accuracy of freestream velocity achieved for the shorter durations. Typically the freestream velocity was kept within 1% tolerance of the required value. This meant that propagation of freestream errors into the thrust and lift estimates was less than 2.01%, well within the estimated error of around +/-4% for the scanning pressure measurements of lift and thrust coefficients.

The pressure transducer also featured high temperature tolerance with accuracy, due to temperature fluctuation, at most 0.01% of full scale. Temperature errors were deemed insignificant in the scanning pressure measurements.

3.9.7 FORCE BALANCE MEASUREMENTS

As with the scanning pressure measurement system, the force balance benefited from its quick data capture. The freestream velocity was kept within 1% of the required value and led to a contribution of error in the thrust and lift coefficients of less than 2.01%.

XFOIL was used to generate predictions for lift and drag coefficient for the internally actuated wing geometry. As the internally actuated wing is fattened towards the trailing edge on the lower surface, there is no existing body of research with which to compare results. FIGURE 3.5 shows the comparison between XFOIL predictions and measured lift coefficients using the LRNFB. Recall that from FIGURE 3.4, it was shown that XFOIL was not predicting the stall region of the aerofoil accurately for similar aerofoil geometries. With that in mind, the lift coefficients measured by the LRNFB would

appear to be accurate to the extent of measuring the predicted trend. Lift was not measured in conjunction with jet excitation due to the mechanical vibration interfering strongly with the lift measurements.

The comparison of drag coefficient measurements with XFOIL is shown in FIGURE 3.6. The comparison suggests good enough agreement to give confidence that the balance arrangement is measuring the force parameters with sufficient accuracy. It was found that unlike the lift axis, jet vibrations affected the drag-thrust measurement axis less. Whilst oscillations in the real time measurements (used only to derive time-averaged values) were observed, the mean measurements gave thrust coefficient increments very similar in trend to the externally powered aerofoil system under the same conditions of momentum coefficient, frequency, incidence and Reynolds number. This also provided confidence that the LRNFB was measuring appropriate forcing coefficients with the jet activated in addition to measurements with the jet deactivated.

Much of any error source with the LRNFB was felt to originate with the electronic amplification and signal conditioning. In section 3.7, it was reported that signal drift was observed during measurements of the very smallest forces. Observing the behaviour of the signal drift confirmed that it was a linear variation. Therefore it was straightforward to average the offset before test and after values of drift. Without the drifting compensation, the measurements were considered to have not more than 25% uncertainty. However, based on repeatability experiments, the compensated results showed less than 10% uncertainty.

3.10 FIGURES

FIGURE 3.1 Diagram of x- and y-axis orientation

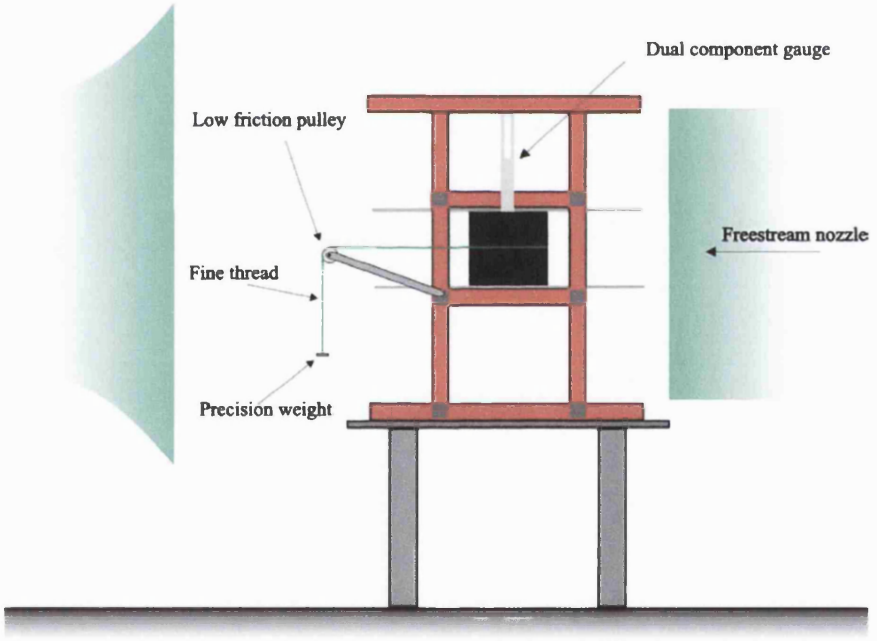

FIGURE 3.2 Strain gauge calibration technique

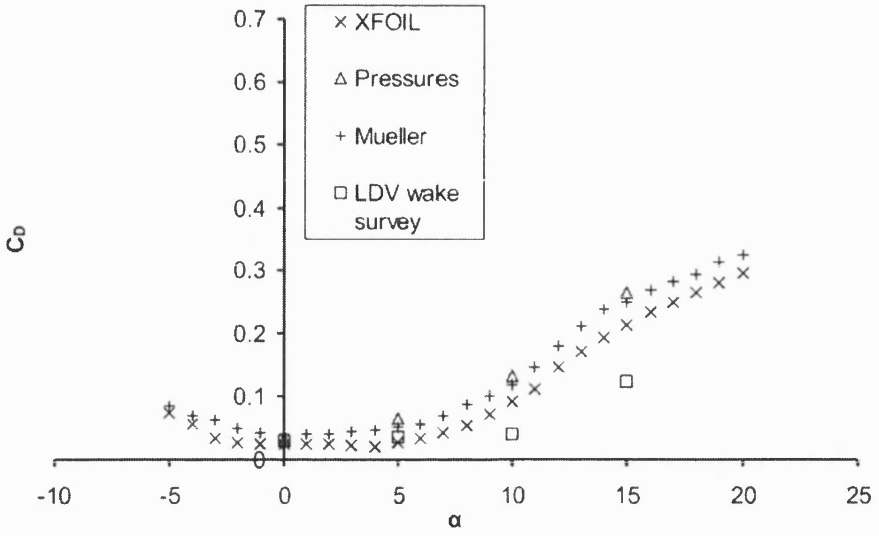

FIGURE 3.3 Comparison of drag estimates with Mueller and XFOIL at Re=60,000 without jet excitation.

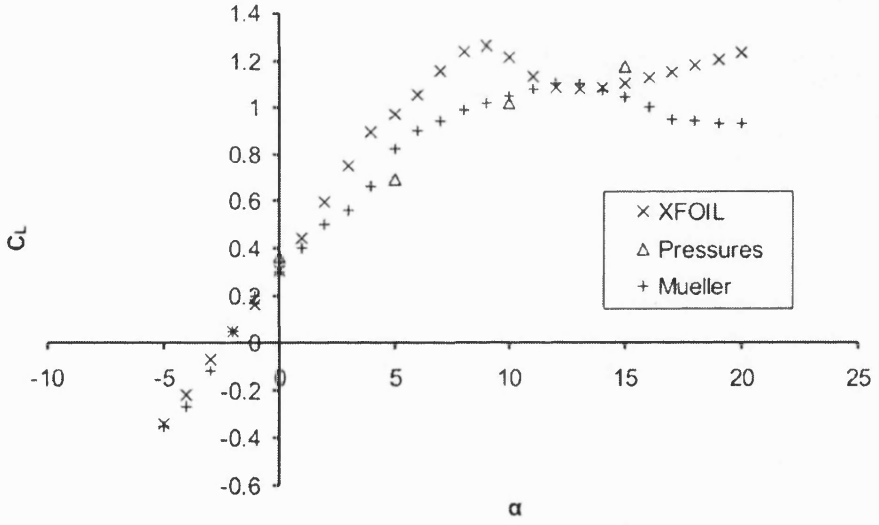

FIGURE 3.4 Comparison of surface pressure based estimates of lift with the CFD solutions of XFOIL and similar studies by Mueller [1999] with Re=60,000 and without jet excitation.

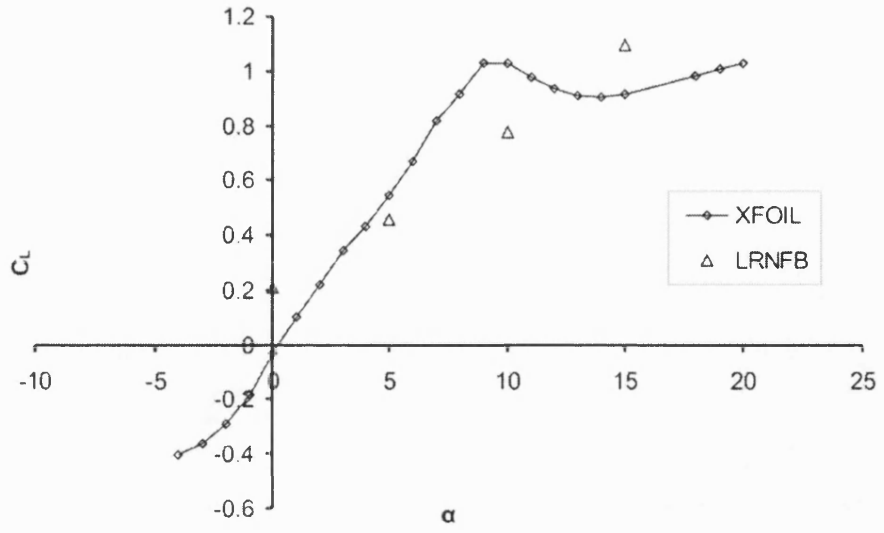

FIGURE 3.5 Comparison of lift coefficient measured on the LRNFB with solutions predicted by XFOIL at Re=20,000 using the internally actuated wing without jet excitation.

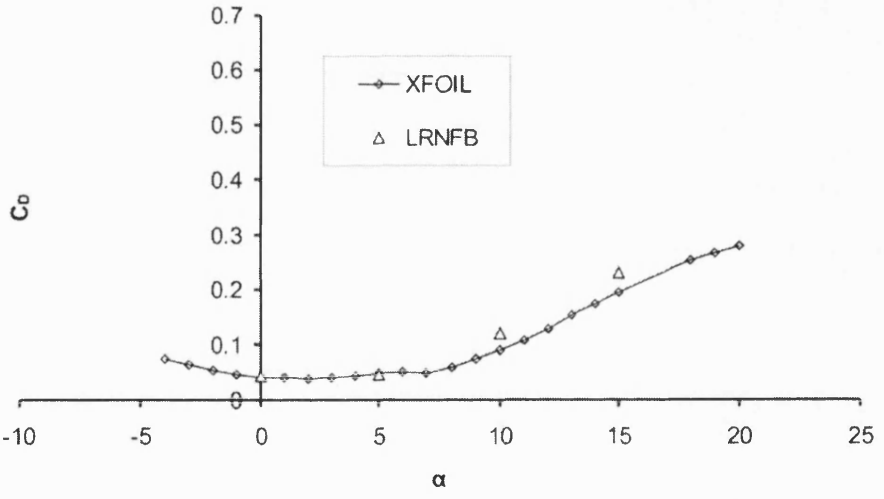

FIGURE 3.6 Comparison of drag coefficient measured on the LRNFB with solutions predicted by XFOIL at Re=20,000 using the internally actuated wing without jet excitation.

CHAPTER 4 PARAMETRIC EFFECTS

4.1 FLOW VISUALISATION

The three wing geometries were used in the water tunnel rig to perform flow visualisation with and without jet excitation. Care was taken about the interpretation of transition and separation of the flow visualisations due to intrusive dye flow injectors and higher TI of the water tunnel. Whilst the flow visualisation of final year student, Zeeshan Khan, shown in FIGURE 4.1 on the tapered wing, does not yield the clearest indication of performance, it does highlight some key features.

At $\alpha=0^{\circ}$, a clear Karman vortex street is highlighted in the wake by injecting dye at the trailing edge. At this incidence there is little if any evidence of separation over the aerofoil. Increasing the incidence to $\alpha=5^{\circ}$ shows slightly separated flow at the trailing edge. The periodic vortex shedding is still evident although more diffuse due to the increase in separated flow. Increasing the incidence still further to $\alpha=15^{\circ}$ does show significant separation right from the leading edge and reverse flow over the wing, indicating the aerofoil has stalled. There is evidence of periodic fluctuations in the wake although the wake region is large and diffuse.

Upon jet excitation at St=20, a jet like structure can be visualised using trailing edge dye injection. At $\alpha=5^{\circ}$, no evidence of separation around the trailing edge can be seen and a clear jet-like structure, as with the lower incidence of $\alpha=0^{\circ}$, is evident. Whilst there is still significant separation at $\alpha=15^{\circ}$, the condition with jet excitation does appear to have a slightly improved flow-field with the separation region at the trailing edge reduced in height in comparison to the 'no jet' aerofoil.

It is interesting to compare the features of the tapered wing with the similar wing of constant thickness as shown in FIGURE 4.2. At $\alpha=5^{\circ}$, the flow over the leading edge of the aerofoil forms a laminar separated shear layer. The shear layer can be seen transitioning to turbulence downstream of the leading edge over the upper surface, before partially reattaching. Fluctuations over the rear half of the aerofoil are evident. At $\alpha=10^{\circ}$ the laminar separation and transition is clearer, as is the enlarged separated region. Upon jet excitation, both $\alpha=5^{\circ}$ and $\alpha=10^{\circ}$ show improved aerodynamic performance with slightly decreased separated regions compared to their 'no jet' counterpart visualisations. The $\alpha=10^{\circ}$ incidence also has decreased laminar region, experiencing transition earlier than without the jet excitation. Instabilities caused by the jet flow oscillations may trigger earlier separation.

From literature, one would expect that introducing slight camber onto the geometry of the constant thickness flat wing would promote enhanced aerodynamic performance at low Reynolds numbers. Visualisation of the key features for the cambered wing is shown in FIGURE 4.3.

The most obvious feature in comparison with the two previous aerofoils is that at low incidence, the cambered wing flow is completely laminar under these conditions. Separation occurs inside the first third of the aerofoil surface and at $\alpha=0^{\circ}$ and $\alpha=5^{\circ}$, appears to a similar extent; the separated region at the trailing edge appears around one and a half to two aerofoils' thickness' away from the aerofoil surface. The $\alpha=5^{\circ}$ separated region varied between one and two aerofoil thickness away from the aerofoil surface due to instabilities at the trailing edge.

At $\alpha=10^{\circ}$, the upper-surface flow shows both laminar and turbulent regions over the aerofoil with transition occurring around the first quarter to one-third of the chord length. The extent of the separation at the trailing edge is comparable, or possibly slightly improved, compared to the flat constant thickness wing.

In conjunction with the synthetic jet, the cambered wing appears to operate with enhanced performance over the other aerofoils. At St=20, the separated region observed in the St=0 case, is controlled with the jet flow causing reattachment at the trailing edge. Use of the term 'complete reattachment' is avoided because the reattachment point

appears to be at the trailing edge and may not be over the complete aerofoil. At $\alpha=10^{\circ}$ the turbulent wake is reduced in size although laminar bursting still occurs around the first third of the aerofoil. At $\alpha=15^{\circ}$ the separated laminar shear layer from the leading edge appears more diffuse, possibly becoming turbulent much earlier. Certainly the separation above the trailing edge is improved.

Considering that there appears to be considerable control influence of the synthetic jet over the sensitive upper surface, the cambered aerofoil was chosen as a good baseline geometry for further study.

4.2 EFFECT OF REYNOLDS NUMBER AND INCIDENCE- NO JET EXCITATION

The variation of geometry and angle of attack has already been shown to have considerable effect on laminar or turbulent separation and transition. Change is Reynolds number is expected to affect these features and the extent of separation at the trailing edge.

FIGURE 4.4 shows features of the cambered aerofoil for Reynolds number 10,000 and 20,000 over low and high range incidences. At low incidence, the effect of increasing the Reynolds number from 10,000 to 20,000 is to change the extent of laminar separation over the aerofoil. As has been shown previously, at Re=10,000 the shear layer is entirely laminar over the aerofoil surface. At Re=20,000, there is evidence of disruption to the laminar shear layer and inspection of the flow visualisation over the trailing edge shows a turbulent region; the transition point is not clear as it lies too close to the aerofoil surface to be seen. At higher Reynolds numbers it was observed that the boundary layer appears transitional at both $\alpha=0^{\circ}$ and $\alpha=5^{\circ}$.

The extent of the separation seen above the trailing edge at Re=10,000 at low incidence is reduced when increasing the Reynolds number to Re=20,000. As stated, part of the problem with low drag, laminar aerofoils is that the laminar boundary layer tends to separate more readily than a turbulent one with high susceptibility to disturbances. The turbulence gives enhanced mixing with the freestream and therefore higher energy content.

At higher incidences, transition is evident at Re=10,000 and Re=20,000 around the first quarter to one third of the chord length. There is less variation in the flow field at higher incidence, although the leading edge separation is more coherent at the lower Reynolds number as would be expected.

A more quantitative study of the effect of Reynolds number using PIV is shown in FIGURE 4.5. The PIV velocity magnitude contours show the reduction in velocity deficit in the wake for higher Reynolds number for both low and higher incidence. There is considerable separation evident in the Re=10,000 examples. Increasing the Reynolds number shows the extent to which the separation over the trailing edge is reduced. Comparing the results of Re=10,000 with those of Re=80,000, provides an excellent example, illustrating the problems of increased separation and increased drag at low Reynolds numbers.

To obtain drag/thrust coefficients in the varying wake structure, a more detailed survey of the wake velocities is required. The high-resolution capabilities of LDV can be used and a thrust/drag coefficient can be estimated.

FIGURE 4.6 confirms the variation in velocity deficit in the wake of the aerofoil at $\alpha=5^{o}$, over varying Reynolds number. The velocity deficits at low Reynolds numbers is proportionally much greater than those found at higher Reynolds number.

FIGURE 4.7 summarises the effect of Reynolds number in the form of drag (negative thrust) coefficient plotted against increasing Reynolds number. At this low incidence, the higher the Reynolds number, the more favourable the conditions for flight within the range tested and therefore the lowest drag coefficients are experienced around Re=150,000-200,000. As the Reynolds number decreases, the drag coefficient is seen to increase. The increase in drag coefficient occurs more quickly once the Reynolds number drops below 80,000. Many other researchers have also reported the drop in aerodynamic performance estimated in the low Reynolds number region, for example Mueller [1999].

4.3 INTRODUCING THE SYNTHETIC JET: EFFECT OF MOMENTUM COEFFICIENT AND STROUHAL NUMBER

Before considering the implications of Reynolds number effects on the combined aerodynamic performance of the synthetic jet and aerofoil in combination, the effect of momentum coefficient has to be introduced before independent study of Strouhal frequency effects can be started. Both momentum coefficient and non-dimensional frequency are parameters that vary in accordance with freestream velocity and consequently vary with Reynolds number.

Whilst the water tunnel apparatus had only coarse settings for studying momentum coefficient, the Strouhal number was easily changed using the motor controller. The water tunnel apparatus did not allow for fully independent control of frequency and momentum coefficient. Increasing the frequency changed the piston amplitude proportionally and therefore the momentum coefficient. FIGURE 4.8 shows flow visulisation of the synthetic jet and aerofoil system in combination running in the water tunnel. The blue dye was injected upstream of the leading edge and the red dye was added into the piston unit of the synthetic jet before it was activated.

Without any excitation, at St=0, the laminar separated shear layer is evident over most of the aerofoil surface, separating inside the first third of the chord length. The jet is then activated at increasing frequency and the visualisations recorded. Increasing the rate of excitation has a pronounced effect on the separated region in addition to providing a time-averaged jet. From St=12 to St=20, the separated shear layer becomes very close to reattaching at the trailing edge suggesting an enhanced aerodynamic performance under such conditions. As the frequency is increased still further, the effect on the shear layer appears to be less until at St=40 only partial control of the shear layer is achieved.

It must be noted that using the water tunnel apparatus did not allow for independent control of frequency and momentum coefficient. Therefore caution must be exercised in interpreting the visualisation as indicative of a frequency effect since the momentum coefficient could not be fixed. It does suggest an effect of momentum coefficient and

Strouhal frequency in combination. Perhaps that can be optimised for increased aerodynamic performance.

To study the effect of momentum coefficient in isolation from Strouhal number, the wind tunnel model is used with independent precise control for each parameter. FIGURE 4.9 shows PIV velocity magnitude contours in the flow field for a fixed Strouhal frequency of 5.7. The momentum coefficient is increased from 0 to 0.277.

Initially, for the lower part of the momentum coefficient range used here, the velocity deficit in the wake is seen to decrease as the momentum deficit is decreased through momentum addition from the jet. For small momentum coefficients, the effect of the jet is to decrease the velocity deficit from below the wake.

In addition, with C_μ=0.071, the separation (evident over the trailing edge of the aerofoil without excitation), is eliminated completely and the wake begins to show similarity to a time-averaged jet. The slight separation still evident at C_μ=0.044 and a time averaged jet evident at C_μ=0.071, implies there exists some critical momentum coefficient, $C_{\mu C}$, with $0.044 < C_{\mu C} < 0.071$, such that a zero nett drag or cruise condition can be achieved when operating at this momentum coefficient under these conditions. Operating the jet at the critical momentum coefficient in ideal conditions would allow the MAV to be catapult launched and its launch speed would then be maintained.

For momentum coefficients above $C_{\mu C}$, a time-averaged jet is formed suggesting the aerofoil experiences a positive nett thrust. With increasing momentum coefficient, the time-averaged jet grows in size and velocity magnitude. At the highest momentum coefficients, a small increase in velocity over the trailing edge is evident, suggesting that the aerofoil might be experiencing a lift enhancement with increasing momentum coefficient in addition to increasing thrust coefficient. The acceleration of the reattached shear layer may be a secondary benefit of such a system.

Analysis of momentum coefficient effect at St=11.4 (double the Strouhal frequency of the previous experiment) yields similar flow field features as the St=5.7 experiments, as shown in FIGURE 4.10. Again, increasing the momentum coefficient from 0 causes a reduction in the velocity deficit in the wake. Initially the jet influences the underside of

the wake. A critical momentum coefficient can be seen to lie in the range $0.050 < C_{\mu C} < 0.107$. In comparison to the critical momentum coefficient range identified with the St=5.7, that leaves open the possibility that the critical momentum coefficient might be different for different Strouhal frequencies; it will be shown later that some frequencies perform better than others.

Increasing the momentum coefficient to the highest values in the range tested shows that the higher Strouhal number is associated with a low velocity region (shown in blue) bounding the time-averaged jet profile in the wake as shown in FIGURE 4.14. The low velocity magnitude region is most evident at C_μ=0.297. It is attributed to increased jet entrainment. In the real-time sense, the synthetic jet consists of vortex pairs propagating from the trailing edge. As the vortex pairs propagate downstream, a jet-like structure occurs between the two vortices but each vortex rolls back on itself against the direction of the freestream therefore causing the low velocity region. These results suggest an effect of frequency evident in the wake and this will be discussed more thoroughly in the next chapter.

4.4 EFFECT OF REYNOLDS NUMBER ON SYNTHETIC JET OPERATION

Having an understanding of the effect of momentum coefficient, and an introduction of the frequency parameter, experiments to investigate effect of Reynolds number on the wing in conjunction with the jet in operation are detailed, noting that at the lowest Reynolds numbers, the aerofoil experiences an increase in drag coefficient due to increased separation.

FIGURE 4.11 shows the variation in wake velocity magnitude with increasing Reynolds number whilst fixing the angle of attack and jet operation parameters. At all Reynolds numbers, the jet momentum was fixed at 0.050, except for Re=10,000 where the momentum coefficient was 0.044. In spite of this small variation, the extent of separation evident above the trailing edge of the aerofoil is clearly decreasing with Reynolds number. That suggests that the loss in aerodynamic performance experienced at low Reynolds numbers still persist in conjunction with the jet operation. The same momentum coefficient would correspond to increasing thrust coefficients at increasing Reynolds numbers due to the baseline performance variation of the aerofoil.

An LDV survey of the wake provides high-resolution mean stream-wise velocity measurements as shown in FIGURE 4.12. Performing a similar experiment at Re=10,000 and Re=20,000 reveals some key features. As has already been shown, the velocity deficit in the wake is greater at the lower Reynolds number, evident when examining the C_μ=0 velocity profile for both Reynolds numbers.

In each case, increase of momentum coefficient changes the wake velocity profile and increases the velocity in the wake region. With momentum coefficients larger than the critical momentum coefficient, a jet-like profile is observed in the wake, as PIV suggested. With increasing momentum coefficient it has been suggested that the initial improvement at Re=20,000 compared to Re=10,000 is propagated throughout the range of C_μ tested here. It is easiest to show the disparity in calculating the corresponding thrust coefficient from the real-time velocity profiles in the wake.

FIGURE 4.13 shows the thrust coefficient variation with increasing momentum coefficient for the two Reynolds numbers. The thrust estimates highlight the benefits of operating at higher Reynolds numbers. The detrimental performance of low Reynolds numbers persists throughout the range of momentum coefficient tested. The increase in thrust coefficient between Re=10,000 and Re=20,000 remains approximately constant throughout the range tested although small momentum coefficients appear to have less effect on thrust coefficient than those closer to and beyond the critical momentum coefficient.

The relationship between momentum coefficient and thrust coefficient appears to be approximately linear over the range tested for all but small values of momentum coefficient. For very small values, the jet may not propagate sufficiently far away from the slot to avoid re-ingestion or at least partial influence from the suction part of the cycle. At higher momentum coefficients, the amplitude of the oscillations increases and propagates the jet further downstream, away from the influence of the suction part of the cycle.

Increasing angle of attack leads to increased separation over the aerofoil surface as indicated by FIGURE 4.14. The figure compares the same operating conditions for the

cambered aerofoil at two incidences of $\alpha=5^{\circ}$ and $\alpha=10^{\circ}$. At $C_{\mu}=0.050$, the lower incidence is becoming close to a completely reattached condition whilst the higher incidence is still indicating a large region of separation above the trailing edge. Therefore, according to expectations, the jet momentum coefficient required for reattachment at higher angles of attack is larger than for lower angles of attack. At $C_{\mu}=0.107$, both $\alpha=5^{\circ}$ and $\alpha=10^{\circ}$ have a small time-averaged jet and have completely reattached flow at the trailing edge. In a similar way to exacerbated separation at low Reynolds number, separation at higher angles of attack also requires greater momentum coefficients to control. Larger angles of attack cause larger momentum loss in the fluid and therefore require larger injection of momentum to recover the loss.

4.5 SUMMARY

Flow visualisation highlighted the key fluid dynamics on a tapered aerofoil, an aerofoil of constant thickness and a cambered aerofoil, all designed with low Reynolds number flight considerations. The variations in laminar and turbulent separation were highlighted along with the extent of separation over the aerofoil.

Angle of attack was shown to affect the extent of separation over the aerofoil, as one would expect. In addition increasing angle of attack was shown to reduce the extent of the laminar boundary layer over the aerofoil surface. Higher angles of attack were shown to be accompanied by shorter laminar shear layers from the leading edge that transition to turbulent regions within the first third of the aerofoil.

The flow visualisation suggested slightly improved performance of the cambered aerofoil, especially in conjunction with the jet operation. Flow visualisation suggested that for certain jet momentum coefficient and Strouhal number, the separated shear layer could be reattached at the trailing edge.

Using the wind tunnel model, it has been shown that momentum coefficient can control the velocity in the wake and control the separation over the trailing edge of the cambered aerofoil. For a critical momentum coefficient, the wake of the aerofoil has no velocity deficit and there is no separation evident at the trailing edge. Increasing the momentum coefficient further strengthens the time-averaged jet. There is a suggestion

that certain Strouhal numbers might offer enhanced performance compared to other frequencies and this will be discussed more fully in the next chapter.

The effect of increased separation and drag coefficient at the lowest Reynolds numbers and higher angles of attack tested was shown to propagate throughout the range of momentum coefficients tested leading to a constant comparative performance drop in the lowest Reynolds number and higher angles of attack.

4.6 FIGURES

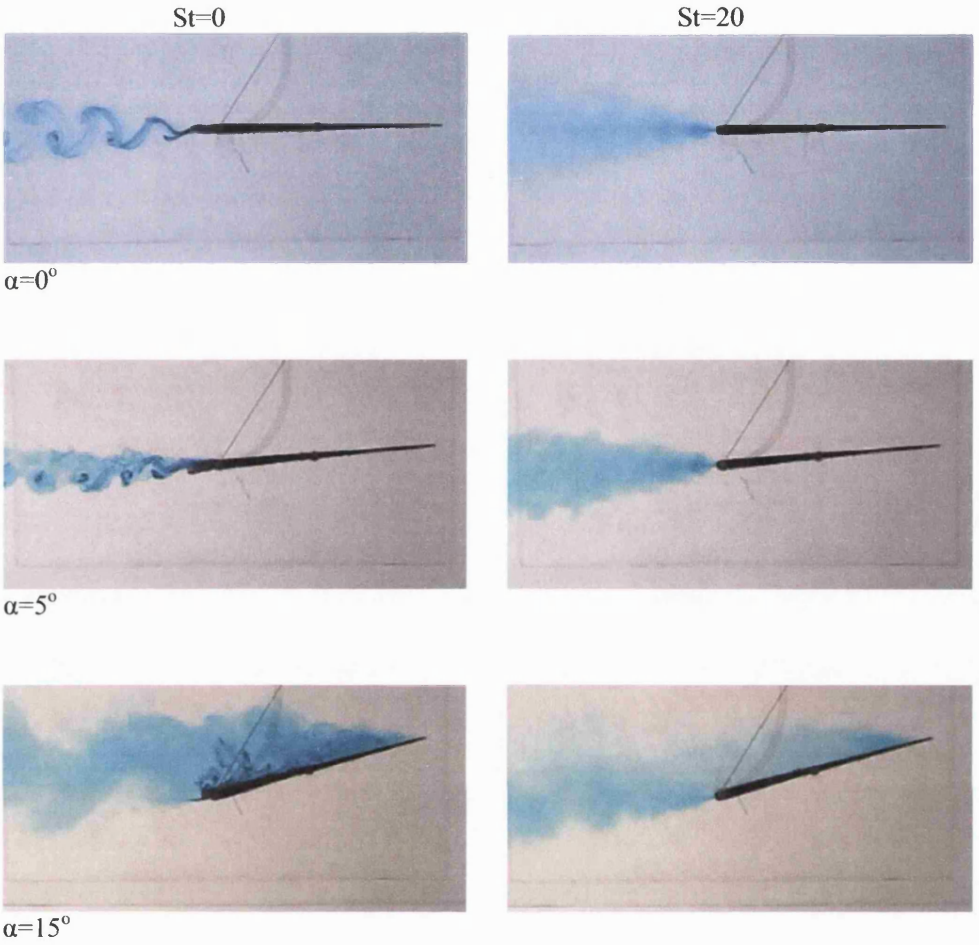

FIGURE 4.1 Re=10,000, tapered wing visualisation.

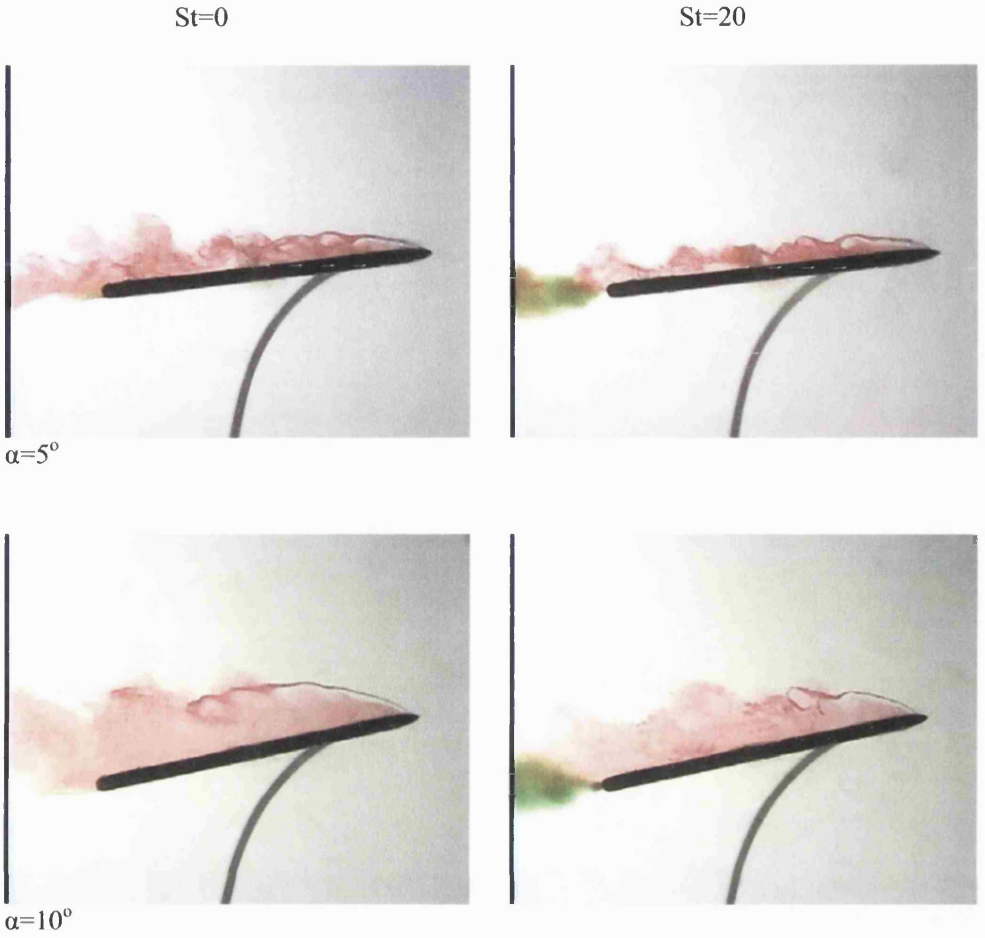

FIGURE 4.2 Re=10,000, constant thickness flat wing visualisation.

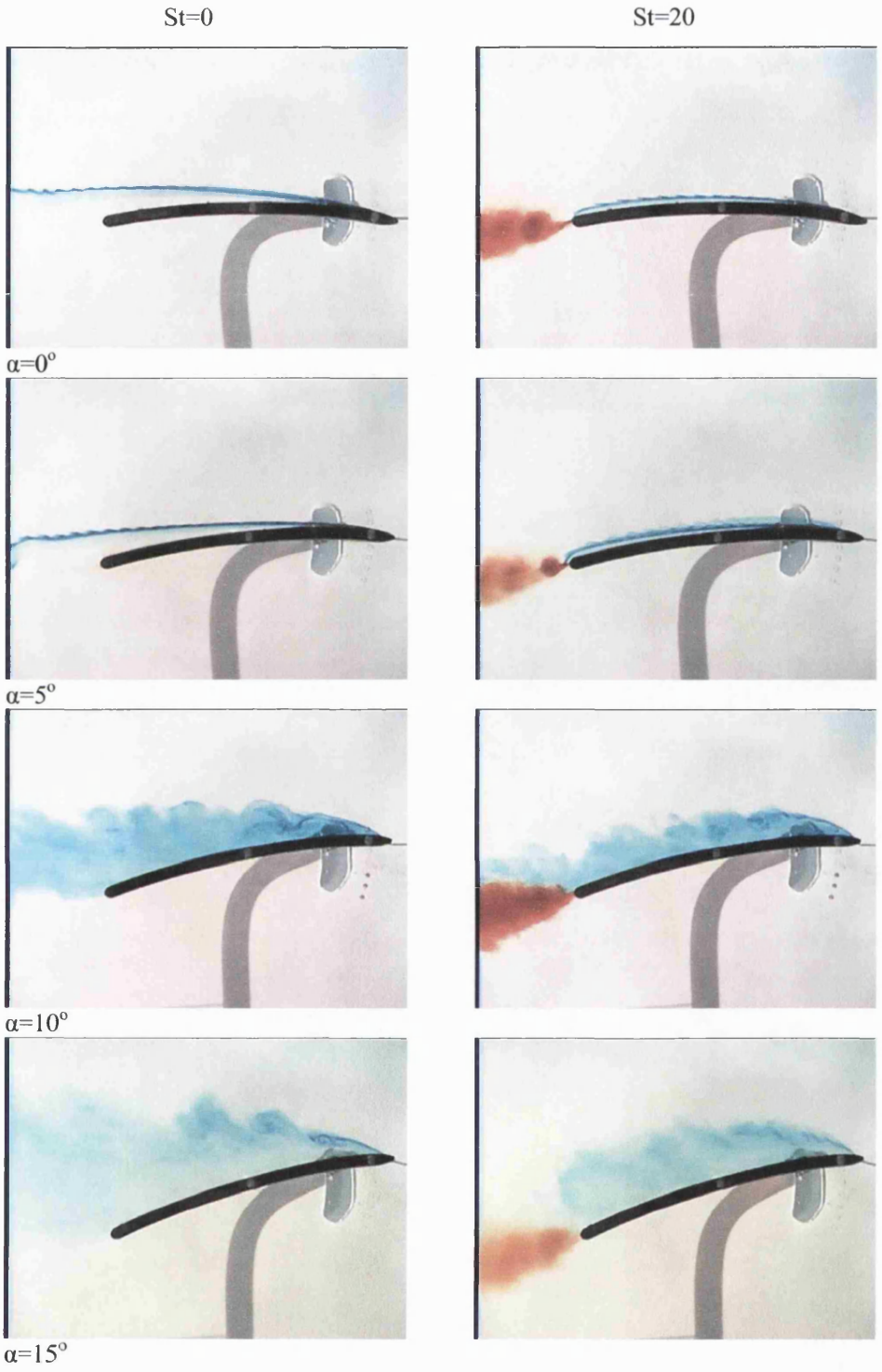

FIGURE 4.3 Re=10,000, cambered wing visualisation.

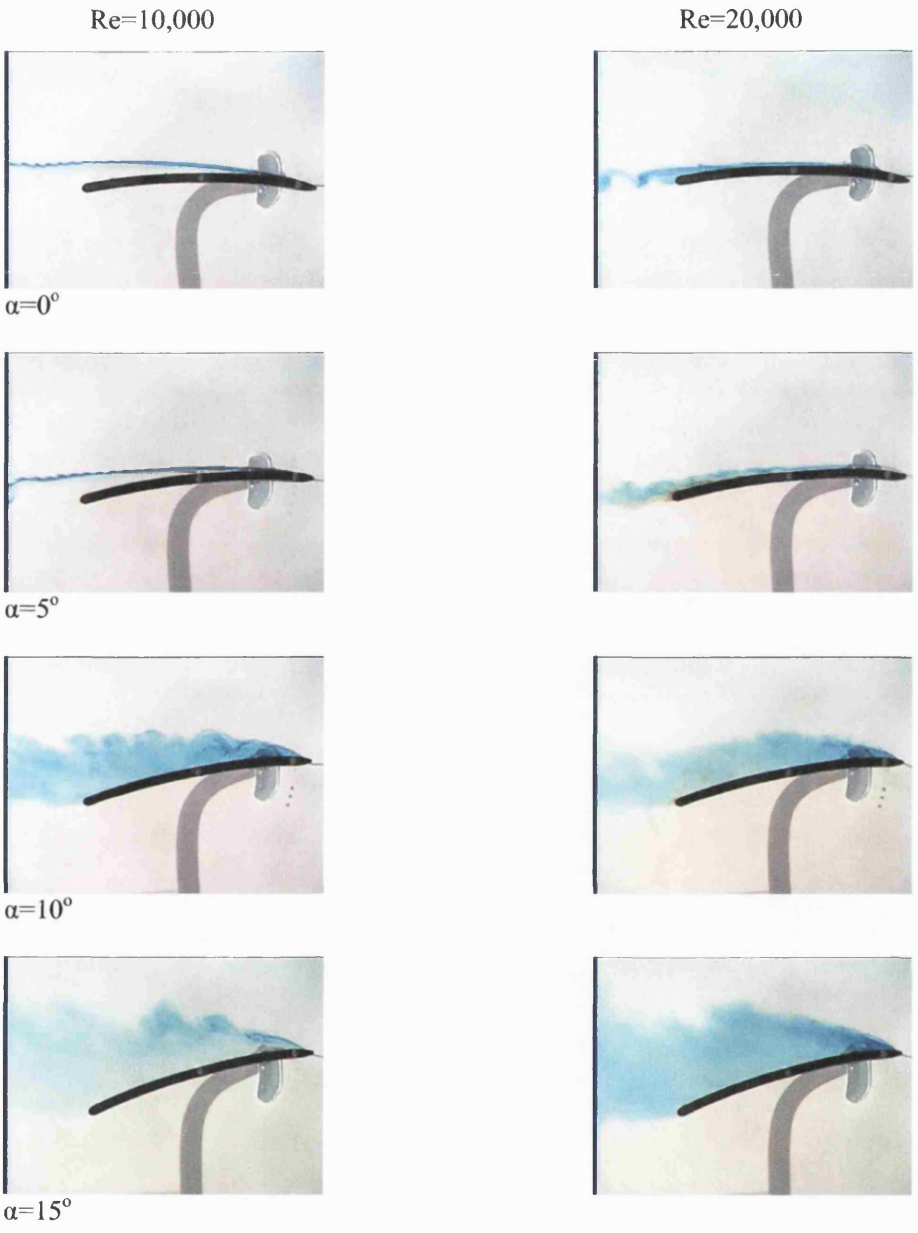

FIGURE 4.4 Effects of variation of α and Re on the cambered aerofoil without jet excitation.

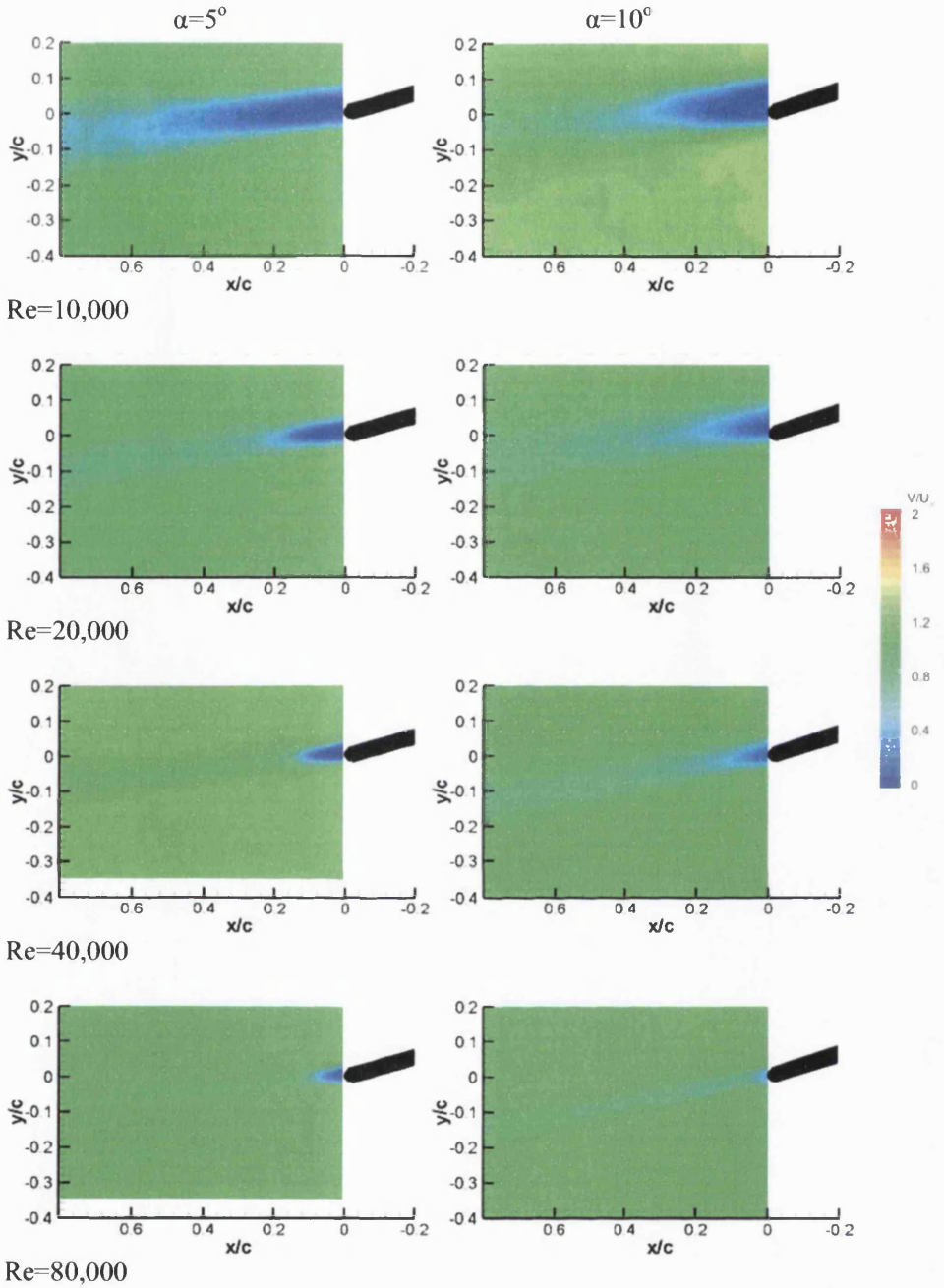

FIGURE 4.5 Time-averaged velocity magnitude plots from PIV without jet excitation for the cambered aerofoil.

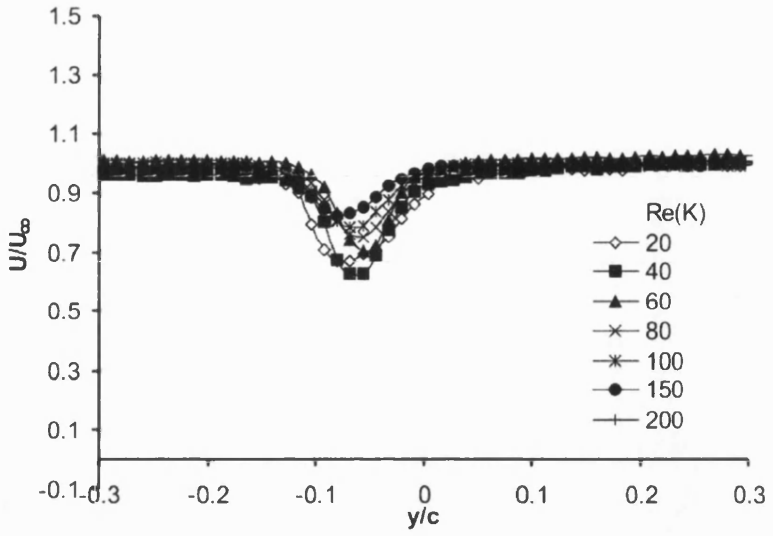

FIGURE 4.6 LDV wake survey at x/c=0.5 with $\alpha=5^{\circ}$ with no jet excitation for the cambered aerofoil.

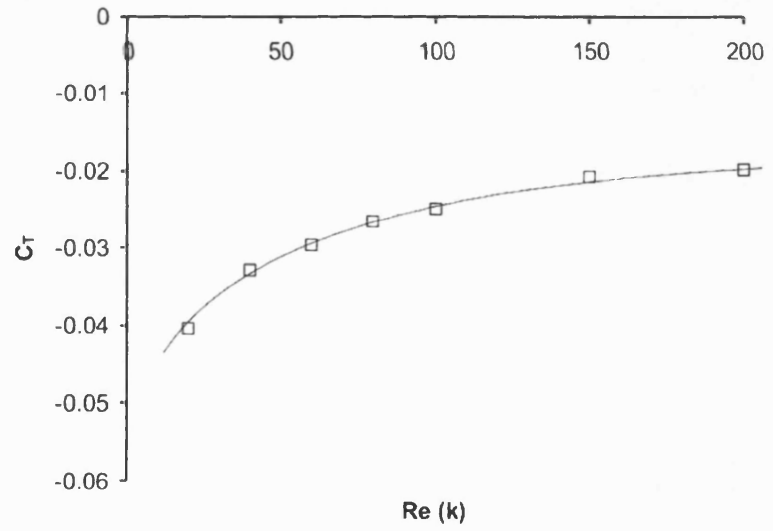

FIGURE 4.7 Thrust coefficient variation with Reynolds number estimated using the velocity wake survey technique at $\alpha=5^{\circ}$ without jet excitation for the cambered aerofoil.

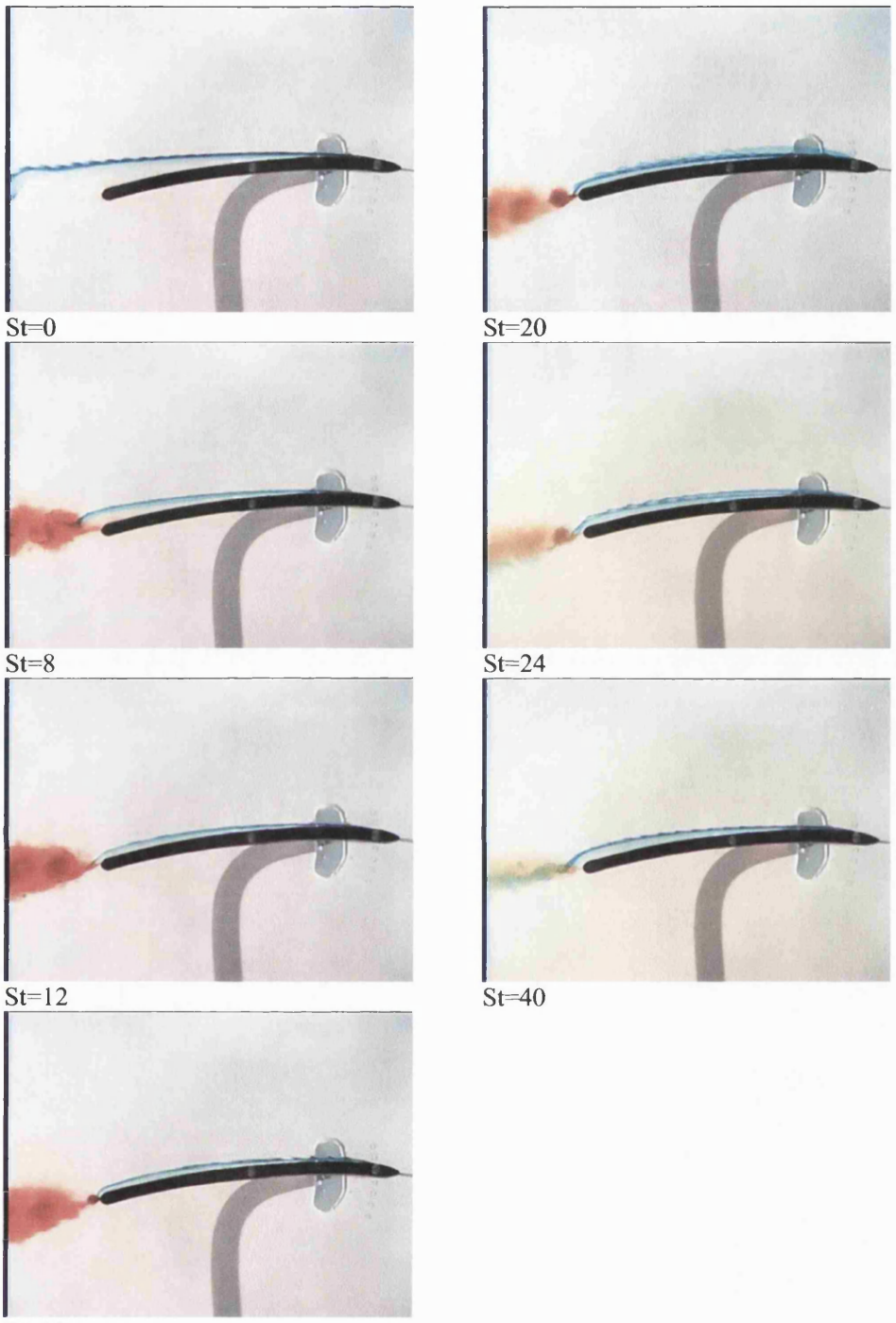

FIGURE 4.8 Re=10,000, $\alpha=5^{o}$, visualization of momentum coefficient and Strouhal frequency effects.

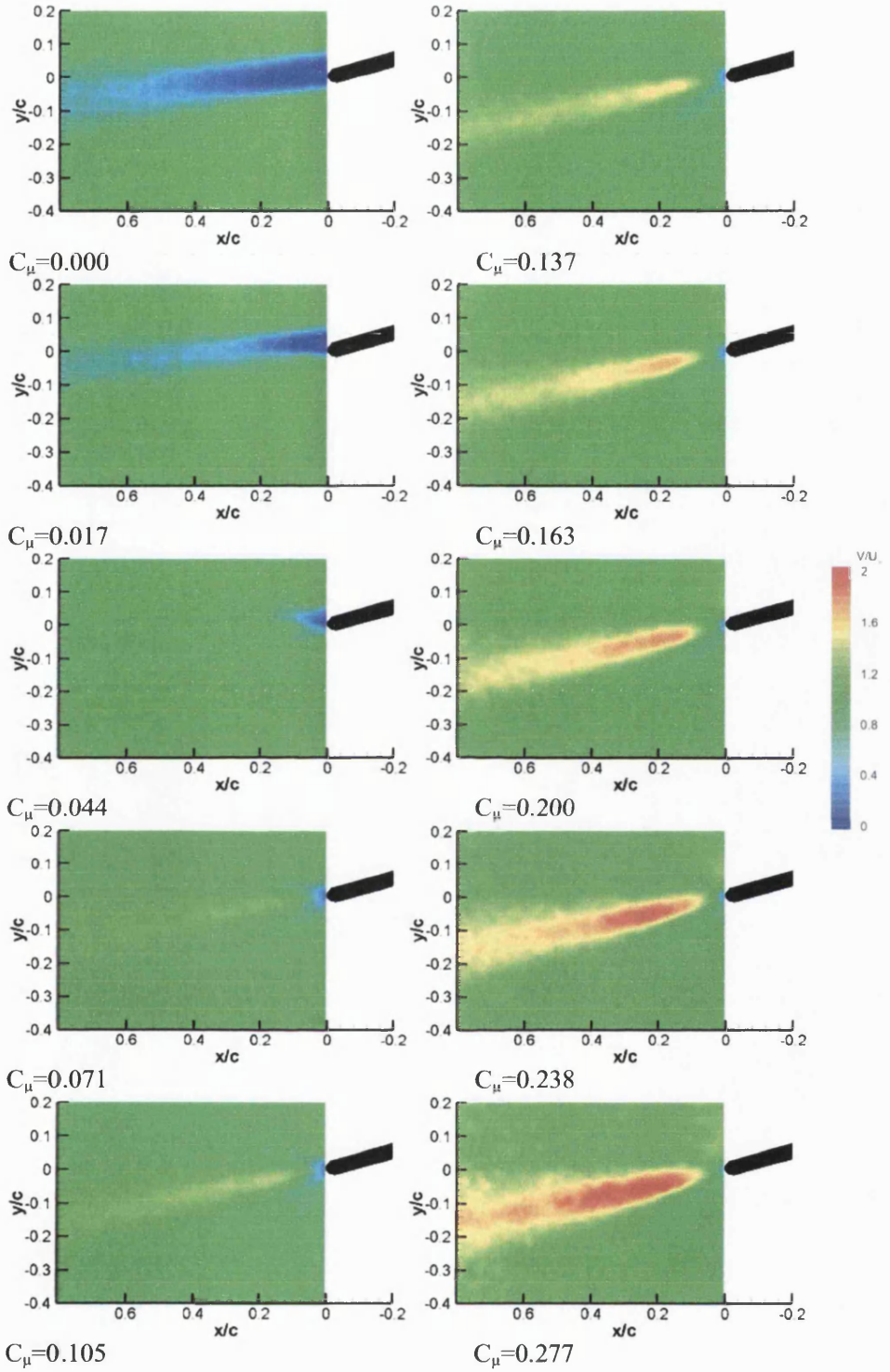

FIGURE 4.9 Velocity magnitudes at Re=10,000, $\alpha=5^o$, St=5.7, from PIV for the cambered aerofoil.

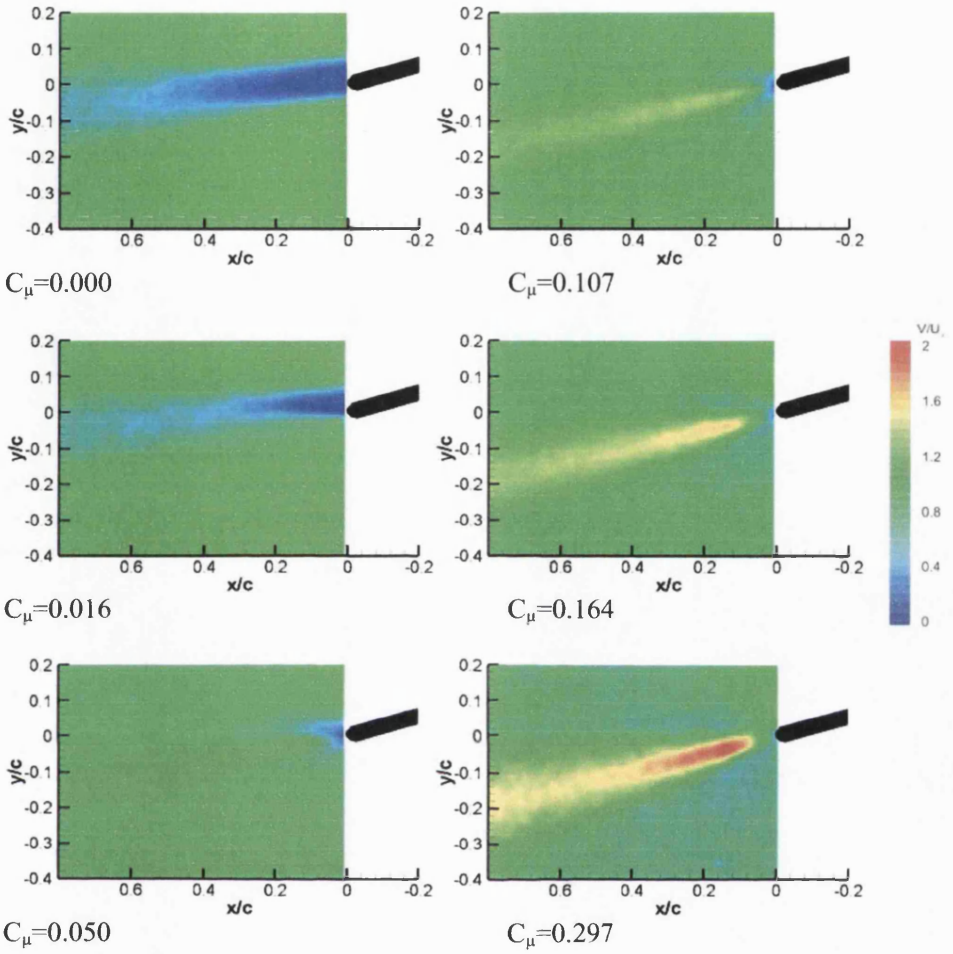

C_μ=0.000 C_μ=0.107

C_μ=0.016 C_μ=0.164

C_μ=0.050 C_μ=0.297

FIGURE 4.10 Velocity magnitudes at Re=10,000, α=5°, St=11.4, from PIV for the cambered aerofoil.

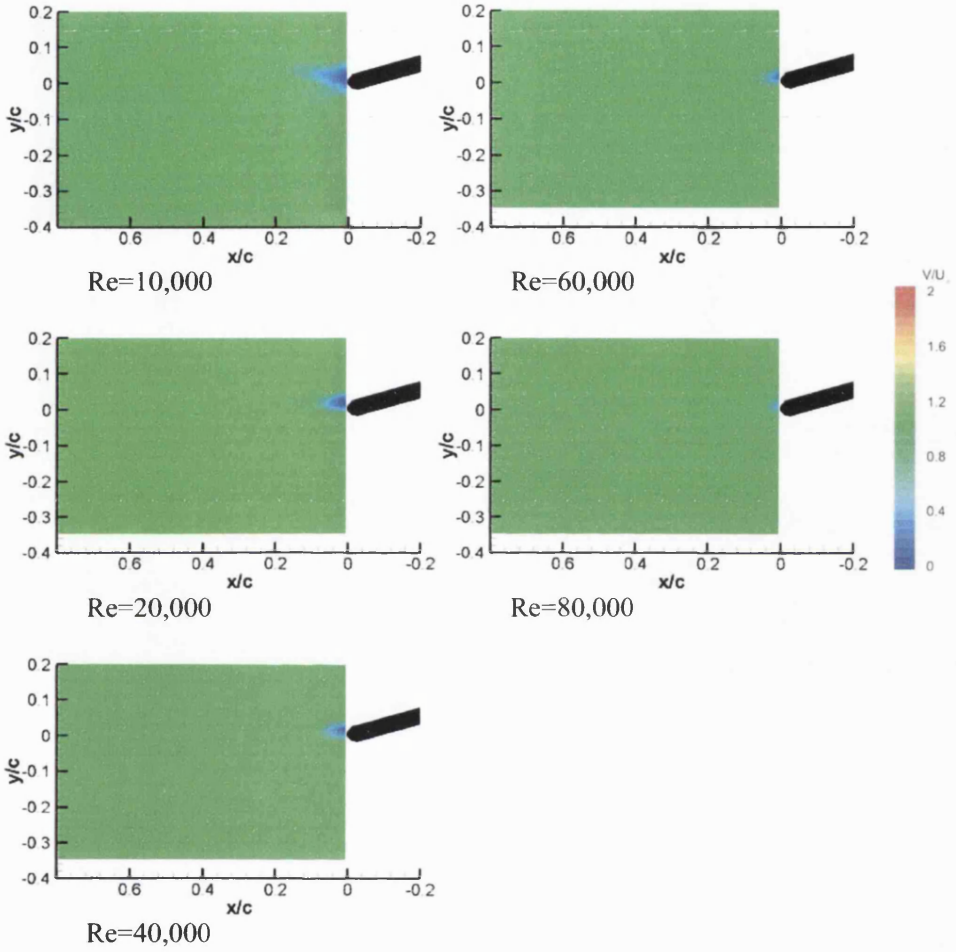

FIGURE 4.11 Velocity magnitude measured by PIV with $\alpha=5^{o}$, St=5.7, $C_{\mu}=0.05$ for the cambered aerofoil.

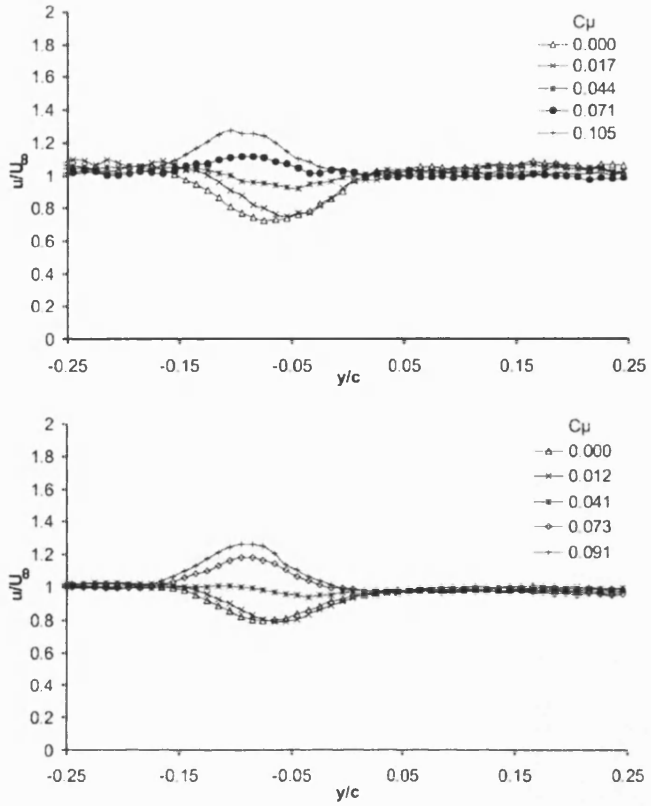

FIGURE 4.12 LDV stream wise mean velocity profiles at x/c=0.5 with Re=10,000 (top) and Re=20,000 (bottom), α=5°, St=5.7 showing effect of momentum coefficient variation for the cambered aerofoil.

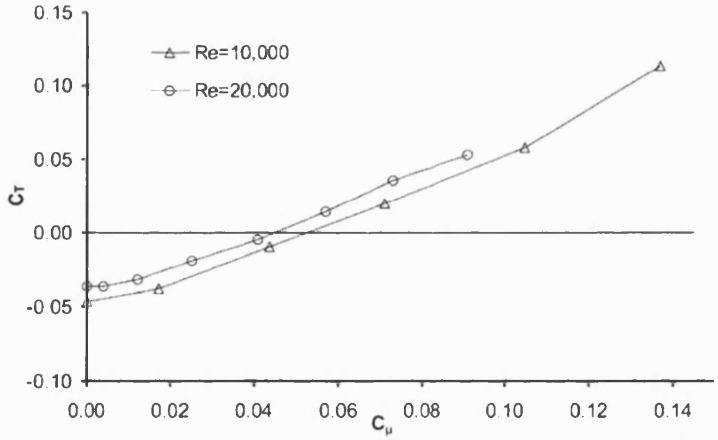

FIGURE 4.13 Variation of thrust coefficient with momentum coefficient at two Reynolds numbers with α=5°, St=5.7 estimated using the LDV wake survey method for the cambered aerofoil.

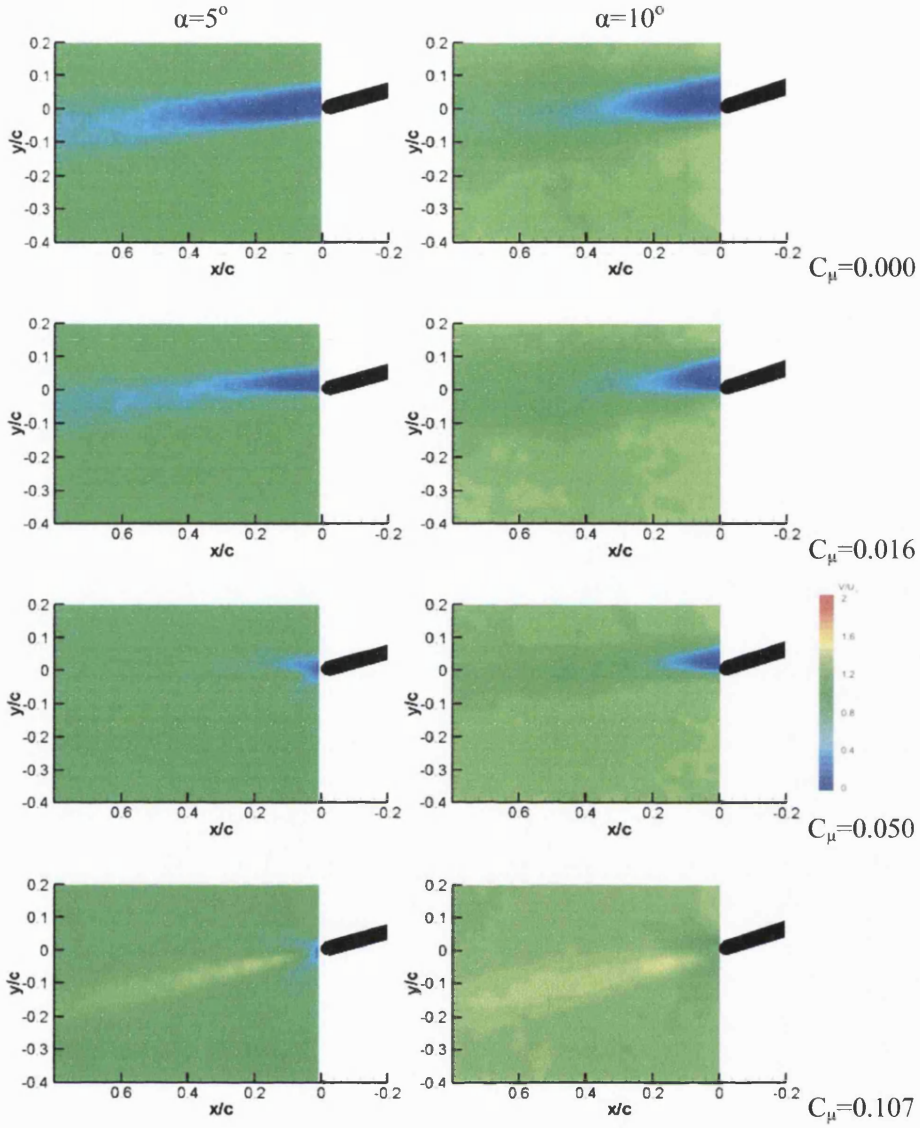

FIGURE 4.14 Velocity magnitude measured y PIV at Re=10,000, St=11.4, with α=5° (left) and α=10° (right) for the cambered aerofoil.

CHAPTER 5 FREQUENCY EFFECTS

In the previous chapter it was noted that higher Strouhal numbers operated at high momentum coefficients gave rise to regions of low velocity above and below the time-averaged jet. In this chapter, the Strouhal number parameter is explored in greater depth in an effort to understand if there are optimum parameter configurations for the system.

FIGURE 5.1 highlights the differences in the wake due to Strouhal number variation. The St=0.0 case is included for reference. With jet excitation at all frequencies, a clear, time-averaged jet is evident in the wake. However, two key features are revealed as the frequency increases.

Perhaps the most striking feature is the gradual increase of the low velocity regions (shown in blue) bounding the jet above and below. At St=34.3, the low velocity regions are very clear and more pronounced above the jet than below. At St=2.9 there is little if any low velocity region bounding the jet. The effect of the increase in frequency is to increase the rate at which the vortex pairs are propagated. The high frequency jet therefore has more frequent vortex pairs, influencing the near wake region of the aerofoil with more circulation than in the low frequency cases. The low frequency jet consists of fewer vortex pairs propagated further downstream due to the long stroke length. The high frequency jet therefore has a more concentrated train of vortex pairs in the near wake giving higher vorticity in the near wake region compared to the low frequency jet. As the vortex pairs roll up against the direction of the freestream, the increased vorticity of the high frequency jet in the near wake causes the slower velocities above and below the jet. Entrainment and vortex roll-up (against the direction of the freestream) does not occur to the same extent in the low frequency conditions.

In addition to the low velocity regions, the time-averaged jets of high excitation frequency appear narrower in width with a slight increase in downward deflection compared to the time-averaged jets of the lower frequencies. The PIV results suggest that the low frequencies of St=2.9 and St=5.7 have a larger region of high velocity (shown in red) than the higher frequency equivalents, and so may cause the aerofoil to experience greater thrust forces at low frequencies. For increasing frequencies from around St=17.1, the difference in time-averaged jet structure appears to be less.

To assess the effect of frequency on estimated thrust coefficients, the LDV wake survey technique was used to provide high-resolution wake velocity surveys. A mean stream-wise velocity survey in the wake at x/c=0.5 shown in FIGURE 5.2 reveals the extent of the variation caused by Strouhal number at constant momentum coefficient. The velocity profile in the wake without jet excitation is added for reference. The lowest frequency, St=0.7, shows a non-symmetric profile in the wake. The maximum velocity occurs around y/c=-0.10, whilst another local maximum, much lower in magnitude, occurs at around y/c=-0.03. The asymmetric profile of the lowest frequency jet would suggest a more complex interaction of the jet with the surrounding fluid. Initially it was thought an interaction with the separated shear layer at the low frequency might yield such a feature in the wake. A clear explanation is provided later in this section. As the frequency is increased to St=5, the width of the jet increases as does the mean peak velocity. The velocity profile changes from a distorted to a more symmetric time-averaged jet-like profile. The distortion in the low frequency profiles, for example with St=0.7 is associated with a lower mean peak velocity compared to that of slightly higher frequencies, like those of St=5. As the frequency is increased beyond St=5, the jet-like wake profiles decrease in both jet width and peak velocity. As the PIV velocity magnitude survey of frequency effect suggested, the minor change in jet profile from St=14.29 to St=17.14 indicates that frequencies above St=17.14 behave with greater similarity.

Estimated thrust coefficients from the wake survey (FIGURE 5.3) for both C_μ=0.12 and C_μ=0.29 show that the relationship between thrust coefficient and Strouhal frequency is irregular. A peak in thrust coefficient is observed around St=2.86 to St=5, corresponding to the largest increases in the wake velocity of these frequencies. Outside

that range, estimated thrust coefficient is appreciably smaller, in some cases less than one quarter of the peak thrust coefficient for high frequencies. The very low frequencies are estimated to yield less thrust for a given momentum coefficient.

The peak associated with the optimum frequency for thrust generation is more pronounced at higher momentum coefficients. Whilst the lower momentum coefficient exhibits a similar range of optimum frequencies, those frequencies either side of that range do not create such a sudden drop in thrust coefficient as the higher momentum coefficient. The effect of the optimum frequency is therefore magnified with increasing stroke length.

On publication [Whitehead and Gursul, 2003, 2004] of the effect of frequency found in the research presented here, researchers suggested that the optimum frequency may occur around the natural shedding frequency of the aerofoil, and the jet was somehow favourably locking in to the shedding to create some favourable performance. Analysis of the PSD in the wake showed that without jet excitation and with $\alpha=5^{\circ}$, the natural shedding frequency of the aerofoil was around St=4 at Re=20,000. However, it should be remembered that with the activation of the jet at sufficiently high momentum coefficients, the fluid dynamics around the aerofoil surface are not separated, oscillating flows, but flows strongly attached at the trailing edge. Flow visualisation showed that the trailing edge attachment feature occurred not only in the time-averaged sense but also in the real-time sense. Under such conditions, there would be no shedding frequency for the jet to lock in to.

Analysis of the power spectrum in the wake for the range of frequencies considered above showed the primary harmonic and reduced higher order harmonics. None of those harmonics were present in the natural case without jet excitation. FIGURE 5.4 shows an example of the PSD for St=0.71. The primary jet frequency is clear and forms the dominant frequency as expected. However, higher order frequencies up to and beyond the fifth order are clearly a feature of the wake. The existence of the higher order frequencies suggests a broader energy content in the wake at the very low frequency. In comparison to St=0.71, St=2.8 shows only a small PSD value for a second order harmonic. The first harmonic, the jet operation frequency, is the only high value PSD in the PSD range shown. Recall that St=2.8 was within the range of optimum frequencies

identified as yielding the highest thrust coefficients. The existence of a single frequency peak in the PSD would suggest a single type of fluid interaction compared to the very low frequency conditions with multiple energy peaks.

An integral function was defined to assist in the study of the spectral content in the wake. The function, denoted I_{PSD}, was the integral of all of the PSD 'spikes' across the entire wake, in essence capturing the energy content across the wake. The I_{PSD} function was used to assess the relative PSD amplitudes in the wake for a range of frequencies of jet operation. FIGURE 5.6 shows the I_{PSD} values plotted against increasing jet frequency for fixed momentum coefficient. The total power of the frequencies in the wake is shown to decrease like St^{-2}. This is in-line with conventional synthetic jet theory [Smith and Swift, 2001, for example]. In addition, the I_{PSD} function shows that there is no particular response at the natural shedding frequency (St=4) of the aerofoil. The I_{PSD} estimates would suggest that the lowest frequencies would offer the optimum performance. Whilst the spectral energy content in the wake decays as expected, it does not explain why low frequency jet operation causes deteriorated performance in terms of the thrust coefficient generated. The I_{PSD} function showed how the high frequency range decreased in spectral content and corresponded to lower thrust coefficient values.

To explore the cause of the variation in low frequency effect on thrust coefficient, experiments were conducted with zero freestream velocity. FIGURE 5.7 shows the thrust coefficients produced by the jet with varying frequency in quiescent flow. The parameters were based on operation at Re=20,000. In line with theory and expectations, as the frequency increases, the thrust coefficient decreases due to less induced velocity. The effect is similar for both high and medium momentum coefficients, although the rate of decay with the higher momentum coefficients is slightly higher than lower momentum coefficients.

Whilst momentum coefficient estimates were made based on techniques used by other researchers, attention was paid to the way in which they were estimated. FIGURE 5.8 shows momentum coefficient as a function of downstream distance for fixed initial momentum coefficients. It can be seen that unlike conventional jets, there is an initial increase in momentum coefficient before it decreases to an asymptotic value, similar to that reported by Smith and Glezer [1998]. They attributed the initial increase in

momentum flux to the existence of stream-wise pressure gradients not present in conventional jets. Whilst that may present an argument that synthetic jet momentum coefficients would be better measured far away from the jet exit in the region of asymptotic values, in this research the conventional measurement technique will be followed. FIGURE 5.8 also shows that the smaller Strouhal frequency jets decrease slower, resulting in larger final momentum fluxes which is consistent with Smith and Swift [2001].

To understand the effect of frequency, experiments with the PIV phase-locked to the driving frequency were performed. FIGURE 5.9 shows the comparative cases for the time-averaged condition without jet excitation. The velocity magnitude plot shows the low velocity region and extent of separation at the trailing edge. Fluctuations in the wake structure were observed over the 50 captures used for the average here. As the phase-locked images were an average of 50 such captures, standard deviation between the 50 captures could be analysed. The corresponding standard deviation contour shows the extent of fluctuations downstream of the trailing edge indicating instabilities in the reference case. The near wake shows stability suggested by the small deviation between the 50 captures. However, the region towards the end of the near wake is seen to deviate up and down from the time-averaged location, exhibiting similar standard deviations in the top and bottom at the end of the near wake.

With the jet in operation, phase-locked measurements were taken as an average of 50 separate phase-locked results to enable representative averaging and to enable standard deviations to be shown, highlighting any variability between cycles. Each jet oscillation was divided into ten equally timed increments with captures taken at the end of each tenth of cycle duration. Therefore the ten captures for each cycle are not equivalent in terms of real time history points as the low frequency cycle takes longer than the higher frequency cycle.

Each phase-locked capture time was accurate to within 10ns of the desired time location in the cycle, which ensured precise locking. FIGURE 5.10 shows the location in the cycle history of the captures. FIGURE 5.11 shows the phase-averaged velocity magnitude contours for three frequencies presented side-by-side in descending chronological order. The three frequencies were chosen with the lowest before the

optimum frequency range, the middle frequency within the optimum frequency range and the high frequency beyond the optimum frequency range. **Error! Reference source not found.** shows the corresponding vorticity contour plots and FIGURE 5.14 shows the corresponding standard deviation in velocity magnitude from the average of the 50 captures.

Due to the larger time delay between captures, the St=0.7 frequency jet propagates the jet outside of the region of interest. The stroke length is long in comparison to the other frequencies, with the highest frequency showing the shortest stroke length indicated by both the velocity magnitude contours and the vorticity contours. Whilst the vortex pairs of the lowest frequency condition are therefore propagated away outside of the field of view, the important differences between the three example frequencies could still be highlighted.

The first five images of each cycle form the blowing part of the cycle. The evolution of the jet out-strokes into the wake are seen in both the velocity magnitude and vorticity contours. In the velocity magnitude contours, the induced velocity and impulse velocity (shown in red) between the jet vortex pairs is bounded by a slow region of velocity (shown in blue) above and below. The slow region is formed as the vortex pairs, highlighted in the vorticity contours, roll back opposing the freestream direction. This suggests the freestream velocity inhibits that vortex roll-up and conversely that the vortex roll-up inhibits the freestream velocity.

At the highest frequency, the vortex pairs are propagated the smallest distance into the wake. The high frequency condition showed the highest vorticity in the field of view. In the time-averaged sense, that would infer that high frequency jet operation led to strong vorticity in the near wake. The concentration of vortex pairs in the near wake associated with such features cause the low velocity region bounding the jet above and below as seen in FIGURE 4.10 and FIGURE 5.1.

Initially, the lower anticlockwise vortex appears to be inhibited in roll-up, propagating slightly further than its clockwise counterpart. This can be seen from both the vorticity and velocity magnitude contours in the first three to four captures of the blowing cycle. Once the vortices have commenced roll-up and become established, the vortex pairs

stabilize and mirror each other about the jet axis more closely. The initial unevenness of the vortex pairs is attributed to the interactions of the fluid velocity gradients around the trailing edge. Freestream velocities on the trailing edge lower surface of an aerofoil are usually higher at positive incidence than those on the upper surface of the aerofoil where loss of momentum is experienced. If the vortex pairs were rolling into an uneven velocity field such as that present around a trailing edge, then it is expected that there would be some variation in vortex roll-up, as observed here. Once the vortex pairs are well established with coherent vortices, stability between the two vortices is observed propagating away at the same rate. The magnitude of the maximum vorticity decays quickly as the vortices are propagated and diffuse into the freestream.

Considering the suction part of the cycle (the last five images of the sequence), there are striking differences between the low and high frequency cases. In all cases the suction cycle causes a region of low velocity in the near wake, as one would expect. In the velocity magnitude contours of the lowest frequency, a large low velocity region (shown in blue) is seen in the wake suggesting the slow suction (associated with the low St=0.71 operation frequency) causes large disruption to the aerodynamics. The low velocity region is many times larger than that seen in the equivalent cycle time with the higher frequencies and indicates an increase in instantaneous drag force under this condition. The nett thrust over one cycle would therefore be lower in comparison to higher jet frequencies without the instantaneous large low velocity regions.

The extent of the low velocity regions caused at the lowest frequency give rise to upper surface disturbance of the aerofoil, particularly towards the end of the suction cycle. The disturbance appears so significant that the attached flow at the trailing edge in most of the PIV captures is not evident towards the end of the suction cycle in the lowest frequency case. Consequently it is clear from the phase locked measurements, that significant disruption to the flow is caused which leads to separation over the upper surface of the aerofoil towards the end of the suction cycle.

The standard deviation contours show the extent of the variation in the wake over the 50 cycles averaged here. Whilst it is expected that each jet impulse would be shown to vary considerably due to the seeding and low resolution of PIV, it was unexpected to find the large fluctuations in the late suction cycle of the lowest frequency. Little variation is

seen in the wake of the other frequencies' suction cycles. The time of the suction part of the cycle is over seven times as long with the St=0.71 jet as the St=5 jet. The extended duration of the low frequency suction causes instability in the wake sufficient to dramatically affect the aerodynamic performance, promoting separation and increased drag. The standard deviation shows that the large low speed region associated with the suction cycle of the lowest frequency, exhibits considerable unsteadiness, often deflected both up and down. The standard deviation contours suggest that the suction cycle undoubtedly causes separation on both the upper and lower surfaces of the aerofoil during its cycle.

Whilst each case produces a time-averaged jet, it is only the very low frequency range considered here that causes large instability in the wake during suction. This undoubtedly contributes to the significantly lower C_T which was found. Choice of a jet operating frequency for maximum thrust coefficient would therefore depend on selection of the lowest frequency sufficient to generate large thrust coefficients, without selection of such a low frequency that would promote instability in the suction cycle. A slow suction cycle causes large low velocity regions in the wake and invokes detrimental unsteadiness causing separation on both the upper and lower surfaces.

The nett result is that whilst there is a larger jet produced at the lowest frequency, the suction cycle is much more drag indicative than the suction cycles of the higher frequencies. It is evidently better to use a weaker jet with corresponding suction cycle that maintains stability in the wake and therefore has better performance over the entire cycle. Whilst the high frequency exhibits great stability, the jet strength is lower than in the other cases, giving a lower nett thrust value than the stronger jets.

5.1 SUMMARY

Experiments explored the effect of jet frequency. It was noticed that a low velocity region bounding the jet above and below accompanied high frequency jets of sufficient momentum. That feature suggested there might be disparity between the thrust coefficients generated by jets of different frequencies. Further investigation found that a specific range of frequencies generating more thrust for a fixed momentum coefficient. It was shown that frequencies in the range $2<St<6$ yield the largest thrust coefficients.

The same effect of frequency was not found when operating the jet in quiescent flow. Instead, the expected decrease in thrust coefficient with increasing frequency was found. That suggested that the optimum frequency range occurred because of external interaction with the external flow around the aerofoil.

Measurements of the PSD in the wake revealed that the very low frequencies created up to fifth order harmonics whilst the optimum frequency range had at most second order higher harmonics evident. An I_{PSD} function was used to show an estimated spectral energy content downstream of the jet, which summarised the decay of spectral energy with increasing frequency. However, it did not give a good account of why the lower frequencies were associated with a considerable drop in jet performance.

Analysis of phase-locked PIV measurements of the near wake revealed the mechanism involved with the lowest frequency ranges. The range of frequencies tested was seen to produce a strong jet-like pulse in the wake with stroke length decreasing with increasing frequency. At very low frequencies, the slow suction part of the cycle causes large low velocity instability and variation in the wake whilst the higher frequencies maintain a much smaller velocity deficit during suction. In the time-averaged sense, whilst the lowest frequency jet produced the stronger impulse, the contributions of the large, drag indicative low velocity region amounted to detrimental performance compared to a higher frequency jet offering greater stability during the suction part of the cycle.

5.2 FGURES

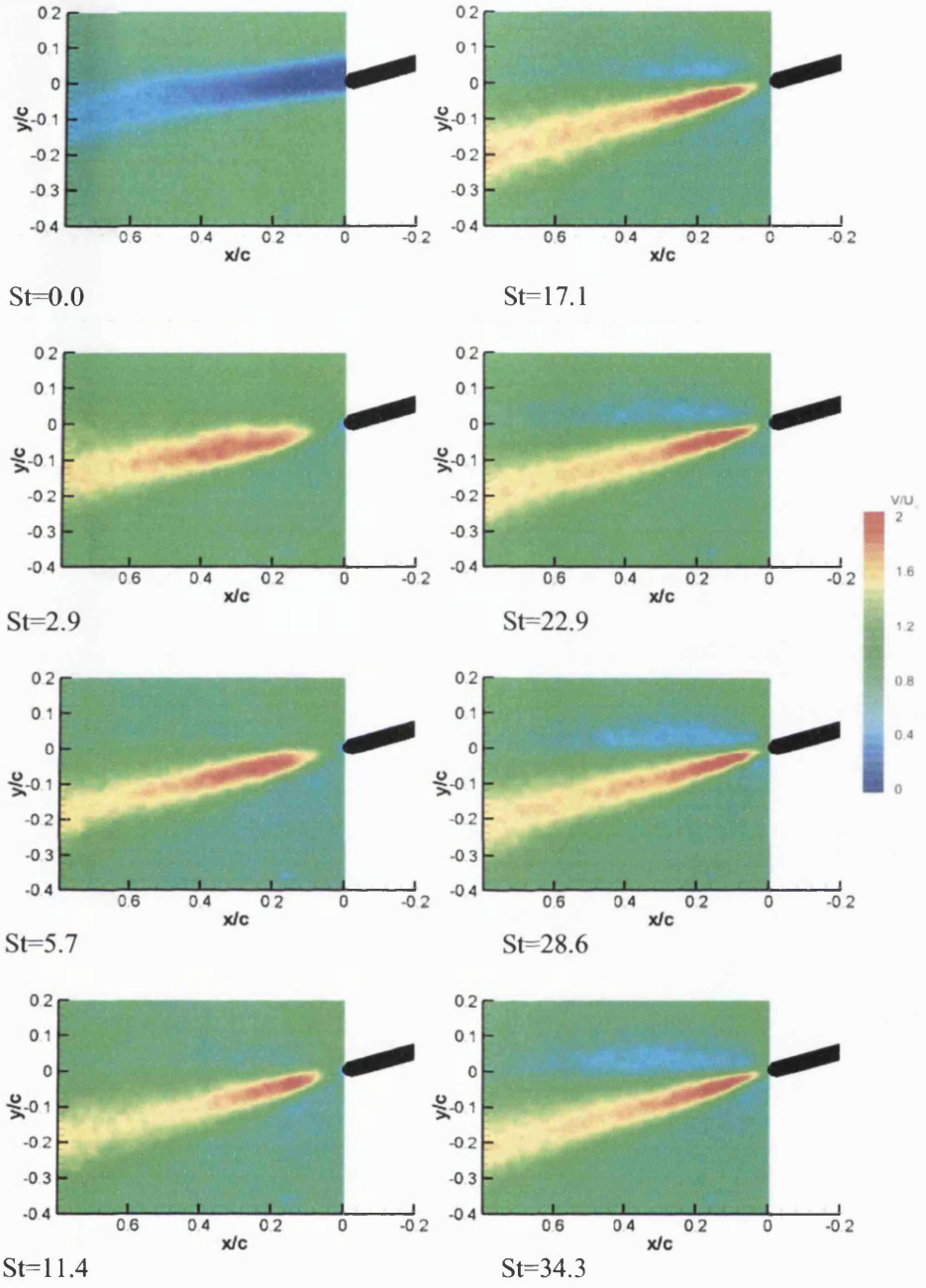

FIGURE 5.1 Time-averaged velocity magnitude contours from PIV showing variation due to Strouhal frequency at Re=10,000, $\alpha=5^{\circ}$ and $C_{\mu}=0.300$.

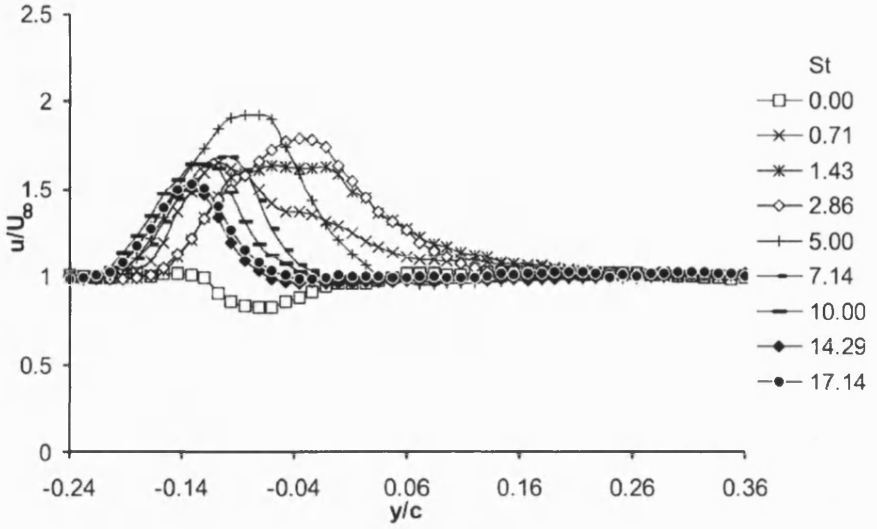

FIGURE 5.2 Mean streamwise velocity profiles measured using LDV with Re=20,000, $\alpha=5^{\circ}$ and $C_{\mu}=0.29$ at x/c=0.5.

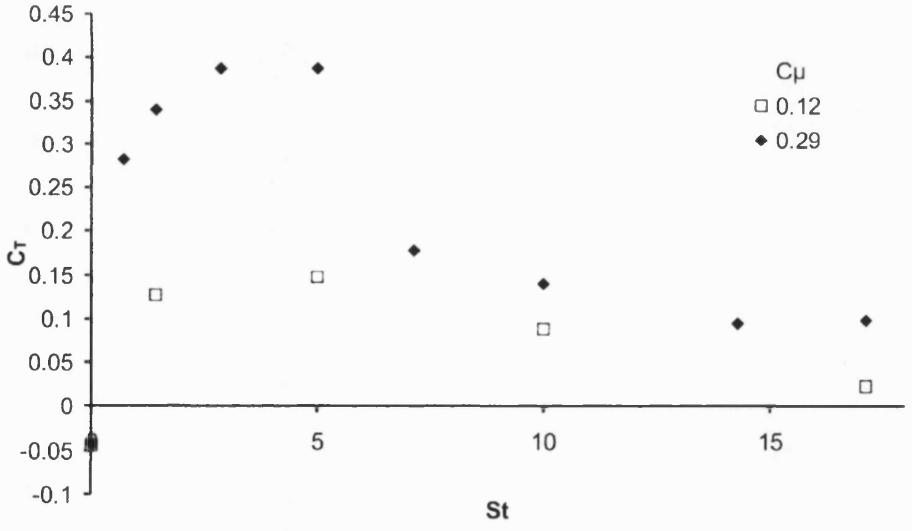

FIGURE 5.3 Thrust coefficient estimates for two momentum coefficients over a range of Strouhal frequencies with Re=20,000, $\alpha=5^{\circ}$.

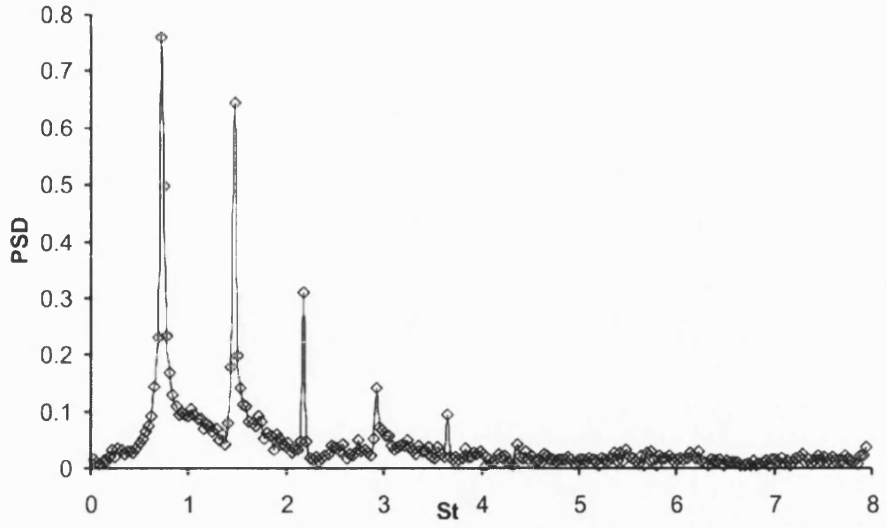

FIGURE 5.4 PSD measured using LDV at x/c=0.5, y/c=0, for St=0.71 at Re=20,000, $\alpha=5^{o}$ and $C_{\mu}=0.29$.

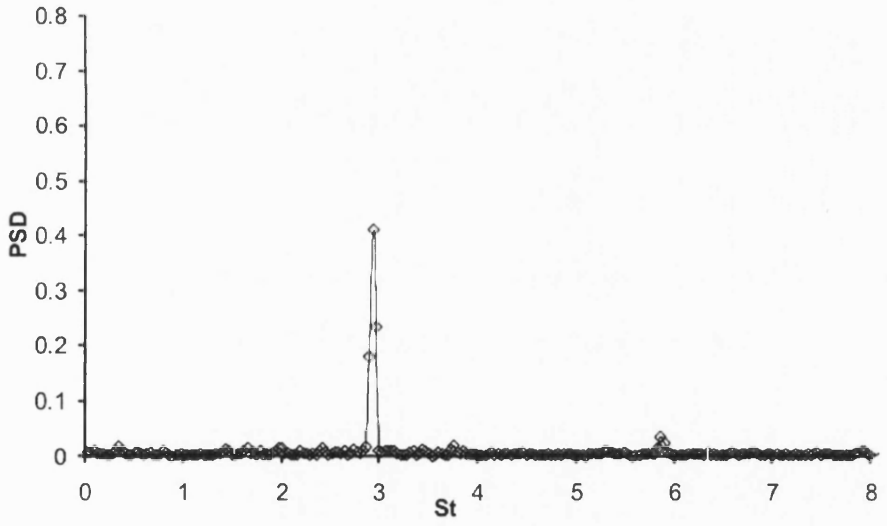

FIGURE 5.5 PSD measured using LDV at x/c=0.5, y/c=0, for St=2.8 at Re=20,000, $\alpha=5^{o}$ and $C_{\mu}=0.29$.

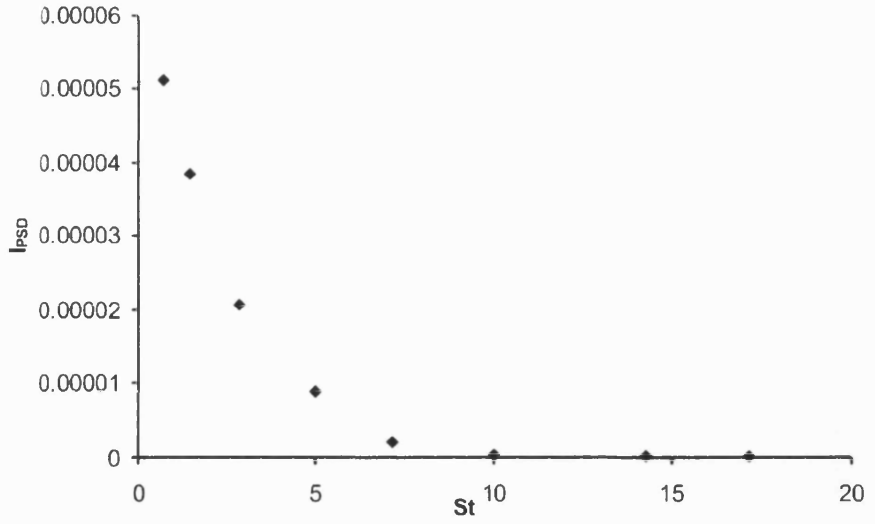

FIGURE 5.6 I_{PSD} variation with frequency at Re=20,000, $\alpha=5^{o}$ and $C_{\mu}=0.29$, measured at x/c=0.5

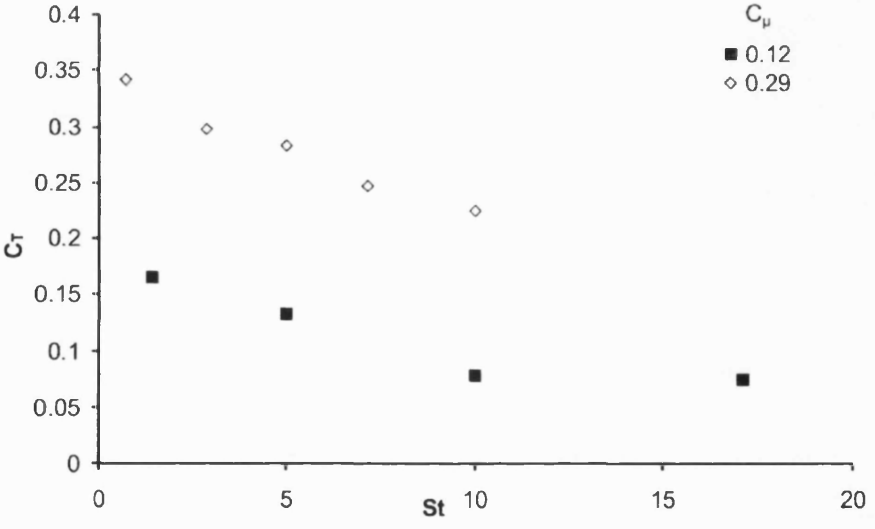

FIGURE 5.7 Variation of thrust coefficient (measured at x/c=0.5) with increasing frequency at zero freestream velocity (C_{μ}, C_T, St based on Re=20,000).

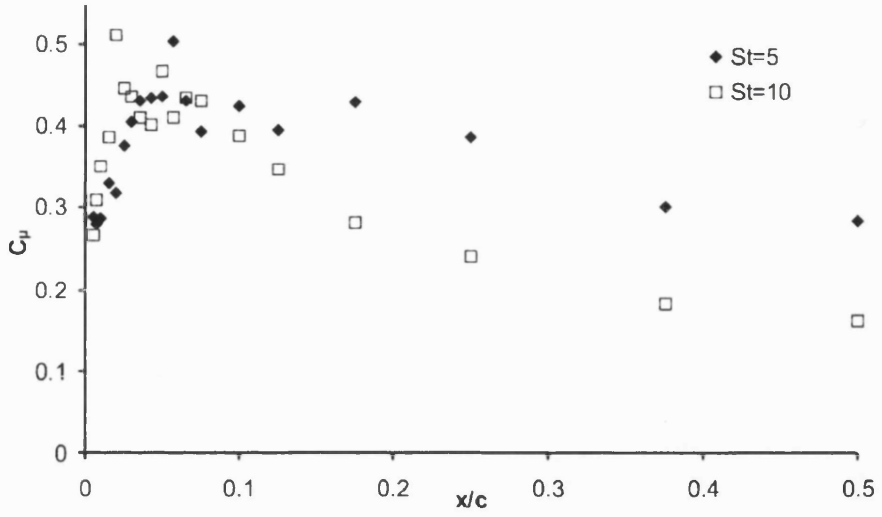

FIGURE 5.8 Variation of momentum coefficient (measured at x/c=0.5) with increasing stream wise distance for C_μ=0.29 at x/c=0.005 at zero freestream velocity (parameters based on Re=20,000).

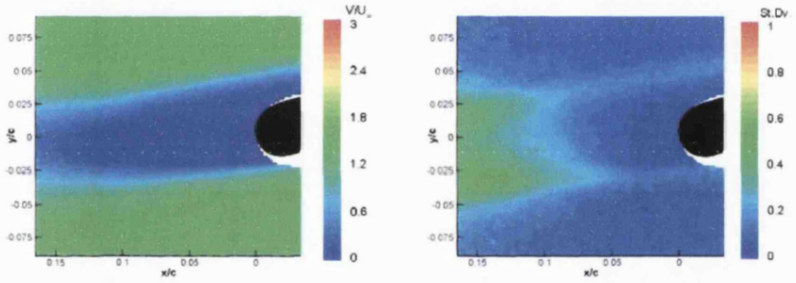

FIGURE 5.9 PIV velocity magnitude (left) and standard deviation (right) contours at Re=20,000, $\alpha=5^o$ without jet excitation (C_μ=0).

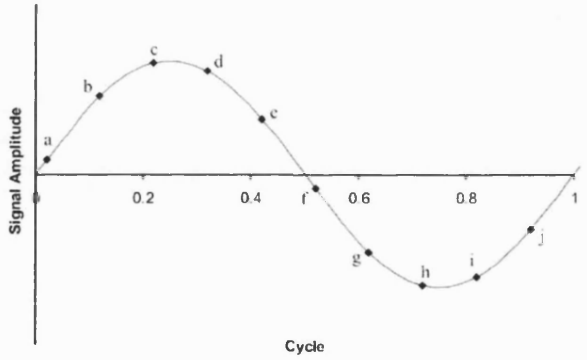

FIGURE 5.10 Plot representing approximate locations in time of 10 phase-locked captures over one jet cycle oscillation cycle.

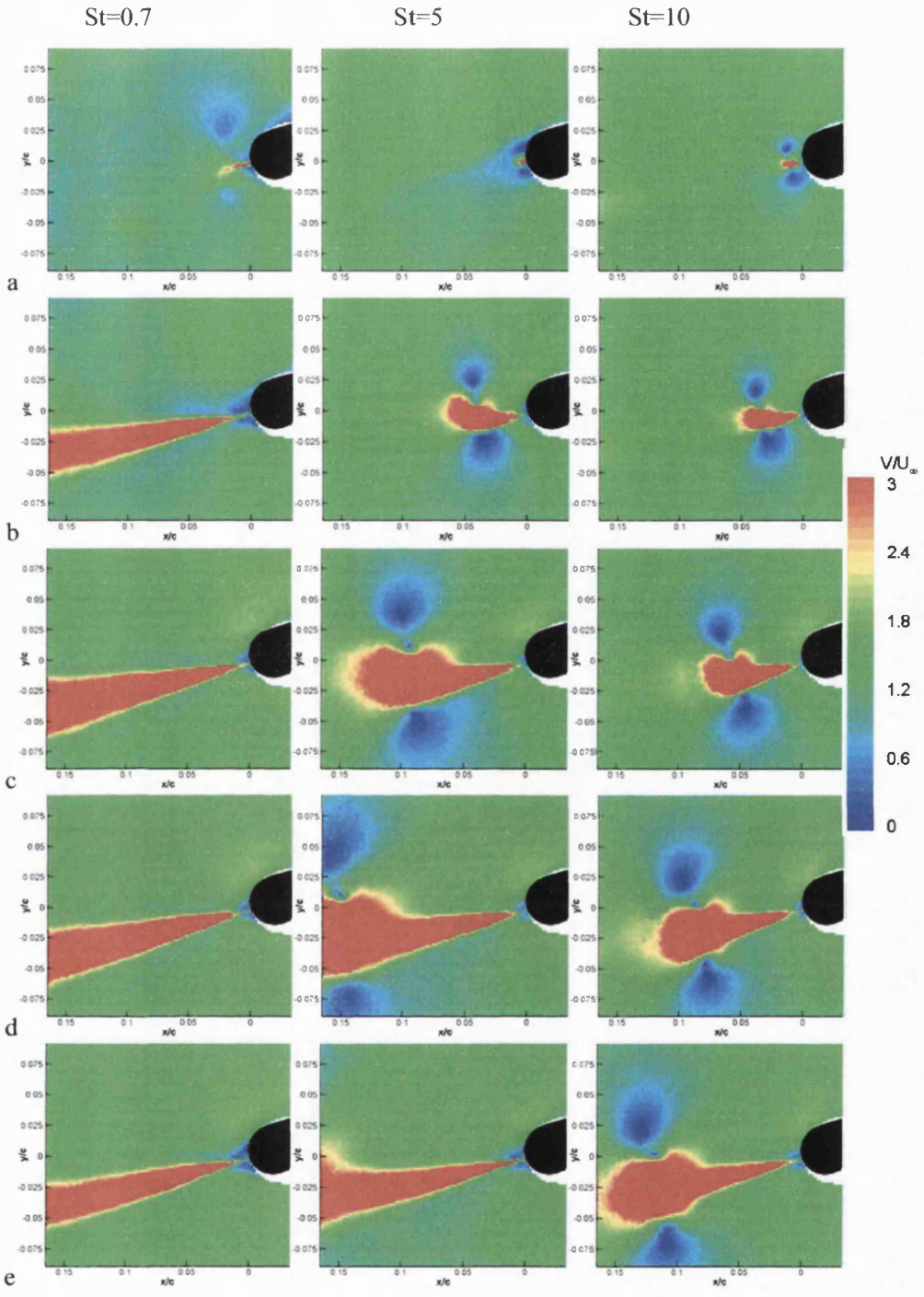

FIGURE 5.11 Phase-averaged velocity magnitude contours at Re=20,000, α=5° and C_μ=0.29 (continued over).

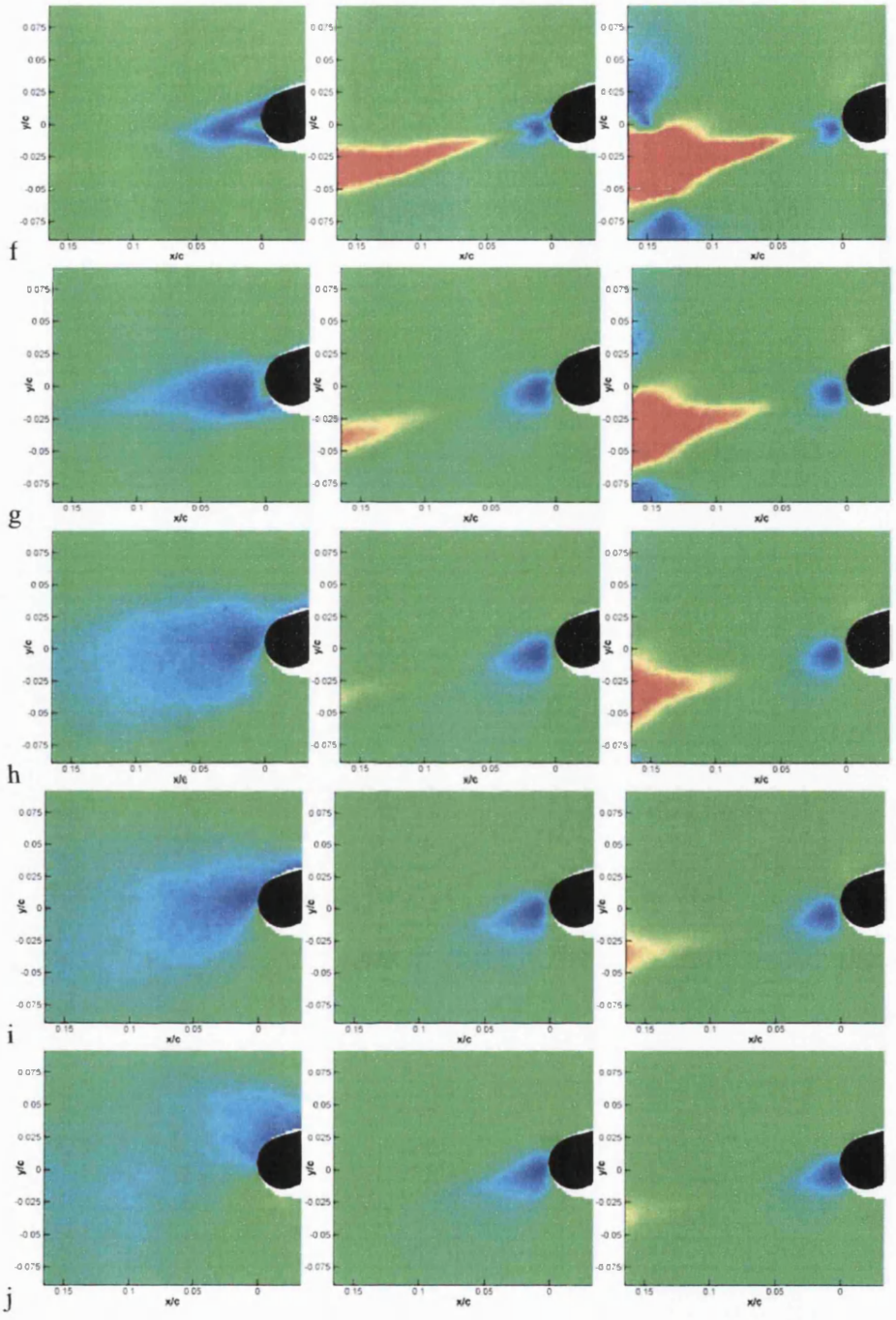

FIGURE 5.12 (Continued).

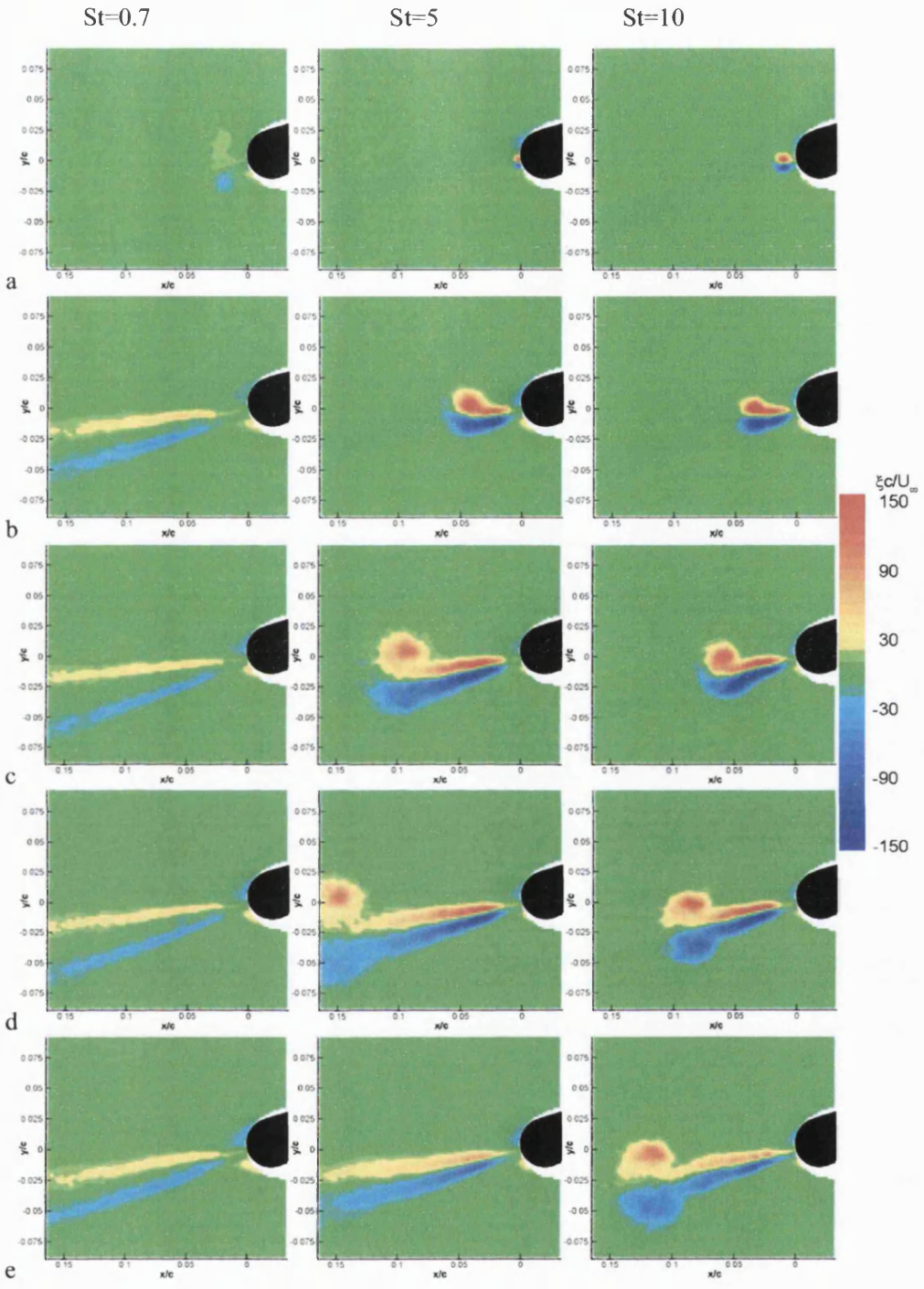

FIGURE 5.13 Phase-averaged vorticity contours at Re=20,000, $\alpha=5^{o}$ and $C_{\mu}=0.29$ (Continued over).

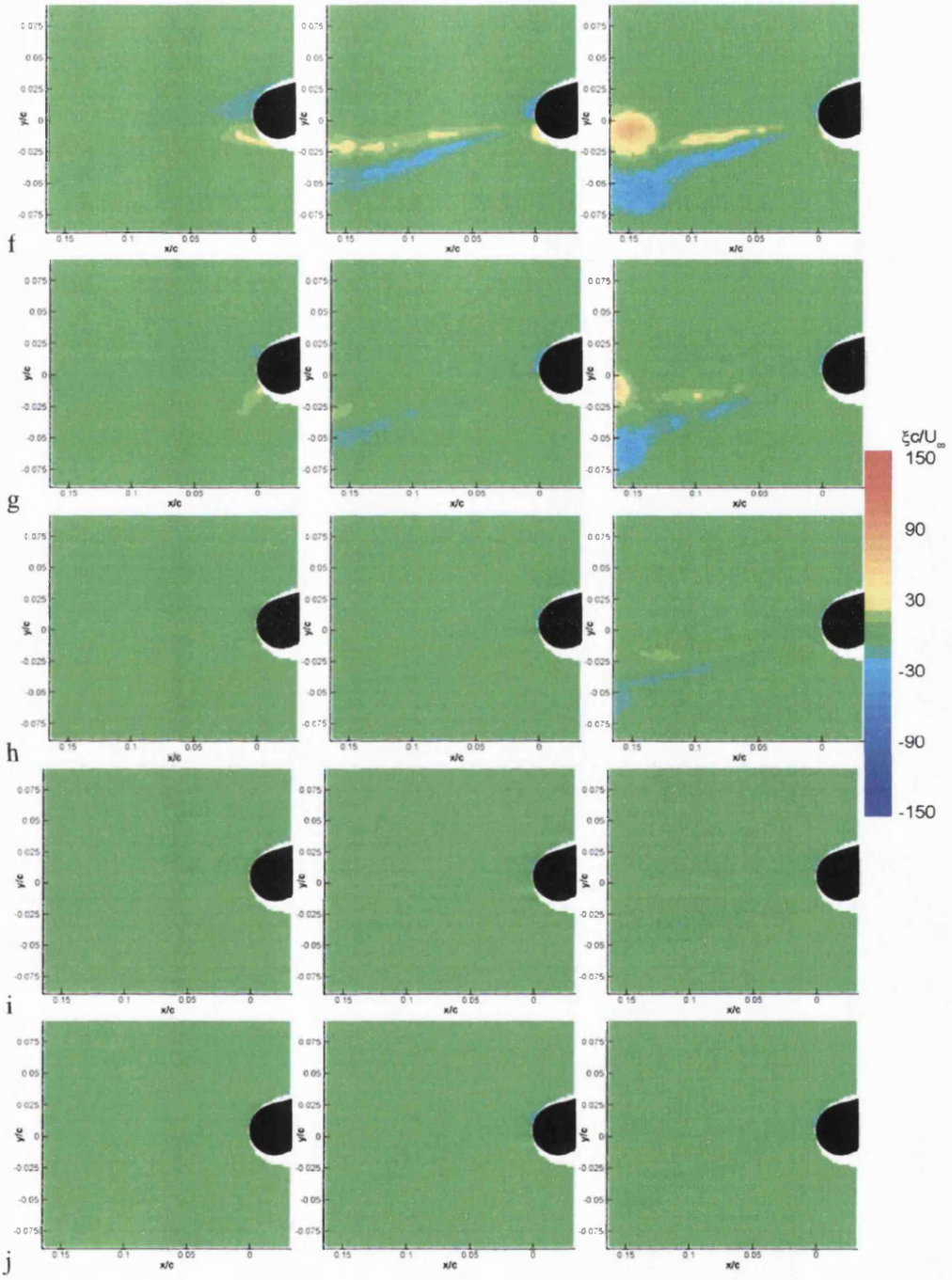

(Continued).

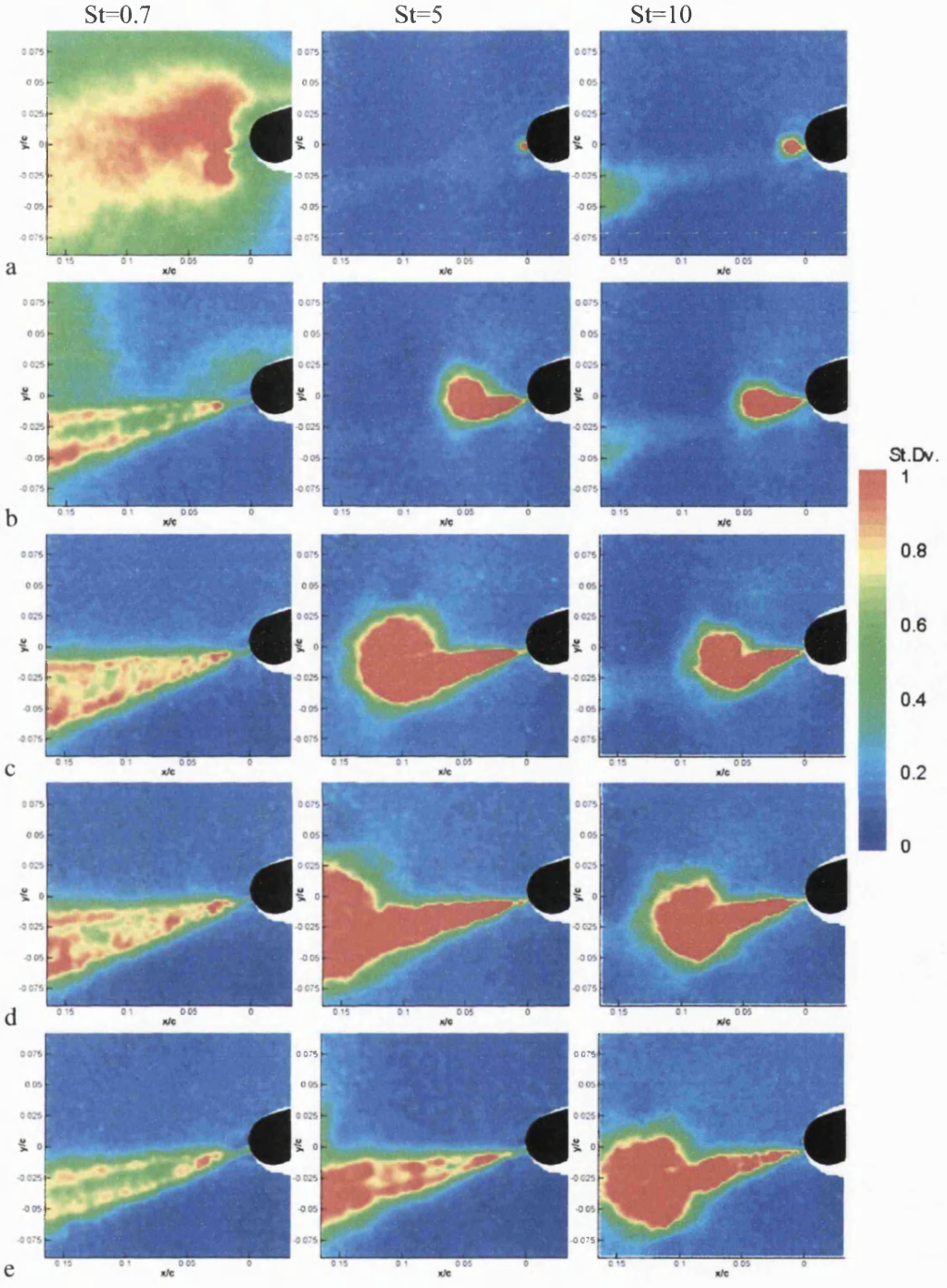

FIGURE 5.14 Standard deviation contours from 50 phase-locked cycles at Re=20,000, $\alpha=5^{o}$ and $C_{\mu}=0.29$ (Continued over).

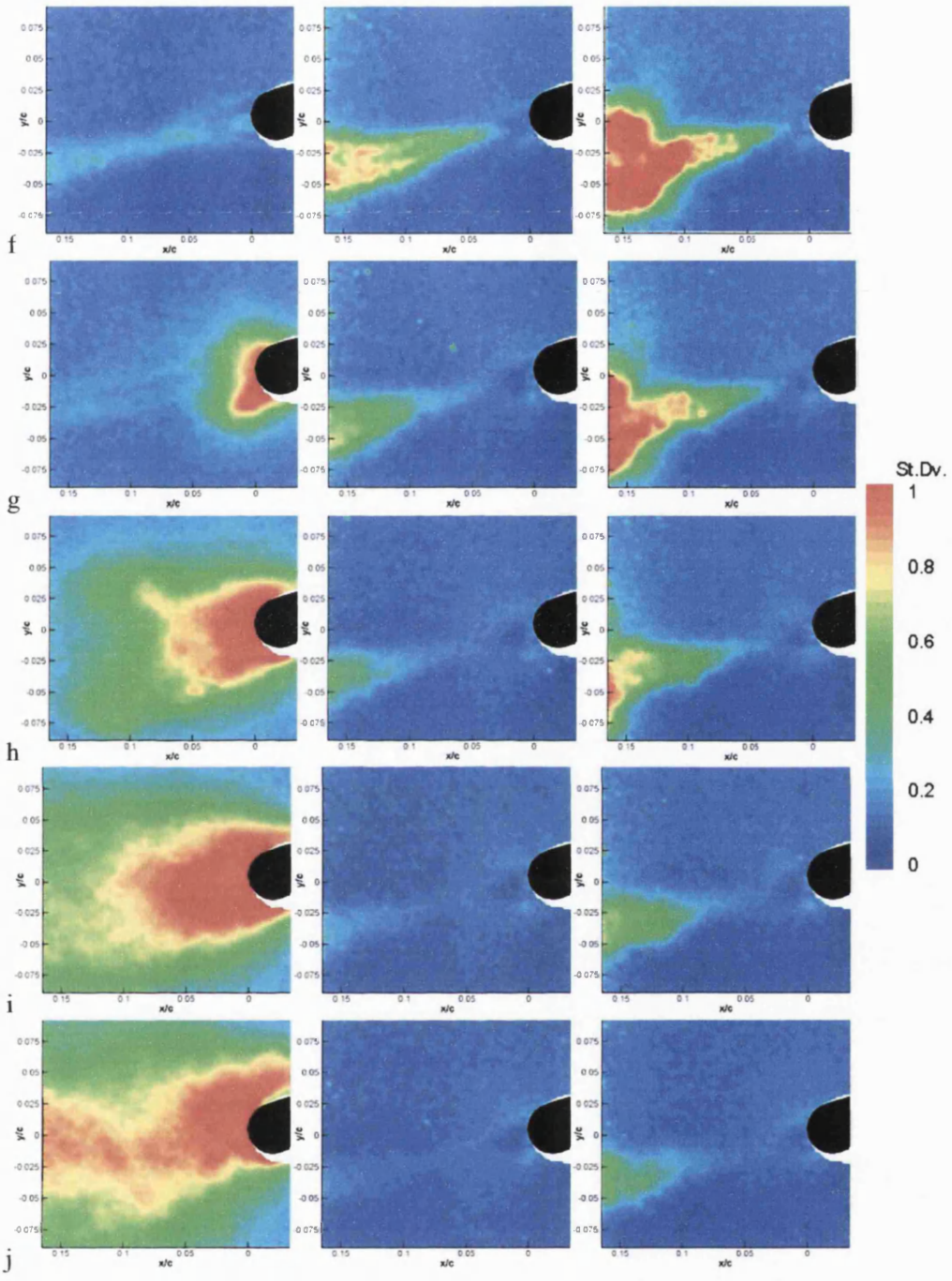

(Continued)

CHAPTER 6 PRESSURE MEASUREMENTS

This chapter presents the results from the pressure measurement system capable of measuring surface pressures for the cambered wing in the range Re=20,000-60,000. Surface pressures were used to estimate lift and thrust forces. In addition, propulsive efficiency was estimated in conjunction to measuring the power consumption of the speaker-powered synthetic jet. The overall aerodynamic performance was considered, as were combinations of propulsive efficiency and aerodynamic coefficients to assess the entire system.

6.1 SURFACE PRESSURE ANALYSIS

Surface pressure measurements were taken for Reynolds numbers 20,000-60,000 for low and high incidence for a range of momentum coefficients. As the pressure-tapped wing contained tubes and fixing epoxy, the wing cavity was smaller and slightly more constrained than the original wing. The additional constraint, coupled with the resistance of the slot to the motion of the actuation system, meant that sufficient momentum coefficients could not be achieved with the 0.5mm slot. To achieve sufficient jet exit velocity, the jet slot height had to be increased from h/c=0.0025 (0.5mm) to h/c=0.0075 (1.5mm). The momentum coefficient was limited to 0.070 at the highest Reynolds number tested owing to limitations in the driving system. The jet frequency was fixed at St=2.86, close to the optimum values of frequency cited in the previous chapter.

Interpretation of the surface pressure coefficient distributions was undertaken consistent with that of Muller [1985] and others. Mueller showed how plateaus in the pressure

coefficient around the upper surface leading edge corresponded to laminar separation bubble effects. The subsequent increase in pressure coefficient corresponded to transition with a secondary increase attributed to a turbulent reattachment.

6.1.1 REYNOLDS NUMBER 20,000

Surface pressure coefficients are shown in FIGURE 6.1 to FIGURE 6.4. Whilst Re=20,000 was the slowest freestream condition that could have surface pressure measurements measured, key features were still highlighted. The surface pressure distributions are smooth considering the very low range of pressure measurement required.

At $\alpha = 0^{\circ}$ and $\alpha = 5^{\circ}$ the small pressure difference between the upper and lower surfaces suggests only small lift coefficients might be generated at Re=20,000. At low incidence, the surface pressure distribution suggests detached flow, separating around the last half of chord as indicated by the increasing pressure gradient in that region. According to Mueller [1985], the separation bubble may even extend into the wake. The effect of activating the jet at a momentum coefficient of C_{μ}=0.220 is to greatly decrease the pressure gradient in that region, suggesting that the flow separation is reduced. At the very least it suggests an increase in lift coefficient. The effect of the jet in invoking reattachment at the trailing edge is confirmed by both PIV and flow visualisation in the previous chapters. The pressure coefficients around the leading edge upper surface are also slightly decreased upon jet excitation indicating accelerated flow. Note also that the addition of the jet causes the trailing edge pressure coefficients to decrease similarly on the upper and lower surfaces. The surface pressures give a good visual indication that the jet excitation can cause a substantial gain in the pressure difference between the upper and lower surface, suggesting an increase in lift coefficient would be experienced under those conditions.

At $\alpha = 10^{\circ}$, the surface pressure coefficients vary significantly from those at a lower incidence. The classic features of a low Reynolds number aerofoil with an upper surface laminar separation bubble are present, in agreement with Mueller [1985]. Both with and without jet excitation, the first 20% (x/c = -1 to x/c = -0.8) of the aerofoil suggests a separated laminar shear layer in nature indicated by the plateau in pressure coefficient variation. This feature was highlighted in the early flow visualisation. The sudden

increase in pressure coefficient suggests the transition to turbulence downstream of that point. As the surface pressures increases from around x/c = -0.5 towards the trailing edge, it is likely that the turbulent region is also separated over the remainder of the aerofoil at this incidence, as confirmed by the dye flow visualisation. The pressure difference between the upper and lower surfaces is substantially greater than the difference observed at the lower incidences.

With the activation of the jet several effects on the surface pressures are noted. The leading edge surface pressures are decreased by around 25% for a momentum coefficient of C_μ=0.220. That suggests enhanced upper surface flow conditions with an increase in the leading edge velocity. Whilst the separated laminar layer from the leading edge and the transition point appear geometrically similar, the downstream surface pressure coefficients from x/c=-0.5 no longer decrease or recover and are maintained at approximately Cp=-1.15 over the remainder of the aerofoil. The jet has significantly changed the pressure gradient over the entire aerofoil suggesting the extent of the separation is greatly reduced upon jet excitation, as shown by the flow visualisation. As with the lower incidences, the jet has caused a significant increase in the pressure difference between upper and lower surfaces compared to the aerofoil without jet excitation. A significant increase in lift coefficient is expected with the jet operated at C_μ=0.220. It is also noted that the jet decreases both the lower and upper surface trailing edge pressures. Generation of the optimum lift coefficient would favour the lower trailing edge pressures to be increased and the upper surface trailing edge pressures to be decreased. The suggestion is therefore made that alternative slot geometries might have more favourable effect on the upper surface than the lower surface. The influence of the slot geometry is discussed in section 6.4.

Similar features occur in the surface pressure distributions at $\alpha = 15^\circ$ compared to those of $\alpha = 10^\circ$, although the laminar region appears slightly shorter at the higher incidence. As the surface pressure magnitudes are slightly reduced compared to those of the $\alpha = 10^\circ$ incidence, the aerofoil may be experiencing a loss of lift and approaching the stall region. Once again though, the activation of the jet is seen to affect most of the upper aerofoil surface. The surface pressures suggest enhanced performance around the leading edge and towards the rear of the aerofoil contributing to a significant decrease of pressure coefficient in those regions. Control of the surface pressures of an aerofoil is

sometimes called virtual aerofoil or virtual aerodynamic shaping [Patel *et al*, 2003, for instance] and is a mechanism of obtaining a pressure distribution of an aerofoil whilst using an aerofoil having another pressure distribution in the natural case. Usually the term is applied to aerofoil surface pressure modifications through flow control, not through the use of a propulsion device as researched here.

Most of the influence of the jet appears to be around the trailing edge region, especially on the upper surface. Studying the effect of momentum coefficient on surface pressure coefficients at the trailing edge of the aerofoil, as shown in FIGURE 6.5 and FIGURE 6.6, shows a reduction of both upper and lower surface trailing edge pressure coefficients with increasing momentum coefficient of the jet. However, for momentum coefficients larger than around C_μ=0.12, the surface pressure on the lower surface trailing edge changes little whilst the surface pressure on the upper surface trailing edge increases faster with increasing momentum coefficient for C_μ>0.12.

This effect could be attributed to the difference in operating the jet at low momentum coefficients insufficient to cause reattachment at the trailing edge, as opposed to operating the jet causing reattachment at the trailing edge. Operating the jet at low momentum coefficients insufficient to cause trailing edge reattachment would alter the upper surface pressures little as the separated shear layer is away from the influence of the jet exit. Once reattachment at the trailing edge is achieved, the shear layer is then within the influence of changes in the jet condition – including further increase in momentum coefficient. Increasing the momentum coefficient in the range tested continues to cause a decrease in the pressure coefficients of the upper surface trailing edge. In other words, no plateau in the performance of the jet has been found inside the range of momentum coefficients tested.

6.1.2 REYNOLDS NUMBER 40,000

Use of the pressure measurement system at Re=40,000 produces even smoother surface pressure measurements due to the higher associated pressures as shown in FIGURE 6.7 to FIGURE 6.10. Similar features to those noted previously at Re=20,000 are found in the Re=40,000 experiments. Again, at low incidence, the pressure coefficient distributions suggest separation over the last one third of the aerofoil. The absence of a leading edge plateau in the pressure distribution indicates that a laminar separation

bubble is not present at this low incidence at Re=40,000. In comparison with the Re=20,000 low incidence pressure distributions, the Re=40,000, $\alpha = 0^{\circ}$ and $\alpha = 5^{\circ}$ generate larger pressure differences between the upper and lower surface. The increase in pressure difference is expected to contribute to slightly improved lift coefficients at Re=40,000 compared to Re=20,000. The activation of the jet causes significant pressure coefficient decrease over the entire aerofoil surface although more pronounced at the trailing edge. The pressure distribution suggests that the jet causes flow acceleration over the upper surface and reattachment of flow at the trailing edge.

Increasing the angle of attack to $\alpha = 10^{\circ}$ and $\alpha = 15^{\circ}$ produces the leading edge pressure plateau indicative of a laminar separation bubble, transitioning within the first 20% of the chord length from the leading edge. The laminar layer separates from the leading edge and diffuses, becoming turbulent. As with the Re=20,000 condition, the $\alpha = 15^{\circ}$ incidence shows characteristics of an aerofoil approaching stall with a considerably increasing pressure gradient over most of the aerofoil surface.

Activation of the jet decreases the surface pressures over the entire aerofoil at the given momentum coefficient; the jet is again seen to influence the surface pressures at the leading edge. The leading edge pressure decrease suggests an increase in velocity of the shear layer caused by the jet. The decrease in pressure coefficient at the leading edge is seen to be approximately constant over the entire aerofoil surface except for the trailing edge where the jet is seen to have greater influence. Once again, it is noted that the jet decreases surface pressures on both the upper and lower surfaces at the trailing edge.

Even at these higher incidences, the jet inhibits the surface pressures recovering to lower pressure coefficients, accelerating the flow near the trailing edge of the aerofoil compared to the baseline condition without jet excitation. The change in surface pressure indicates an improved aerodynamic performance caused by the jet, decreasing the separation. A decrease in drag and increase in lift is expected.

Analysis of the trailing edge surface pressure variation with increasing momentum coefficient shows similar features to the Re=20,000 condition. Whilst the lower surface pressure initially increases then stabilises with increasing momentum coefficient, the upper surface initially fluctuates within a small range before increasing for larger

momentum coefficients. Recall from the Re=20,000 conditions, that for $C_\mu<0.12$, the lower surface trailing edge pressures were influenced more than the upper surface trailing edge pressures. The contrary was true for $C_\mu>0.12$ at Re=20,000. Whilst the momentum coefficient changing the behaviour seen with the Re=20,000 condition was estimated to be around $C_\mu=0.12$, at Re=40,000 that momentum coefficient was estimated to be around $C_\mu=0.07$. Whilst the effect of the momentum coefficient increase is similar, the different momentum coefficients of $C_\mu=0.12$ and $C_\mu=0.07$ therefore suggests that reattachment at the trailing edge may occur earlier in the momentum coefficient range at Re=40,000. Recall that the variation in the influence of momentum coefficient at the trailing edge over the upper and lower surfaces was attributed to whether or not the trailing edge was experiencing attached or separated flow. Separated flow was further away from the influence of the trailing edge jet. The smaller momentum coefficient identified at Re=40,000 would therefore imply that a smaller momentum coefficient was necessary to achieve reattachment at the trailing edge. As higher Reynolds numbers behave more favourably than lower Reynolds numbers and the effect of Reynolds number was shown to persist throughout the momentum coefficient range in section 4.4, it would be sensible to suggest that separation is less at the higher Reynolds number case, requiring less momentum injection to control.

It is expected that the variation of upper and lower surface trailing edge behaviour over the momentum coefficient range may cause a non-linear variation in lift coefficient with the momentum coefficient range tested here. A momentum coefficient may exist inside the range tested that gives the largest pressure difference over the upper and lower surfaces and therefore generates most lift.

6.1.3 REYNOLDS NUMBER 60,000

In the low Reynolds number range, it is expected and has been shown that aerodynamic performance increases with increasing Reynolds number. FIGURE 6.13 to FIGURE 6.16 show the surface pressure measurements for the four incidences studied at Re=60,000. At Re=60,000, the surface pressure distribution shows a greater difference between upper and lower surface pressures over a larger proportion of the aerofoil surface than was observed with Re=20,000 or Re=40,000 conditions. A larger pressure difference indicates an improvement in lift coefficient generation by the aerofoil. The

larger pressure differences persist throughout the range of incidences tested, as one would expect in the more favourable conditions.

Even at the higher Reynolds number, and with a reduced momentum coefficient of 0.07, activation of the jet causes significant changes in the surface pressure distributions over the aerofoil. At Re=20,000 and Re=40,000, experiments showed that for small momentum coefficient, the lower surface pressures at the trailing edge decreased quickly whilst the upper surface trailing edge pressures changed little. As a momentum coefficient of C_μ=0.07 was the maximum achievable at Re=60,000, comparison is drawn to the low momentum coefficient effects at the trailing edge.

The trend is similar for the four angles of attack tested. Surface pressures show how the lower trailing edge pressure coefficients are decreased more than the upper surface pressure coefficients. For all four of the incidences tested here, the lower surface pressure decreases to values below the upper surface pressure at the trailing edge upon jet excitation of C_μ=0.07. Therefore it is expected that for C_μ=0.07, the jet causes the aerofoil to experience a loss of lift compared to the conventional aerofoil without jet excitation.

Little variation is seen in the upper surface pressure coefficients when activating the jet at C_μ=0.07. The greatest variation in upper surface pressure coefficient upon jet excitation is found at $\alpha = 10^\circ$, although $\alpha = 15^\circ$ also shows a significant decrease in pressures around the leading edge.

The decrease in lower surface pressure around the trailing edge is expected to lead to a decrease in lift coefficient compared to the baseline 'no jet' aerofoil. As there is only small variation in surface pressure over the upper surface, little decrease in drag is expected using the small momentum coefficient of C_μ=0.07 at Re=60,000. Analysis of the trailing edge pressures both on the lower and upper surfaces (FIGURE 6.17 and FIGURE 6.18 respectively) repeats the trends of the small momentum coefficients observed at Re=20,000 and Re=40,000. That is, that the lower surface trailing edge pressures are affected greatly by the increase in momentum coefficient up to around C_μ=0.06, in comparison with the upper surface trailing edge pressures which are

affected less. It is expected than if greater momentum coefficients were available, the trends would continue in the same manner as those of Re=40,000 and Re=20,000.

6.2 ESTIMATES OF LIFT AND THRUST COEFFICIENTS

Surface pressure measurements were used to estimate both lift and thrust coefficients. At Reynolds number Re=20,000, the lift coefficient generally increases over the range of momentum coefficients tested as shown in FIGURE 6.19. At the maximum momentum coefficient, the lift coefficient could be increased up to 50% (as for example in the case of $\alpha = 0^{\circ}$). However, as predicted on analysis of the pressure distributions, in some cases the lift coefficient decreases for small momentum coefficients of less than about C_{μ}=0.1. Some incidences appear more susceptible to deteriorated performance at low momentum coefficients than others. At $\alpha = 10^{\circ}$ the lift coefficient increases linearly throughout the momentum coefficient range tested. However at $\alpha = 15^{\circ}$ and $\alpha = 5^{\circ}$, a momentum coefficient of around C_{μ}=0.05 causes a loss in lift coefficient of around 10% and 20% respectively. It can be surmised that at $\alpha = 10^{\circ}$, the flow field is approaching stall and perhaps more easily influenced by momentum injection throughout the range of momentum coefficients. At $\alpha = 0^{\circ}$ the extent of the separation is less and perhaps reattachment and consequent influence of the upper surface is allowed to occur for lower momentum coefficients. At $\alpha = 5^{\circ}$ larger separated regions exist. Until sufficient momentum coefficient is used to cause reattachment at the trailing edge, the separated boundary layer is not close enough to the jet exit to be accelerated and therefore cannot cause reduced upper surface pressure coefficients.

For Re=20,000, at $\alpha = 10^{\circ}$, the linearity of the lift coefficient behaviour with increasing momentum coefficient is not seen at other Reynolds numbers with the same jet operation parameters. The drop in lift does not occur at $\alpha = 10^{\circ}$ due to the difference in surface pressure changes caused by the jet at this incidence. At the trailing edge, it can be seen that the upper surface pressure decrease is the largest of the four incidences tested at Re=20,000 for small momentum coefficients. Therefore, the lift reflects the optimum performance of $\alpha = 10^{\circ}$ in terms of lift increment for small momentum coefficient.

Analysis of the thrust coefficient shown in FIGURE 6.20 reveals an increasing linear effect of momentum coefficient on thrust coefficient. For Re=20,000, at $\alpha = 0^{\circ}$, the critical momentum coefficient required for a cruise condition of zero nett drag is estimated to be around 0.05. At $\alpha = 5^{\circ}$, the critical momentum coefficient increases to be about 0.07. At $\alpha = 10^{\circ}$, the critical momentum coefficient increases to 0.2, with zero nett drag at $\alpha = 15^{\circ}$, outside of the range of momentum coefficients considered here. The increase in momentum required to achieve the cruise condition is proportional to the baseline drag coefficient of the aerofoil without jet excitation. At high incidence, the thrust coefficient increases more slowly with momentum coefficient than at low incidences. At low incidence therefore, the thrust coefficient is directly proportional to the momentum coefficient.

There are only small differences in lift and thrust coefficient at Re=40,000 compared to Re=20,000 as shown in FIGURE 6.21 and FIGURE 6.22 respectively. Estimates for baseline lift coefficient, with no jet excitation, show an improved performance at all incidences compared to the lower Reynolds number. With jet excitation there are similar larger lift coefficient increases at high momentum coefficients. At all incidences except $\alpha = 0^{\circ}$, very small momentum coefficients cause increase in lift coefficients. Increasing the momentum coefficient slightly causes the characteristic drop in lift, as shown with Re=20,000. In addition, the increase in lift coefficient caused by maximum momentum coefficient of around $C_{\mu} = 0.2$, is slightly less than that estimated for the Re=20,000 equivalent cases. With increasing freestream velocity, the influence of the jet fluctuations upstream of the trailing edge becomes less. The pressure surveys showed large changes in the upper surface pressures even at the leading edge for Re=20,000, but at Re=40,000, the pressure change appears to be less.

The estimated thrust coefficient trends at Re=40,000 shows little variation from those of Re=20,000 compared to the variation in performance observed between conditions of Re=10,000 and Re=20,000 shown in Chapter 4. The critical momentum coefficients associated with each incidence are slightly lower with Re=40,000 compared to those of the Re=20,000 conditions. For the smallest non-zero momentum coefficient tested here, there is less effect on thrust coefficient at the Re=40,000 condition compared to the

Re=20,000 condition. Very small momentum coefficients seem to generate smaller thrust coefficients at higher Reynolds numbers.

At Re=60,000, the small range of momentum coefficients available revealed finer detail of the effects of the small momentum coefficient range on lift and thrust coefficient as shown in FIGURE 6.23 and FIGURE 6.24 respectively.

For $C_\mu < 0.02$, the lift coefficient for all incidence is increased by jet excitation. However for $C_\mu > 0.02$, increasing the momentum coefficient has the effect of decreasing the lift coefficient, most noticeable at lower incidences. From FIGURE 6.23 it would appear than as the momentum coefficient approaches $C_\mu \sim 0.06$, the drop in lift coefficient reaches a plateaux. Based on the results of Re=20,000 and Re=40,000, it is estimated that from around $C_\mu \sim 0.06$, the lift coefficient increases, eventually beyond that of the aerofoil without jet excitation for sufficiently high momentum coefficients.

For very small momentum coefficients (with $C_\mu < 0.025$), there is an initial small decrease in the thrust coefficient. For momentum coefficients greater than these, an increase in thrust coefficient occurs. The lift coefficient on the other hand shows an initial increase before the 'dip' in performance observed at the other Reynolds numbers before reattachment is achieved. At this higher Reynolds number, the baseline lift coefficients are seen to increase, and drag coefficients are seen to decrease due to the increasingly favourable flight conditions. The critical momentum coefficients are estimated to be slightly smaller than those for Re=20,000 and Re=40,000 corresponding to the more favourable conditions at higher Reynolds numbers.

6.3 ASSESSMENT OF EFFICIENCY

Given the complex variations in lift and thrust force coefficients over the range of momentum coefficients considered here, it is important to identify the most efficient operating conditions for the synthetic jet and aerofoil system. The ways in which the smaller and larger momentum coefficients affect the aerodynamic parameters in different ways suggest that there may be an optimum overall aerodynamic performance within the range of momentum coefficients tested.

To obtain an understanding of the optimum operating conditions, three parameters are considered. The first, termed the aerodynamic efficiency, A_E, is a lift to drag ratio for the 'no jet' condition, but accounts for the increasing momentum coefficient when jet excitation is non-zero:

$$A_E = \frac{C_L}{C_\mu - C_T}$$

The aerodynamic efficiency is the one parameter of the three considered here that would be most transferable and of most use to researchers working in this field.

The propulsive efficiency, P_E, unique to the synthetic jet driving system used here, is also considered. Whilst no attempt was made to design the laboratory speaker driven system as efficiently as possible, analysis of P_E would undoubtedly go some way to helping with design issues at a later date:

$$P_E = \frac{\Delta T \cdot U_\infty}{P} = \frac{\Delta C_T}{C_E},$$

where ΔT is the increment in thrust and ΔC_T is the increment in thrust coefficient seen between the no-jet condition and operation of the jet at power coefficient of C_E or power, P.

P_E gives a relationship between the increase in thrust coefficients achieved compared to the power used in driving the jet.

Finally a figure of merit is created by combining the aerodynamic efficiency and propulsive efficiency, A_E x P_E, as a means of reflecting both the aerodynamic and propulsive performance of the system.

Estimates of the aerodynamic efficiency are shown for Re=20,000, Re=40,000 and Re=60,000 in FIGURE 6.25, FIGURE 6.26, and FIGURE 6.27 respectively. First it should be noted that in general, A_E increases with increasing Reynolds numbers for all

incidences tested except where $\alpha = 15^{\circ}$. The increase in A_E with Reynolds number reflects the greater lift and thrust coefficients estimated for the higher Reynolds number conditions. The $\alpha = 15^{\circ}$ incidence is near to stall regardless of Reynolds number effects. Features of commonality exist in the analysis of the three Reynolds numbers. At low incidence small momentum coefficients cause a marked decrease in A_E, reaching a local minimum around $C_\mu = 0.05$. Increasing the momentum coefficient above $C_\mu = 0.05$ causes a slow recovery in the A_E values at low incidence. The large initial decrease in A_E is most strongly affected by the initial decrease in lift observed in the low momentum coefficient range. At Re=40,000 and Re=60,000, the drop in A_E at $\alpha = 5^{\circ}$, for small momentum coefficients, does not experience such a subsequent recovery when increasing the momentum coefficient to higher values. The low incidence experiments show that the most significant decrease in aerodynamic efficiency is at low momentum coefficients and therefore operation inside that range should be carefully considered. Recall, that most of the deterioration in performance for low momentum coefficient is due to the drop in lift coefficient. If more than sufficient lift coefficient for a typical MAV mission is found at these low incidence, then to some extent, a loss of lift might be considered an acceptable trade-off for the corresponding increase in thrust coefficient.

At high incidence, momentum coefficient has little effect on the aerodynamic efficiency in the Reynolds number range tested here, the values of A_E remaining constant with only small decay over the entire momentum coefficient range tested. Recall that higher incidence appeared more resilient to the lift coefficient drop off seen at lower incidences for low momentum coefficients. Consequently it was expected that higher incidence would not see a drop in aerodynamic performance at low momentum coefficient jet operation.

In consideration of the power consumption of the driving system, P_E is estimated for the three Reynolds numbers as shown in FIGURE 6.29, FIGURE 6.30, and FIGURE 6.31 respectively. At Re=20,000 the propulsive efficiency is seen to be generally decreasing for the range of momentums coefficient tested. The only exception is for $\alpha = 5^{\circ}$, where a local maximum in P_E of around 1% occurs near $C_\mu = 0.05$. The propulsive efficiencies of the other incidences decay from around 1-1.5% to around 0.6% over the range tested.

As the laboratory actuator system was not designed as an efficient driving solution, the large power requirements were expected to reduce the efficiencies greatly over the range under test.

At Re=40,000, all of the incidences showed a local maximum propulsive efficiency near C_μ = 0.07 with P_E reaching around 0.5%. Comparison of maximum P_E achieved at Re=60,000 shows that the propulsive efficiency appears to decrease with increasing Reynolds number. The requirement for achieving a fixed momentum coefficient at higher Reynolds numbers obviously means that more power is consumed. As the system is mains powered, and not designed with efficiency of operation in mind, the propulsive efficiency is bound to reflect the decreasing efficiency of a system running at increasingly high power.

At Re=60,000, recall that the very low range of momentum coefficient was observed to cause an initial increase in the baseline drag of the aerofoil system. Consequently, the propulsive efficiency of those conditions is negative. The extremely low range of momentum coefficient would therefore be avoided in jet operating conditions.

Combining both features found in the propulsive efficiency analysis and the aerodynamic efficiency in the figure of merits (FMs) or A_E x P_E, shows how the propulsive efficiency variation largely dominates the trends in the combined figures shown in FIGURE 6.31, FIGURE 6.32, and FIGURE 6.33 respectively. Over the three Reynolds numbers, the FM generally shows a decrease with lower Reynolds numbers (requiring less power) showing the highest estimated values. At very low momentum coefficients both the propulsive efficiency and aerodynamic efficiency are lowest, showing clear degradation in the combined FM. As the momentum coefficient range of the Re=60,000 condition was limited to C_μ = 0.07, that feature is most clearly shown in FIGURE 6.33 estimated with Re=60,000. The FM of FIGURE 6.31, corresponding to conditions of Re=20,000, shows that this lowest Reynolds number is the most resilient condition to the drop in performance whilst Re=60,000 is the most susceptible.

It is expected that improvements in the design of the driving system would greatly enhance the propulsive efficiency of the jet operation. That would contribute significantly to enhanced summary FMs for the three cases presented here.

6.4 CONSIDERATION OF SLOT GEOMETRY

Whilst no complete study was conducted with regard to the jet exit slot geometry and orientation, the effects of the jet on surface pressures at the trailing edge suggest that slot orientation should be a consideration in the system design.

It was shown in certain cases that the surface pressures above and below the trailing edge were affected differently. For example, FIGURE 6.14, showed how the lower surface pressures were decreased more strongly than the upper surface pressures. It was also shown that for small momentum coefficients there was little change in the thrust coefficient generated. This was attributed to the separated boundary layer being outside of the influence of the synthetic jet as sufficient momentum was not yet injected to cause reattachment. That would suggest that a reorientation of the jet to inject momentum more directly into the separated region might provide enhanced performance.

Three slot geometries were considered. The original 0.5mm slot (h/c=0.0025) used on the existing aerofoil, the similar 1.5mm slot (h/c=0.0075) required for Re=60,000 operation, and a 1.5mm slot angled 20° upwards compared to the other slots. All of the jet exits are centred in the same geometrical position on the trailing edge.

Analysis of the surface pressure measurements for the three slots operated under similar conditions showed the variation in resultant surface pressures that slot geometry can cause (FIGURE 6.34). All three slots showed significant variation from the no-jet condition. The 1.5mm straight jet exit slot caused a much larger decrease in the surface pressures of the lower surface than the upper surface, suggesting a decrease in lift coefficient using that slot.

Operating the original 0.5mm slot or 1.5mm angled slot under the same conditions shows a significant change in the pressure distribution. The surface pressure of the

baseline aerofoil around the underside of the trailing edge is largely unchanged, whilst the surface pressure over the upper surface is greatly increased, suggesting an enhancement of lift coefficient using one of the two slots. Whilst a thorough analysis of the fluid dynamics of the three slots has not been performed, the narrower slot has narrower jet with larger jet exit velocities compared to the broad slot for a constant momentum coefficient. The high exit velocities and greater stroke length therefore affect a larger region of surrounding fluid. The angled slot opens directly into the separated region.

Analysis of the trailing edge pressure variation with increasing momentum coefficient for the three slots shows the trends clearly in FIGURE 6.35 and FIGURE 6.36. At a mid-range momentum coefficient, the surface pressures are decreased significantly with the 1.5mm straight slot on the lower surface, but little changed on the upper surface. The converse is found with the other two geometry slots. Towards the high momentum coefficients in the range tested, the disparity is decreasing and the performance of the slots appears to converge causing similar variations in surface pressure regardless of slot geometry.

Estimating the corresponding lift and thrust coefficients in FIGURE 6.37 and FIGURE 6.38 shows the effects of the surface pressure variations on the aerofoil due to the slot geometry. Using the 1.5mm slot, the jet causes a drop in lift coefficient below the lift coefficient estimated without excitation for a certain range of momentum coefficients. Such a drop in lift coefficient is not a feature of the performance of the 0.5mm or 1.5mm angled slots; quite the opposite. At low momentum coefficients both the 0.5mm and 1.5mm angled slots exhibit superior performance to the 1.5mm slot and increase the lift coefficient. Whilst the largest increase is seen with the 0.5mm slot, this gain in performance is a local peak. Additionally, the gain in performance with the 1.5mm angled slot is approximately constant throughout the momentum coefficient range tested. It is not until the highest momentum coefficient is reached that the lift force associated with the 1.5mm straight slot shows superior performance. The suggestion from such an observation is that there is significant aerodynamic performance to be gained by using a jet vectoring system.

The almost opposite effects on thrust coefficient would complicate the use of a vectoring system. Conversely to the effects on lift coefficient, the 1.5mm slot generates greater thrust coefficients throughout most of the momentum coefficient range until the highest momentum coefficients are reached, compared to the performance of the other slot geometries. Analysis of the thrust coefficients shows that an increase in lift coefficient is accompanied by less successful thrust generation. The converse is also true. Whilst the 1.5mm slot performs poorly in terms of lift coefficient enhancement, it performs well in generating the highest thrust coefficients. Depending on the nature of the flight profile required for a specific MAV mission, the critical aerodynamic performance issues could be highlighted and pre-determined before flight. For instance a heavy MAV payload would require greater lift coefficients whilst a light MAV for a fast flight might require larger thrust coefficients in preference.

In terms of aerodynamic efficiency, all three slots tested perform similarly over the range of momentum coefficient studied here. Whilst it has been shown that some slots increase lift coefficients more than others, and other slots generate larger thrust coefficients than others, the combination of these effects leads to similar total aerodynamic performance for the three slots tested (FIGURE 6.39). As FIGURE 6.40 shows, whilst the propulsive efficiency converges over the momentum coefficient range for all three slots, the 0.5mm slot exhibits the greatest propulsive efficiencies for low to medium momentum coefficients.

As the aerodynamic efficiency of the three slots was similar, and the propulsive efficiency shown in FIGURE 6.40 varies greatly between slots, it is the propulsion efficiency, which dominates the FM of FIGURE 6.41. Due to the significant gains in thrust coefficient generation, the 0.5mm slot performs best for most of the momentum coefficient range tested. The 1.5mm straight slot is highlighted as the least efficient slot geometry over most of the range tested due to the smaller lift coefficient estimates over its range.

Whilst a thorough analysis of slot geometry has not been performed, initial experiments on the effect of slot geometry show how significant changes in aerodynamic performance can occur with geometrical slot variation. This is undoubtedly an area to highlight for future work. Additionally, slots placed on the upper surface of the aerofoil

could possibly be used in harmony with a trailing edge slot to achieve aerodynamic performance benefits larger than trailing edge synthetic jets alone.

6.5 SUMMARY

In this chapter, surface pressure measurements were taken from a dedicated aerofoil. The effects of momentum coefficient, incidence and Reynolds number on the surface pressure distributions were observed. It was shown that larger pressure differences between the upper and lower surfaces of the aerofoil were caused at higher Reynolds numbers. Features of low Reynolds number flows, in particular the separation bubble, were evident. Sufficient momentum coefficients were shown to alter the surface pressure distributions significantly, in particular decreasing the upper surface pressure coefficients at the trailing edge.

Estimates of lift and thrust coefficients from the surface pressures were derived. They showed how small values of momentum coefficient caused a decrease in the lift coefficient but larger momentum coefficients led to significant increases in lift coefficients. The relationship between momentum coefficient and thrust coefficient was shown to be approximately linear for all but the largest incidence at $\alpha = 15^{\circ}$. Critical momentum coefficients were identified which created a zero nett drag or cruise condition.

Performance in terms of aerodynamic and propulsive efficiency was assessed. Aerodynamic efficiency reflected that low Reynolds numbers offered more favourable conditions for flight. Smallest aerodynamic efficiency values were shown to occur at low incidence for small momentum coefficients, relating to a drop in lift coefficient under those conditions. Aerodynamic efficiency for $\alpha = 15^{\circ}$ incidence remained approximately constant throughout the range of momentum coefficient and Reynolds number tested.

The effects of controlling the surface pressure around the trailing edge were shown to vary with slot geometry. A 1.5mm slot angled upwards exhibits greater influence over the separated region and cause a greater initial increase in lift coefficient than the

straight 1.5mm slot operated at smaller momentum coefficients. On the other hand, the straight 1.5mm slot was shown to exhibit superior performance in generating higher thrust coefficients. The suggestion is made that thrust-vectoring, variable slot geometry or multi-slot configurations should offer an improved overall aerodynamic performance although the exact solution would depend on the mission criteria for a particular MAV.

6.6 FIGURES

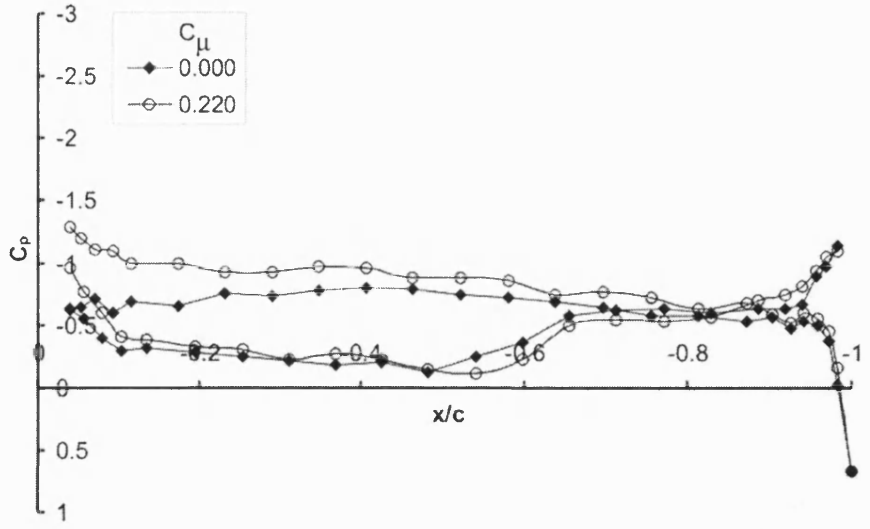

FIGURE 6.1 Surface pressure coefficients at Re=20,000, $\alpha = 0^{o}$, St=2.86.

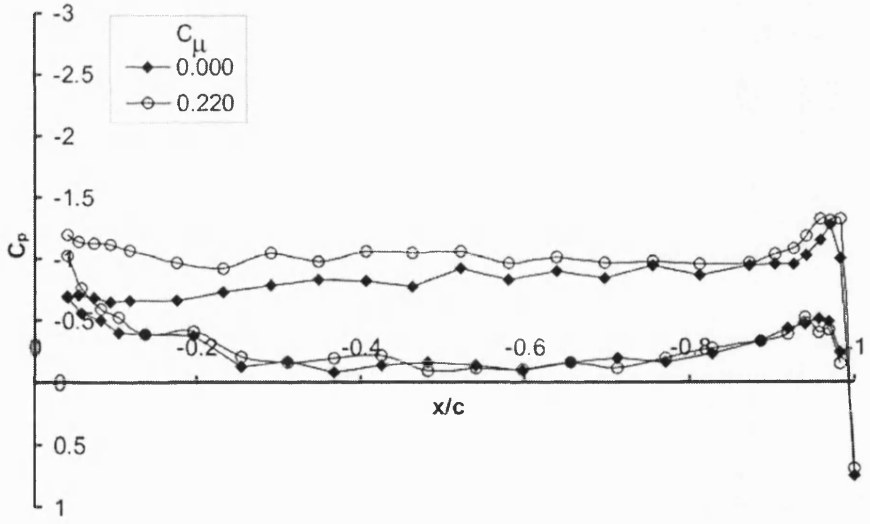

FIGURE 6.2 Surface pressure coefficients at Re=20,000, $\alpha = 5^{o}$, St=2.86.

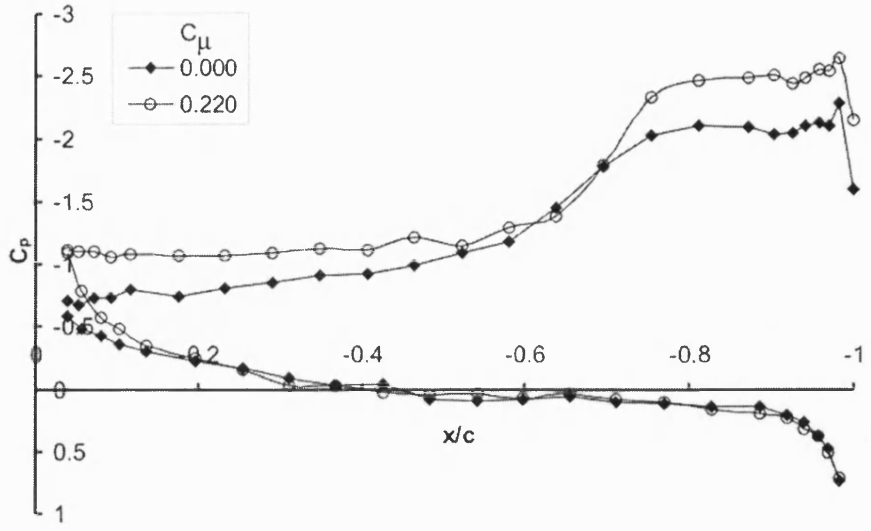

FIGURE 6.3 Surface pressure coefficients at Re=20,000, $\alpha = 10^{o}$, St=2.86.

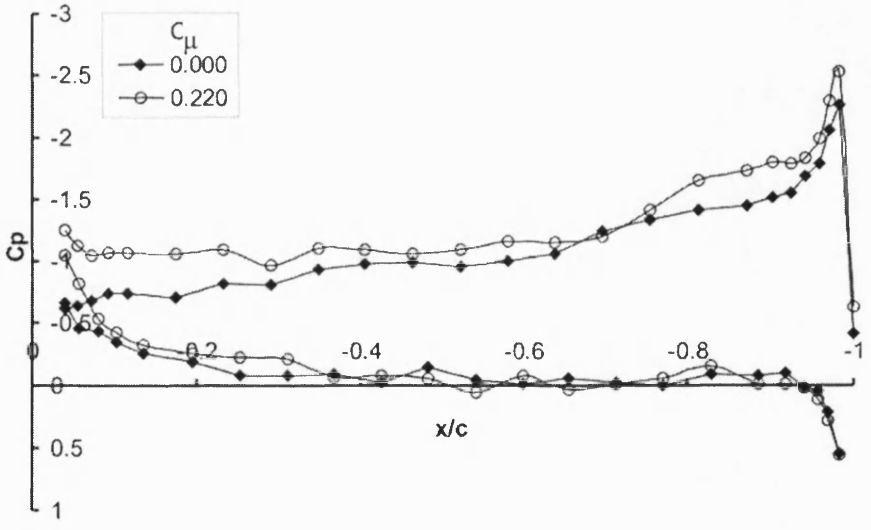

FIGURE 6.4 Surface pressure coefficients at Re=20,000, $\alpha = 15^{o}$, St=2.86.

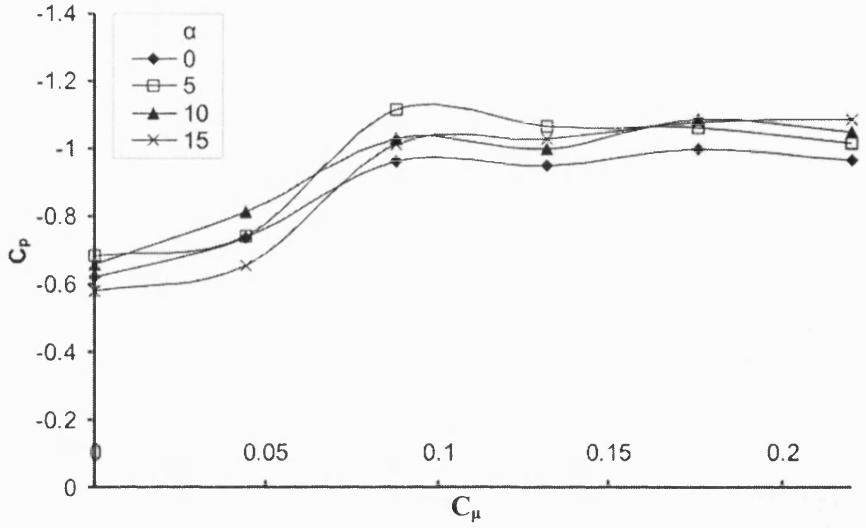

FIGURE 6.5 Lower surface trailing edge pressures (x/c = -0.025) at Re=20,000 with St=2.86.

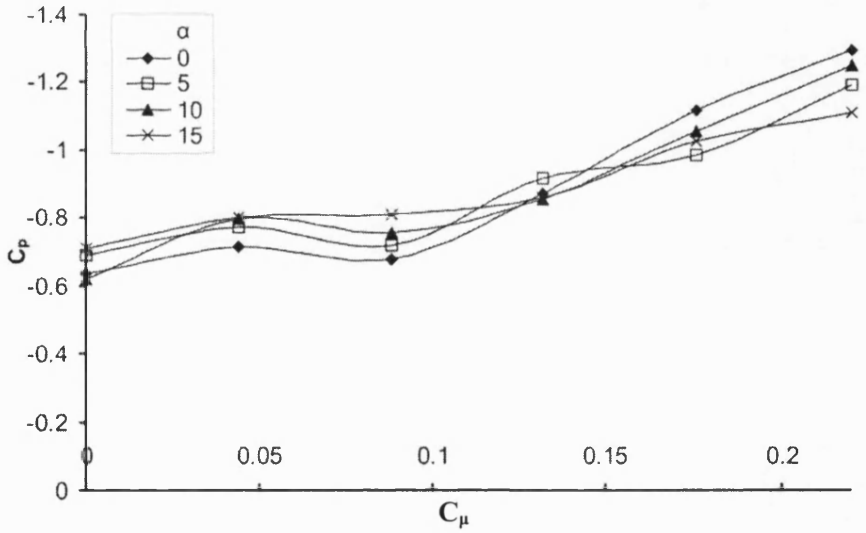

FIGURE 6.6 Upper surface trailing edge pressures (x/c = -0.025) at Re=20,000 with St=2.86.

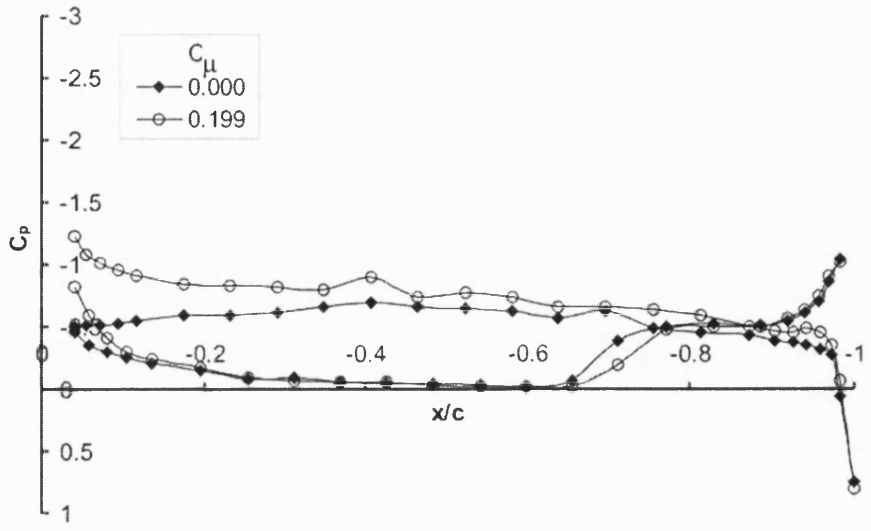

FIGURE 6.7 Surface pressure coefficients at Re=40,000, $\alpha = 0^{o}$, St=2.86.

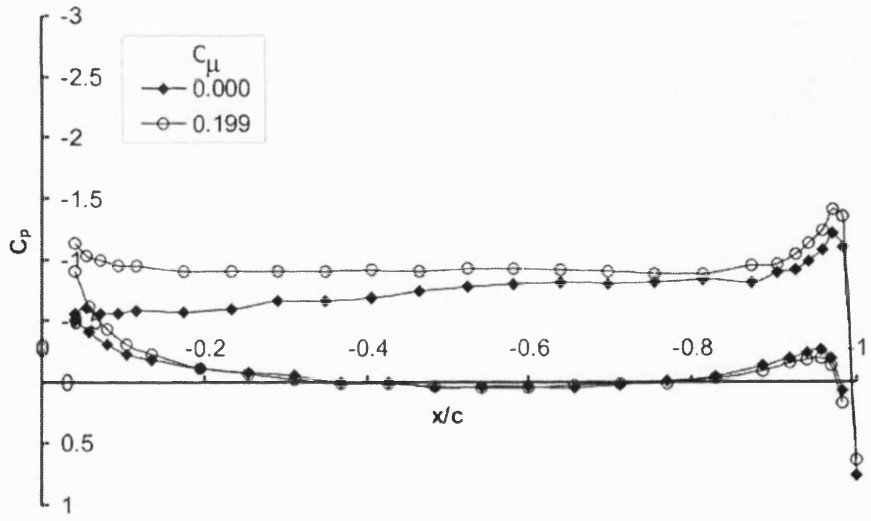

FIGURE 6.8 Surface pressure coefficients at Re=40,000, $\alpha = 5^{o}$, St=2.86.

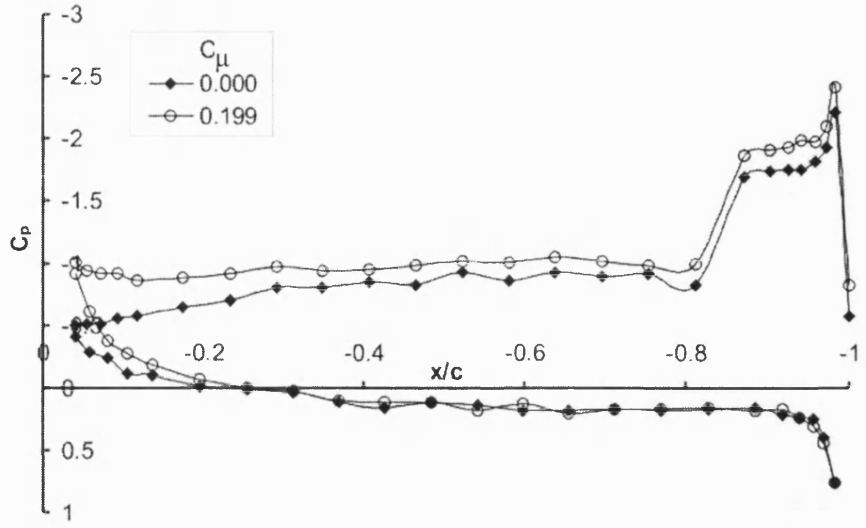

FIGURE 6.9 Surface pressure coefficients at Re=40,000, $\alpha = 10^o$, St=2.86.

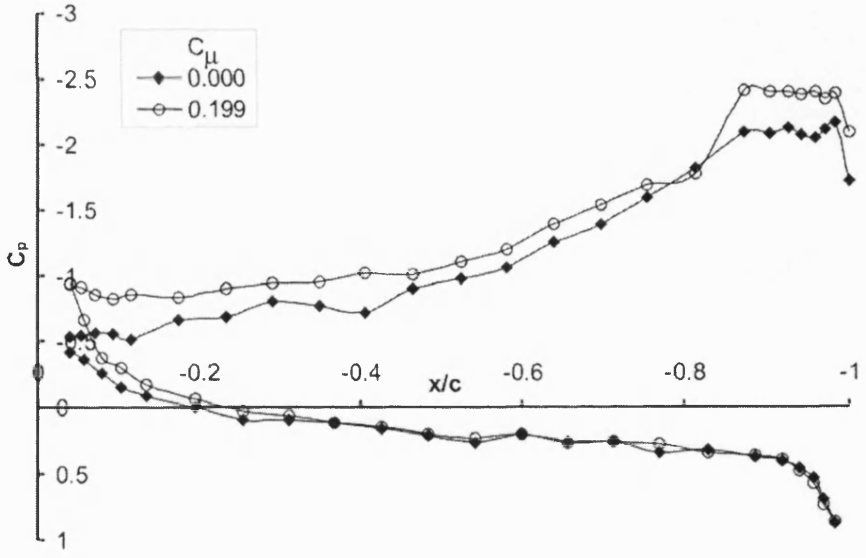

FIGURE 6.10 Surface pressure coefficients at Re=40,000, $\alpha = 15^o$, St=2.86.

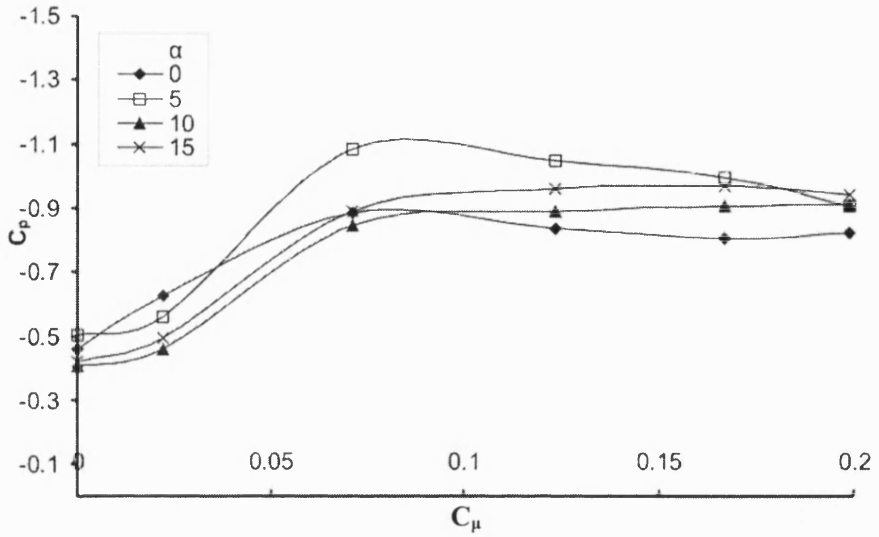

FIGURE 6.11 Lower surface trailing edge pressures (x/c = -0.025) at Re=40,000 with St=2.86.

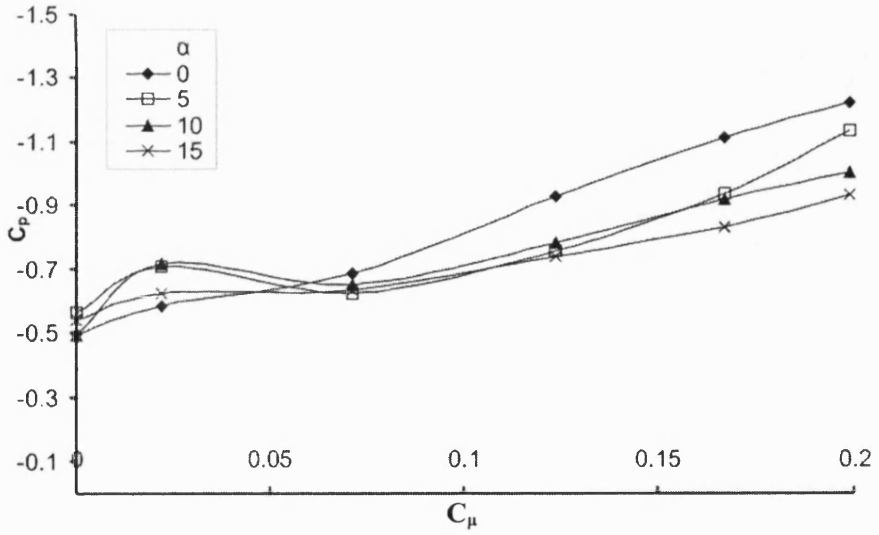

FIGURE 6.12 Upper surface trailing edge pressures (x/c = -0.025) at Re=40,000 with St=2.86.

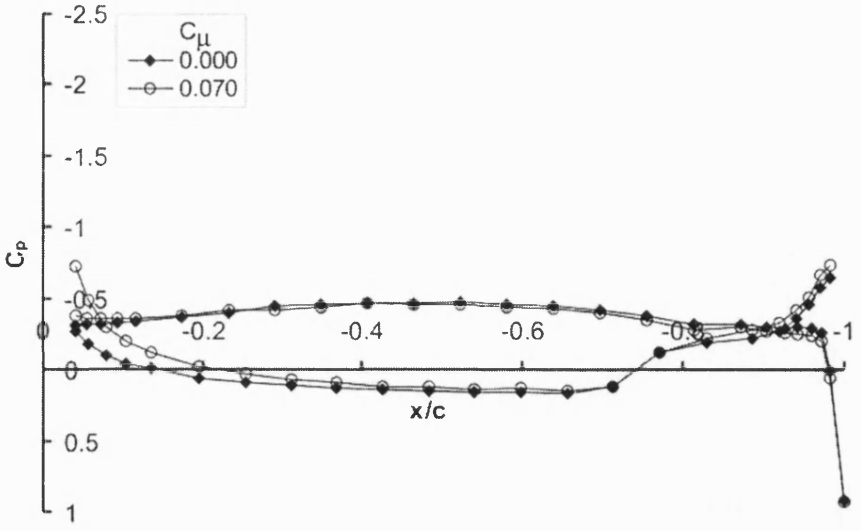

FIGURE 6.13 Surface pressure coefficients at Re=60,000, $\alpha = 0^{o}$, St=2.86.

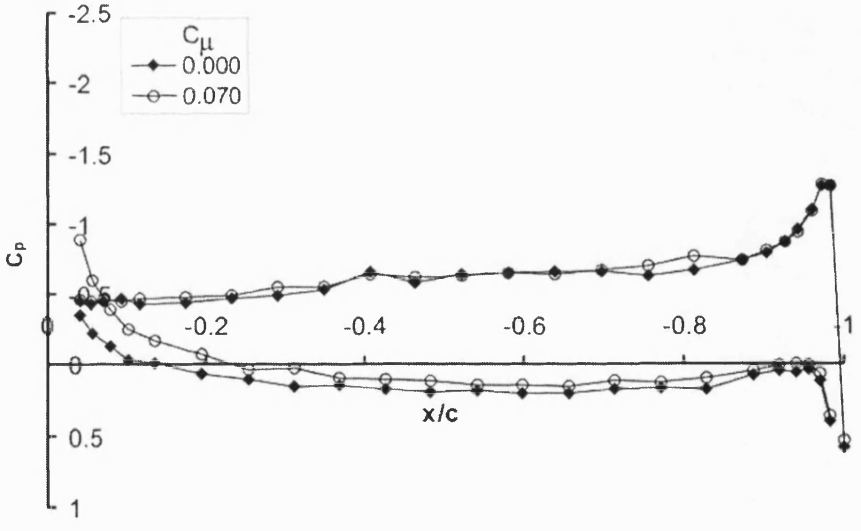

FIGURE 6.14 Surface pressure coefficients at Re=60,000, $\alpha = 5^{o}$, St=2.86.

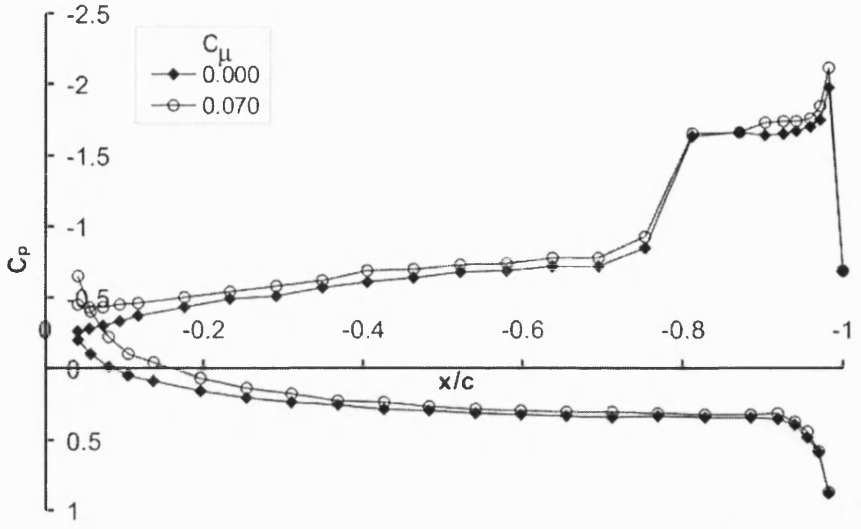

FIGURE 6.15 Surface pressure coefficients at Re=60,000, $\alpha = 10^{o}$, St=2.86.

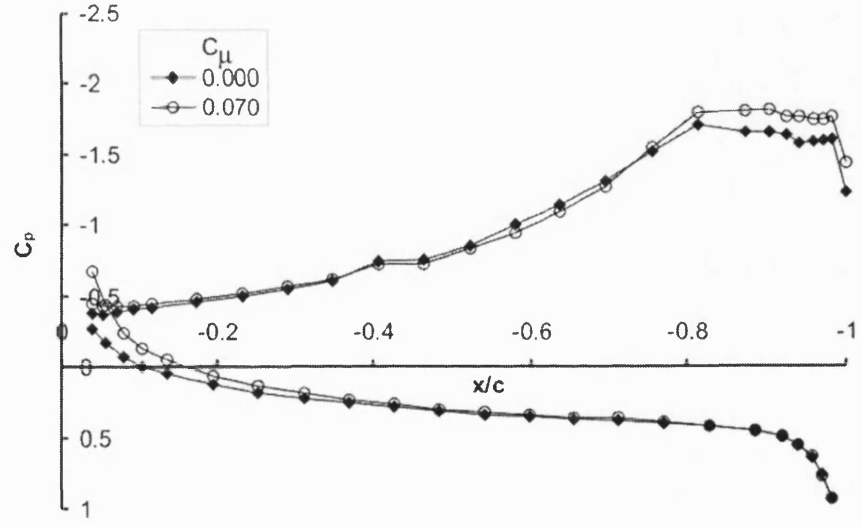

FIGURE 6.16 Surface pressure coefficients at Re=60,000, $\alpha = 15^{o}$, St=2.86.

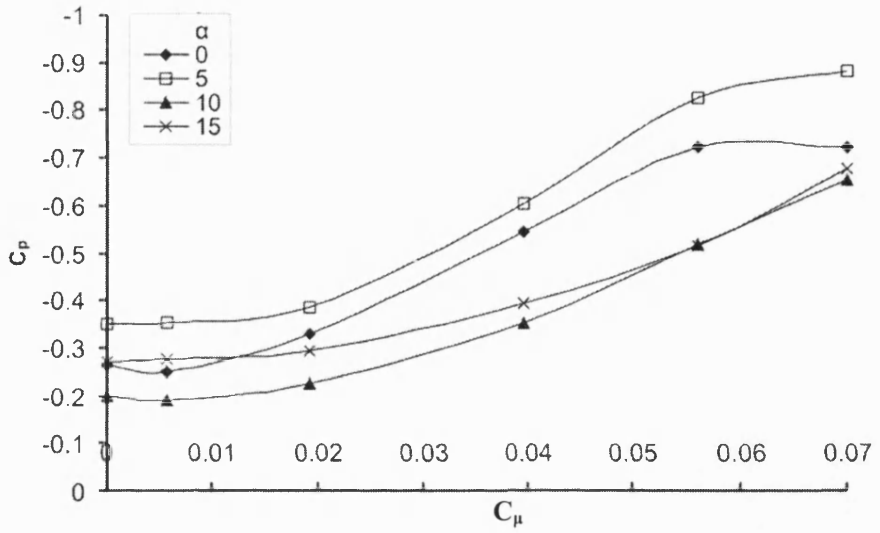

FIGURE 6.17 Lower surface trailing edge pressures (x/c = -0.025) at Re=60,000 with St=2.86.

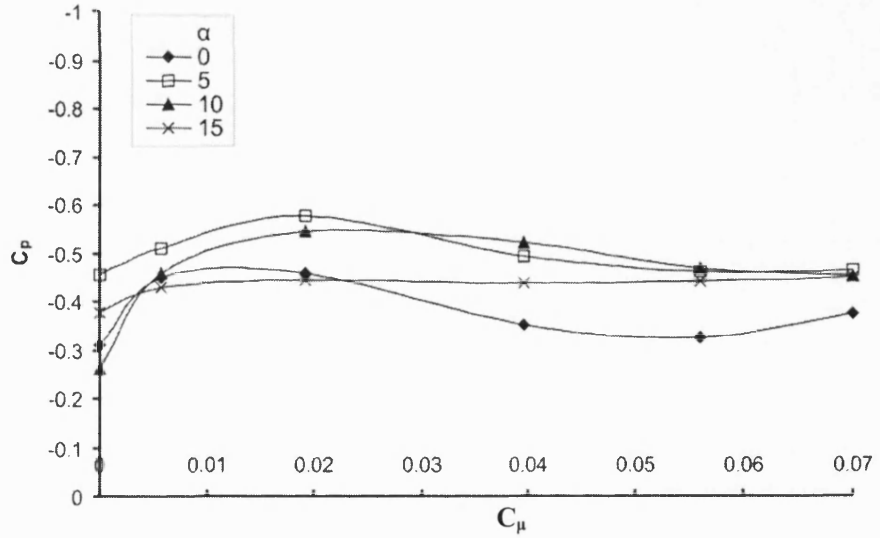

FIGURE 6.18 Upper surface trailing edge pressures (x/c = -0.025) at Re=60,000 with St=2.86.

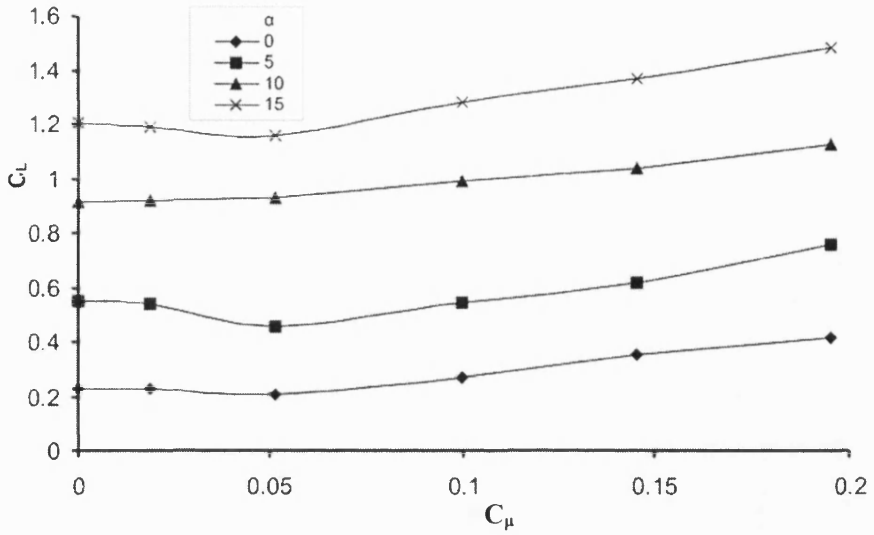

FIGURE 6.19 Lift coefficient variation with increasing momentum coefficient estimated from surface pressures at Re=20,000.

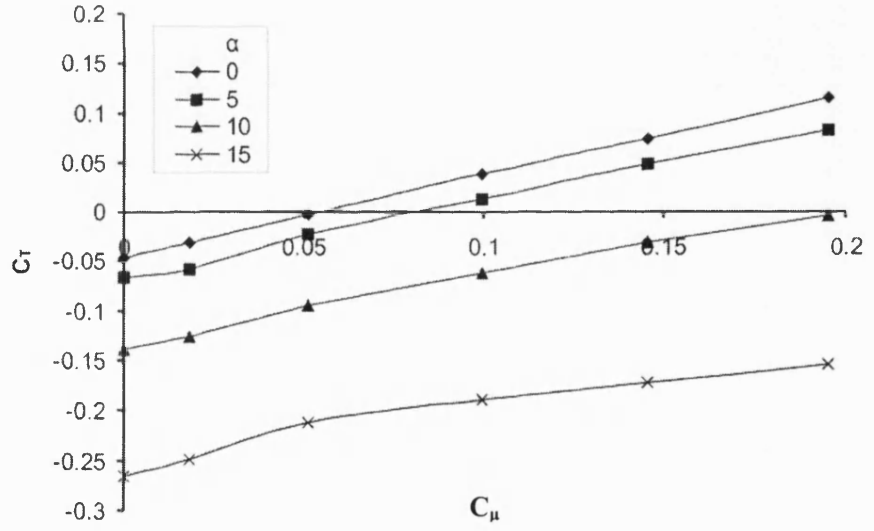

FIGURE 6.20 Thrust coefficient variation with increasing momentum coefficient estimated from surface pressures at Re=20,000.

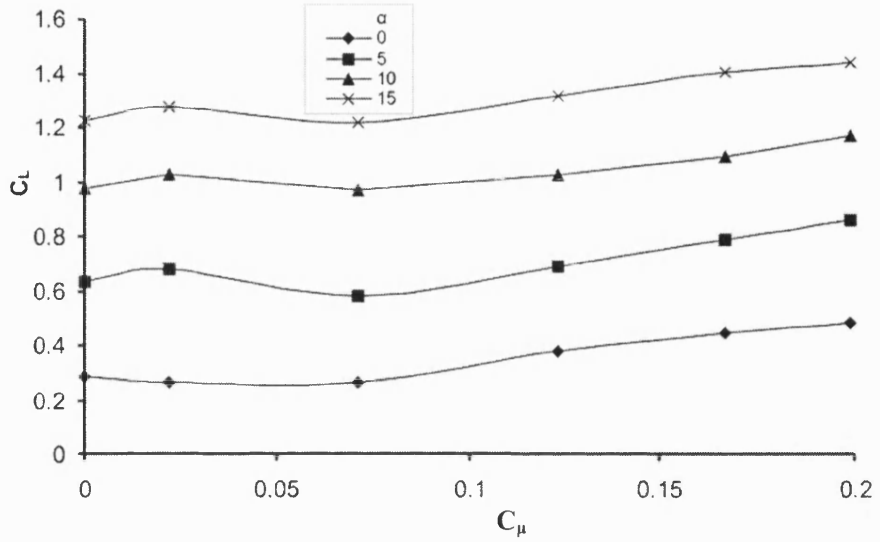

FIGURE 6.21 Lift coefficient variation with increasing momentum coefficient estimated from surface pressures at Re=40,000.

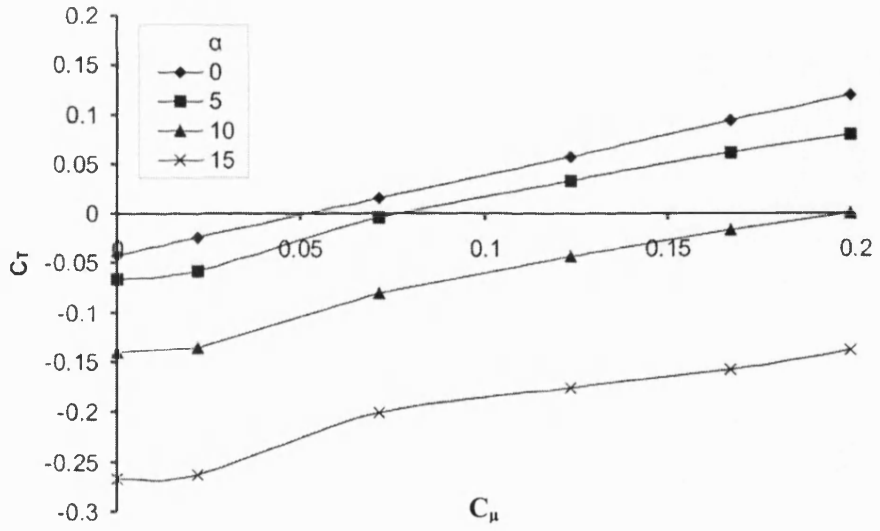

FIGURE 6.22 Thrust coefficient variation with increasing momentum coefficient estimated from surface pressures at Re=40,000.

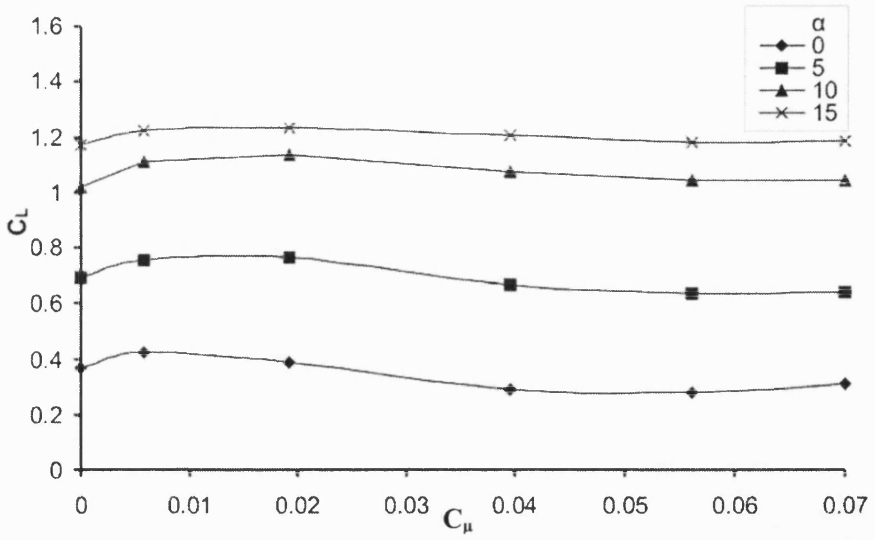

FIGURE 6.23 Lift coefficient variation with increasing momentum coefficient estimated from surface pressures at Re=60,000.

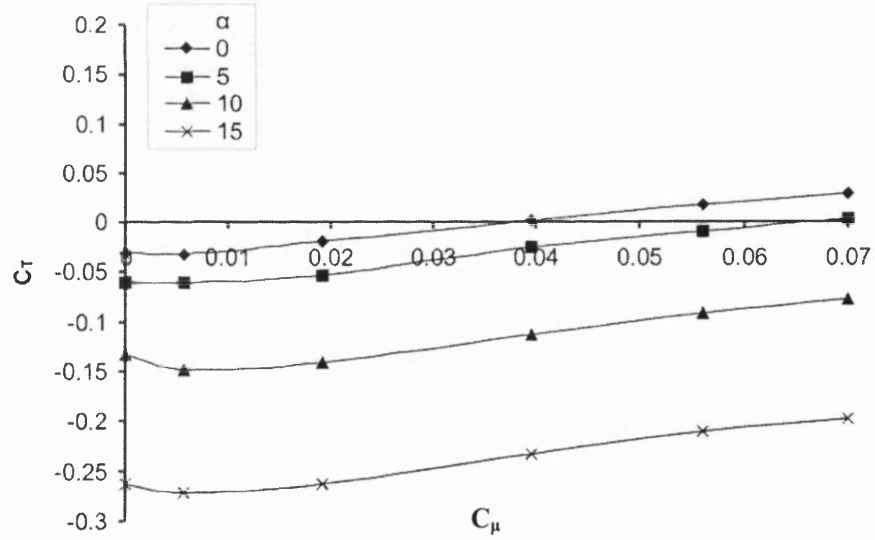

FIGURE 6.24 Thrust coefficient variation with increasing momentum coefficient estimated from surface pressures at Re=60,000.

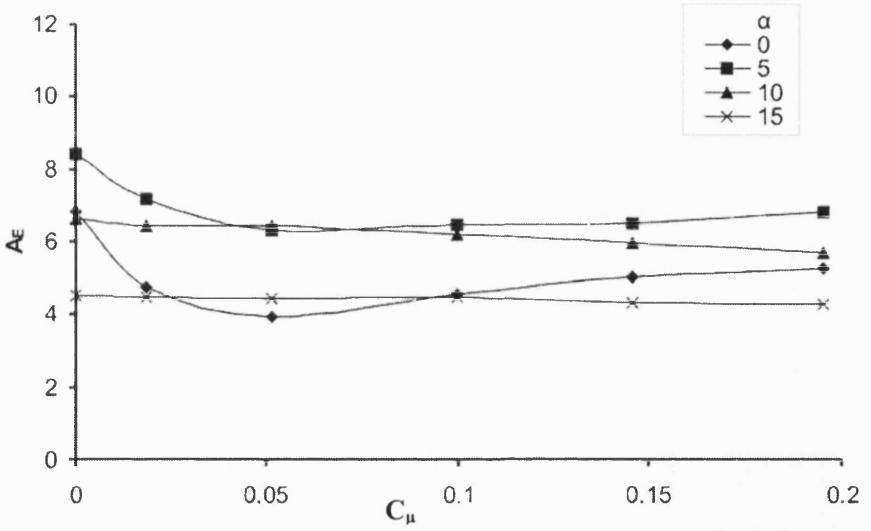

FIGURE 6.25 Variation of aerodynamic efficiency with increasing momentum coefficient at Re=20,000.

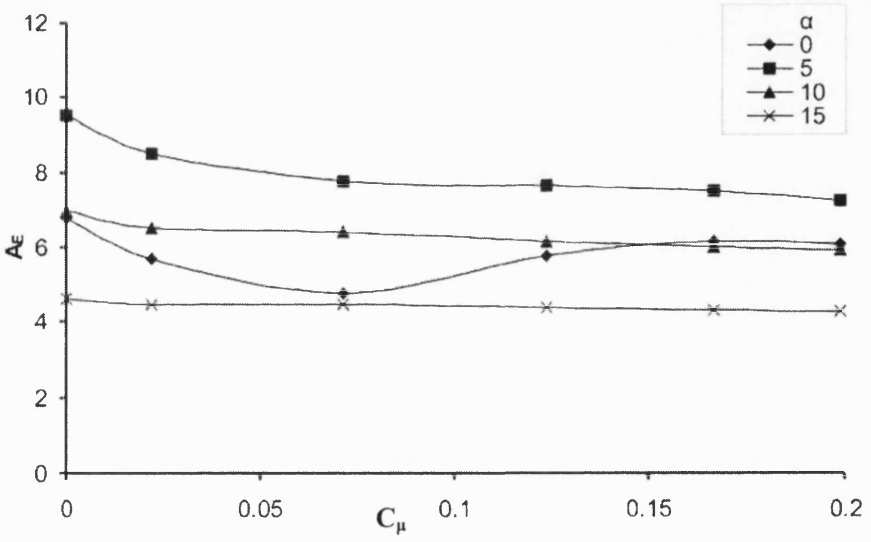

FIGURE 6.26 Variation of aerodynamic efficiency with increasing momentum coefficient at Re=40,000.

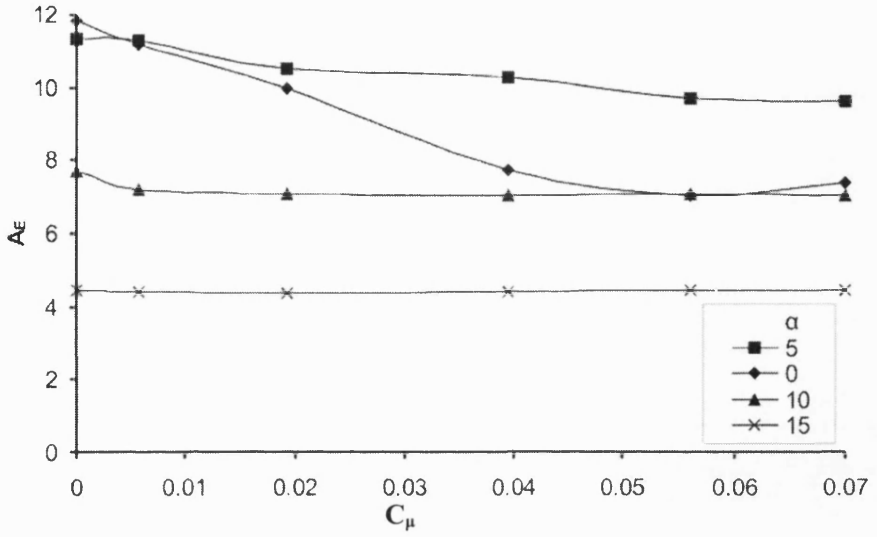

FIGURE 6.27 Variation of aerodynamic efficiency with increasing momentum coefficient at Re=60,000.

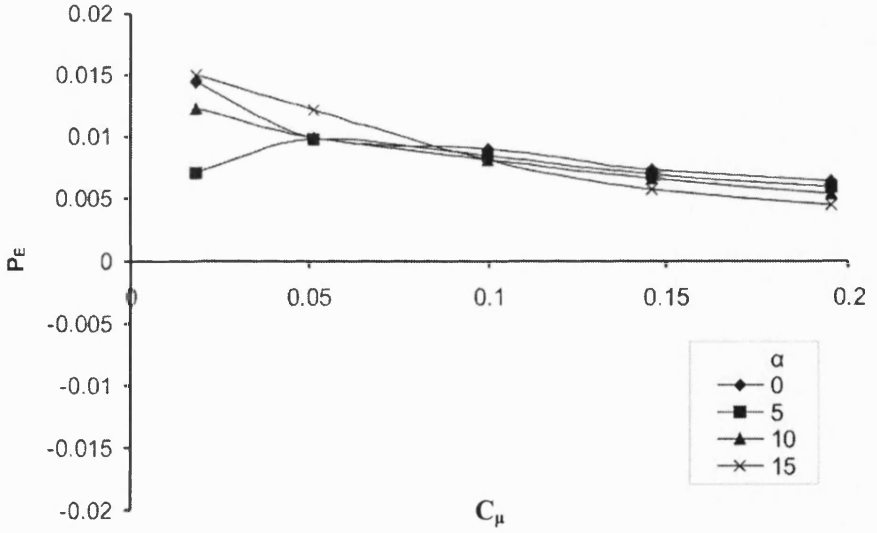

FIGURE 6.28 Variation of propulsive efficiency with increasing momentum coefficient at Re=20,000.

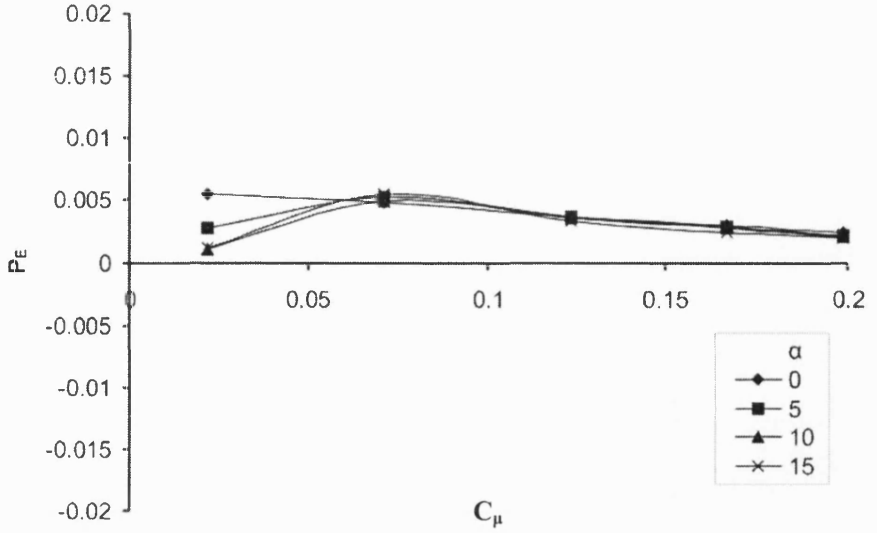

FIGURE 6.29 Variation of propulsive efficiency with increasing momentum coefficient at Re=40,000.

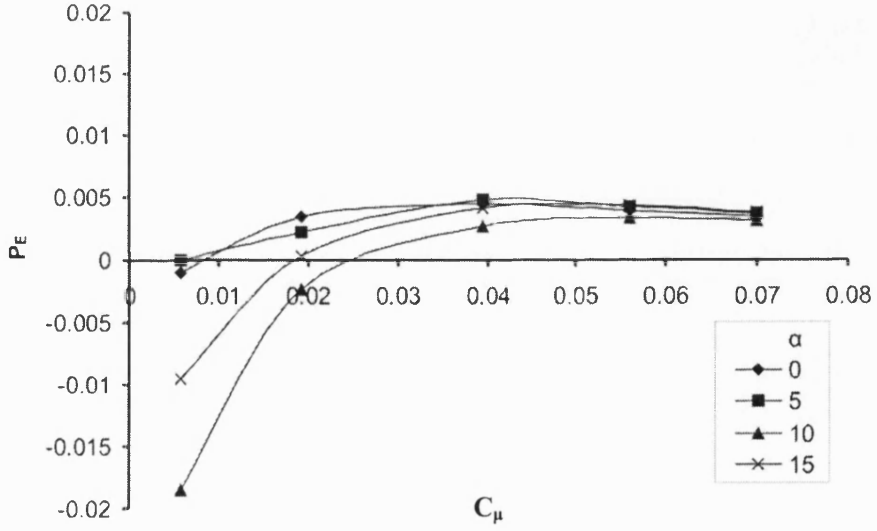

FIGURE 6.30 Variation of propulsive efficiency with increasing momentum coefficient at Re=60,000.

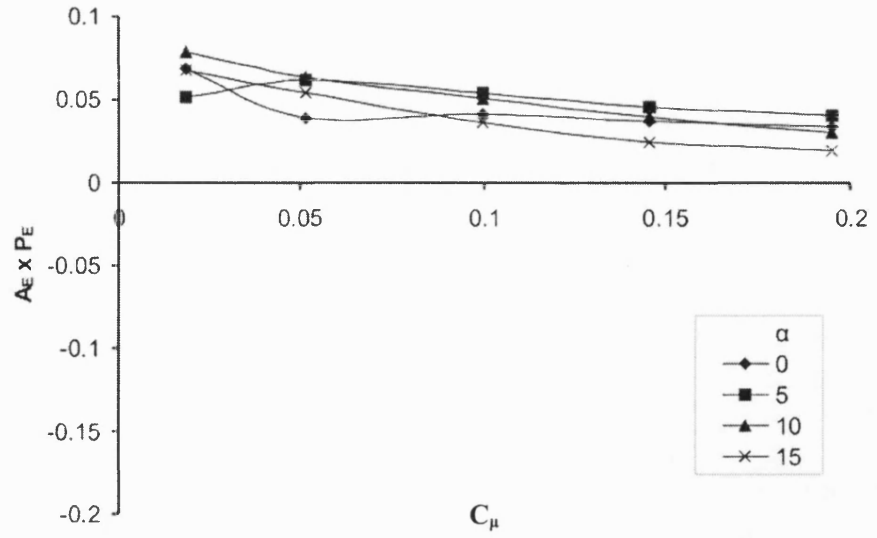

FIGURE 6.31 Variation of combined efficiency with increasing momentum coefficient at Re=20,000.

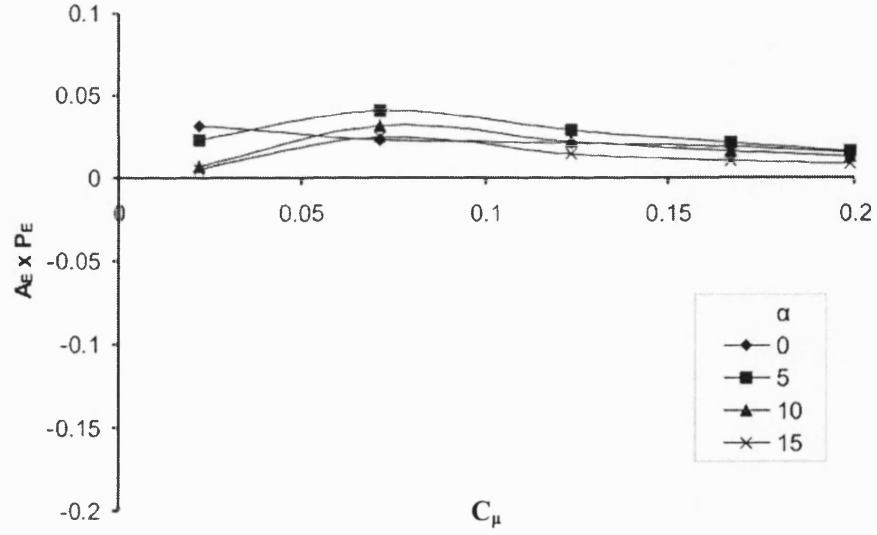

FIGURE 6.32 Variation of combined efficiency with increasing momentum coefficient at Re=40,000.

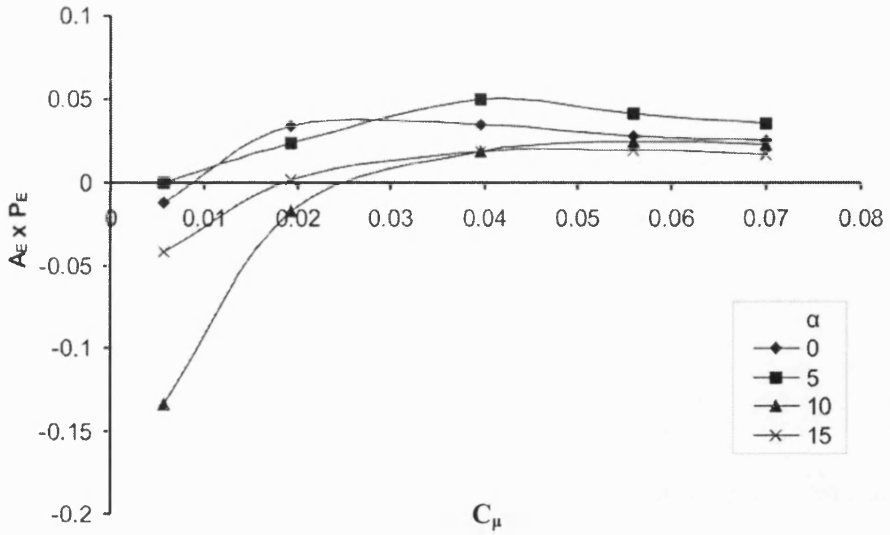

FIGURE 6.33 Variation of combined efficiency with increasing momentum coefficient at Re=60,000.

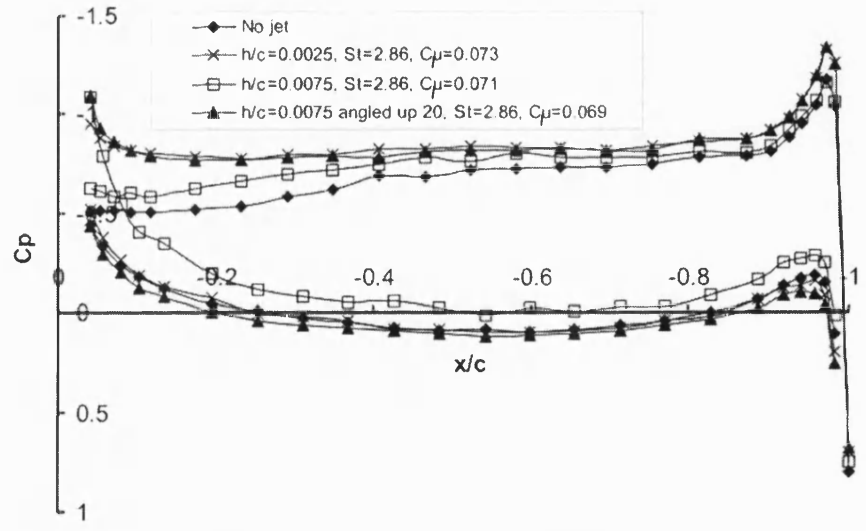

FIGURE 6.34 Surface pressure coefficients at Re=40,000, $\alpha = 5^o$, St=2.86, for varying slot geometries.

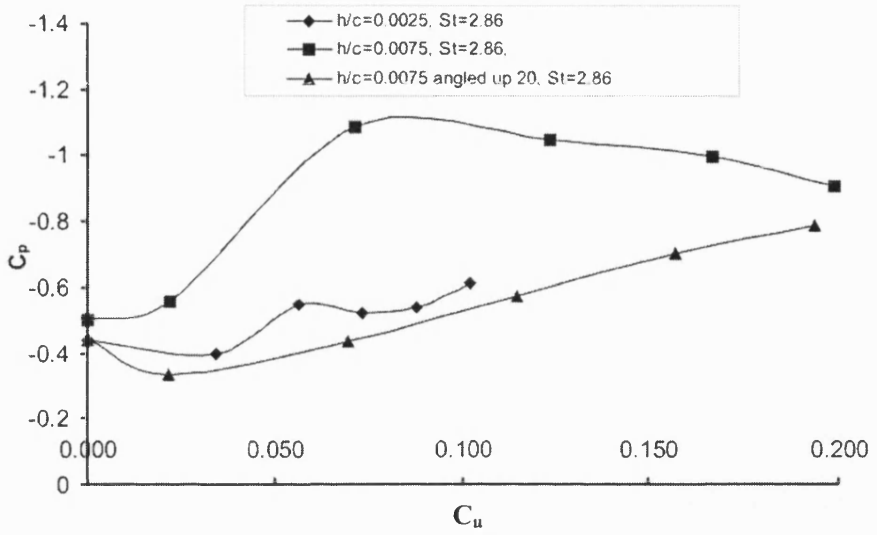

FIGURE 6.35 Lower surface trailing edge pressures (x/c = -0.025) at Re=40,000 with St=2.86, for varying slot geometries

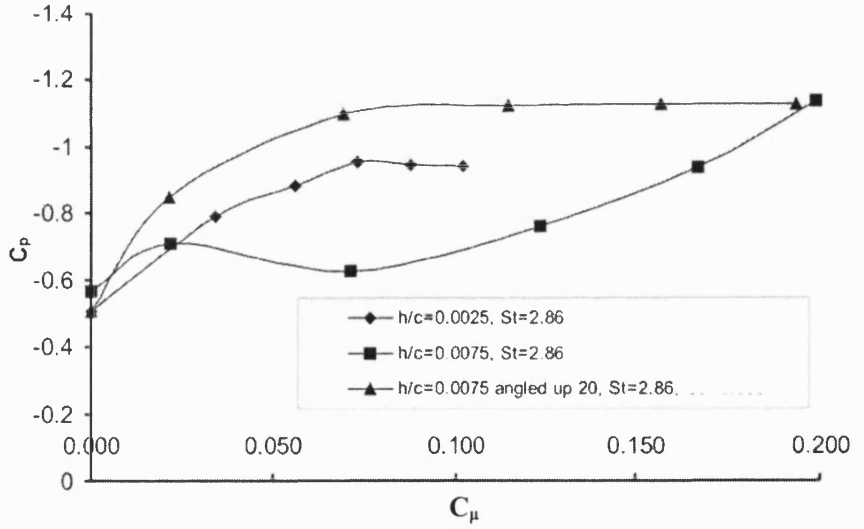

FIGURE 6.36 Upper surface trailing edge pressures (x/c = -0.025) at Re=40,000 with St=2.86, for varying slot geometries.

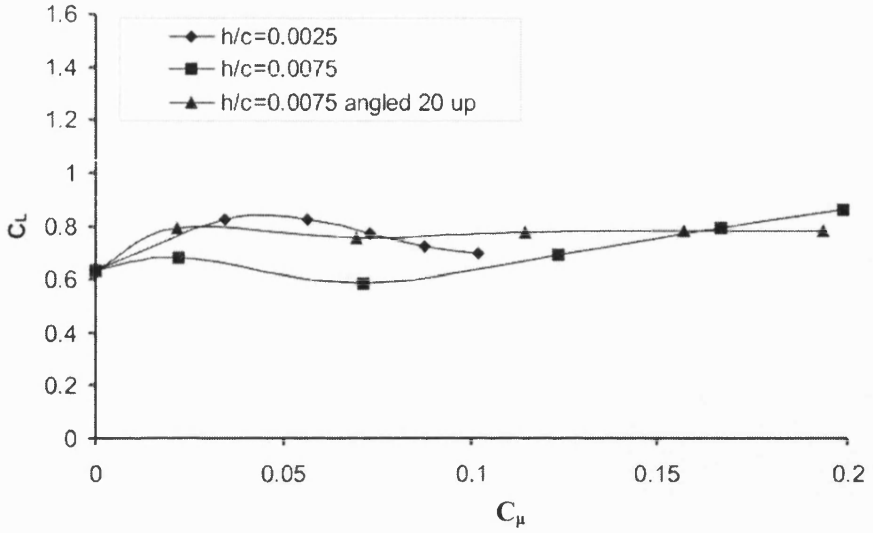

FIGURE 6.37 Variation in lift coefficient with increasing momentum coefficient at Re=40,000, $\alpha = 5^{\circ}$, with varying slot geometries.

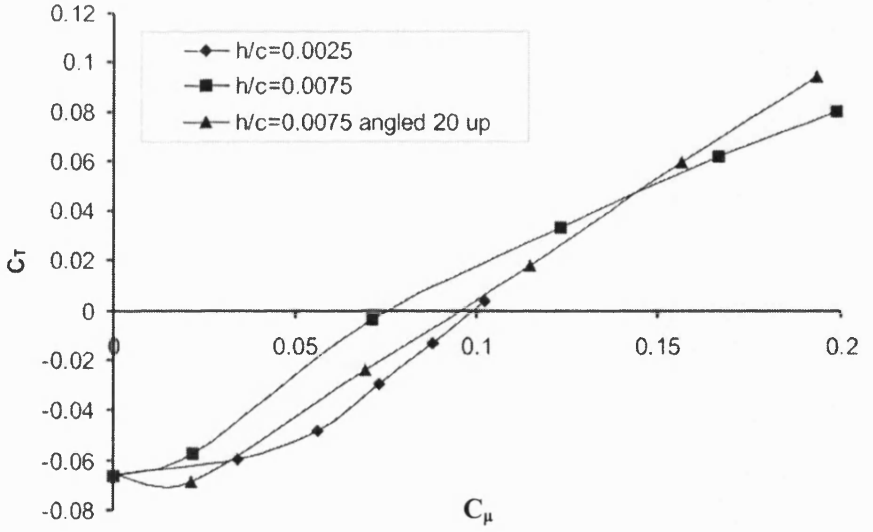

FIGURE 6.38 Variation in thrust coefficient with increasing momentum coefficient at Re=40,000, $\alpha = 5^{\circ}$, with varying slot geometries.

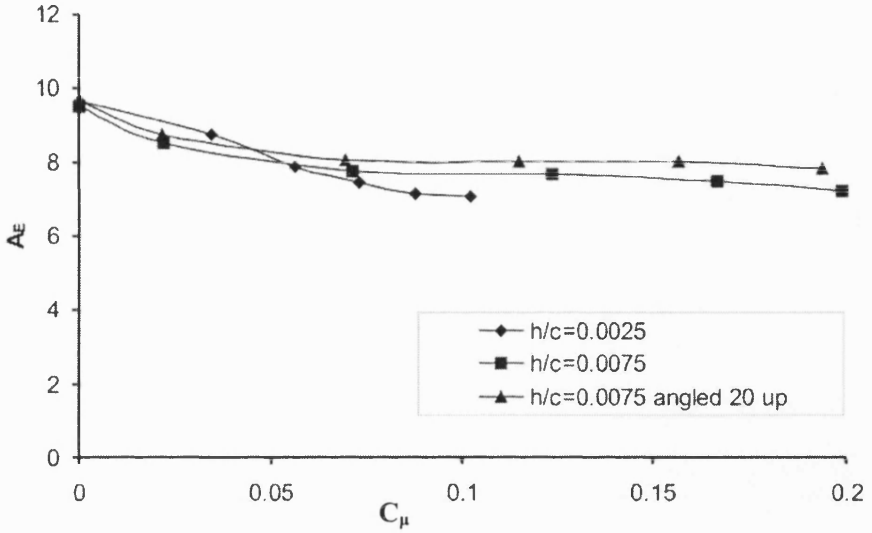

FIGURE 6.39 Variation in aerodynamic efficiency with increasing momentum coefficient at Re=40,000, $\alpha = 5^{\circ}$, with varying slot geometries.

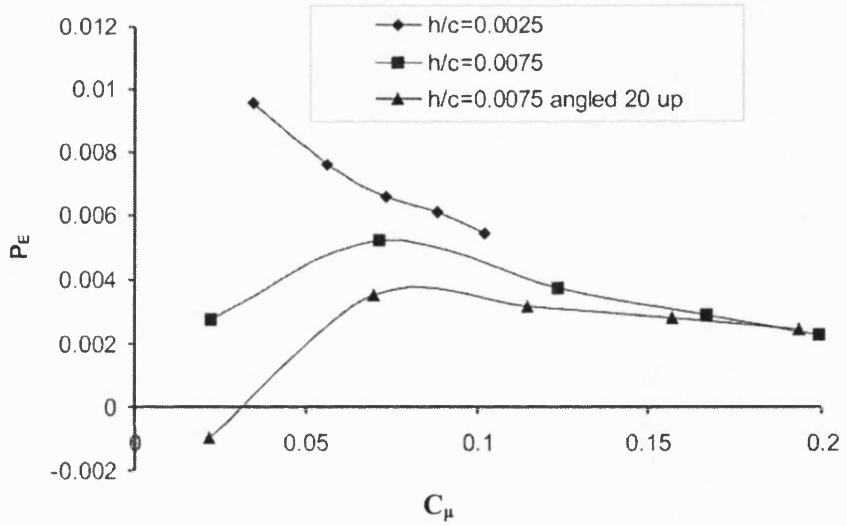

FIGURE 6.40 Variation in propulsive efficiency with increasing momentum coefficient at Re=40,000, $\alpha = 5^{\circ}$, with varying slot geometries.

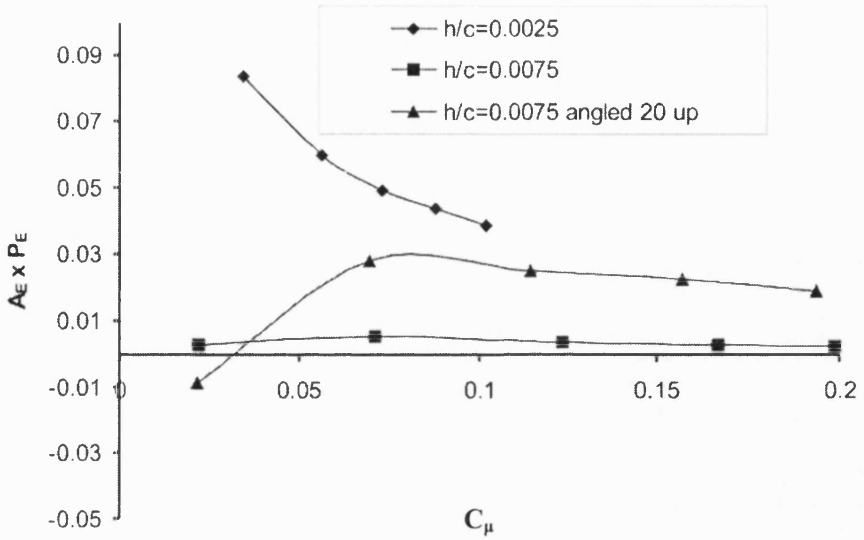

FIGURE 6.41 Variation in overall efficiency with increasing momentum coefficient at Re=40,000, $\alpha = 5^{o}$, with varying slot geometries.

CHAPTER 7 INTERNAL ACTUATOR DEVELOPMENT

7.1 INITIAL DEVELOPMENT

As the wing using an internal mechanism was designed only for very low speed, the internally actuated wing was operated at a chord Reynolds number of 20,000. Initial angle of attack was set to low incidence of $\alpha=5^{\circ}$ to assess performance.

LDV was used to estimate a momentum coefficient whilst the maximum voltage of 368V peak-to-peak was applied to the Thunder actuators. The maximum C_{μ} was estimated at 0.056, close to the critical value of C_{μ} required for the externally powered wing to experience a zero nett drag coefficient.

As shown in FIGURE 7.1, PIV was used first to study the wake velocities of the aerofoil without jet excitation, including any obvious differences in the fluid dynamics around the enlarged rear section compared to the slimmer externally actuated wing. The jet was then activated at maximum voltage and time averaged PIV captured. Particular attention was paid to observing the effect of the underside vibrations of the membrane on the fluid flow around the aerofoil. Whilst it can be seen that the velocity deficit in the wake is greatly reduced upon maximum excitation compared to the natural case, the PIV results suggest the level of excitation achieved was not sufficient to cause complete reattachment over the trailing edge. As the internally actuated wing was thickened, the drag coefficient was larger. A wake survey, shown in FIGURE 7.2, confirmed that the drag coefficient without excitation corresponded to $C_T = -0.046$, slightly larger than that

of the thinner aerofoil. With maximum excitation, a wake survey confirmed that zero nett drag was almost achieved (C_T=-0.002 was estimated from the wake survey); a condition corresponding closely to cruise for an MAV using the synthetic jet propulsion system.

Clearly, the requirements for the flight of an MAV in such a low Reynolds number regime would require the ability to accelerate, enabling, if nothing else, flight through gusting and transient conditions.

In order to achieve a greater thrust, greater amplitude of synthetic jet diaphragm motion has to be achieved using the internal actuators. After general studies to find a reasonably successful flexible membrane, the main area of restriction on the motion of the actuators was the level of resistance offered by the 0.5mm slot. The amplitude of the motion of the membrane whilst using the 0.5mm slot was around 4-5mm.

7.2 DECREASING SYSTEM RESISTANCE

The 0.5mm slot was replaced with a 1mm slot, then a 1.5mm slot and finally the slot fitting was removed completely leaving a 6mm slot. The goal was to get closer to the maximum amplitude of motion offered by the piezoelectric actuators in decreasing the slot restriction. Membrane flexibility would remain a restriction on the actuator movement although every effort was used to obtain a flexible, compliant membrane that would not 'balloon' under pressure fluctuations.

Both the resistance of the membrane to vertical displacement and the resistance to air displacement through the slot contribute as damping effects on the actuator mechanism. With increased damping effects, the actuators are less free to resonate. It is precisely the resonance property of the actuators that makes them so useful for such a purpose requiring maximum force and amplitude. In order to allow maximum resonance, the piezo-electrics should be as unrestricted in their movement as possible. Maximum resonance occurs in free air. Final experiments on the actuators showed that displacements of more than 30mm peak-to-peak could be achieved when operating the piezo-electrics in cantilever mode resonating in free air.

Whilst only 4-5mm of membrane displacement was achieved with the 0.5mm slot configuration, 8-10mm was achieved with the larger slot heights of 1mm to 6mm tested.

Using the 1mm slot, estimates of maximum momentum coefficient were obtained running the jet at maximum voltage of 368V peak-to-peak. The use of the 1mm slot, decreasing the effective resistance on the actuators, gave a significant increase in the available momentum coefficient; from a maximum of 0.054 with the 0.5mm slot to 0.136 with the 1mm slot. It was expected that with the increased range of momentum coefficient, greater levels of drag reduction could be achieved and a positive thrust force could also be applied in order to accelerate the MAV.

Observation of the mean velocity-squared profiles (used to estimate C_μ) taken 1mm from the exit of each slot (0) showed not only that the jet widened with slot width, but also that the 0.5mm slot width produced an even narrower jet than expected. The non-linear behaviour of the jet width to slot width relationship on the 0.5mm slot was attributed to development of vorticity and boundary layers through the slot. Enlarging the slot width to 1mm appeared to produce a jet scaling linearly with the 1.5mm slot height.

Additionally it is possible to observe that the maximum U^2 value of around 40 is attained with the 0.5mm slot and the 1mm slot. However, a clear decrease in value in the jet centre is seen on both the 1mm and 1.5mm slot. In fact the 1.5mm slot achieves values of around half the 0.5mm maximum. That said, the 1.5mm slot velocities obviously occur over three times of the geometrical width of the 0.5mm slot. The 1mm slot profiles show clearly how, when traversing across the slot exit, high velocities in the jet shear layers can be seen before a region of lower velocities in the jet core. The 1.5mm slot velocities suggest that the shear layers are less of a dominant feature in the lower velocities associated with it. Reducing the restriction of the slot experienced by the actuator caused a more free resonance condition. The 1mm slot might therefore offer a good balance between decreased slot resistance compared to the 0.5mm slot, yet maintaining a sufficiently high jet velocity to be of use in accelerating an MAV (for acceleration, the jet velocity clearly has to be higher than the free stream velocity). FIGURE 7.4 shows how the slot geometry affects the jet centreline (y/h = 0) performance. The peak positive velocity can be seen to decrease with increasing slot

height. Whilst the peak velocity of the 0.5mm slot is around 13m/s, the peak velocity of the 1.5mm slot is around 9.5m/s. The choice of slot would require the highest exit velocities over the broadest area of influence. The 1mm slot might therefore offer the best compromise.

A short demonstration of a high rate PIV system by TSI allowed instantaneous PIV data to be captured comparing the performance of the 0.5mm, 1mm and 1.5mm slots. FIGURE 7.5 shows the approximate locations of the captures, shown in 0, in the cycle history. Whilst the velocity magnitudes are not of the best quality (due to being instantaneous captures), they do show the comparative jet performance, particularly in captures 'e' to 'g', where the exit velocities of the 0.5mm are very much smaller than those of the other two slots.

Wake surveys using the LDV were performed and estimates of the thrust coefficient calculated for the three slot widths at low incidence of $\alpha=5^{\circ}$. Studies of the 6mm aperture (the wing without any slot fitted) were not pursued after it was found that uniform jet velocity in the spanwise direction was not obtained, changing the character of the tests from two dimensional to strongly three dimensional fluid dynamics outside the scope of this research. The wake survey revealed that velocity deficits in the wake at low incidence could be overcome using the 1mm and 1.5mm slot heights. An example of the wake profiles is given in FIGURE 7.7 where activation of the jet with a maximum voltage of 368V peak-to-peak, $C_{\mu}=0.136$, causes a jet-like profile indicative of positive thrust coefficient under these conditions. Estimates of momentum coefficient had been increased by a factor of between two and three in using the larger slot heights, decreasing the restriction on the membrane.

Time-averaged PIV captures showed the clear difference in jet performance of the 0.5mm, 1mm and 1.5mm slots as shown in FIGURE 7.8. The increased height of the 1mm and 1.5mm slots decreased the restriction on the actuators significantly enough to enable larger resonance giving nearly double the actuator amplitude compared to the 0.5mm slot. Whilst the 0.5mm slot does not enable a strong jet to be formed, the 1mm and 1.5mm slots do.

As the momentum coefficients for the 1mm and 1.5mm slots were similar and the exit velocities of the 1mm slotwere shown to be higher, just the 1mm slot was used to test at different incidences. PIV neasurements were conducted first with the internal actuators turned off and then turned on to maximum voltage for $\alpha=\{0^{\circ}, 5^{\circ}, 10^{\circ}\}$ as shown in FIGURE 7.9. Even at a higher incidence of 10°, a jet-like profile is clearly evident as regions of high velocity emanating away from the jet exit. Whilst the drag coefficient for the aerofoil without jet excitation at higher incidences is greater than for the externally driven wing, a sufficient momentum coefficient can be achieved on maximum voltage in order to overcome the deficit and produce a thrusting force. FIGURE 7.10 shows the downstream velocity profiles for the higher incidence of $\alpha=10^{\circ}$ without jet excitation compared to maximum jet excitation using the 1mm slot, confirming that a jet-like profile is achieved indicative of positive thrust.

7.3 FORCE MEASUREMENTS

In order to measure the forces experienced by the aerofoil with and without the use of the jet, the aerofoil was fixed to the low Reynolds number force balance (LRNFB) designed by Russell Jones in conjunction with the author as part of a final year project at the University of Bath. Whilst the balance had measurement gauges (see experimental set-up) for both lift and drag/thrust force measurements, the resonance of the membrane on the lower surface of the aerofoil was expected to inhibit measurements in the lift direction; the vibration occurring in the direction of the lift force.

FIGURE 7.11 shows how the momentum coefficient affects the thrust coefficient at four incidences using the LRNFB. Unlike the behaviour observed using the externally actuated wing, small momentum coefficients are seen to cause larger changes in thrust coefficients for all of the incidences tested. It is expected that this feature may be due to a positive effect of the membrane vibration on the flow around the aerofoil. Whilst the feature is not investigated further here, it should be the subject of further study. Consequently, whilst the drag coefficients of no excitation measured on the LRNFB are in line with expectations, the critical momentum coefficients required for a zero nett drag condition are lower than those of the externally powered aerofoil. It is known that manipulating the aerofoil surface using trips or active vibration can cause increased

aerodynamic performance. Perhaps if the membrane could have been fitted to the upper surface, the performance gains may have been larger. Once again though, it is shown that at the highest incidence, the increase of momentum coefficient only has a limited effect on the thrust coefficient due to the stalled nature of the aerofoil.

FIGURE 7.12 summarises the effect of incidence on thrust coefficient without excitation compared to with maximum excitation. At all incidences tested, measurements confirmed that sufficient momentum coefficients cause significant decreases in drag coefficient, sufficient to generate positive thrust at lower incidences.

Whilst measurements of lift coefficient were not possible with non-zero jet excitation due to vibrations in the lift measurement direction, FIGURE 7.13 shows the variation in lift coefficient with Reynolds number for no jet excitation. Whilst the small lift coefficient corresponding to $\alpha=0^{o}$ remains approximately constant, the lift coefficients of the other higher incidences are seen to increase with increasing Reynolds number, in line with observations of improved aerodynamic performance at higher Reynolds numbers.

7.4 POWER AND EFFICIENCY MEASUREMENTS

To understand the power requirements in comparison to other driving mechanisms, considerable effort was made to find both the real time power consumption as well as the mean power consumption. It is interesting and insightful to find the real time variation in voltage and current drain to understand how and when the actuator requires power.

Whilst the input to the actuator driver circuitry was a pure sine wave, the measured voltage fluctuations across the actuators, shown in FIGURE 7.14, varies due to the load on the signal generator and complex fluctuations in the electrical properties of piezoelectrics; variable capacitance, variable resistance as well as non-linearity. Application of a positive voltage to the actuator causes a deflection upwards. Application of a negative voltage causes a deflection downwards.

The corresponding current drain in real time (as shown in FIGURE 7.15) shows unsurprisingly how the piezoelectrics draw most current close to when most positive or most negative voltages are supplied (deflecting the actuator away from the neutral 'at rest' position). The current drain returns quickly to zero, corresponding to when the piezoelectric returns from deflected position to undeflected (neutral) position. The change in electrical properties of the actuators during the cycle causes spurious but periodic spikes in the current waveform, shown here around t=0. Note also that there is a small phase lag between the voltage signal and the current signal due to the constantly changing electrical characteristics of the actuators.

As shown in FIGURE 7.16, the resultant real-time power drawn shows fluctuations from 0W to around 5.5W. The actuator draws most power when large positive or negative voltages are applied (deflecting away from the neutral position) but, as one would expect, requires 0W power moving from peak deflection towards the neutral position close to when the voltage supply is zero. When passing through the neutral position, a small blip is seen in the real-time power consumption again caused by an inductance-capacitance change in the actuators' electrical properties.

The mean power consumption of the two actuators running at maximum voltage of 368V peak-to-peak at 34Hz was found to be 2.14W, C_E=31.83, with mean current drain around 20mA. Similar real-time electrical analysis was performed for a range of excitation voltages other than the maximum voltage to understand the power-voltage relationships. It was shown (FIGURE 7.17), that the power consumption has a squared relationship to the supplied voltage; the implication being that it becomes increasingly inefficient from a power consumption view to run the actuators at higher and higher voltages. FIGURE 7.18 shows that the relationships between momentum coefficient and power coefficient are linear. Therefore, whilst momentum coefficient will remain the parameter of study rather than power coefficient, the relationship is interchangeable by a linear transformation of the parameters.

Considering the propulsive efficiency of the system in relation to the magnitude of the momentum coefficient achieved, the propulsive efficiency is seen to decrease with increasing momentum coefficient as shown in FIGURE 7.19. As a result it can be said that presently, the system would operate considerably more efficiently for low values of

momentum coefficient compared to higher momentum coefficients. The variation in thrust coefficient with momentum coefficient (discussed previously, shown in FIGURE 7.11) was seen to show large increases for small momentum coefficients. The effectiveness of the small momentum coefficients is reflected in the propulsive efficiency at small nomentum coefficients. From the power consumption perspective, it would therefore be best to fly the MAV with as small a momentum coefficient as necessary.

However, consideration must be given to the likely effect on lift coefficient whilst operating the jet at low momentum coefficients. Recall that from the externally actuated, pressure tapped wing experiments, estimates of lift coefficient suggest a drop in lift force at around the critical momentum coefficient, recovering and then increasing beyond base level after around one and a half to two times the critical momentum coefficient is reached.

As lift coefficients could not be measured for non-zero jet excitation, the following assumption had to be made. It was assumed that the momentum coefficient caused similar increases and decreases in lift coefficient as those estimated from the externally actuated aerofoil. The percentage change in lift coefficient with momentum coefficient from the external aerofoil was therefore applied to the lift coefficients of the internally actuated aerofoil without jet excitation to derive estimates of lift coefficients for the non-zero jet excitation performance of the internally actuated aerofoil. Whilst the estimates derived do not account for the effect of lower surface vibration on lift coefficients, the surface vibrations suggest enhanced performance therefore the estimates are likely to be conservative. They offer the most sensible underestimated guide to the expected performance of the internally actuated wing.

Accounting for the likely lift performance with the effect on drag and thrust caused by the jet, the aerodynamic efficiency parameter was used, the results of which are shown in FIGURE 7.20. Optimum positive efficiency is seen to be achieved above about $0.01 < C_\mu < 0.05$ over the range tested. As the momentum coefficient increases, the total efficiency converges to a similar value for all incidences. Note that the maximum aerodynamic efficiency values are higher in relation to those found with the externally actuated wing. Largely this is due to the low momentum coefficients' causing greater

increases in thrust coefficients compared to the performance of the externally actuated system. Whilst it is not investigated further during the research presented here, the surface vibration is a feature meriting considerable further investigation.

FIGURE 7.21 combines the aerodynamic and propulsive efficiency parameters in a figure of merit (FM). The FM reflects the benefits of using very small momentum coefficients to generate comparatively large improvements in the aerodynamic performance of the aerofoil system. In addition the larger momentum coefficients FM values converge in the range tested as suggested by both the A_E and P_E parametric studies.

7.5 FURTHER IMPROVEMENTS

Considering that the thrust to weight ratio of the internal mechanism is around 34 times greater than that of the speaker used in the laboratory experiments, considerable savings in weight and increase in thrust had been made to the internal actuator mechanism with only modest efforts.

The piezoelectric actuators weigh around 18g each. As a typical MAV might weigh around 60g - 120g in total, a mechanism of 36g is comparatively heavy and would require significant further work to reduce weight. However, around 65%-75% of the actuator weight is composed of the rolled steel shim. Whilst the pre-stressed property provided by the steel shim is necessary, it may be possible to use a substitute material offering better performance for less weight. Besides the weight, the rigidity of the steel shim also contributes to resisting the motion of the piezoelectric sheet. Whilst a less rigid shim might offer less pre-stress potential, perhaps the shortfall could be overcome in resisting the driver motion less. Considerable further work would e required in actuator development in order to achieve a mechanism with capabilities closely matching those required by a realistic MAV concept.

With the weight and efficiency of the actuators in mind, considerable efficiency gains could be achieved by replacing the membrane with a self-powered membrane or piezoelectric sheet, negating the need to have a stiff piezo-electric bender. Using a self-deforming structure either on the underside as with the existing experiments, or on the

upper-side for further aerodynamic benefit, or even on both surfaces. Use of deformable surfaces on the top and bottom of the MAV would reduce the required amplitude proportional to the increase in actuated area.

The maximum forcing level found with the laboratory speaker gave a momentum coefficient around C_μ=0.63 at Re=20,000; 4.5 times the thrust offered by the internal mechanism and sufficient to obtain a critical momentum coefficient for Re=60,000 at low incidence. In changing the nature of the internal actuation system to cover both upper and lower surfaces and allow more efficient deformation of the flexible areas, it might be realistic to anticipate a gain in maximum thrust of a factor of two or three, maybe more with detailed analysis. Assuming that could be achieved, a calculation based on available maximum momentum coefficient reveals that the MAV could reach a critical momentum coefficient around Re=47,000 to Re=58,000 at low incidence, which could support a vehicle of weight around 20g-40g (FIGURE 7.22). With upper surface excitation, improved lift coefficients are also likely making the system yet more capable. At around Re=40,000, the MAV would be able to support a total mass of around 20g at high incidence or around 10g at lower incidence.

Considering a typical MAV, the usual flight speed is around 8-15m/s. Flight at those speeds is not yet possible with a synthetic jet propulsion solution and considerable work is required to achieve that. In addition, whilst by no means optimised, the maximum propulsive efficiency of the system was found to be around 7%. Some of the best MAV propellers to date have efficiencies of around 80%, although in combination with a motor (and possibly gearbox apparatus) that is often reduced to less than 50%. To offer a realistic alternative to propeller propulsion systems, the efficiency of the existing system would need to be improved by a factor of 6 or 7. Considering the optimum Strouhal number identified in Chapter 5, if the flight speed of the synthetic jet powered MAV were increased by a factor of between 5 and 10, the optimum Strouhal number would be closer to, and may overlap, the Helmholz frequency of the cavity geometry. Matching the resonance of the actuator to this Helmholz resonance at the optimum Strouhal number might offer an order of magnitude improvement in propulsive efficiency. To achieve that, considerable work is required with development and evaluation of improved actuators and cavity arrangements.

Furthermore, existing systems for driving propellers either rely on small-scale internal combustion engines or low voltage electric motors. Providing the high voltages required by the piezo-electric devices investigated here is possible at small scales, but with a considerable weight penalty. Extensive further research would be required into the power sources for high voltage, low current actuators with a particular focus on lightweight design.

7.6 FIGURES

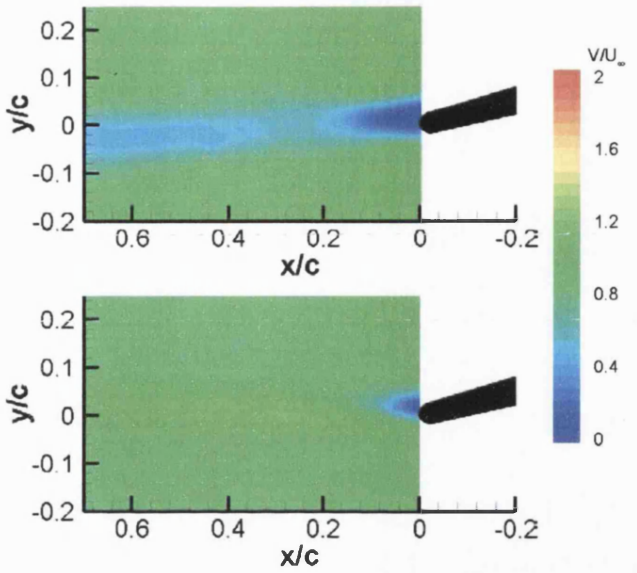

FIGURE 7.1 Time-averaged velocity magnitude contour plots taken by PIV showing no jet excitation (top) and maximum jet excitation (bottom) with the 0.5mm slot.

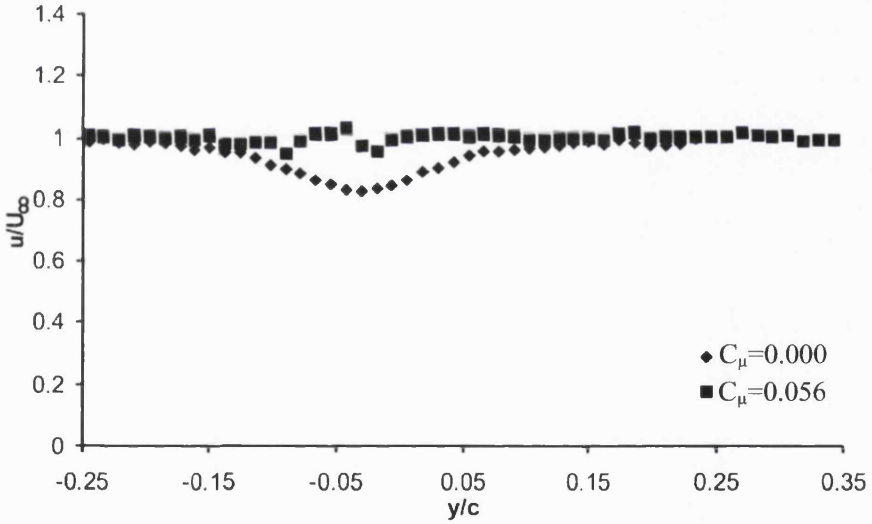

FIGURE 7.2 Time-averaged streamwise velocity profiles taken using LDV at x/c=0.5, Re=20,000, $\alpha=5^{o}$, with and without jet excitation at St=4.86

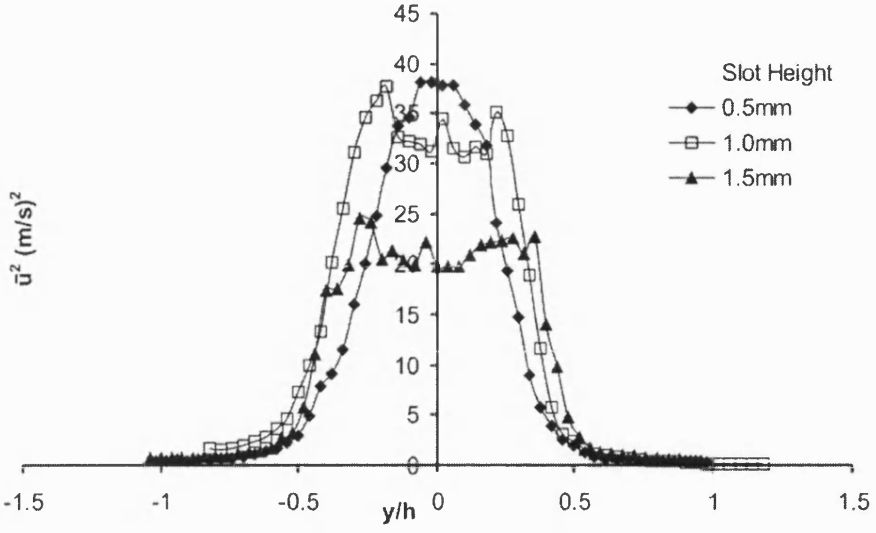

FIGURE 7.3 Mean $\bar{u}^2$ profiles for the three slot widths taken by LDV at 1mm from the slot with actuators resonating at St=4.86 at maximum voltage 368Vpp in quiescent flow.

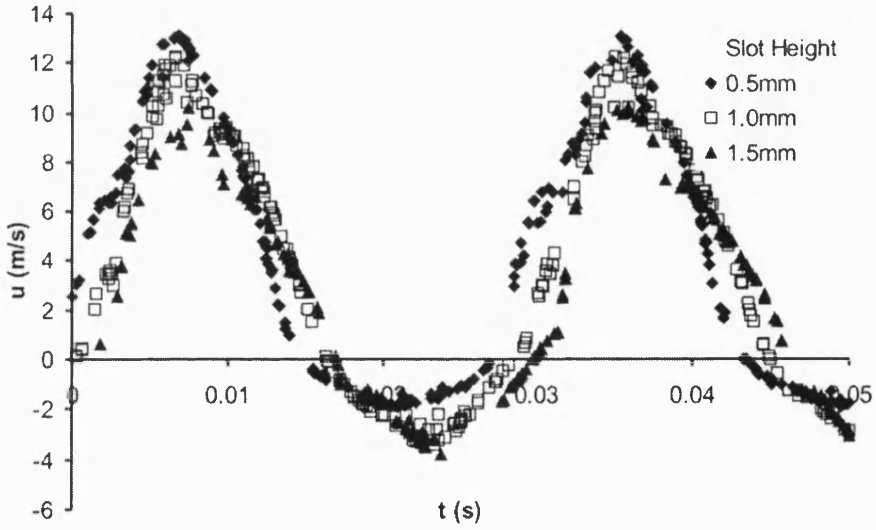

FIGURE 7.4 Real time jet centreline u-velocity signal captured by LDV for 3 different slot heights with U_∞=0 at 1mm from the slot exit with actuators resonating at St=4.86 at maximum voltage 368Vpp.

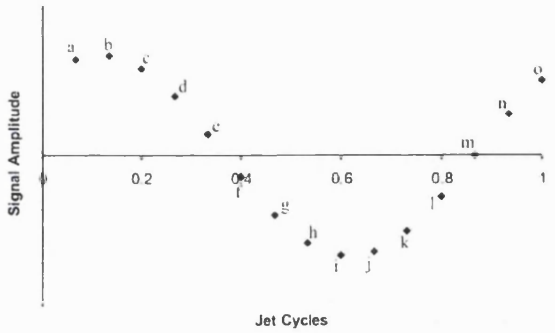

FIGURE 7.5 Plot showing location of 30 instantaneous PIV captures (below) in 1 cycle duration.

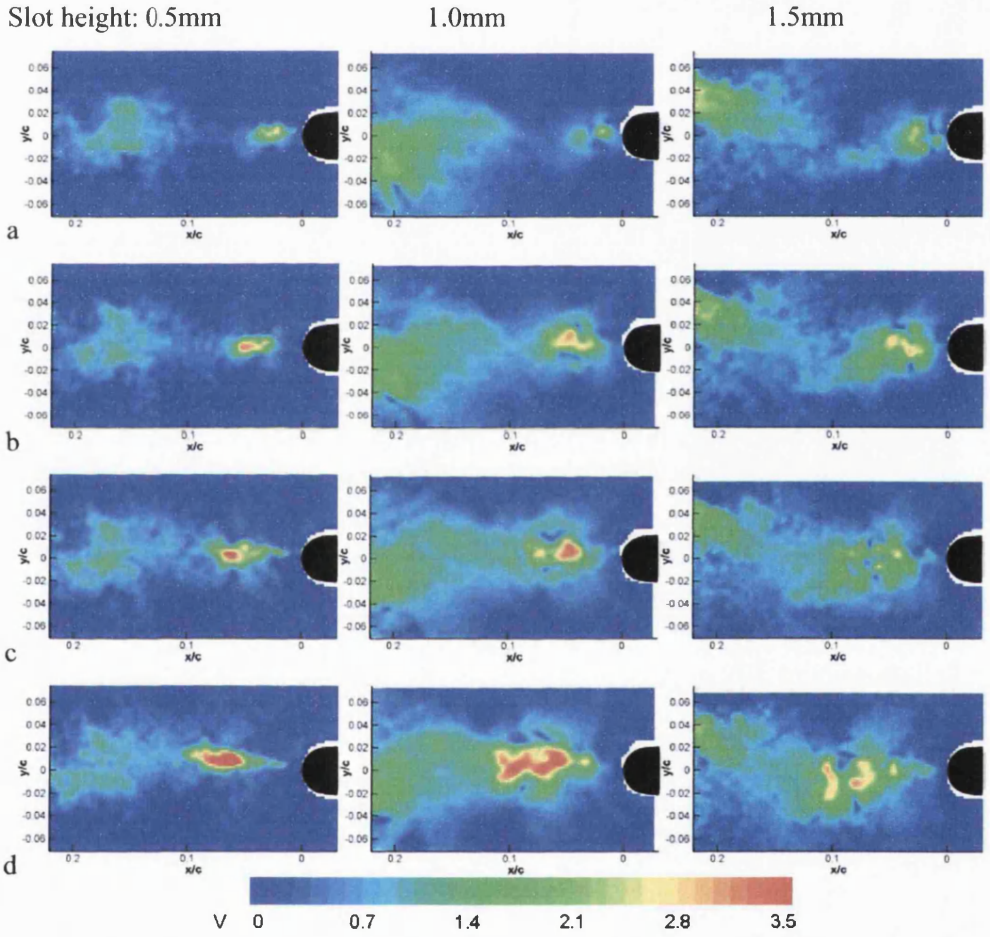

FIGURE 7.6 One complete cycle of instantaneous velocity magnitude plots taken by real time PIV showing one cycle of each slot – 0.5mm, 1.0mm and 1.5mm – in quiescent flow at maximum voltage of 368Vpp operating at 34Hz (which would give St=4.86 at Re=20,000) (continued overleaf).

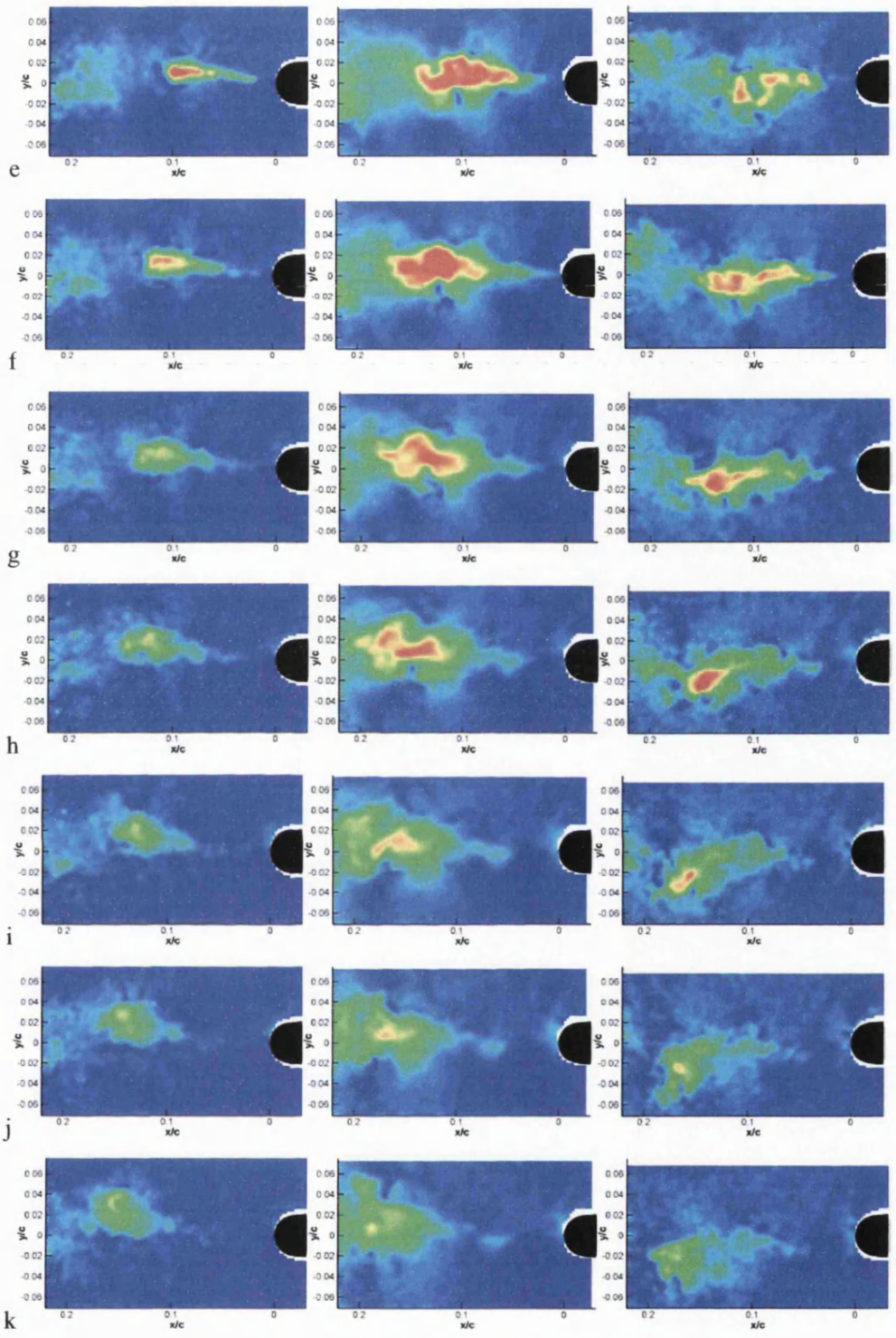

Continued.

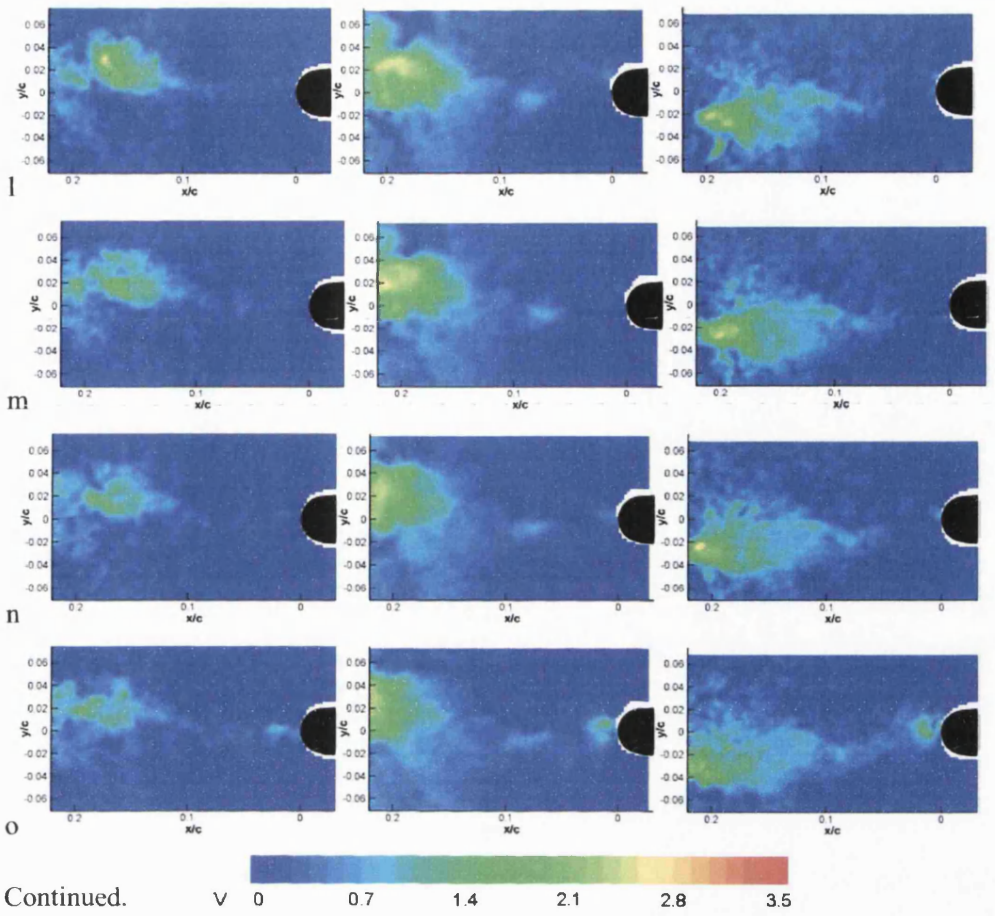

Continued.

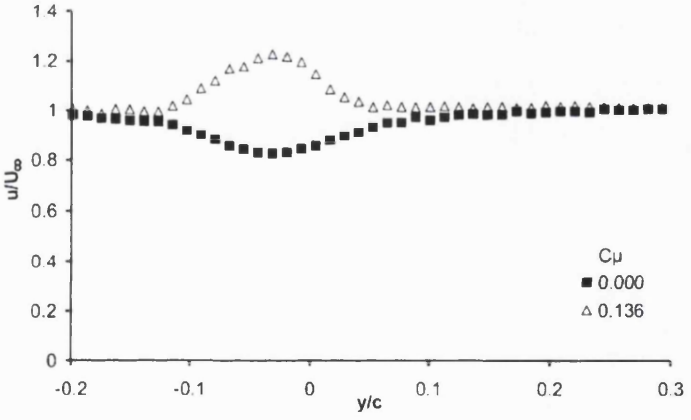

FIGURE 7.7 Time-averaged wake velocity profile by LDV at Re=20,000, a=5°, at x/c=0.5 using the 1mm slot showing cases with and without full jet activation.

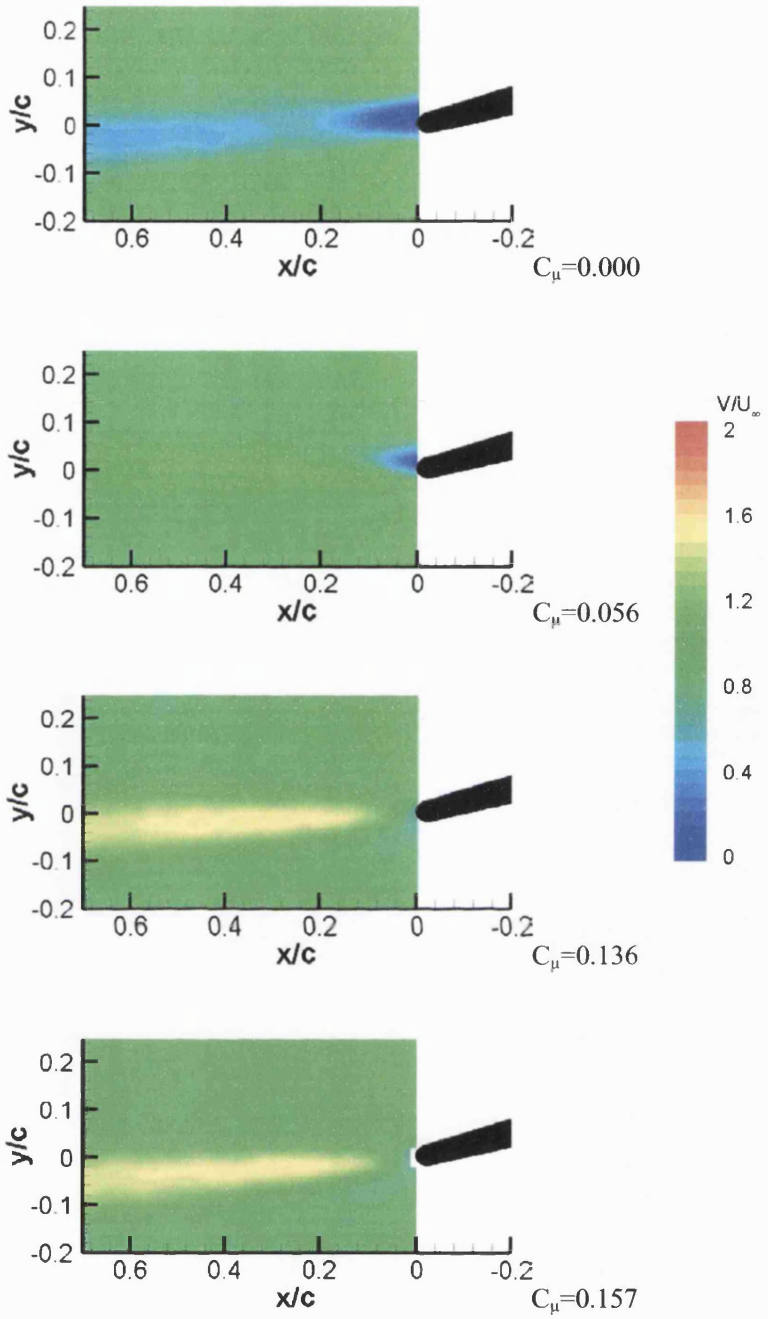

FIGURE 7.8 Time-averaged PIV velocity magnitude contour plots for Re=20,000 at $\alpha=5^{\circ}$ showing the effect of slot width compared to the no-jet excitation case.

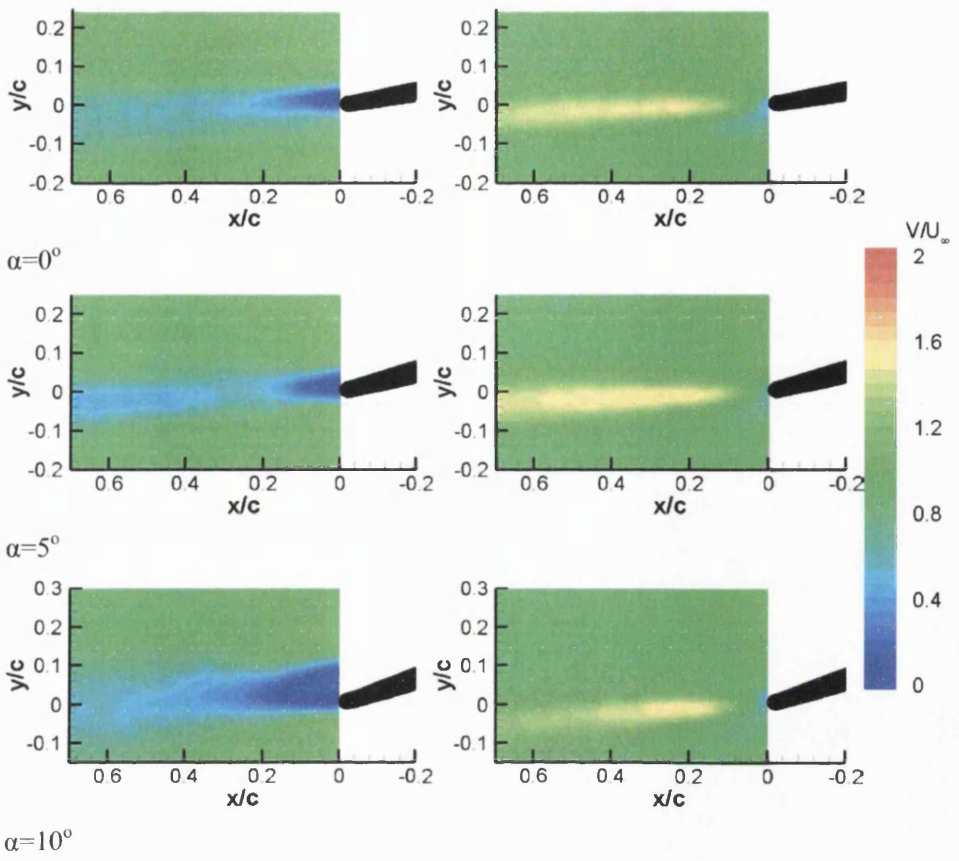

FIGURE 7.9 Time-averaged velocity magnitude plots taken using PIV with Re=20,000, showing differences at increasing incidence between conditions without jet excitation and maximum jet excitation with C_μ=0.136.

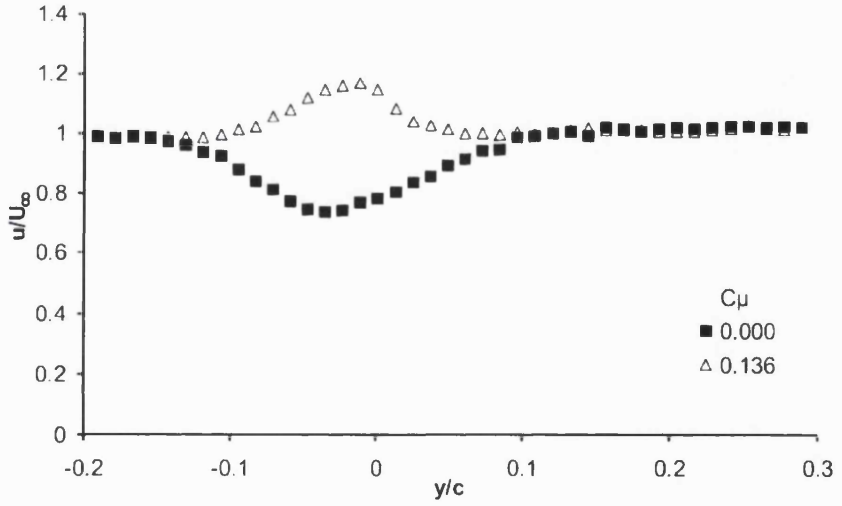

FIGURE 7.10 Time-averaged streamwise velocity profiles taken by LDV showing about the velocity deficit in the wake is replaced by a nett gain in velocity upon jet activation at Re=20,000, α=10°, at x/c=0.5.

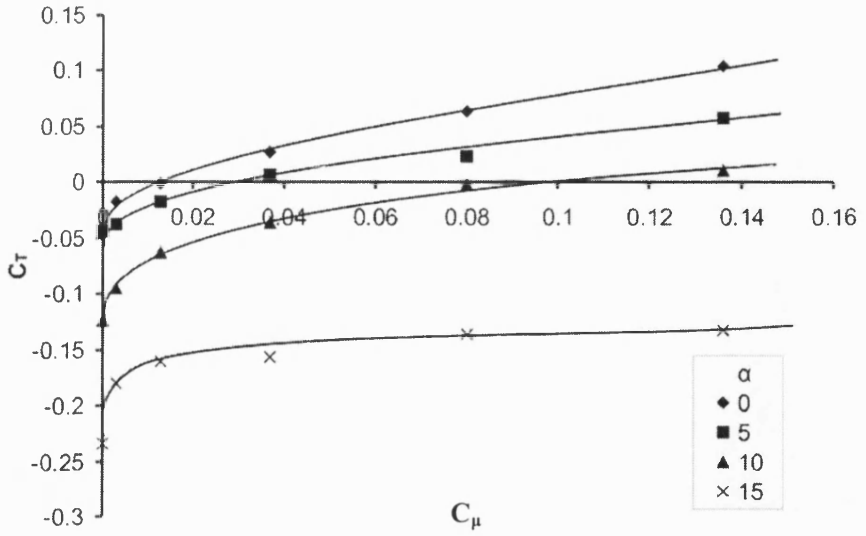

FIGURE 7.11 Effect of momentum coefficient on thrust coefficient measured using the LRNFB at Re=20,000, 1mm slot.

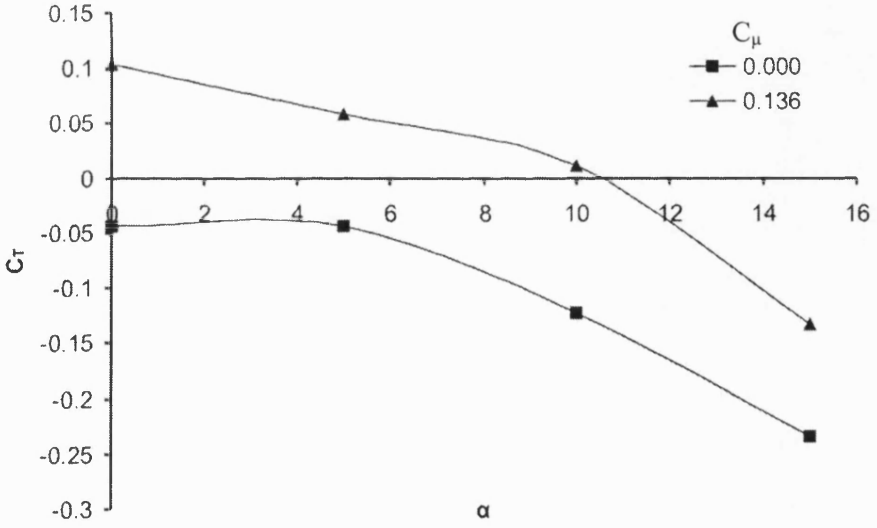

FIGURE 7.12 Effect of incidence on thrust coefficient, measured using the LRNFB at Re=20,000.

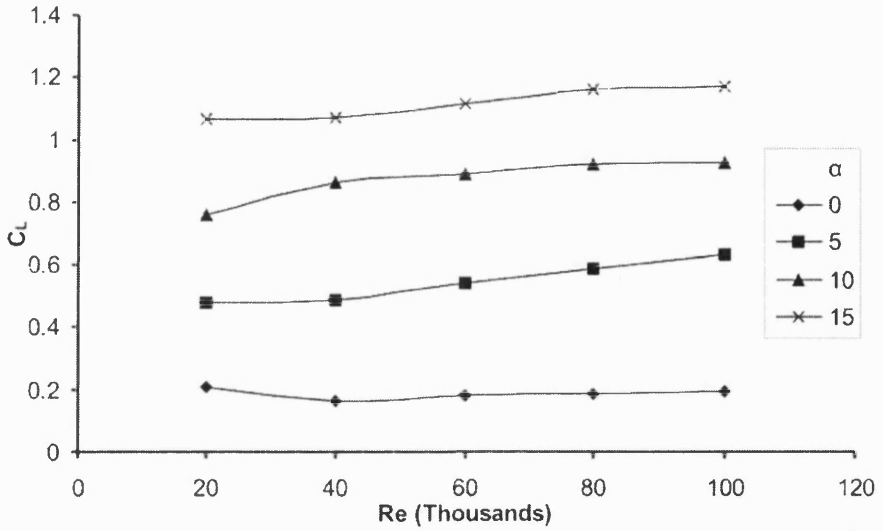

FIGURE 7.13 Effect of increasing Reynolds number on lift coefficient without jet excitation measured using the LRNFB.

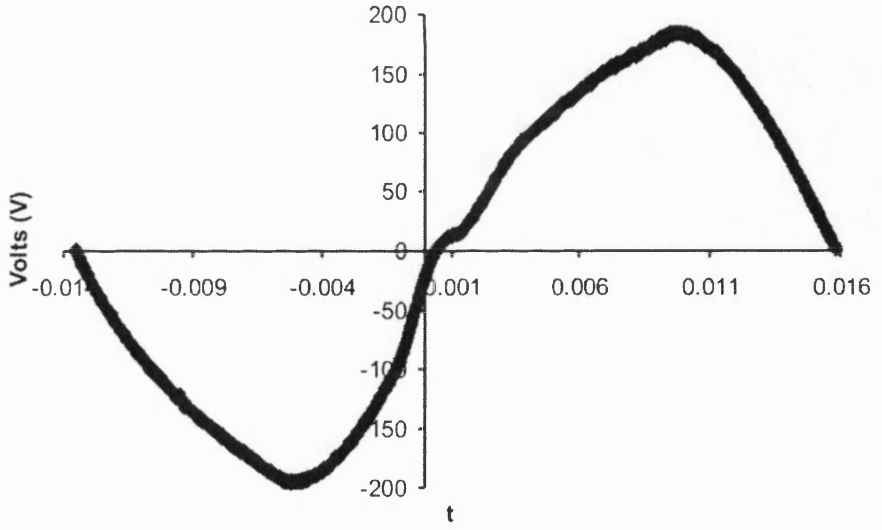

FIGURE 7.14 Voltage signal measured across actuator showing deviation from its pure sine wave input due to varying inductance, impedance and capacitance. Captured using digital oscilloscope with actuators resonating in free air at St=4.86, on maximum voltage of 368Vpp.

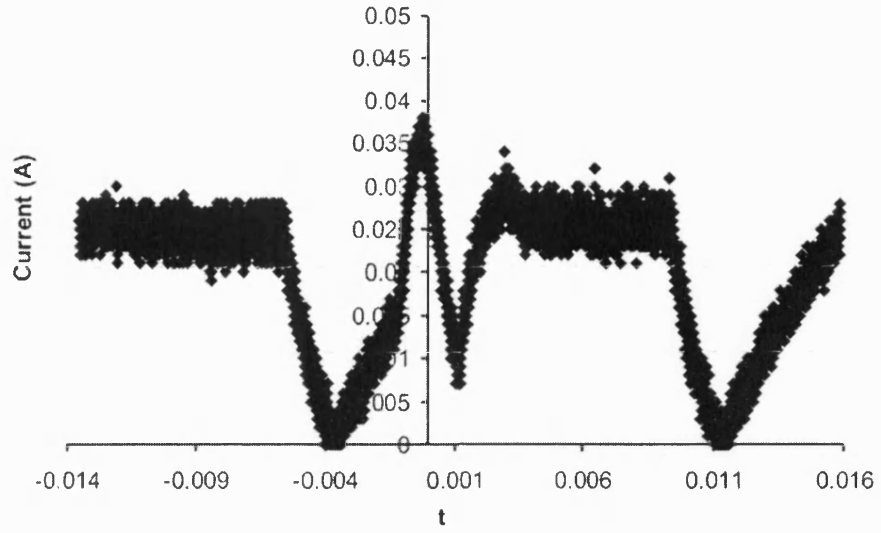

FIGURE 7.15 Current supplied to the actuator (read indirectly) captured using digital oscilloscope, actuators resonating at St=4.86 on a maximum voltage of 368Vpp at Re=20,000.

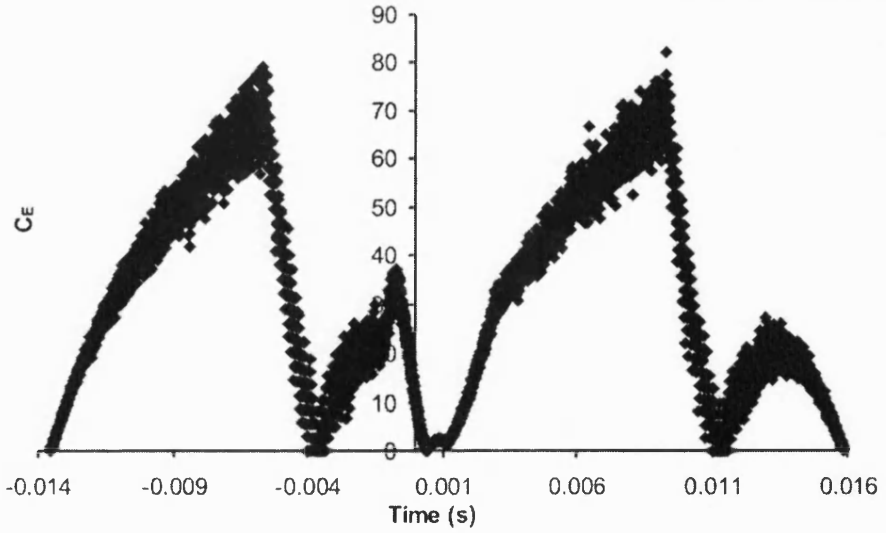

FIGURE 7.16 Resultant real-time power coefficient curve for internal actuators resonating at St=4.86 at a maximum voltage of 368Vpp at Re=20,000.

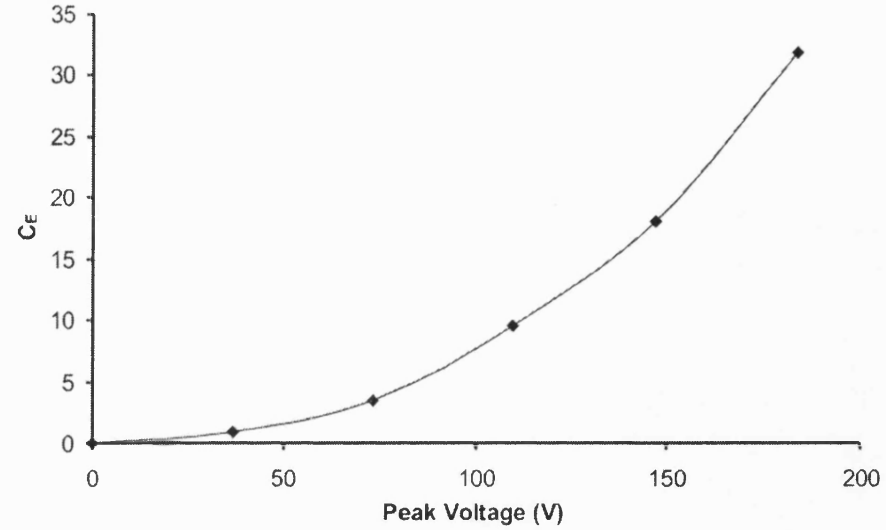

FIGURE 7.17 Variation in mean power coefficient drawn by the actuators due to increasing peak supply voltage resonating at St=4.86 at Re=20,000.

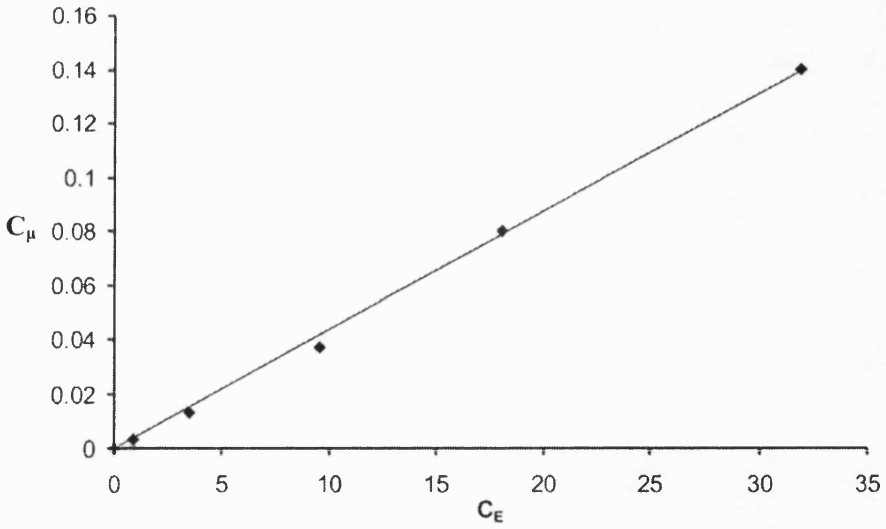

FIGURE 7.18 Plot showing linear relationship between power coefficient and momentum coefficient.

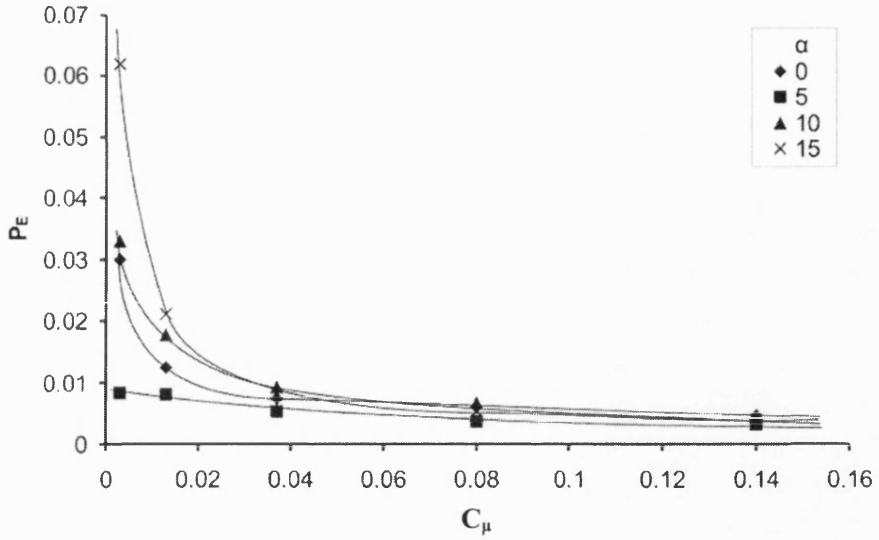

FIGURE 7.19 Variation of propulsive efficiency with increasing momentum coefficient (accounting for forces contributing only to thrust) operating the jet at St=4.86, Re=20,000, with 1mm slot.

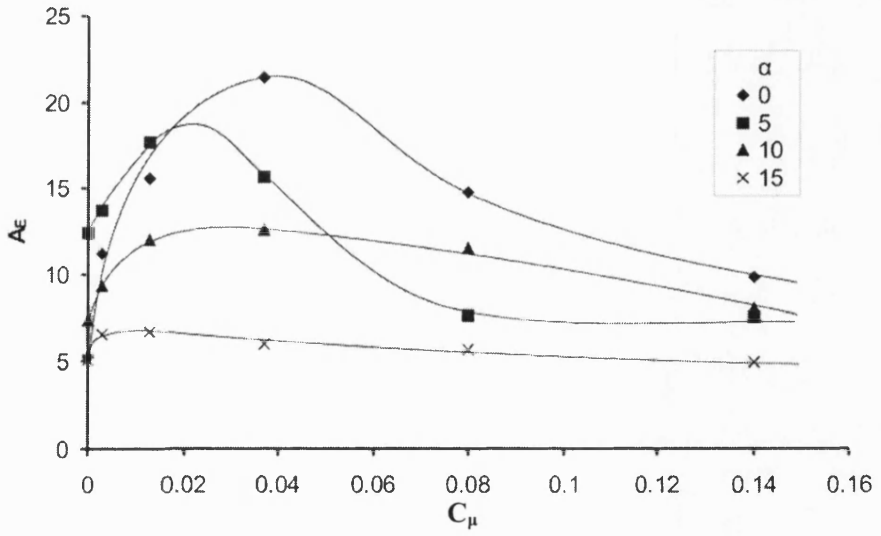

FIGURE 7.20 Effect of increasing momentum coefficient on aerodynamic efficiency at Re=20,000, St=4.86, 1mm slot.

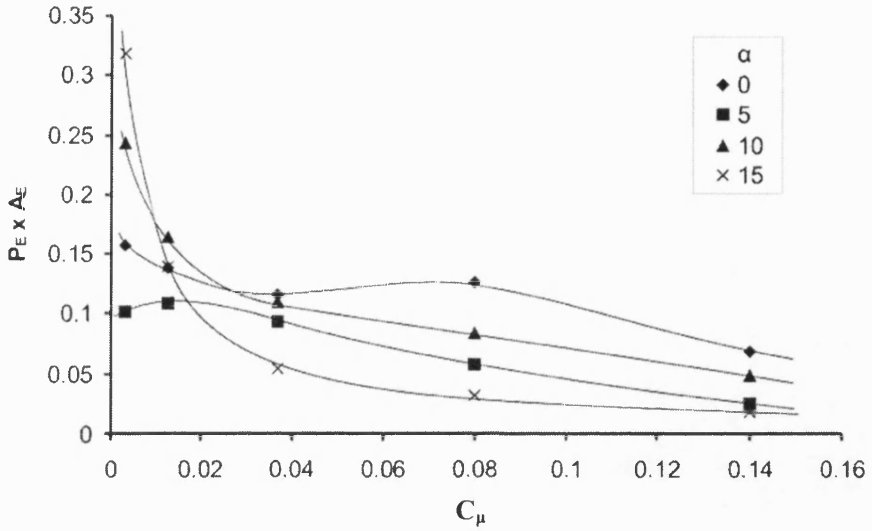

FIGURE 7.21 Effect of increasing momentum coefficient on overall efficiency of MAV aerodynamics and power systems operating the jet at St=4.86, with 1mm slot at Re=20,000.

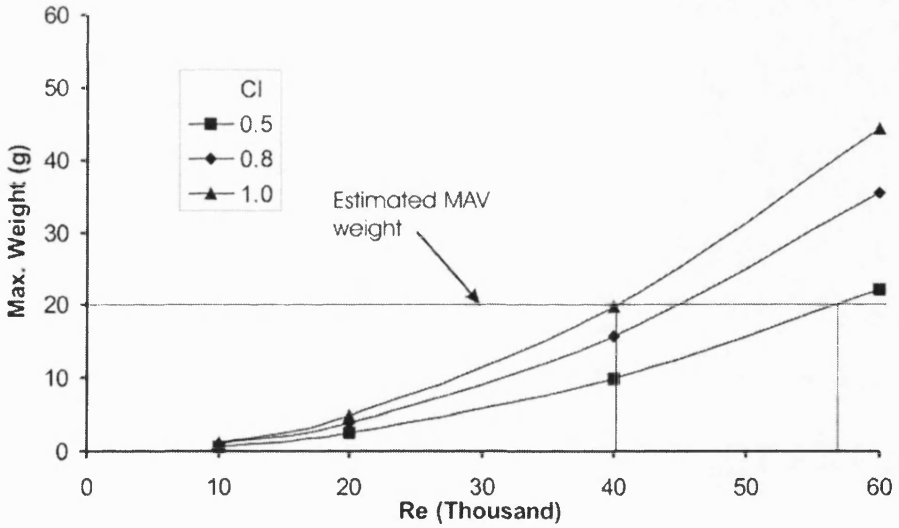

FIGURE 7.22 Plot showing the effect of increasing flight speed on sustainable MAV total weight, indicating that a 20g MAV could be supported in flight by a lift force created at around Re=40,000 or at around Re=56,000 at lower incidence.

CHAPTER 8 CONCLUSIONS AND FURTHER WORK

8.1 CONCLUSIONS

The primary aim of the research was to provide an understanding of the groundbreaking use of synthetic jets to propel and enhance aerodynamics of MAVs, assessing feasibility and providing insight into the key parameters.

The University of Bath water tunnel was used for initial flow visualization, identifying some key fluid dynamic features of the system and enabling a choice of a low Reynolds number aerofoil for further study in conjunction with a trailing edge synthetic jet system.

Whilst the University of Bath open jet wind tunnel did not offer the cleanest freestream quality for low Reynolds number studies, analysis of the turbulence levels showed that the flow quality was satisfactory for the study to produce accurate results, especially with the advent of the replacement motor and controller system.

The effects of jet momentum coefficient were studied. It was found that, given sufficient momentum coefficient, zero nett drag could be achieved, corresponding to a cruise condition for a MAV. Increasing the momentum coefficient beyond this critical momentum coefficient caused a positive thrust coefficient and would accelerate the MAV.

Significant effect on the fluid dynamics over the aerofoil surface was noticed. Without jet excitation, a particular low Reynolds number aerofoil was shown to experience significant separation, laminar in nature at very low Reynolds numbers, but increasingly turbulent at higher Reynolds numbers. Jet activation at low incidence caused the separated shear layer to be drawn closer to the trailing edge. Given sufficient momentum, close to the critical momentum coefficient, the separated shear layer could be seen to reattach at the trailing edge suggesting an enhancement in lift over the aerofoil.

Operation of the synthetic jet and aerofoil system at higher Reynolds numbers within the low Reynolds number regime, showed the benefits of operating in those more favourable conditions. Without jet excitation, lift coefficients and thrust coefficients were seen to increase with increasing Reynolds number. The benefits of operating at higher Reynolds numbers were shown to persist throughout the range of momentum coefficient used with jet excitation. Even at higher incidences, near stall, jet excitation was shown to considerably enhance the performance of the aerofoil, reducing drag coefficients and, under certain conditions, causing positive thrust coefficients.

Whilst a strong jet and reattachment was shown to be possible for a range of Strouhal frequencies, greatest thrust coefficients were achieved for $2<St<5$ for a fixed momentum coefficient. Whilst the performance of high frequency jets was expected to decay, the low frequency jets were seen to cause significant instability and deteriorated performance in the suction half of the jet cycle.

Significant effort was made to estimate the effect of trailing edge jet excitation on lift coefficient of the aerofoil system. It was found that as the jet angle changed in relation to the wake by changing the aerofoil incidence, the surface pressures around the trailing edge could be altered on the upper and lower surface to varying degrees. In general, low momentum coefficients were seen to cause a reduction in lift estimates due to greater influence on the lower surface pressures. However, as the momentum coefficient increased sufficiently to bring the separated shear layer within the influence of the trailing edge (around the critical momentum coefficient), the lift coefficient could be increased significantly above the baseline lift coefficient of the plane aerofoil without a jet. Estimates of thrust based on surface pressures and injected momentum coefficient

from the jet produced reasonable estimates of thrust for higher incidence. The improvement of flow over the upper surface was suggested by the decrease in surface pressures caused by sufficient jet momentum. An efficiency parameter similar to a lift-to-drag ratio was used to show the aerodynamic effect of momentum coefficient, showing that the synthetic jet system was most effective at higher Reynolds numbers at low incidence. Low incidence conditions were shown to experience deterioration in the aerodynamic efficiency at low momentum coefficients due to the deteriorating lift coefficient in this range. Careful analysis of a particular MAV mission profile would identify the most desirable trade-off between lift and thrust for the mission. A lightweight MAV would not require the lift coefficients needed for a heavier MAV and therefore the importance of a reduced lift coefficient could be an acceptable alternative to a zero nett drag or higher nett thrust system.

Whilst the laboratory speaker driven test rig was not designed with efficiency of operation in mind, it was shown how the inefficiencies of the high power range of the system would impact on the overall efficiency of the system becoming the dominant issue for the design of the complete system. For that reason, low Reynolds numbers performed best requiring the low power range of greater efficiency. An optimum overall efficiency figure of merit showed that whilst the very low momentum coefficient range was extremely inefficient, slightly higher momentum coefficients ($C_\mu < 0.08$) showed the most efficient performance. As the momentum coefficient increased further, the efficiency was seen to gradually reduce and converge for all of the incidences tested.

Several slot geometries were tested showing considerable variations in their respective aerodynamic performances. The biggest difference was shown to be in the propulsive efficiency associated with the three slot geometries experimented with. A narrow 0.5mm slot outperformed both a 1.5mm and a 1.5mm deflected slot. The disadvantage of the narrow slot is increased resistance on the actuation mechanism, which limits the maximum range of momentum coefficient achievable.

An innovative internal mechanism was designed and implemented to demonstrate potential enabling technologies for synthetic jet driven MAVs. Large 'Thunder' piezoelectric actuators were used to activate a membrane built into the lower surface of the aerofoil as an internal synthetic jet actuation system. The actuators were chosen for

their natural resonance around the optimum range of excitation frequency identified in earlier experiments. Whilst the 0.5mm slot proved a large restriction for the performance of the actuators and reduced the maximum momentum coefficient to 0.056, experimentation with a variety of slot heights showed a significant increase in system performance with the use of a 1mm slot. The maximum momentum coefficient achieved was 0.136, enabling a jet like profile to be achieved at low and high incidence in PIV experiments.

A key advantage of the internal mechanism built into a lightweight SLS prototyped wing, was the ability to suspend the aerofoil in the custom made LRNFB. Whilst the most advanced electronic amplification and conditioning were not available, significant repeatability and accuracy were demonstrated on the LRNFB, sufficient to give confidence in the measurements taken. The measurements of lift were only possible without jet excitation due to vibration although this was sufficient to suggest reasonable accuracy had been achieved with the pressure measurement system. Measurement of thrust was possible over the entire range of momentum coefficient and showed the positive thrust that could be produced by the synthetic jet system or sufficient momentum coefficient. Whilst similar performance of the internal mechanism was not expected to compare to the speaker driven system due to the oscillating under-surface, sensible comparison of the baseline lift and drag could be made with allowance for the thickened mid-section of the internally actuated wing. These agreed well, both showing that with momentum coefficients of $0.15 < C_{\mu} < 0.20$, positive thrust coefficients could be achieved for incidence beyond $\alpha=10^{o}$. The internally actuated aerofoil provided improved aerodynamic efficiency compared to the externally actuated aerofoil, suggesting that the lower surface excitation contributed to an increase in overall aerodynamic performance. Future work should explore this effect further. Propulsive efficiency was increased by a factor of four using the internal mechanism for low momentum coefficient, but was found to be similar to the external system for higher momentum coefficients. Consequently the overall performance of the internally actuated wing was significantly greater than the external system for low momentum coefficient but comparable for higher momentum coefficients.

8.2 FUTURE WORK

Discussion and analysis following the development of the internally actuated system showed that the desired performance of a real mechanism was within sight of existing technology. In changing the nature of the internal actuation system to cover both upper and lower surfaces and allow more efficient deformation of the flexible areas, it might be realistic to anticipate a gain in maximum thrust of a factor of two, although careful consideration would have to be given to the effects of surface distortions on the aerodynamics. Assuming that could be achieved, a calculation based on available maximum momentum coefficient reveals that the MAV could reach a critical momentum coefficient around Re=40,000 at high incidence, which could support a vehicle of weight around 20g. Estimating a possible configuration weight of around 20-25g of the synthetic jet powered MAV, the improved configuration may be sufficient to propel and support the MAV and payload in flight given significant further work on actuation mechanisms, power supplies and cavity designs.

If current rapid progress in smart material technology continues, the availability of high torque, lightweight actuators might enable a capable mechanism for propulsion of MAVs in conjunction with large developments in other areas. It is hoped that the study performed here would be an important precursor to future developments in this area, especially to provide insight into and understanding of the associated parameters and the effect of surface pressures, as well as motivating a realistic mechanism for driving the actuation.

Future work should consider the location and geometry of the jet exit slot more thoroughly. Location on the upper surface might enable easier reattachment capability of the jet and location of the flexible membrane on the upper surface may enhance the upper surface flow.

The piezoelectric drivers used against the membrane in cantilever mode could be significantly improved in efficiency if an electro-active polymer (EAP) film or similar could be used as an active membrane. Whilst the Thunders are excellent for high force and amplitude applications, EAPs show increasing capability. EAPs may offer new challenges of controlled displacement shape but they may be a technology worth

exploring. The use of a resistant membrane also decreases jet performance. High power fixed boundary actuators are growing in capability and it may be within the realms of current technology to develop a suitable actuator for this application.

Consideration should be given to three-dimensional geometries of complete MAV systems. With multiple jets, it would be theoretically possible to eliminate the need for control surfaces carrying an otherwise heavy drag penalty. Left and right jet control may enable complete three-dimensional control of the MAV without the weight penalty of mechanical control surface drivers and mechanisms.

Whilst the focus of this study was on a uniform two-dimensional jet, consideration of distributed jets may also be able to create two-dimensionality during operation. Momentum injection along the entire span may not be necessary for reattachment. Saving on propulsive efficiency and therefore overall system efficiency could be achieved if span-wise narrower slots could be used. More generally, further research is required on the implications of using a three dimensional aircraft on predicted performance, weight implications and interaction with the synthetic jet system.

CHAPTER 9 REFERENCES

9.1 REFERENCES

1. **Adrian, R. J., (1997)** "Dynamic ranges of velocity and spatial resolution of particle image velocimetry," *Measurement Science Technology*, Vol.8, pp.1393-1398.

2. **Adrian, R. J. (1978),** "Estimation of LDA Signal Strength and Signal-to-Noise Ratio," *TSI Monthly*, Vol. IV, Issue 1, February-March.

3. **Adrian, R. J. (1991),** "Particle-Imaging Techniques for Experimental Fluid Mechanics," *Annual Review of Fluid Mechanics*, Vol.23, pp.261-304.

4. **Ahmed, A. and Bangash, Z. (2001),** "Bifurcation and Connectivity in a Synthetic Jet Vortex Train", 31st Fluid Dynamics Conference and Exhibit, Anaheim, CA, 11-14 June 2001.

5. **Amitay, M. and Glezer, A. (2002),** "Role of Actuation Frequency in Controlled Flow Reattachment over a Stalled Airfoil," *AIAA Journal*, Vol. 40, No. 2, February, pp. 209-216.

6. **Amitay, M., Smith, D. R., Kibens, V., Parekh, D. E. and Glezer, A. (2001),** "Aerodynamic Flow Control over an Unconventional Airfoil Using Synthetic Jet Actuators", *AIAA Journal*, Vol. 39, No. 3, March, pp. 361-370.

7. **Attinello, J. S. (1961),** "Design and Engineering Features of Flap Blowing Installations," In "Boundary Layer and Flow Control, its principals and applications," Ed. Lachmann, G. V., Vol. 1, Pergamon Press Ltd, 1961, pp. 463-515.

8. **Antonia, R. A., and Rajagopalan, S. (1990)**, "Determination of Drag of a Circular Cylinder," *AIAA Journal*, Vol.28, No.10, October, pp.1833-1834.

9. **Arai, N., Kuramoto, S., Horio, M., and Hiraoka, K. (2003)**, "Flow Around Propeller and Thrust Characteristics in Low Reynolds Number Field", AIAA-2003-3520, 21st AIAA Applied Aerodynamics Conference, Orlando, Florida, June 23-26, 2003.

10. **Arena, A. V., Mueller, T. J. (1979)**, "On the Laminar Separation, Transition, and Turbulent Reattachment of Low Reynolds Number Flows Near the Leading Edge of Airfoils", AIAA-79-0004, 17th AIAA Aerospace Sciences Meeting, New Orleans, LA, January 15-17, 1979.

11. **Argarwal, J. K., and Keady, P. (1980)**, "Theoretical Calculation and Experimental Observation of Laser Velocimeter Signal Quality," *TSI Monthly*, Vol.VI, Issue 1, February-March.

12. **Ashley, S. (1998)**, "Palm-size spy plane," Mechanical Engineering On-line http://www.memagazine.org, February.

13. **Avihar, E., Shemesh, N., Seifert, A., and Pack, G. L. (2002)**, "Rotation of a Rectangular Jet by Periodic Excitation", *Journal of Aircraft* Engineering Notes, Vol. 40, No. 1, October, pp. 217-219.

14. **Bannasch, R. (2000)**, "From Soaring and Flapping Bird Flight to Innovative Wing and Propeller Constructions," In *Fixed and Flapping Wing Aerodynamics for Micro Air Vehicle Applications, Progress in Astronautics and* Aeronautics, Vol.195, Ed. Muller, T. J., Pub. American Institute of Aeronautics and Astronautics, pp.453-471.

15. **Barlow, J. B., Rae Jr., W. H., and Pope, A. (1999)**, *Low Speed Wind Tunnel Testing*, 3rd Edition, John Wiley and Sons, Inc..

16. **Bastedo Jr., W. G., and Mueller, T. J. (1985)**, "Performance of Finite Wings at Low Reynolds Numbers", Conference on Low Reynolds Number Airfoil Aerodynamics, Notre Dame, Indiana, June, 1985.

17. **Bastedo Jr., W. G., and Mueller, T. J. (1986)**, "Spanwise Variation of Laminar Separation Bubbles on Wings at Low Reynolds Numbers", *Journal of Aircraft*, Vol.23, No.9, September, pp. 687-694.

18. **Batill, S. M., and Mueller, T. J. (1981),** "Visualization of Transition in the Flow over an Airfoil Using the Smoke-Wire Technique," *AIAA Journal*, Vol.19, No.3, March, pp.340-345.

19. **Bell, W. A. (2001),** "Spectral Analysis of Laser Velocimeter Data with the Slotted Correlation Method", Appendix B, Technical Paper published in *Laser Doppler Velocimeter*, Operations Manual, TSI Incorporated, December, pp.B1-B12.

20. **Béra, J. C., Chiekh, M. B., Michard, M., Comte-Bellot, G., and Sunyach, M. (2003),** "Control of a Plane Jet by Fluidic Wall Pulsing," Technical Note, *AIAA Journal*, Vol.41, No.5, February, pp.972-975.

21. **Betz, A. (1912),** "Ein Beitrag zur Erklarung des Segelfluges," *Zeitschrift fur Flugentechnik und Motorluftschiffahrt*, Vol. 3, January, pp.269-272.

22. **Bloch, D. R., Mueller, T. J. (1986),** "Effects of Distributed Grit Roughness on Separation and Transition on an Airfoil at Low Reynolds Numbers", AIAA-1986-1788, 4th Applied Aerodynamics Conference, San Diego, CA, 9-11 June, 1986, Technical Papers (A86-37801 17-02), New York, AIAA, pp. 152-161.

23. **Bolinder, J. (1999),** "On the accuracy of a digital particle image velocimetry system," Technical Report ISSN 0282 – 1990, Institutionen för värme- och kraftteknik, June.

24. **Brendel, M., and Mueller, T. J. (1988),** "Boundary-Layer Measurements on an Airfoil at Low Reynolds Numbers", *Journal of Aircraft*, Vol.25, No.7, pp.612-617.

25. **Brendel, M., and Mueller, T. J. (1985),** "Preliminary Experiments in Unsteady Flow on Airfoils at Low Reynolds Numbers", Conference on Low Reynolds Number Airfoil Aerodynamics, Notre Dame, Indiana, June, 1985.

26. **Brennan, M. C., and McGowan A.-M., R. (1997),** "Piezoelectric Power Requirements for Active Vibration Control," SPIE's 4th Annual Symposium on Smart Structures and Materials, San Diego, March 3-6, 1997.

27. **Bridges, A., and Smith, D. R. (2003),** "Influence of Orifice Orientation on a Synthetic Jet-Boundary-Layer Interaction", *AIAA Journal*, Vol.41, No.12, December, pp.2394-2402.

28. **Britz, D., and Antonia, R. A. (1996),** "A Comparison of methods of computing power spectra of LDA signals", *Measurement Science Technology*, Vol.7, pp.1042-1053.

29. **Broeren, A. P., and Bragg, M. B. (2001),** "Spanwise Variation in the Unsteady Stalling Flowfields of Two-Dimensional Airfoil Models", *AIAA Journal*, Vol.39, No.9, September, pp.1641-1651.

30. **Broersen, P. M. T., Waele, S. de, and Bos, R. (2000),** "The Accuracy of Time Series Analysis for Laser-Doppler Velocimetry," 10th International Symposium on Application of Laser Techniques to Fluid Mechanics, Lisbon, July 10-13, 2000.

31. **Brune, G. W. (1994),** "Quantitative Low-Speed Wake Surveys", *Journal of Aircraft*, Vol.31, No.2, March-April, pp.249-255.

32. **Bryant, R. G., Effinger IV, R. T., and Copeland Jr., B. M. (2002),** "Radial Field Piezoelectric Diaphragms," paper A1.3, Actuator 2002 Conference, June 10-12, 2002.

33. **Bryant, R. G., Effinger IV, R. T., Aranda Jr., I., Copeland Jr., B. M., and Covington III, E. W. (2002),** "Active Piezoelectric Diaphragms," paper 4699-40, proceedings of SPIE, Smart Structures and Materials – Active Materials: Behaviour and Mechanics, San Diego, CA, 2002.

34. **Bryant, R. G., Mossi, K. M., and Selby, G. V. (1997),** "Thin-layer Composite Unimorph ferroelectric driver and sensor properties," *Materials Letters*, August.

35. **Calkins, F. T. and Mabe, J. H. (2001),** "Multilayer PVDF Actuators for Active Flow Control", AIAA-2001-1560, 42nd AIAA Structures, Structural Dynamics and Materials Conference Exhibit, Seattle, WA, 16-19 April, 2001.

36. **Calkins, F. T., Mabe, J. H., Smith, J. P., and Arbogast, D. J. (2002),** "Low Frequency (F^+=1.0) Multilayer Piezopolymer Synthetic Jets for Active Flow Control", AIAA-2002-2823, 1st Flow Control Conference, St. Louis, Missouri, 24-26 June, 2002.

37. **Camussi, R., Guj, G., and Stella, A. (2002),** "Experimental study of a jet in crossflow at very low Reynolds number," *Journal of Fluid Mechanics*, Vol.454, pp.113-144.

38. **Cattafesta III, L. N., Garg, S., and Shukla, D. (2001),** "Development of Piezoelectric Actuators for Active Flow Control," *AIAA Journal*, Vol. 39, No. 8, August, pp. 1562-1568.

39. **Chandrasekaran, S., and Linder, D. K. (2000),** "Power Flow Through Controlled Piezoelectric Actuators," *Journal of Intelligent Material Systems and Structures*, Vol. 11, No. 6, October, pp. 469-481.

40. **Charmichael, B. H. (1981),** "Low Reynolds Number Airfoil Survey", NASA Contractor Report 165803, Volume I.

41. **Chen, F.-J., and Beeler, G. B. (2002),** "Virtual Shaping of a Two-dimensional NACA 0015 Aifoil Using Synthetic Jet Actuator", AIAA-2002-3273, 1st Flow Control Conference, St. Louis, Missouri, 24-26 June, 2002.

42. **Cheung, W. S., and Tilston, J. R. (2001),** "Testing of a novel propulsion system for micro air vehicles", Proceedings of the Institution of Mechanical Engineers, Vol.215, Part G, pp.207-218.

43. **Choi, J., Jeon, W., and Choi, H. (2002),** "Control of Flow Around an Airfoil Using Piezoceramic Actuators," *AIAA Journal*, Vol. 40, No. 5, May, pp. 1008-1010.

44. **Chol, S. H., Song, K. D., Golemblewskii, W., Chu, S.-H., and King, G. C. (2004),** "Microwave power for smart material actuators," *Smart Materials and Structures*, Vol.13, pp.38-48.

45. **Coiro, D. P., and deNicola, C. (1989),** "Prediction of Aerodynamic Performance of Airfoils in Low Reynolds Number Flows," Proceedings of the Low Reynolds Number Aerodynamics Conference, Notre Dame, Indiana, 5-7 June, 1989, "*Lecture Notes in Engineering number 54*", Springer-Verlag 1989, Ed. Mueller, T. J., pp.13-23.

46. **Collins, F. G., and Zelenevitz, J. (1975),** "Influence of Sound upon Separated Flow over Wings," *AIAA* Journal, Vol. 13, No. 3, pp. 408-410.

47. **Conrad, Y. L., and Goldstein, D. B. (2002),** "Two-Dimensional Synthetic Jet Simulation," *AIAA Journal*, Vol. 40, No. 3, March, pp. 510-516.

48. **Corke, T. C., and Morkovin, M. V. (1985),** "On Effects of Three-Dimensional Roughness on Transition and Receptivity to Disturbances", Conference on Low Reynolds Number Airfoil Aerodynamics, Notre Dame, Indiana, June, 1985.

49. **Crompton, M. J., and Barrett, R. V. (2000),** "Investigation of the separation bubble formed behind the sharp leading edge of a flat plate at incidence", Proceedings of the Institute of Mechanical Engineers, Vol.214, Part G, pp.157-176.

50. **Crook, A., Crowther, W. J., and Wood, N. J. (2000),** "A Parametric Study of a Synthetic Jet in a Cross Flow," 22nd Congress of the International Council on the Aeronautical Sciences (ICAS) 2000 Congress, Harrogate, UK, 27-31 August, 2000.

51. **Crook, A., Sadri, A.M. and Wood, N.J. (1999),** "The development and implementation of synthetic jets for the control of separated flow," AIAA 99-3176, 17th AIAA Applied Aerodynamics Conference, Norfolk, VA.

52. **Cui, J., and Cary, A. W. (2003),** "Numerical Simulation of the Interaction of a Synthetic jet with a Turbulent Boundary Layer", Paper AIAA-2003-3458, 33rd AIAA Fluid Dynamics Conference and Exhibit, Orlando, Florida, June 23-26, 2003.

53. **Cybk, B. Z., Wilkerson, J. T., Grossman, K. R., and Van Wie, D. M. (2003),** "Computational Assessment of the Sparkjet Flow Control Actuator", Paper AIAA-2003-3711, 33rd AIAA Fluid Dynamics Conference and Exhibit, Orlando, Florida, 23-26 June 2003.

54. **Dahai, G., Cary, A. W., and Agarwal, R. K. (2003),** "Numerical Simulation of Vectoring of a Primary Jet with a Synthetic Jet," *AIAA Journal*, Vol. 41, No. 12, December, pp. 2364-2370.

55. **Dausch, D. E., and Wise, S. A. (1998),** "Compositional Effects on Electromechanical Degradation of RAINBOW Actuators," NASA Technical Memorandum TM-1998-206282, January.

56. **Diez, F. J., and Dahm, W. J. A. (2003),** "Electrokinetic Microactuator Arrays and System Architecture for Active Sublayer Control of Turbulent Boundary Layers," *AIAA Journal*, Vol.41, No.10, October, pp.1906-1915.

57. **Donovan, J. F., and Selig, M. S. (1989),** "Low Reynolds Number Airfoil Design and Wind Tunnel Testing at Princeton University", Proceedings of the Low Reynolds Number Aerodynamics Conference, Notre Dame, Indiana, 5-7 June, 1989, "Lecture Notes in Engineering number 54", Springer-Verlag 1989, Ed. Mueller, T. J., pp.39-57.

58. **Douglas, J. F., Gasiorek, J. F., Swaffield, J. A. (1985),** *Fluid Mechanics*, 2nd edition, published Longman Scientific & Technical with ELBS.

59. **Drela, M. (2001),** "Higher-Order Boundary Layer Formulations and Application to Low Reynolds Number Flows," In *Fixed and Flapping Wing Aerodynamics for Micro Air Vehicle Applications, Progress in Astronautics and* Aeronautics, Vol.195, Ed. Muller, T. J., Pub. American Institute of Aeronautics and Astronautics, pp.13-33.

60. **Drela, M. (1988),** "Low-Reynolds-Number Airfoil Design for the M.I.T. Daedalus Prototype: A Case Study", *Journal of Aircraft*, Vol.25, No.8, August, pp.724-732.

61. **Drela, M. (1989),** "XFOIL: An Analysis and Design System for Low Reynolds Number Airfoils", Proceedings of the Low Reynolds Number Aerodynamics Conference, Notre Dame, Indiana, 5-7 June, 1989, "*Lecture Notes in Engineering number 54*", Springer-Verlag 1989, Ed. Mueller, T. J., pp.1-23.

62. **Duraisamy, K., and Baeder, J. D. (2003),** "Control of Tip-Vortex Structure Using Steady and Oscillatory Blowing", AIAA-2003-3407, 21st AIAA Applied Aerodynamics Conference, Orlando, Florida, 23-26 June, 2003.

63. **Ellington, C. P. (1995),** "Unsteady Aerodynamics of Insect Flight", *Journal of Experimental Biology*, No. 202, pp.109-129.

64. **Eppler, R., and Somers, D. M. (1985),** "Airfoil Design for Reynolds Numbers Between 50,000 and 500,000", Conference on Low Reynolds Number Airfoil Aerodynamics, Notre Dame, Indiana, June, 1985.

65. **Epstein, A. H. (2003),** "Millimeter-scale, MEMS Gas Turbine Engines," GT-2003-38866, Proceedings of ASME Turbo Expo 2003, Power for Land, Sea and Air, Atlanta, Georgia, 16-19 June, 2003.

66. **Espenlaub, L. (1922),** "Problem of Glider Models", *Flugsport*, March 15, 1922, pp.84-88. Translated by NACA and reprinted as NACA Technical Memorandum No.136, September.

67. **Eustace, R., and Barrett, R. V. (1999),** "The use of suction to suppress disturbances in laminar flow caused by insect and other surface debris", Proceedings of the Institution of Mechanical Engineers, Vol.213, Part G, pp.277-292.

68. **Finaish, F., Freymuth, P., and Bank, W. (1985),** "Streamwise and Spanwise Vortical Patterns Visualized over Airfoils in Unsteady Flow", Conference on Low Reynolds Number Airfoil Aerodynamics, Notre Dame, Indiana, June, 1985.

69. **Freymuth, P. (1990),** "Thrust Generation by an Airfoil in Hover Modes", *Experiments in Fluids,* Vol. 9, pp. 17-24.

70. **Gad-el-Hak, M. (1989),** "Control of Low-Reynolds-Number Airfoils: A Review", Proceedings of the Low Reynolds Number Aerodynamics Conference, Notre Dame, Indiana, 5-7 June, 1989, *Lecture Notes in Engineering number 54*, Springer-Verlag 1989, Ed. Mueller, T. J., pp.246-270.

71. **Gad-el-Hak, M. (2001),** "Flow Control: The Future", *Journal of Aircraft*, Vol.38, No.3, May-June, pp.402-418.

72. **Gad-el-Hak, M. (2001),** "Micro-Air-Vehicles: Can They be Controlled Better?", *Journal of Aircraft*, Vol.38, No.3, May-June, pp.419-429.

73. **Gallas, Q., Holman, R., Nishida, T., Carroll, B., Sheplak, M., and Cattafesta, L. (2003),** "Lumped Element Modelling of Piezoelectric-Driven Synthetic Jet Actuators," *AIAA Journal*, Vol.41, No.2, February, pp.240-247.

74. **Gallas, Q., Wang, G., Papila, M., Sheplak, M., and Cattafesta, L. (2003),** "Optimization of Synthetic Jet Actuators", AIAA-2003-0635, 41st Aerospace Sciences Meeting and Exhibit, Reno, Nevada, 6-9 January, 2003.

75. **Gault, D. E. (1955),** "An experimental investigation of regions of separated laminar flow," NACA TN-3505.

76. **Ghia, K. N., Osswald, G., and Ghia, U. (1989),** "Study of Low-Reynolds Number Separated Flow Past the Wortmann FX 63-167 Airfoil,", Proceedings of the Low Reynolds Number Aerodynamics Conference, Notre Dame, Indiana, 5-7 June, 1989, "*Lecture Notes in Engineering number 54*", Springer-Verlag 1989, Ed. Mueller, T. J., pp.58-69.

77. **Gjelstrup, P., Nobach, H., Jorgensen, F. E., and Meyer K. E. (2000),** "Experimental verification of novel spectral analysis algorithms for Laser Doppler Anemometry data," 10th International Symposium on Applications of Laser Techniques to Fluid Mechanics, Lisbon, Portugal, 10-13 July, 2000.

78. **Gleyzes, C., Cousteix, J., and Bonnet, J. L. (1985),** "Theoretical and Experimental Study of Low Reynolds Number Transitional Separation Bubbles", Conference on Low Reynolds Number Airfoil Aerodynamics, Notre Dame, Indiana, June, 1985.

79. **Glezer, A., and Amitay, M. (2002),** "Synthetic Jets," *Annual Review of Fluid Mechanics*, Vol.34, January, pp.503-529.

80. **Goodman, J. (2002),** "Piezoelectric Foil Propulsion for Micro Air Vehicles," Presented for the N.E.Rowe Medal Award for the Royal Aeronautical Society, May, 2002.

81. **Gopalarathnam, A., Broughton, B. A., McGranahan, B. D., and Selig, M. S. (2003),** "Design of Low Reynolds Number Airfoils with Trips", *Journal of Aircraft*, Vol.40, No.4, July-August, pp.768-775.

82. **Gopalarathnam, A., and Selig, M. S. (2001),** "Low-Speed Natural-Laminar-Flow Airfoils: Case Study in Inverse Airfoil Design", *Journal of Aircraft*, Vol.38, No.1, January-February, pp.57-63.

83. **Grasmeyer and Keenon (2001),** "Development of the Black Widow Micro Air Vehicles," In *Fixed and Flapping Wing Aerodynamics for Micro Air Vehicle Applications, Progress in Astronautics and* Aeronautics, Vol.195, Ed. Muller, T. J., Pub. American Institute of Aeronautics and Astronautics, pp.519-535.

84. **Greenblatt, D., and Wygnanski, I. J. (2000),** "Use of Periodic Excitation to Enhance Airfoil Performance at Low Reynolds Numbers", *Journal of Aircraft Engineering Notes*, Vol. 38, No.1, October, pp. 190-192.

85. **Guglielmo, J., J., and Selig, M. S. (1996),** "Spanwise Variations in Profile Drag for Airfoils at Low Reynolds Numbers", *Journal of Aircraft*, Vol.33, No.4, July-August, pp. 699-707.

86. **Gullman-Strand, J., and Angele, K. (2000),** "Wake analysis and measurements", documentation in support of IVS course 2000, available from http://www.tech.volvo.se/ivs/courses/kurs_veh_aero_rapp_jgs_ka.pdf, August 29, 2000.

87. **Guo, D., Cary, A. W., and Agarwal, R. K. (2003),** "Numerical Simulation of Vectoring of a Primary Jet with a Synthetic Jet", *AIAA Journal*, Vol.41, No.12, December, pp.2364-2370.

88. **Gursul, I. (2003),** "Vortex Flows on UAVs: Issues and Challenges", Royal Aeronautical Society CEAS Aerospace Aerodynamics Research Conference, 10-12 June, 2003, London, UK.

89. **Gursul, I., Taylor, G., and Wooding, C. L. (2002),** "Vortex Flows over Fixed-Wing Micro Air Vehicles", invited paper AIAA-2002-0698, 40th AIAA Aerospace Sciences Meeting and Exhibit, Reno, Nevada, 14-17 January, 2002.

90. **Hall, K.C., and Hall, S.R. (2001),** "A Rational Engineering Analysis of the Efficiency of Flapping Flight", *Fixed and Flapping Wing Aerodynamics for Micro Air Vehicle Applications,* Ed. Mueller, T. J., pub. AIAA.

91. **Hansman Jr., R. J., and Craig, A. P. (1987),** "Low Reynolds Number Tests of NACA 64-210, NACA 0012, and Wortmann FX67-K170 Airfoils in Rain", *Journal of Aircraft*, Vol.24, No.8, August, pp.559-566.

92. **Hart, D. P. (1988),** "The Elimination of Correlation Errors in PIV Processing," 9th International Symposium on Applications of Laser Techniques to Fluid Mechanics, Lisbon, Portugal, July, 1988.

93. **Hassan, A. A. (1985),** "A Viscous-Inviscid Coupling Method for the Design of Low Reynolds Number Airfoil Sections", Conference on Low Reynolds Number Airfoil Aerodynamics, Notre Dame, Indiana, June, 1985.

94. **Hassan, A. A. (2003),** "Improving Flap Aerodynamics Using Oscillatory Jet Control", Paper AIAA-2003-3664, 21st AIAA Applied Aerodynamics Conference, Orlando, Florida, 23-26 June 2003.

95. **Hess, D. E., and Fu, T. C. (2003),** "Impact of Flow Control Technologies on Naval Platforms", Paper no. AIAA-2003-3568, 33rd AIAA Fluid Dynamics Conference, Orlando, Florida, 23-26 June 2003.

96. **Höcker, R., and Kompenhaus, J. (1989),** "Some technical improvements of Particle Image Velocimetry with regard to its application in wind tunnels," International Congress on Instrumentation in Aerospace Simulation Facilities, Göttingen, W. Germany, September 18-21, 1989.

97. **Holman, R., Gallas, Q., Carroll, B., and Cattafesta, L. (2003),** "Interaction of Adjacent Synthetic Jets in an Airfoil Separation Control Application", Paper AIAA 2003-3709, 33rd AIAA Fluid Dynamics Conference and Exhibit, Orlando, Florida, 23-26 June 2003.

98. **Hooley, A. (2000),** "Helimorph," available from web-site http://www.1limited.com/tech/helimorph/index.html, 1 Ltd, St John's Innovation Centre, Cambridge, 2000.

99. **Horner, G. C., and Taleghani, B. K. (1999),** "Single Axis Piezoceramic Gimbal," NASA Technical Memorandum TM-1999-209721, November.

100. **Horton, H. P. (1968),** "Laminar Separation Bubbles in two and three dimensional compressible flow," PhD Thesis, University of London, UK.

101. **Horowitz, S., Kasyap, A., Liu, F., Johnson, D., Nishida, T., Ngo, K., Sheplak, M., and Cattafesta, L. (2002),** "Technology Development for Self-Powered Sensors", AIAA-2002-2702, 1st AIAA Flow Control Conference, 24-26 June, 2002, St. Louis, MO.

102. **Howard, R. M., and Kindelspire, D. W. (1990),** "Freestream Turbulence Effects on Airfoil Boundary-Layer Behaviour at Low Reynolds Numbers", *Journal of Aircraft*, Engineering Notes, Vol.27, No.5, May, pp.468-470.

103. **Hsiao, F.-B., Liu, C.-F., and Shyu, J. Y. (1990),** "Control of Wall-Separated Flow by Internal Acoustic Excitation", *AIAA Journal*, Vol. 28, No. 8, pp. 1440-1446.

104. **Hsiao, F.-B., Liu, C.-F., and Tang, Z. (1987),** "Experimental Studies of Airfoil Performance and Flow Structures on a Low Reynolds Number Airfoil", AIAA-87-1267, 19th AIAA Fluid Dynamics, Plasma Dynamics and Lasers Conference, Honolulu, Hawaii, June 8-10, 1987.

105. **Huang, H., Dabiri, D., and Gharib, M. (1997),** "On errors of digital particle image velocimetry," *Measurement Science Technology*, Vol.8, pp.1427-1440.

106. **Huber II, A. F., and Mueller, T. J. (1985),** "The Effect of Trip Wire Roughness on the Performance of the Wortmann FX 63-137 Airfoil at Low Reynolds Numbers", Conference on Low Reynolds Number Airfoil Aerodynamics, Notre Dame, Indiana, June, 1985.

107. **Hyer, M. W., and Jilani, A. B. (2002),** "Deformation characteristics of circular RAINBOW actuators," *Smart Materials and Structures*, Vol.11, pp.175-195.

108. **Ifju, P. G., Jenkins, D. A., Ettinger, S., Lian, Y., and Shyy, W. (2002),** "Flexible-Wing Based Micro Air Vehicles," AIAA-2002-0705, 40th AIAA Aerospace Sciences Meeting and Exhibit, Reno, Nevada, 14-17 January, 2002.

109. **Ingard, U. and Labate, S. (1950),** " Acoustic Circulation Effects and the Nonlinear Impedance of Orifices", *Journal of the Acoustical Society of America*, Vol.22, No.2, March, pp.211-218.

110. **Ingard, U. (1953),** "On the Theory and Design of Acoustic Resonators", The *Journal of the Acoustical Society of America*, Vol. 25, No. 6, November, pp 1037-1059.

111. **Jacobs, E. N., and Sherman, A. (1936),** "Airfoil Section Characteristics as affected by variations of the Reynolds Number", N.A.C.A Technical Report No. 586, June 24.

112. **Jacobson, S. A., and Reynolds, W. C. (1998),** "Active control of streamwise vortices and streaks in boundary layers", *Journal of Fluid Mechanics*, Vol.360, pp.179-211.

113. **Janacek, G. J. (1998),** "Spectral Analysis," *Encyclopaedia of Biostatistics*, John Wiley & Sons Ltd., ISBN 0471 975761, Ed. Armitage, P, and Colton, T..

114. **Jones, B. M. (1933),** "An Experimental Study of the Stalling of Wings," NACA Report No. 1588, December.

115. **Jones, K. D., Dohring, C. M., and Platzer, M. F. (1996),** "Wake Structures Behind Plunging Airfoils: A Comparison of Numerical and Experimental Results," Paper AIAA-1996-0078, 34th Aerospace Sciences Meeting and Exhibit, Reno, Nevada, January 15-18, 1996.

116. **Jones, K. D., and Platzer, M. F. (2003),** "Experimental Investigation of the Aerodynamic Characteristics of Flapping-Wing Micro Air Vehicles", Paper AIAA-2003-0418, 41st AIAA Aerospace Sciences Meeting & Exhibit, Reno, Nevada, 6-9 January, 2003.

117. **Jones, K. D. and Platzer, M. F. (2000),** "Flapping-Wing Propulsion for a Micro Air Vehicle", AIAA-2000-0897 38th Aerospace Sciences Meeting and Exhibit, 10-13 January 2000.

118. **Jones, K. D., and Platzer, M. F. (1997),** "Numerical Computation of Flapping-Wing Propulsion and Power Extraction," Paper AIAA-1997-0826, 35th Aerospace Sciences Meeting and Exhibit, Reno, Nevada, January 6-10, 1997.

119. **Jones, K. D., and Platzer, M. F. (2001),** "On the Use of Vortex Flows for the Propulsion of Micro-Air and Sea Vehicles", NATO Applied Vehicle Technology (AVT) Meeting Week, Norway, 7-11 May, 2001.

120. **Jones, B. M. (1936),** "Measurement of Profile Drag by the Pitot-Traverse Method," Aeronautical Research Committee Report and Technical Memoranda No.1688, January.

121. **Jordan, T. L., Ounaies, Z. (2001),** "Piezoelectric Ceramics Characterization", Joint NASA and ICASE Reports, NASA CR-2001-211225 or ICASE 2001-28, September.

122. **Jordan, T., Ounaies, Z., Tripp, J., and Tcheng, P. (2000),** "Electrical Properties and Power Considerations of a Piezoelectric Actuator," NASA ICASE Report No.2000-8, CR-2000-209861, February.

123. **Kaufman, S. L. (1986),** "Fiberoptics in Laser Doppler Velocimetry," *Lasers & Applications*, July, pp.71-73.

124. **Keane, R. D., and Adrian, R. J. (1990),** "Optimization of particle image velocimeters. Part 1: Double pulsed systems," *Measurement Science and Technology*, Vol.1, pp.1202-1215.

125. **Keane, R. D., and Adrian, R. J. (1991),** "Optimization of particle image velocimeters. Part 2: Multiple pulsed systems," *Measurement Science and Technology*, Vol.2, pp.963-974.

126. **Kim, K., and Sung, H. J. (2003),** "Effects of Periodic Blowing from Spanwise Slot on a Turbulent Boundary Layer", *AIAA Journal*, Vol.41, No.10, October, pp.1916-1924.

127. **Knoller, R. (1909),** "Die Gesetze des Luftwiderstandes," *Flug- und Motortechnik (Wein)*, Vol. 3, No. 21, pp. 1-7.

128. **Kothari, A. P., and Anderson Jr., J. D. (1985),** "Computational Study of Flow Over Miley and Wortmann Airfoils", Conference on Low Reynolds Number Airfoil Aerodynamics, Notre Dame, Indiana, June, 1985.

129. **Kumar, A., and Hefner, J. N. (2000),** "Future Challenges and Opportunities in Aerodynamics," 22nd Congress of the International Council on the Aeronautical Sciences (ICAS) 2000 Congress, Harrogate, UK, 27-31 August, 2000.

130. **Kunz, P. J., and Kroo, I. (2001),** "Analysis and Design of Airfoils for Use at Ultra-Low Reynolds Numbers," In *Fixed and Flapping Wing Aerodynamics for Micro Air Vehicle Applications, Progress in Astronautics and* Aeronautics, Vol.195, Ed. Muller, T. J., Pub. American Institute of Aeronautics and Astronautics, pp.35-59.

131. **Laitone, E. V. (1996),** "Aerodynamic Lift at Reynolds Numbers below $7x10^4$", *AIAA Journal*, vol. 34, no. 9, pp. 1941-1942 September.

132. **Laitone, E. V. (1997),** "Wind tunnel tests of wings at Reynolds numbers below 70000", *Experiments in Fluids*, Vol.23, pp.405-409

133. **Laitone, E. V. (2001),** "Wind Tunnel Tests of Wings and Rings at Low Reynolds Numbers," In *Fixed and Flapping Wing Aerodynamics for Micro Air Vehicle Applications, Progress in Astronautics and* Aeronautics, Vol.195, Ed. Muller, T. J., Pub. American Institute of Aeronautics and Astronautics, pp.83-90.

134. **Lee, Y., and Goldstein, D. B. (2002),** "Two Dimensional Synthetic Jet Simulation," *AIAA Journal*, Vol. 40, No. 3, March, pp. 510-516.

135. **Lee, C., Hong, G., Ha, P. Q., and Mallinson, S. G. (2003),** "A piezoelectrically actuated micro synthetic jet for active flow control", *Sensors and Actuators*, Vol.108, pp.168-174.

136. **Lian, Y., Shyy, W., and Haftka, R. T. (2004),** "Shape Optimization of a Membrane Wing for Micro Air Vehicles", *AIAA Journal* Technical Notes, Vol.42, No.2, February, pp.424-426.

137. **Lian, Y., Shyy, W., and Ifju, P. G. (2004),** "Membrane Wing Model for Micro Air Vehicles", *AIAA Journal* Technical Notes, Vol. 41, No. 12, December, pp. 2492-2494.

138. **Lian, Y., Steen, J., Trygg-Wilander, M., and Shyy, W. (2003),** "Low Reynolds number turbulent flows around a dynamically shaped airfoil", *Computers and Fluids*, Vol.32, pp.287-303.

139. **Lin, J. C., Walsh, M. J. (1984),** "Turbulent Roughness Drag Due to Surface Waviness at Low Roughness Reynolds Numbers", *Journal of Aircraft*, Engineering Notes, Vol.21, No.12, December, pp.978-979.

140. **Lissaman, P. B. S. (1983),** "Low-Reynolds-Number Airfoils," *Annual Review of Fluid Mechanics*, Vol. 15, pp. 223-239.

141. **Lu, B., and Bragg, M. B. (2002),** "Experimental Investigation of the Wake-Survey Method for a Bluff Body With a Highly Turbulent Wake," AIAA-2002-3060, 20th Applied Aerodynamics Conference, St.Louis, Missouri, 24-26 June 2002.

142. **Lyon, C. A., Selig, M. S., and Broeren, A., P. (1997),** "Boundary layer trips on airfoils at low Reynolds numbers", AIAA-97-0511, 35th AIAA Aerospace Sciences Meeting and Exhibit, Reno, NV, January 6-9, 1997.

143. **Mallinson, S. G., Reizes, J. A., and Hong, G. (2001),** "An experimental and numerical study of synthetic jet flow," *The Aeronautical Journal*, January, pp. 41-49.

144. **Mallinson, S. G., Reizes, J. A., Hong, G., and Westbury, P. S. (2004),** "Analysis of hot-wire anemometry data obtained in a synthetic jet flow", *Experimental Thermal and Fluid Science*, Vol.28, pp.265-272.

145. **Mangalam, S., Meyers, J. F., Dagenhart, J. R., and Harvey, W. D. (1985),** "A Study of Laminar Separation Bubble in the Concave Region of an Airfoil Using Laser Velocimetry", presented at Symposium on Laser Anemometry, ASME 1985 Winter Annual Meeting, Miami, Florida, 17-21 November, 1985.

146. **Marchman III, J. F. (1987),** "Aerodynamic Testing at Low Reynolds Numbers", *Journal of Aircraft*, Vol.24, No.2, February, pp.107-114.

147. **Marchmann III, J. F., Robertson, E. A., and Emsley, H. T. (1987),** "Rain Effects at Low Reynolds Number", *Journal of Aircraft*, Vol.24, No.9, September, pp.638-644.

148. **Margalit, S., Greenblatt, D., Seifert, A., and Wygnanski, I. (2002),** "Active Flow Control of a Delta Wing at High Incidence Using Segmented Piezoelectric Actuators," AIAA 2002-3270, 1st Flow Control Conference, St. Louis, MO, 24-26 June 2002.

149. **Mateescu, D., and Abdo, M. (2004),** "Aerodynamic Analysis of Airfoils at very Low Reynolds Numbers", AIAA-2004-1053, 42nd AIAA Aerospace Sciences Meeting and Exhibit, Reno, Nevada, 5-8 January 2004.

150. **Matovic, D., and Tropea, C. (1991),** "Spectral peak interpolation with application to LDA signal processing," *Measurement Sciences Technology*, Vol.2, pp.1100-1106.

151. **Maughmer, M. D., and Selig, M. S. (1985),** "Low Reynolds Number Airfoil Design", Conference on Low Reynolds Number Airfoil Aerodynamics, Notre Dame, Indiana, June, 1985.

152. **McCormick, D. C. (2000),** "Boundary Layer Separation Control with Directed Synthetic Jets", AIAA-2000-0519, 38th Aerospace Sciences Meeting and Exhibit, Reno, NV, 10-13 January 2000.

153. **McGhee, R. J., and Walker, B. S. (1989),** "Performance Measurements of an Airfoil at Low Reynolds Numbers", Proceedings of the Low Reynolds Number Aerodynamics Conference, Notre Dame, Indiana, 5-7 June, 1989, "Lecture Notes in Engineering number 54", Springer-Verlag 1989, Ed. Mueller, T. J., pp.131-145.

154. **McLachlan, B. G. (1989),** "Study of a Circulation Control Airfoil with Leading/Trailing-Edge Blowing", *Journal of Aircraft*, Vol.26, No.9, September, pp.817-821.

155. **McMichael and Francis (1997),** discussion of MAVs, http://www.darpa.mil/tto/mav/mav_auvsi.html, 8 July, 1997.

156. **Melling, A. (1997),** "Tracer particles and seeding for particle image velocimetry," *Measurement Science Technology*, Vol.8, pp.1406-1416.

157. **Melton, L. P., Yao, C. S, and Seifert, A. (2003),** "Active Separation From the Flap of a Supercritical Airfoil", Paper AIAA-2003-4005, 33rd AIAA Fluid Dynamics Conference and Exhibit, Orlando, Florida, June 23-26 2003.

158. **Menon, R. (1982),** "Laser Doppler Velocimetry: Performance and Applications," *American Laboratory*, February.

159. **Menon, R., Jenson, L., and Buddhavarapu, J. (1993),** "Comparison of signal extraction techniques in LDV signal processing," 5th International Conference on Laser Anemometry, Netherlands, August, 1993.

160. **Menon, R., and Lai, W. T. (1991),** "Key Considerations in the Selection of Seed Particles for LDV Measurements," 4th International Conference on Laser Anemometry, Cleveland, Ohio, August, 1991.

161. **Miley, S. J., Howard, R. M., and Holmes, B. J. (1985),** "Propeller Slipstream/Wing Boundary Layer Effects at Low Reynolds Numbers", Conference on Low Reynolds Number Airfoil Aerodynamics, Notre Dame, Indiana, June, 1985.

162. **Morris, S. J., and Holden, M. (2000),** "Design of Micro Air Vehicles and Flight Test Validation," MLB Company, http://www.spyplanes.com, 2000.

163. **Mueller, T. J. (1999),** "Aerodynamic Measurements at Low Reynolds Numbers for Fixed Wing Micro-Air Vehicles", RTO for RTO AVT/VKI Special Course on "Development and Operation of UAVs for Military and Civil Applications" September 13-17, 1999.

164. **Mueller, T. J. (1985),** "Low Reynolds Number Vehicles," AGARD-AG-288.

165. **Mueller, T. J., and Batill, S. M. (1982),** "Experimental Studies of Separation on a Two-Dimensional Airfoil at Low Reynolds Numbers," *AIAA Journal*, Vol.20, No.4, April, pp.457-463.

166. **Mueller, T. J., and DeLaurier, J. D. (2003),** "Aerodynamics of Small Vehicles", *Annual Review of Fluid Mechanics*, pp.89-111.

167. **Munday, D., and Jacob, J. (2002),** "Active Control of Separation on a Wing With Oscillating Camber," *Journal of Aircraft*, Vol.39, No.1, January, pp. 187-189.

168. **Munday, D., and Jacob, J. (2001),** "Active Control of Separation on a Wing with Conformal Camber", AIAA-2001-0293, 39th AIAA Aerospace Sciences Meeting and Exhibit, Reno, Nevada, January 8-11, 2001.

169. **Munday, D., Jacob, J., and Huang, G. (2002),** "Active Flow Control of Separation on a Wing with Oscillatory Camber," AIAA-2002-0413, 40th AIAA Aerospace Sciences Meeting and Exhibit, Reno, Nevada, January 14-17, 2002.

170. **Murthy, A. V. (1988),** "Effects of Aspect Ratio and Sidewall Boundary-Layer in Airfoil Testing," *Journal of Aircraft*, Vol.25, No.3, March, pp.244-249.

171. **Nagamatsu, H. T., and Cuche, D. E. (1981),** "Low Reynolds Number Aerodynamic Characteristics of Low-Drag NACA 63-208 Airfoil", *Journal of Aircraft*, Vol.18, No.10, October, pp.833-837.

172. **NASA Technical Briefs (2002),** "Optimization of Synthetic Jet Actuators," LAR-16234, NASA Technical Support Package, Langley Research Center.

173. **Nelson, R. C. (1984),** "The Influence of Airfoil Roughness on the Performance of Flight Vehicles at Low Reynolds Numbers", AIAA-84-0540, 22nd AIAA Aerospace Sciences Meeting, Reno, Nevada, January 9-12, 1984.

174. **Noca, F., Shiels, D., and Jeon, D. (1997),** "Measuring Instantaneous Fluid Dynamic Forces on Bodies, using only Velocity Fields and their derivatives," *Journal of Fluids and Structures,* Vol.11, pp. 345-350.

175. **Nogueira, J., Lecuona, A., and Rodriguez, P. A. (1997),** "Data validation, false vectors correction and derived magnitudes calculation on PIV data," *Measurement Science Technology*, Vol.8, pp.1493-1501.

176. **Null, W., Wagner, M., Shkarayev, S., Jouse, W., and Brock, K. (2002),** "Utilizing Adaptive Wing Technology in the Control of a Micro Air Vehicle," SPIE's 9th Annual International Symposium on Smart Structures and Materials, San Diego, CA, 17-21 March, 2002.

177. **O'Meara, M. M., and Mueller, T. J. (1987),** "Laminar Separation Bubble Characteristics on an Airfoil at Low Reynolds Numbers", *AIAA Journal*, Vol.25, No.8, August, pp.1033-1041.

178. **Orkwis, P., and Filz., C. (2003),** "Characterization of Dual Two Dimensional Synthetic Jets in Cross Flow at Low Mach Number", Paper AIAA-2003-3457, 33rd AIAA Fluid Dynamics Conference and Exhibit, Orlando, Florida, 23-26 June 2003.

179. **Ounaies, Z., Mossi, K., Smith, R., and Bernd, J. (2001),** "Low-field and High-field Characterization of THUNDER actuators," NASA ICASE Contract Report CR-2001-210859, April.

180. **Pack, L. G., and Seifert, A. (2000),** "Dynamics of Active Separation Control at High Reynolds Numbers", AIAA-2000-0409, 38th AIAA Aerospace Sciences Meeting and Exhibit, Reno, Nevada, January 10-13, 2000.

181. **Pack, L. G., and Seifert, A. (1999),** "Periodic Excitation for Jet Vectoring and Enhanced Spreading", AIAA-99-0672, 37th AIAA Aerospace Sciences Meeting and Exhibit, Reno, Nevada, January 11-14, 1999.

182. **Pankhurst, R. C., and Holder, D. W. (1969),** "Wind-Tunnel Technique," published Sir Isaac Pitman & Sons Ltd., 1952, 2nd edition 1969.

183. **Parry-Jones, N., Warwick, K., and Alldridge, J. (2001),** "From unmanned aircraft to micro-air vehicles," *Journal of Defence Science*, Vol. 6, No. 3, pp.254-261.

184. **Patel, M. P., Kolacinski, R. M., and Prince, T. S. (2003),** "Flow Control Using Intelligent Control Modules for Virtual Aerodynamic Shaping", Paper AIAA-

2003-3663, 21st AIAA Applied Aerodynamics Conference, Orlando, Florida, 23-26 June, 2003.

185. **Patil, M. J. (2003),** "From Fluttering Wings to Flapping Flight: The Energy Connection", *Journal of Aircraft*, Vol.40, No.2, March-April, pp. 270-276.

186. **Patrick, W. P., and Edwards, D. E. (1985),** "Low Reynolds Number Separation Bubble Research at UTRC", Conference on Low Reynolds Number Airfoil Aerodynamics, Notre Dame, Indiana, June, 1985.

187. **Pelletier, A., and Mueller, T. J. (2001),** "Effect of Endplates on Two-Dimensional Airfoil Testing at Low Reynolds Number," *Journal of Aircraft*, Vol.38, No.6, November-December, pp.1056-1059.

188. **Pelletier, A. and Mueller, T. J. (2000),** "Low Reynolds Number Aerodynamics of Low-Aspect-Ratio, Thin/Flat/Cambered-Plate Wings", *Journal of Aircraft*, Vol:37, No. 5, September-October, pp. 825-832.

189. **Peterson, B., Erath, B., Henry, K., Lyon, M., Walker, B., Powell, N., Fowkes, K., and Bowman, W. J. (2003),** "Development of a Micro Air Vehicle for Maximum endurance and Minimum size," paper AIAA-2003-416, 41st AIAA Aerospace and Sciences Meeting and Exhibit, Reno, Nevada, 6-9 January, 2003.

190. **Pfenninger, W., and Vemuru, C. S. (1990),** "Design of Low Reynolds Number Airfoils: Part I", *Journal of Aircraft*, Vol.27, No.3, March, pp.204-210.

191. **Pinkerton, J. L., McGowan, A.-M. R., Moses, R. W., Scott, R. C., and Heeg, J. (1996),** "Controlled Aeroelastic Response and Airfoil Shaping Using Adaptive Materials and Integrated Systems," SPIE's 1996 Symposium on Smart Structures and Integrated Systems, San Diego, CA, February 26-29, 1996.

192. **Pinkerton, J. L., Moses, R. W. (1997),** "A Feasibility Study To Control Airfoil Shape Using THUNDER," NASA Technical Memorandum 4767, November.

193. **Pinkerton, R. M. (1937),** "The Variation with Reynolds Number of Pressure Distribution over an Airfoil Section", N.A.C.A Technical Report No. 613, July, 1937.

194. **Poisson-Quentin, P. H. (1948),** "Recherches theoriques et experimentales sur le controle de couche limits," 7th International Congress of Applied Mechanics, London, September, 1948.

195. **Poisson-Quentin, P., H., and Lepage, L. (1961),** "Survey of French research on the control of boundary layer and circulation," in *Boundary Layer and Flow Control, its principals and applications*, Ed. Lachmann, G. V., Vol. 1, Pergamon Press, pp. 21-73.

196. **Porsin-sirirak, T. N., Lee, S. W., Nassef, H., Grasmeyer, J., Tai, Y. C., Ho, C. M., and Keennon, M. (2000),** "MEMS Wing Technology for Battery Powered Ornithopter," Institute of Electrical and Electronics Engineers, New York, January, pp. 799-804.

197. **Prandtl, L. (1904),** "Uber Flussigkeitsbewegung bei sehr kleiner Reibung," *Proceedings of the Third International Mathematics Congress*, 1904, pp. 484-491.

198. **Quinn Jr., J. H. (1944),** "Tests on the NACA 653-018 Airfoil Section with Boundary-Layer Control by Suction", NACA Bulletin L4H10, October.

199. **Raghunathan, S., Harrison, J. R., and Hawkins, B. D. (1988),** "Thick Airfoil at Low Reynolds Number and High Incidence", *Journal of Aircraft*, Technical Notes, Vol.25, No.7, July, pp.669-671.

200. **Ramaprian, B. R., and Chandrasekhara, M. S. (1985),** "LDA Measurements in Plane Turbulent Jets," *Journal of Fluids* Engineering, Transactions of the ASME, Vol.107, June, pp.264-271.

201. **Raney, D. L., and Slominski, E. C. (2003),** "Mechanization and Control Concepts for Biologically Inspired Micro Aerial Vehicles," AIAA Guidance, Navigation & Control Conference, 11-14 August 2003, Austin, Texas.

202. **Raney, D. L., and Waszak, M. R. (2003),** "Biologically Inspired Micro-Flight Research," SAE paper number SAE-2003-01-3042, January.

203. **Reaves, M. C., Horta, L. G., Waszak, M. R., and Morgan, B. G. (2004),** "Model Update of a Micro Air Vehicle (MAV) Flexible Wing Frame with Uncertainty Quantification," NASA TM-2004-213232, 2004.

204. **Reid, E. G., and Bamber, M. J. (1928),** "Preliminary investigation on Boundary Layer Control by means of Suction and Pressure with the U.S.A.27 Airfoil", N.A.C.A Technical Note No.286, May.

205. **Richards, C. D., Anderson, M. J., Bahr, D. F., and Richards, R. F. (2004),** "Efficiency of energy conversion for devices containing a piezoelectric component," *Journal of Micromechanics and Microengineering*, Vol.14, pp.717-721.

206. **Rizzetta, D. P., Vibal, M. R., and Stanek, M. J. (1999),** "Numerical Investigation of Synthetic-Jet Flowfields," *AIAA Journal*, Vol. 37, No. 8, August, pp. 919-927.

207. **Roberts, W. B. (1979),** "Calculation of Laminar Separation Bubbles and Their Effect on Airfoil Performance", AIAA-79-0285, 17th AIAA Aerospace Sciences Meeting, New Orleans, LA, January 15-17, 1979.

208. **Roos, F. (1997),** "Synthetic-jet Microblowing for Vortex Asymmetry Management on a Hemisphere-Cylinder Forebody", AIAA-1997-1973, 4th Shear Control Conference, Snowmass Village, CO, 29 June – 2 July, 1997.

209. **Sane, S. P. (2003),** "Review: The Aerodynamics of Insect Flight", *The Journal of Experimental Biology*, Vol.206, pp.4191-4208.

210. **Saric, W. S., Reed, H. L., and Kerschen, E. J. (2002),** "Boundary-Layer Receptivity to Freestream Disturbances," *Annual Review of Fluid Mechanics*, Vol.34, January, pp.291-319.

211. **Schaeffler, N. W. (2003),** "The Interaction of a Synthetic Jet and a Turbulent Boundary Layer", 41st Aerospace Sciences Meeting & Exhibit, Reno, Nevada, January 6-9, 2003.

212. **Schaeffler, N. W., Hepner, T. E., Jones, G. S., and Kegerise, M. A. (2002),** "Overview of Active Flow Control Actuator Development at NASA Langley Research Center", AIAA-2002-3159, 1st AIAA Flow Control Conference, St. Louis, Missouri, June 24-26, 2002.

213. **Schmidt, G. S., Mueller, T. J. (1987),** "A Study of the Laminar Separation Bubble on an Airfoil at Low Reynolds Numbers Using Flow Visualization Techniques", AIAA-87-0242, 25th AIAA Aerospace Sciences Meeting, Reno, Nevada, January 12-15, 1987.

214. **Schmidt, G. S., O'Meara, M. M., and Mueller, T. J. (1985),** "An Analysis of a Separation Bubble Transition Criterion at Low Reynolds Numbers", Conference on Low Reynolds Number Airfoil Aerodynamics, Notre Dame, Indiana, June, 1985.

215. **Schmitz, F. W. (1942),** "Aerodynamik des Flugmodells," Tragflugelmessungen I. C. J. E. Volckmann Nachf. E. Wette, Berlin-Charlottenburg, 1942.

216. **Schrenk, M. (1922),** "Aerodynamic Computation of Gliders", *Flugsport*, May 24, 1922, pp.170-177, translated by NACA as NACA Technical Memorandum No.140, September.

217. **Schrenk, O. (1926),** "Experiments with a Sphere from Which the Boundary Layer is Removed y Suction," NACA Technical Memorandum No. 395.

218. **Schubauer, G. B. (1948),** "Laminar Boundary Layer Oscillations and Transition on a Flat Plate," NACA Report 909, 1948.

219. **Seifert, A., Eliahu, S. and Greenblatt, D. (1998),** "Use of Piezoelectric Actuators for Airfoil separation Control", *AIAA Journal Technical Notes*, Vol. 36, No. 8, August, pp. 1535-1537.

220. **Seifert, A. and Pack, L.G. (2002),** "Active Flow Separation Control on Wall-Mounted Hump at High Reynolds Numbers", *AIAA Journal*, Vol.40, No.7, July, pp. 1363-1372.

221. **Seifert, A., and Pack, L. G. (2003),** "Compressibility and Excitation Location Effects on High Reynolds Numbers Active Separation Control", *Journal of Aircraft*, Vol.40, No.1, January-February, pp.110-119.

222. **Seifert, A. and Pack, L.G. (1998),** "Oscillatory Control of Separation at High Reynolds Numbers", AIAA-1998-214, 36th Aerospace Sciences Meeting and Exhibit, Reno, NV, 12-15 January, 1998,

223. **Seifert, A., and Pack, L. G. (1999),** "Oscillatory Excitation of Unsteady Compressible Flows over Airfoils at Flight Reynolds Numbers", AIAA-99-0925, 37th AIAA Aerospace Sciences Meeting and Exhibit, Reno, Nevada, January 11-14, 1999.

224. **Selig, M. S., Guglielmo, J. J., Broern, A. P., and Giguere, P. (1996),** "Experiments on airfoils at low Reynolds numbers", AIAA-96-0062, 34th AIAA Aerospace Sciences Meeting and Exhibit, Reno, Nevada, January 15-18, 1996.

225. **Selig, M. S., Gopalarathnam, A., Giguere, P., and Lyon, C. A. (2001),** "Systematic Airfoil Design Studies at Low Reynolds Numbers," In *Fixed and Flapping Wing Aerodynamics for Micro Air Vehicle Applications, Progress in*

Astronautics and Aeronautics, Vol.195, Ed. Muller, T. J., Pub. American Institute of Aeronautics and Astornautics, pp.143-166.

226. **Shepshelovich, M., and Koss, D. (1980),** "Active Flow Control on Low Reynolds Number Airfoils", AIAA-90-3039, 8th AIAA Applied Aerodynamics Conference, Portland, Orlando, August 20-22, 1980.

227. **Shyy, W., Berg, M., and Ljungqvist, D. (1999),** "Flapping and Flexible Wings for biological and Micro Air Vehicles," *Progress in Aerospace Sciences*, Vol. 35, pp. 455-505.

228. **Smith, B. L. and Glezer, A. (1998),** "The formation and evolution of synthetic jets," *Physics of Fluids*, Vol. 10, No. 9, September, pp. 2281-2297.

229. **Smith, B. L. and Glezer, A. (1997),** "Vectoring and Small-Scale Motions Effected in Free Shear Flows Using Synthetic Jet Actuators", AIAA-1997-213, 35th Aerospace Sciences Meeting and Exhibit, Reno, NV, 6-9 January, 1997.

230. **Smith, B. L. and Swift, G. W. (2001),** "Synthetic Jets at Large Reynolds Number and Comparison to Continuous Jets", AIAA-2001-3030, 31st AIAA Fluid Dynamics Conference and Exhibit, Anaheim, CA, 11-14 June, 2001.

231. **Smith, D. R., Amitay, M., Kibens, V., Parekh, D. and Glezer, A. (1998),** "Modification of Lifting Body Aerodynamics Using Synthetic Jet Actuators", AIAA Paper 98-0209, January 1998.

232. **Smith, D. R. (2002),** "Interaction of a Synthetic Jet with a Crossflow Boundary Layer," *AIAA Journal*, Vol. 40, No. 11, November, pp. 2277-2288.

233. **Somers, D. M., Stack, J. P., and Harvey, W. D. (1982),** "Influence of Surface Static-Pressure Orifices on Boundary-Layer Transition", NASA Technical Memorandum 84492, NASA Langley Research Centre, July.

234. **Sumantran, V., Sun, Z., and Marchman III, J. F. (1985),** "Acoustic and Turbulence Influence on Low-Reynolds Number Wing Pressure Distributions", Conference on Low Reynolds Number Airfoil Aerodynamics, Notre Dame, Indiana, June, 1985.

235. **Sunada, S., and Kawachi, K. (2004),** "Effects of Reynolds Number on Characteristics of Fixed and Rotary Wings", *AIAA Journal* Engineering Notes, Vol.41, No.1, January, pp.189-192.

236. **Sunada, S., Yasuda, T., Yasuda, K. and Kawachi, K. (2002),** "Comparison of Wing Characteristics at an Ultralow Reynolds Number", *Journal of Aircraft*, Vol:39, No.2, March-April, pp. 331-338.

237. **Takahashi, T. T. (1997),** "On the decomposition of drag components from wake flow measurements," Paper AIAA-97-0717, 35th AIAA Aerospace Sciences Meeting and Exhibit, Reno, Nevada, January 6-9, 1997.

238. **Taleghani, B. K., and Campbell, J. F. (1999),** "Non-Linear Finite Element Modelling of THUNDER Piezoelectric Actuators," NASA Technical Memorandum TM-1999-209322, May.

239. **Taleghani, B. K. (2000),** "Validation of High Displacement Piezoelectric Actuator Finite Element Models," NASA Technical Memorandum TM-2000-210309, ARL-TR-2253, August.

240. **Tani, I. (1964),** "Low Speed Flows involving Bubble Separations," *Progress in Aeronautical Sciences*, Vol. 5, MacMillan Co., 1964.

241. **Thomas, R. H., and Chouhari, M., M. (2002),** "Flow and Noise Control: Review and Assessment of Future Directions," NASA TM-2002-211631.

242. **Torres, G. E., and Mueller, T. J. (2001),** "Aerodynamic Characteristics of Low Aspect Ratio Wings at Low Reynolds Numbers," In *Fixed and Flapping Wing Aerodynamics for Micro Air Vehicle Applications*, *Progress in Astronautics and* Aeronautics, Vol.195, Ed. Muller, T. J., Pub. American Institute of Aeronautics and Astornautics, pp.115-141.

243. **Torres, G. E., and Mueller, T. J. (2004),** "Low-Aspect-Ratio Wing Aerodynamics at Low Reynolds Numbers," *AIAA Journal*, Vol.42, No.5, May, pp.865-873.

244. **Torres, G., and Mueller, T. J. (2000),** "Micro Aerial Vehicle Development: Design, Components, Fabrication, and Flight-Testing", AUVSI Unmanned Systems 2000 Symposium and Exhibition, Orlando, Florida, July 11-13, 2000.

245. **Traub, L., Miller, A., Singla, P., Tandale, M., Junkins, J., and Rediniotis, O. (2004),** "Distributed Hingeless Flow Control and Rotary Synthetic Jet Actuation", AIAA-2004-0224, 42nd Aerospace Sciences Meeting and Exhibit, Reno, Nevada, January 5-8, 2004.

246. **Unal, M. F., Lin, J. C., and Rockwell, D. (1997),** "Force Prediction by PIV Imaging: A Momentum Based Approach," *Journal of Fluids and Structures*, Vol.11, pp. 965-971.

247. **Utturkar, Y., Holman, R., Mittal, R.,Carroll, B., Sheplak, M., and Cattafesta, L. (2003),** "A Jet Formation Criterion for Synthetic Jet Actuators," AIAA 2003-0636 41st Aerospace Sciences Meeting and Exhibit, Reno, NV, 6-9 January 2003

248. **Utturkar, Y., Mittal, R., Rampunggoon, P., and Cattafesta, L. (2002),** "Sensitivity of Synthetic Jets to the Design of the Jet Cavity", AIAA-2002-124, 40th AIAA Aerospace Sciences Meeting and Exhibit, Reno, NV, 14-17 January, 2002.

249. **Wang, F. H., Jiang, G. D., and Lam, K. (2004),** " A study of velocity fields in the near wake of a wave (varicose) cylinder by LDA", *Flow Measurement and Instrumentation*, January.

250. **Warner, E. P. (1922),** "Miniature Airplanes", N.A.C.A Technical Report No.141, September.

251. **Waszak, M. R., and Jenkins, L. N. (2001),** "Stability and Control Properties of an Aeroelastic Fixed Wing Micro Air Vehicle," AIAA 2001-4005 Atmospheric Flight Mechanics Conference, Montreal, Canada, 6-9 August 2001.

252. **Waterfield, G. (2003),** "High Performance Pre-stressed Piezoelectric Bender Actuator for Digital Valves," proceedings of the 105th Annual Meeting & Exposition of the American Ceramic Society, Nashville, Tenn., 27-30 April, 2003, pp.157.

253. **Watson, M., Jaworski, A. J., and Wood, J. N. (2002),** "Contribution to the Understanding of Flow Interactions Between Multiple Synthetic Jets", *AIAA Journal* Technical Note, Vol.41, No.4, August, pp747-749.

254. **Westerweel, J.,** "Fundamentals of digital particle image velocimetry," *Measurement Science Technology*, Vol.8, pp.1379-1392.

255. **Wieman, R., Smith, R. C., Kackley, T., Ounaies, Z., and Bernd, J. (2001),** "Displacement Models for THUNDER Actuators having General Loads and Boundary Conditions," NASA ICASE Contractor Report CR-2001-211061, September.

256. **Willert, C. E., and Charib, M. (1991),** "Digital particle image velocimetry," *Experiments in Fluids*, Vol.10, pp.181-193.

257. **Williams, D., Acharya, M., Bernhadt, J. and Yang, P. (1991),** "The Mechanism of Flow Control on a Cylinder with the Unsteady Bleed Technique", AIAA-1991-39, 29th Aerospace Sciences Meeting, Reno, NV, 7-10 January, 1991.

258. **Williams, D. and Papazian, H. (1991),** "Forebody Vortex Control with the Unsteady Bleed Technique", *AIAA Journal*, Vol. 29, No. 5, pp. 853-855.

259. **Wilson, C., Nutbean, J., and Bond, I. (2000),** "Aerodynamics and structural design of a solar-powered micro unmanned air vehicle", Proceedings of the Institute of Mechanical Engineers, Vol.214, Part G, pp.97-106.

260. **Winkelmann, A. (1990),** "Flow Field Studies Behind a Wing at Low Reynolds Numbers", AIAA-90-1471, AIAA 21st Fluid Dynamics, Plasma Dynamics and Lasers Conference, Seattle, WA, June 18-20, 1990.

261. **Wooding, C. L., and Gursul, I. (2003),** "Unsteady Aerodynamics of Low Aspect Ratio Wings at Low Reynolds Numbers", Royal Aeronautical Society CEAS Aerospace and Aerodynamics Research Conference, 10-12 June, 2003, London, UK.

262. **Woods, M. I., Henderson, J. F. and Lock, G. D. (2001),** "Energy requirements for the flight of micro air vehicles", Paper No. 2546, *The Aeronautical Journal*, March, pp.135-149.

263. **Wu, J.-Z., Lu, X.-Y., Denny, A. G., Fan, M., and Wu, J.-M. (1998),** "Post-stall flow control on an airfoil by local unsteady forcing", *Journal of Fluid Mechanics*, Vol.371, pp.21-58.

264. **Yarusevych, S., Kawall, J. G., and Sullivan, P. E. (2003),** "Effect of Acoustic Excitation on Airfoil Performance at Low Reynolds Numbers", *AIAA Journal* Technical Notes, Vol.41, No.8, August, pp.1599-1601.

265. **Yarusevych, S., Sullivan, P. E., and Kawall, J. G. (2003),** "Control of Airfoil Wake Structure at Low Reynolds Numbers by Acoustic Excitation", Paper AIAA-2003-4163, 33rd Fluid Dynamics Conference and Exhibit, Orlando, Florida, 23-26 June, 2003.

266. **Yoon, K. J., Park, K. H., Lee, S. K., Goo, N. S., and Park, H. C. (2004),** "Analytical design model for a piezo-composite unimorph actuator and its verification

using lightweight piezo-composite curved actuators," *Smart Materials and Structures*, Vol.13, pp.459-467.

267. **Yoon, K. J., Shin, S., Park, H. C., and Goo, N., S. (2002),** "Design and manufacture of a lightweight piezo-composite curved actuator," Technical Note, *Smart Materials and Structures*, Vol.11, pp.163-168.

268. **Zaman, K. B. M., Bar-sever, A., and Mangalam, S. M. (1987),** "Effect of acoustic excitation on the flow over a low-Re airfoil," *Journal of Fluid Mechanics*, Vol. 182, pp. 127-148.

269. **Zaman, K. B. M. (1992),** "Effect of Acoustic Excitation on Stalled Flows over an Airfoil," *AIAA Journal*, Vol. 30, No. 6, pp.1492-1499.

270. **Zheng, L., and Ramaprian, B. R. (2000),** "A Piezo-electrically Actuated Wing for a Micro Air Vehicle", AIAA-2000-2302, AIAA Fluids 2000 Conference, Fluid Dynamics Symposium, Denver, Colorado, June, 2000.